

MODELLING DIRECTIONAL SOLIDIFICATION

NAS8-34891

Final Report

1 June 1982 to 30 September 1985

Clarkson University

Potsdam, New York 13676

Principal Investigator: Dr. William R. Wilcox, Professor and
Chairman of Chemical Engineering
315-268-6650

Co-Investigator: Dr. Theodore S. Papatheodorou, formerly
Associate Professor of Mathematics and
Computer Science

Graduate Student Research Assistants:

Mr. R. Balart, Doctoral Candidate in Mathematics
and Computer Science

Ms. Rahda Sen Jayaraj, Doctoral Candidate in Chemical
Engineering (Completed May 1985)

Mr. Greg Neugebauer, M.S. Candidate in Chemical
Engineering (Completed May 1986)

Ms. Hilary Potts, M.S. Candidate in Chemical
Engineering (Completed May 1984)

Ms. Lorraine Ruggiano, Doctoral Candidate in Chemical
Engineering

(NASA-CR-179325) MODELLING DIRECTIONAL
SOLIDIFICATION Final Report, 1 Jun. 1982 -
30 Sep. 1985 (Clarkson Univ.) 11 p

N88-70725

Unclas
00/76 0133321

MODELLING DIRECTIONAL SOLIDIFICATION

NAS8-34891

Final Report

1 June 1982 to 30 September 1985

Clarkson University

Potsdam, New York 13676

Principal Investigator: Dr. William R. Wilcox, Professor and
Chairman of Chemical Engineering
315-268-6650

Co-Investigator: Dr. Theodore S. Papatheodorou, formerly
Associate Professor of Mathematics and
Computer Science

Graduate Student Research Assistants:

Mr. R. Balart, Doctoral Candidate in Mathematics
and Computer Science

Ms. Rahda Sen Jayaraj, Doctoral Candidate in Chemical
Engineering

Mr. Greg Neugebauer, M.S. Candidate in Chemical
Engineering

Ms. Lorraine Ruggiano, Doctoral Candidate in Chemical
Engineering

CONTENTS

	Page
Summary.....	1
1. Convection and heat transfer in the Bridgman-Stockbarger technique.....	3
2. Mathematical model of heat conduction in the Bridgman-Stockbarger technique.....	5
3. Melt behavior during solidification in space.....	6
4. Influence of solidification parameters on twinning.....	7
<u>Appendices</u> (Manuscripts, papers and thesis)	
A. Thermal fields in the Bridgman-Stockbarger technique	
B. Chaotic asymmetric convection in the Bridgman-Stockbarger technique	
C. Influence of heater configuration on convection in the Bridgman- Stockbarger technique	
D. A quasi-analytical solution to the steady state Bridgman-Stockbarger model	
E. Behavior of a non-wetting melt in free fall: experimental	
F. Behavior of a non-wetting melt in free fall: theoretical	
G. Twinning of dodecanedicarboxylic acid	

Acknowledgement

This report is the results of work carried out under NASA Contract NAS8-34891. This research effort was sponsored by NASA Headquarters Microgravity Science and Applications Division. Also, the authors would like to thank the Applications Payload Projects Office of the Spacelab Payload Projects Office, Marshall Space Flight Center, AL for their invaluable assistance in programming the total research effort over several years.

6. In space, a liquid which partially fills a non-wetted ampoule either separates into columns or traps a gas bubble on the wall. The gas bubble is unstable beyond a critical size which decreases as the contact angle increases.
7. In a triangular ampoule the liquid contacts the walls only over finite widths which decrease as the contact angle increases.
8. In dodecanedioc acid (DDA) the number of twins increases with increasing temperature gradient, increasing freezing rate, and increasing impurity content when the impurity molecules are similar in size and shape to DDA.

convection observed in the melt.

2. Experimental

The design of the transparent model of a Bridgman-Stockbarger apparatus used in the present work evolved from that used by Potts [11,12]. The convective flows she observed suggested that the thermal field surrounding the sample was not perfectly axisymmetric. However the nature of her set-up precluded any attempt at controlling the azimuthal temperature field. Our goal in redesigning Potts's apparatus was therefore to build a furnace in which the azimuthal temperature field could be both measured and controlled. We used a clear plastic furnace in which was embedded vertical nichrome wires [13]. Since the ampoule was heated by conduction, the thermal asymmetries created by the convecting media were eliminated. Also, because the heating wires were mounted vertically rather than helically, the symmetry of the azimuthal temperature profile could be accurately controlled by supplying different amounts of power to groups of wires.

Our apparatus consisted of a main heater on top, a circulating cooling bath below, and a short independently controlled booster heater between. The booster heater could be used to create a steep axial temperature gradient near the interface. It also afforded additional control over the position of the melt-solid interface. The Pyrex ampoule contained salol, mp 43.2°C , and had an inner diameter of 30 mm and a wall thickness of 4 mm. (The physical properties of salol are summarized in Table 1.) The lower portion of the apparatus was immersed in a 2 liter tempering beaker which served as a circulating cooling bath. The cooling bath stood on a magnetic stirrer. Agitation of the coolant in the beaker was sufficient such that no temperature variations over 0.2°C were recorded throughout

the bath.

The temperatures in the heaters and cooler were measured using Teflon-coated copper-constantan thermocouples (AWG=36, diameter=0.005 inch). The thermocouples were connected through a selector switch to a digital thermometer with a built-in electronic ice point. Temperatures were read to $\pm 0.1^{\circ}\text{C}$. The thermocouples were attached to the outer wall of the sample ampoule as shown in Figure 1.

Convection was revealed in the melt using sublimated sulfur tracer particles and streak photography. Under low power magnification, the sulfur particles appeared as irregularly shaped flakes. The maximum dimension of a flake was $0.054 \pm 0.010\text{mm}$. In order to visualize convection within the core of the melt, it was necessary to illuminate a relatively narrow slab down the center of the melt. This was done using a light-slit technique similar to that described by Schwabe and Scharmann [14]. The light source was a 0.5 mW He-Ne laser. Approximately 3 cm from the laser was a cylindrical lens which elongated the beam. Approximately 50 cm away was a second cylindrical lens which focused the beam into a slit. At 90 cm from the laser, the light slit entered the top of the apparatus and shined straight down through the melt. At the top of the furnace, the light slit was shaped like an elongated ellipse, with a major axis of 31 mm and a minor axis of 5 mm.

Convection studies were begun after temperatures in the heaters and the cooler varied less than 0.2°C over a one hour period. The convective streamlines in the melt were visualized by photographically recording the pathlines of the sulfur suspended in the melt. After steady state conditions were reached, 2 to 3 mg of sublimated sulfur particles were sprinkled into the melt. The upper portion of the melt

was mildly agitated with a stirring rod in order to disperse the sulfur. Visual inspection of the melt revealed that approximately 75% of the sulfur remained suspended for 3 hours, and approximately 25% remained suspended for at least 24 hours.

Pictures were taken using a Nikon FM2 camera with a 55 mm Nikon Micro-Nikkor macro lens mounted on a tripod. The shutter was manually operated with a remote cable release. Exposures ranged from 2s to over 2 minutes. The velocities of the particles in the melt were calculated from the length of the streaks on the photograph caused by the motion of the particles, the magnification, and the length of the exposure.

SUMMARY

The overall objective of this research was to elucidate phenomena of importance to directional solidification in space. We used a combination of theory, laboratory experiments, and experiments in the KC135. The research has produced 5 papers, a completed Ph.D. thesis, progress toward another Ph.D. thesis, a completed M.S. thesis, the major part of another M.S. thesis, and the beginning of a Ph.D. project. The latter M.S. thesis is included here as an appendix. It will yield one paper. When the second Ph.D. thesis is complete it will result in several papers.

Conclusions of our research are as follows:

1. In the vertical Bridgman-Stockbarger technique (BS), convection is often non axi-symmetric and may not be steady, even when very gentle. (See Appendix B).
2. Convection in BS depends critically on the vertical and circumferential temperature variations in the heater. For example, the convection near the solid-liquid interface increases as the vertical temperature gradient becomes more negative. (See Appendix C).
3. When the temperature increases with height in BS there may be negligible convection near the freezing interface and the interface remains planar over a wide range of vertical positions. (See Appendix C).
4. In moderate Prandtl number melts the temperature field and the interface shape in BS are sensitive to convection. (See Appendix A).
5. The two-dimensional temperature field in BS with conduction only may be computed rapidly using our new methods. (See Appendix D).

3. Results

Chang and Brown's [7] and Carlson et al.'s [9] theoretical investigations of the Bridgman technique assumed that the temperature of the furnace was constant. In the typical Bridgman-Stockbarger configuration the temperature of the furnace actually reaches a maximum about half way up. Since, in the lower half, convection is inhibited by the stabilizing axial temperature gradient, this configuration is often referred to as the vertically stabilized configuration. The buoyancy driven convection that is predicted in the vertically stabilized configuration is caused by radial temperature gradients in the melt. These gradients arise from heat transfer between the sample and the surrounding furnace. In an actual Bridgman-Stockbarger set-up the radial temperature gradients may not be sufficient to cause convection.

If the positions of the heating and cooling furnaces are switched, solidification occurs when the sample is translated from the heater up into the cooler. In this configuration, the axial temperature gradient near the freezing interface is destabilizing because the temperature in the melt decreases with height. Since both the axial and the radial gradients promote buoyancy driven convection, convective velocities are much larger than when the heater is on top.

A short booster heater inserted between the main heater and the cooler can be used to control convection in the stabilized configuration (melt on top). As power to the booster is increased, the position of the maximum temperature moves downward until it is just above the interface. When this occurs, the axial temperature gradient is destabilizing throughout, promoting convection in much the same manner as if the heater was on the bottom and the cooler on top.

Therefore, if a Bridgman furnace with a booster heater is used, it may be either thermally stabilizing or destabilizing depending on the power supplied to the booster.

Figure 2a is a typical plot of the temperature vs. height as measured at the outer wall of the sample ampoule for a stabilized condition near the interface. The convection produced by this temperature profile is shown ^(if) Figure 2b. A schematic representation of this convection showing the velocities is given in Figure 2c.

Figure 3a is a typical temperature profile for another run when the power supplied to the booster was much greater. Since a maximum in temperature was produced near the interface, this condition is typical of a destabilized condition. The resulting convective velocity field is pictured in Figure 3b and shown schematically in Figure 3c. Other temperature profiles at the outerwall of the sample ampoule and schematic velocity profile sketches are shown in Figures 4 to 9.

For comparative purposes, several dimensionless groups which describe this system are summarized. The Prandtl number, $Pr = \mu C_p / k$, of salol is approximately 15. The Grashof may be defined as $Gr = R^3 g \beta \Delta T / \nu^2$. For this system $Gr = 6.19 \times 10^4 \Delta T$ where ΔT is a characteristic temperature difference. The Peclet number is defined by $Pe = \rho R C_p V / k = 3.46 \times 10^2 V$ where V is a characteristic convective velocity in mm/s.

4. Discussion

Two basic convective flow regimes, characteristic of the temperature profile in the furnace, were observed. A typical convection pattern for the vertically stabilized condition is shown in Figure 2. The flow field in this figure is divided into two regions. In the upper half of the melt, convective velocities on the order of 1 mm/s were typical. In the lower half of the melt, the suspended sulfur particles moved at a rate of 0.03 to 0.05 mm/s. The movement in the lower half was imperceptible to the eye and could only be visualized with a time exposure photograph at least 30 seconds long. In the vertically destabilized condition, the flow field was again divided into two regions, upper and lower counter rotational sections. In both the upper and lower areas of the melt, convective velocities were on the order of 1 mm/s.

The velocity sketches in Figure 4b exemplify the behavior of the convection in the vertically stabilized condition. When viewed from the front, the flow in the upper portion of the melt consisted of a single circular cell with flow velocities of 1 mm/s being typical. When viewed from the side, the flow bore no relation to the flow observed from the front, although the magnitude of the convective velocities was the same. The temperature profiles, ³8a to ⁹10a, show that the temperature of the ampoule at the top of the furnace decreased with height. This destabilizing temperature gradient was probably the major driving force for convection in the upper portion of the melt. The very slow motion of the sulfur particles in the lower portion of the melt indicated that the convection there was nearly nonexistent.

All long exposure photographs of convection in the vertically

stabilized configuration showed that the sulfur moved vertically at a rate of 0.03 to 0.05 mm/s in the lower portion of the melt. As noted above, this motion was imperceptible to the eye. The streaks traced by the sulfur particles in this region of the melt were so uniform, both in magnitude and direction, that they probably were an indication of sedimentation of sulfur in an undisturbed melt.

Although the sedimentation of the sulfur was uniformly downward throughout the lower half of the melt, the streaklines showed a definite curvature within 1 cm of the interface. This is clearly shown in the photograph in Figure 2b. Although the streaks are curved, their lengths, under steady state conditions, yield an extremely slow velocity, approximately 0.05 mm/s. Convection this slow near the interface was difficult to resolve photographically due to overexposure of the film.

The second basic flow regime observed in this work was that associated with the thermally destabilized profile created by the booster heater. The major features of this type of flow are summarized in Figure 3b. The flow in this figure can be divided into two regions. In the lower region the flow rises at the wall and descends in the center. In the upper region the flow descends at the wall and rises in the center. As in the destabilized condition, the flow was complex and usually couldn't be characterized solely on the basis of one view. The two exceptions are the results shown in Figures 7b and 8b. In these runs, convection was so symmetrical that both views, front and side, presented the same flow field.

Even though the flow patterns in Figures 7b and 8b are highly symmetrical, a measurable azimuthal thermal asymmetry nevertheless existed in the heater. The question this raises is, how large a

thermal asymmetry is necessary to destroy the symmetrical character of the flow? A comparison of Figure 6b and Figure 8b indicates that very little thermal asymmetry was necessary to completely destroy the symmetrical behavior of the flow.

The azimuthal temperature variation was characterized by calculating the standard deviation of the temperatures measured by the circumferentially mounted thermocouples. The difference in the standard deviation of the temperatures indicated by thermocouples 4 to 7 between Figures 6b and 8b is only 0.1 °C. (Thermocouple 6 failed to operate, therefore the standard deviation of these temperature measurements has only two degrees of freedom.) The standard deviations of the temperatures read by thermocouples 8 to 11 are the same in Figures 6b and 8b. Even though the magnitude of the azimuthal temperature variations is nearly the same in these two runs, there are great differences in the symmetry of the flow. Since temperature was measured at the outer wall of a 4 mm thick Pyrex ampoule, the measured thermal asymmetry was probably greater than that felt by the melt, because the ampoule should have dampened out the thermal asymmetry by conduction. In any case, no clear boundary emerged from this work about the minimum thermal asymmetry which will produce asymmetrical convection, although it is probably small, on the order of 1 °C at the outer wall of the thick-walled ampoule.

In the run pictured in Figure 9 a thermal asymmetry of several degrees was created. In agreement with the work of Potts [10,11], the melt rose along the hot portion of the ampoule and descended along the cooler side.

Figures 2a to 9a are plots of the temperature of the outer wall of the sample ampoule versus vertical position. The location of the

melt/solid interface was measured from the photographs and is noted in these figures. From these plots, the temperature of the outer wall of the ampoule at the point where the interface intersects the inner wall could be read directly. Were there no temperature difference across the ampoule, the temperature at the outer wall would be equal to the melting point of the sample material. As shown in Table 2, there was often a significant difference between the outer wall temperature adjacent to the interface and the melting point of the sample material. (The melting point of a fresh sample of phenyl salicylate was 43.0 to 43.5 °C. The phenyl salicylate used in the convective studies had been in the molten state for over a month and had a melting point of 41.0 to 43.0 °C. Degradation of this organic compound was therefore minimal.)

An interesting feature about the outer wall temperature adjacent to the interface is that no wall temperature was significantly less than the observed experimental melting point, but several were nearly 10 °C larger. Figure 7a yields an outer wall temperature 13.7 °C over the experimental melting point range. Significant deviations are noted in Figures 3a, 8a, and 9a as well. These figures correspond to the destabilized condition, with convection throughout the entire melt.

These data suggest that the temperature difference across the ampoule wall was often large. Under conditions in which mixing of the melt is significant, the effective Biot number on the melt side of the tube is increased due to the increased convective heat transfer within the melt. When convective mixing is large, the relatively cool fluid from the upper regions of the furnace descends through the center of the melt and rises along the walls of the ampoule. This cools the

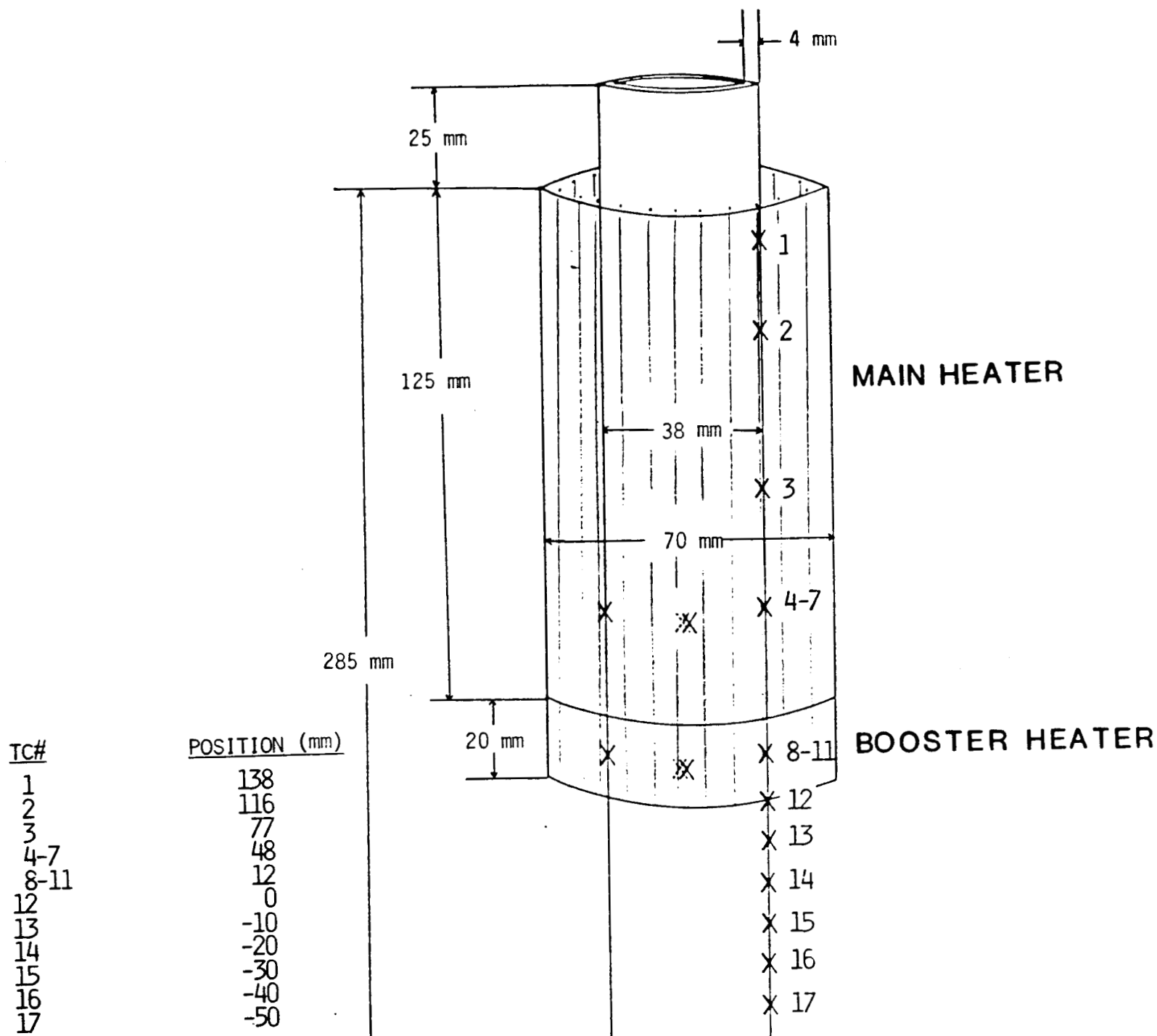


Figure 1. Schematic diagram of apparatus. "X" denotes the position of a thermocouple (TC). The positions of the thermocouples are measured from the bottom of the booster heater. Thermocouples 4 to 7 and 8 to 11 were circumferentially mounted and were equally spaced. TC# 4 and TC# 8 were mounted on the front of the furnace. Thermocouples 1 to 3 and 12 to 17 were actually positioned on the rear of the furnace but are pictured as being on the side for clarity. The furnace and booster heater each contained 27 nichrome heating wires spaced 8.1 mm apart.

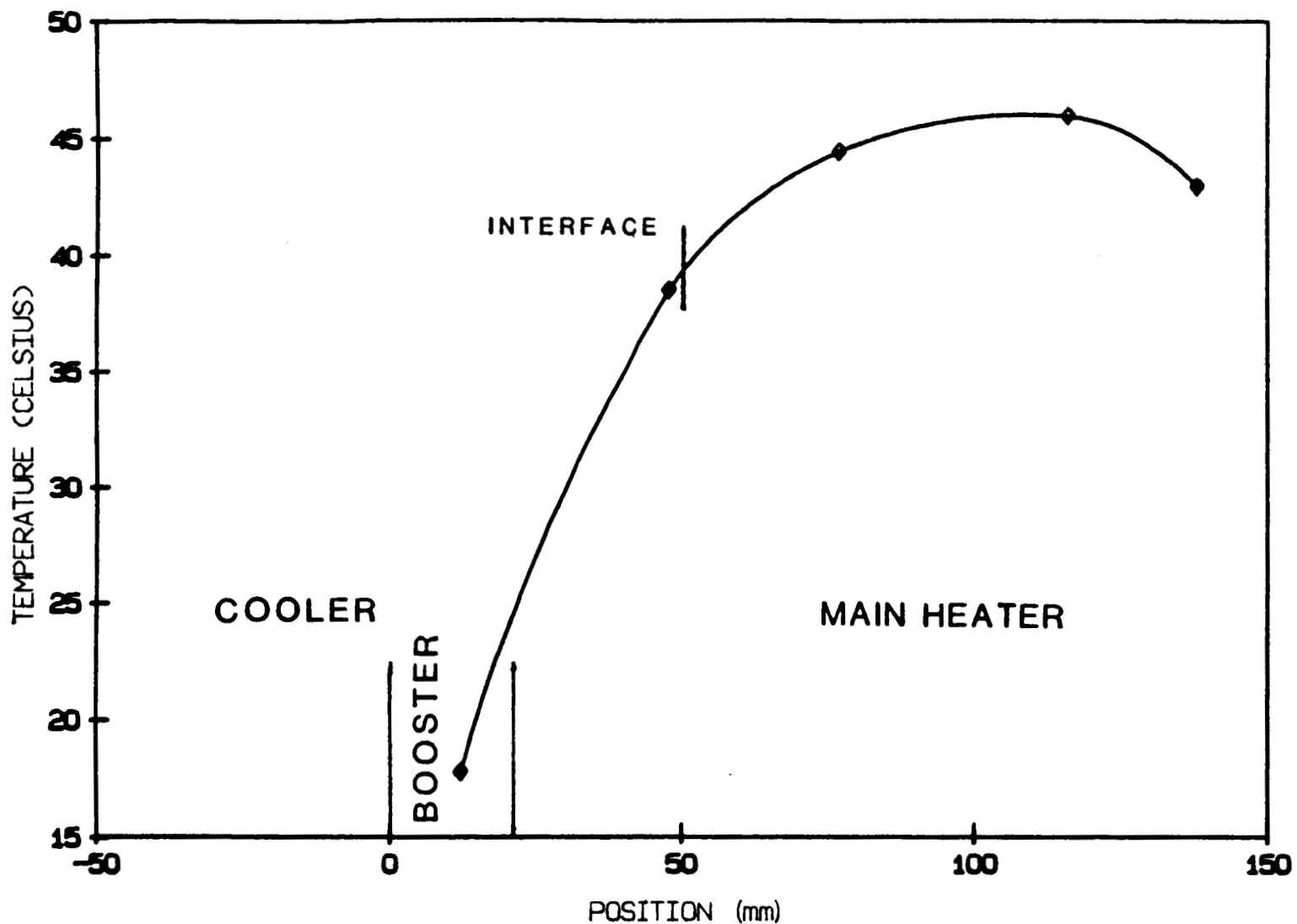
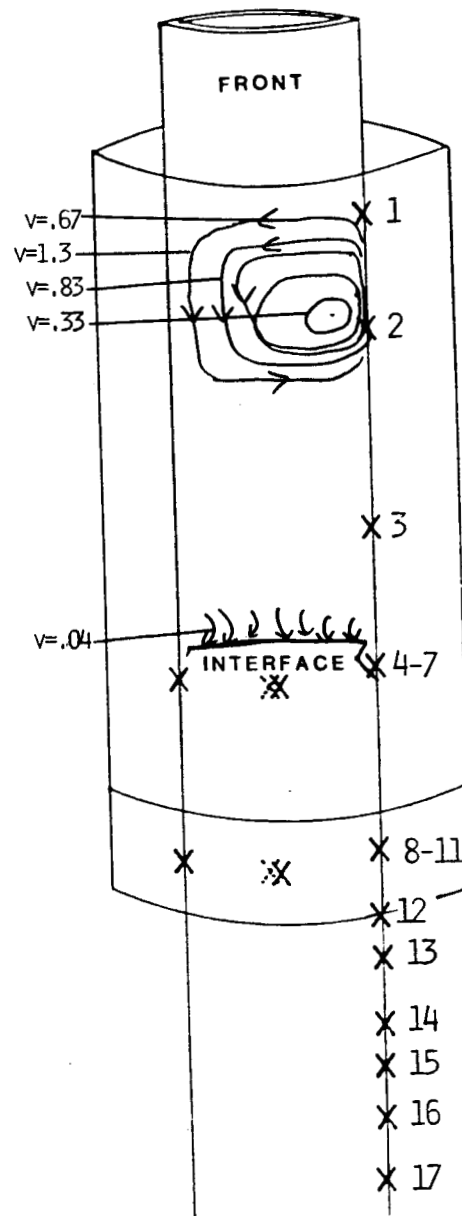


Figure 2a. Temperature of the outer wall of the Pyrex sample ampoule vs. vertical position for run I-44. The location of the melt-solid interface was 48.5 mm above the bottom of the booster heater. The temperature of the cooling bath was 1.5 °C.



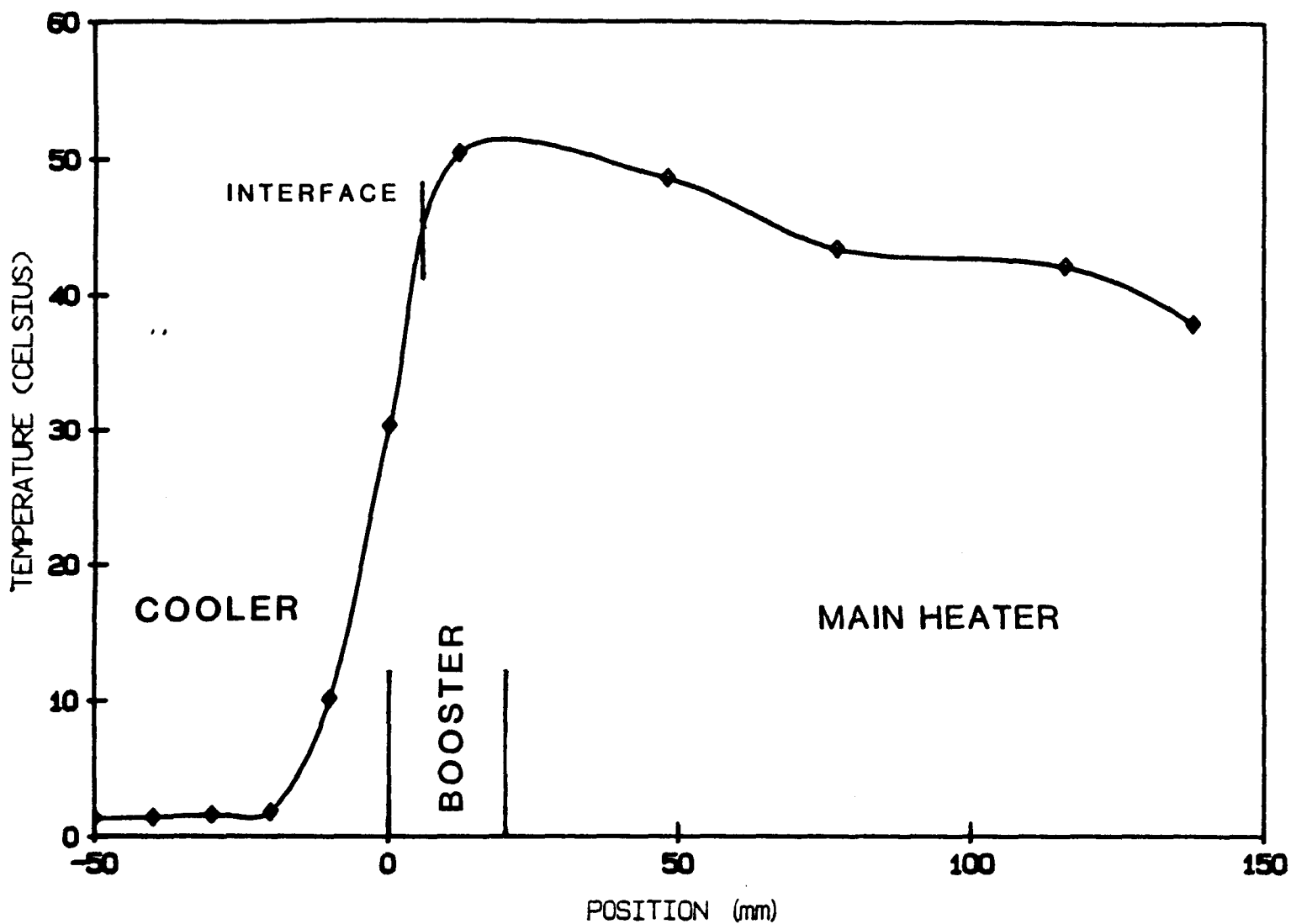


Figure 3a. Temperature of the outer wall of the Pyrex ampoule vs. vertical position for run I-21. The location of the melt-solid interface was 5.8 mm above the bottom of the booster heater. The temperature of the cooling bath was 1.4 °C.

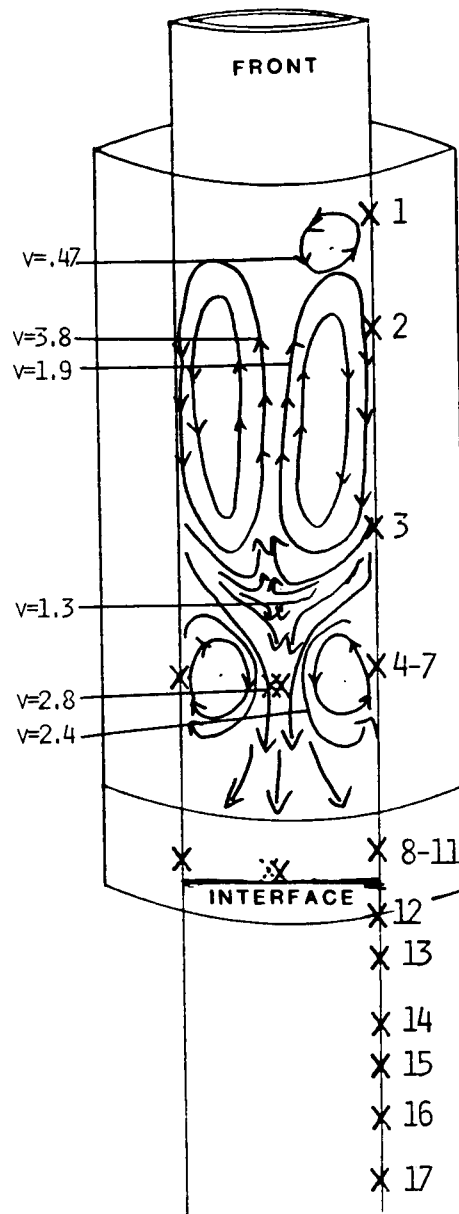
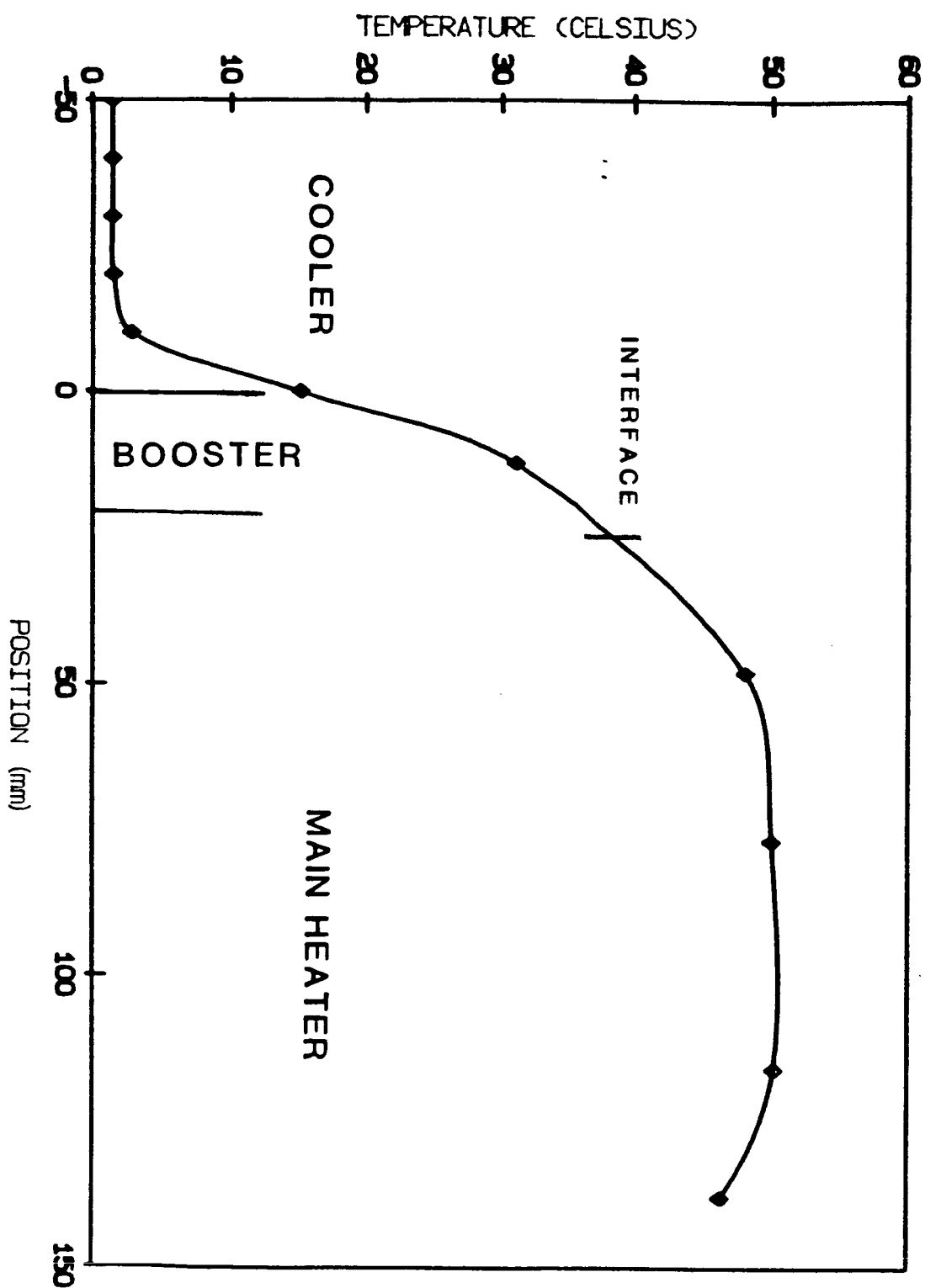
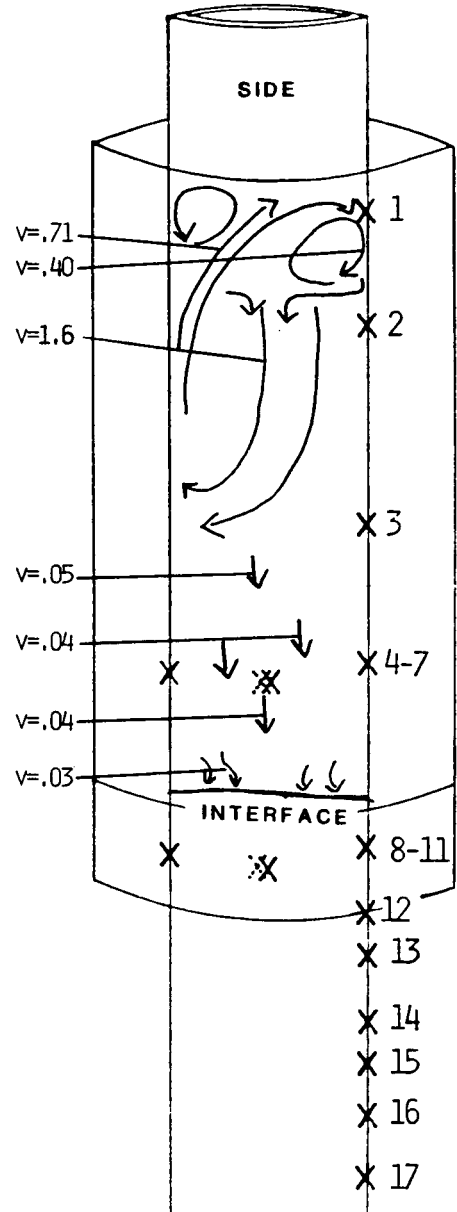
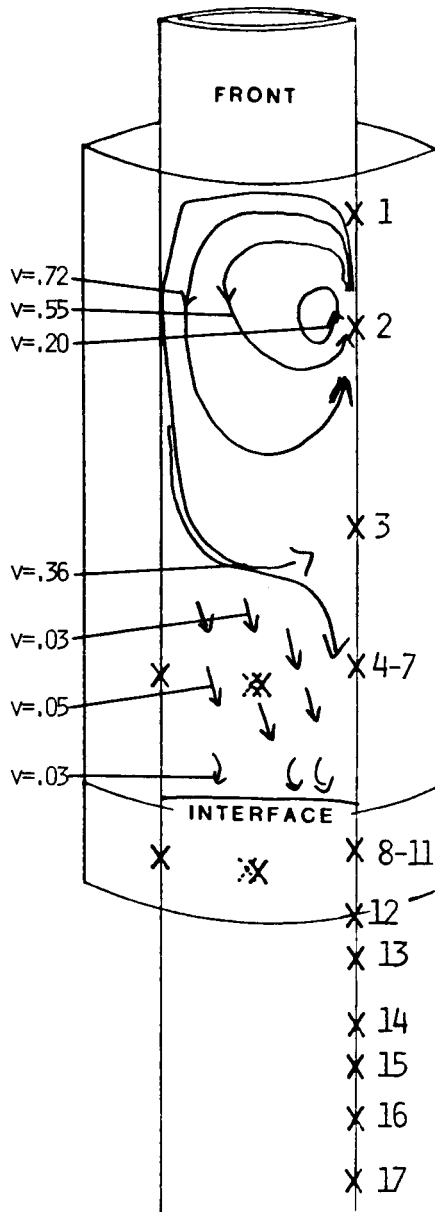


Figure 4a. Temperature of the outer wall of the Pyrex sample ampoule vs. vertical position for run I-47. The location of the melt-solid interface was 25.8 mm above the bottom of the booster heater. The temperature of the cooling bath was 1.4 °C.





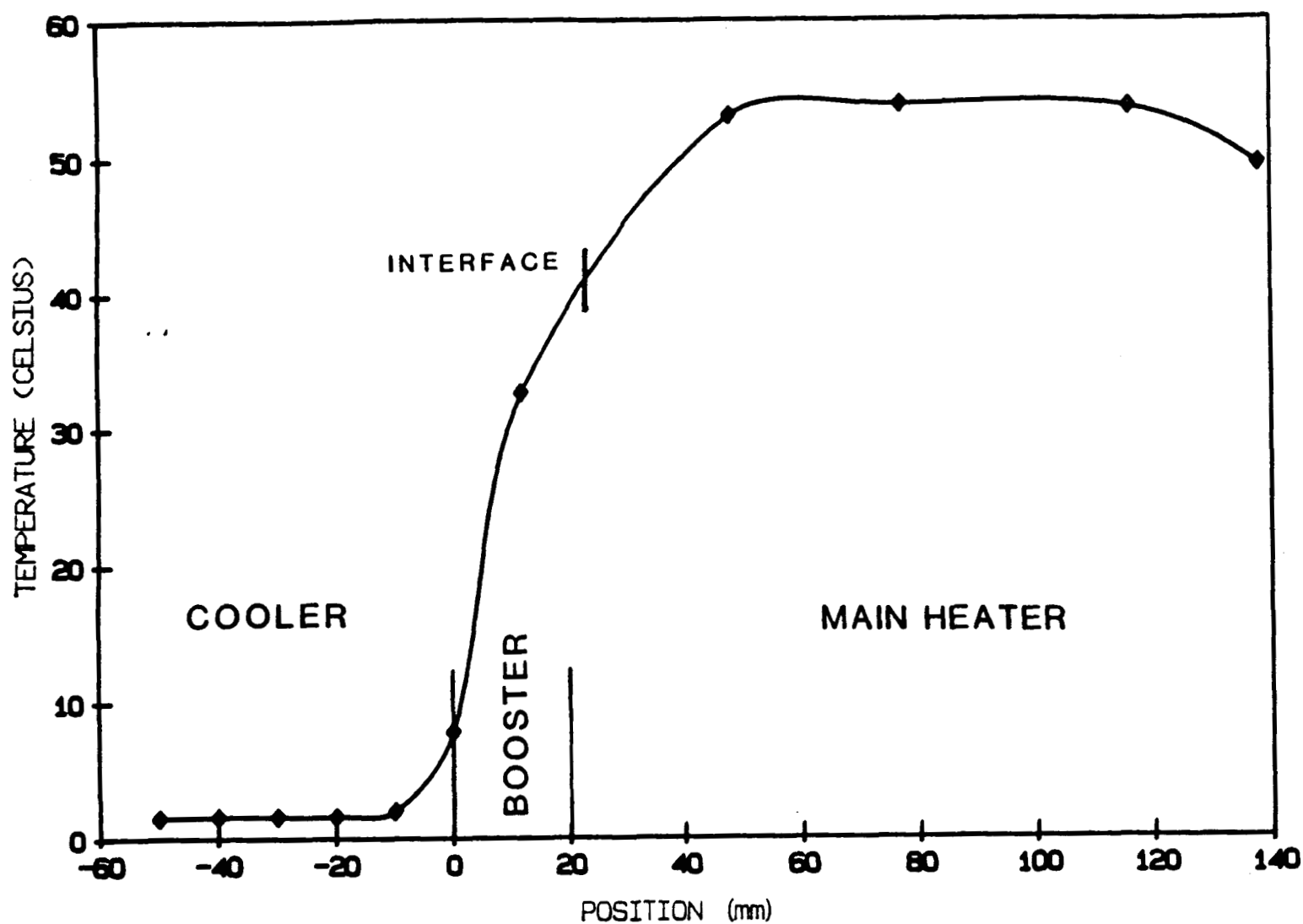


Figure 5a. Temperature of the outer wall of the Pyrex sample ampoule vs. vertical position for run I-49. The location of the melt-solid interface is 23.3 mm above the bottom of the booster heater. The temperature of the cooling bath was 1.5 °C.

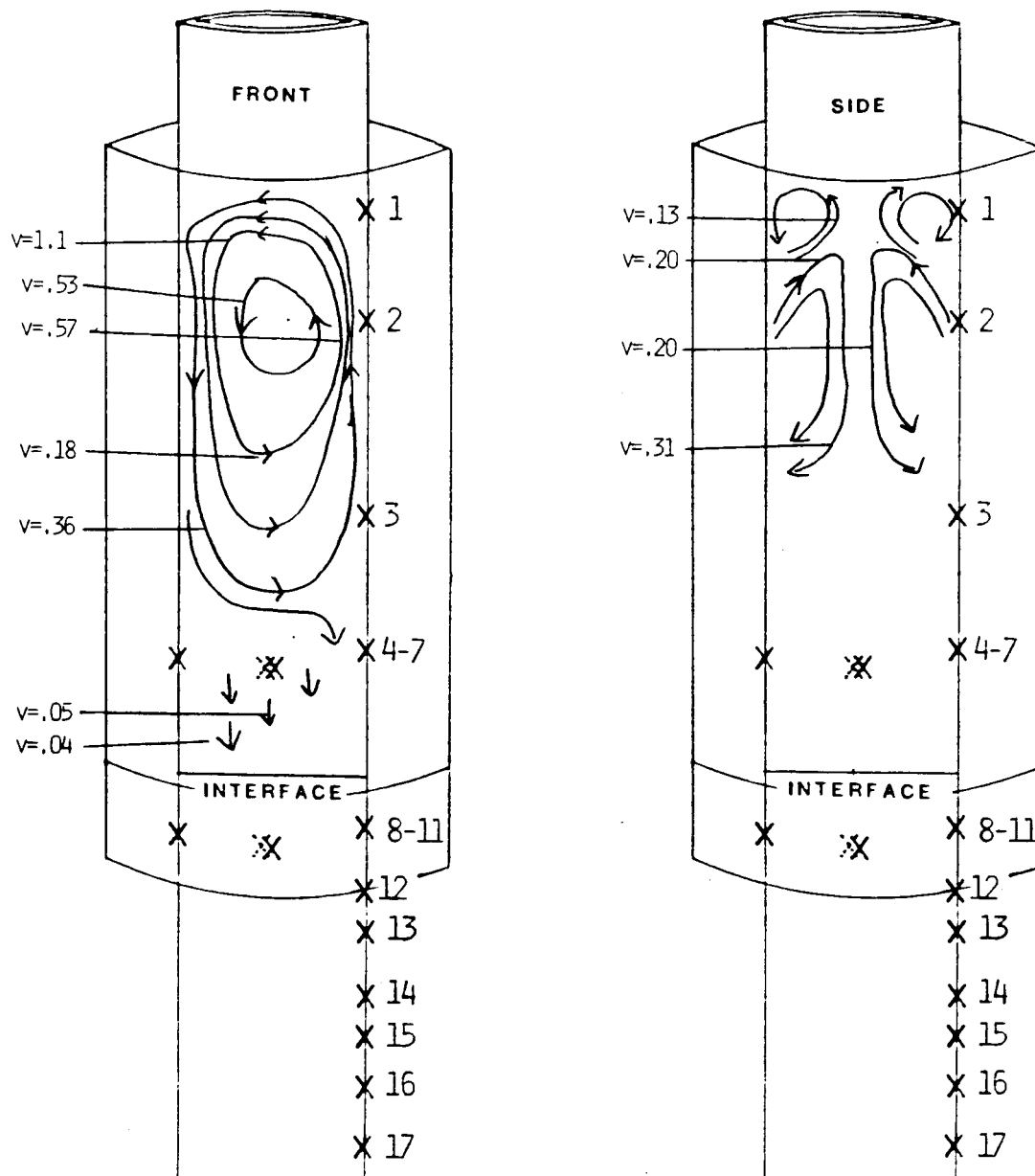


Figure 5b. Schematic representation of the convective velocity field corresponding to the temperature profile in Figure 5a. Velocities are in mm/s.

TC# Temp (°C)

1 49.4
2 53.6
3 53.8
--
4 53.4
5 53.2
6 --

7 52.4 $\bar{T} = 53.0 \pm 0.5$

--
8 32.6
9 32.8
10 33.0

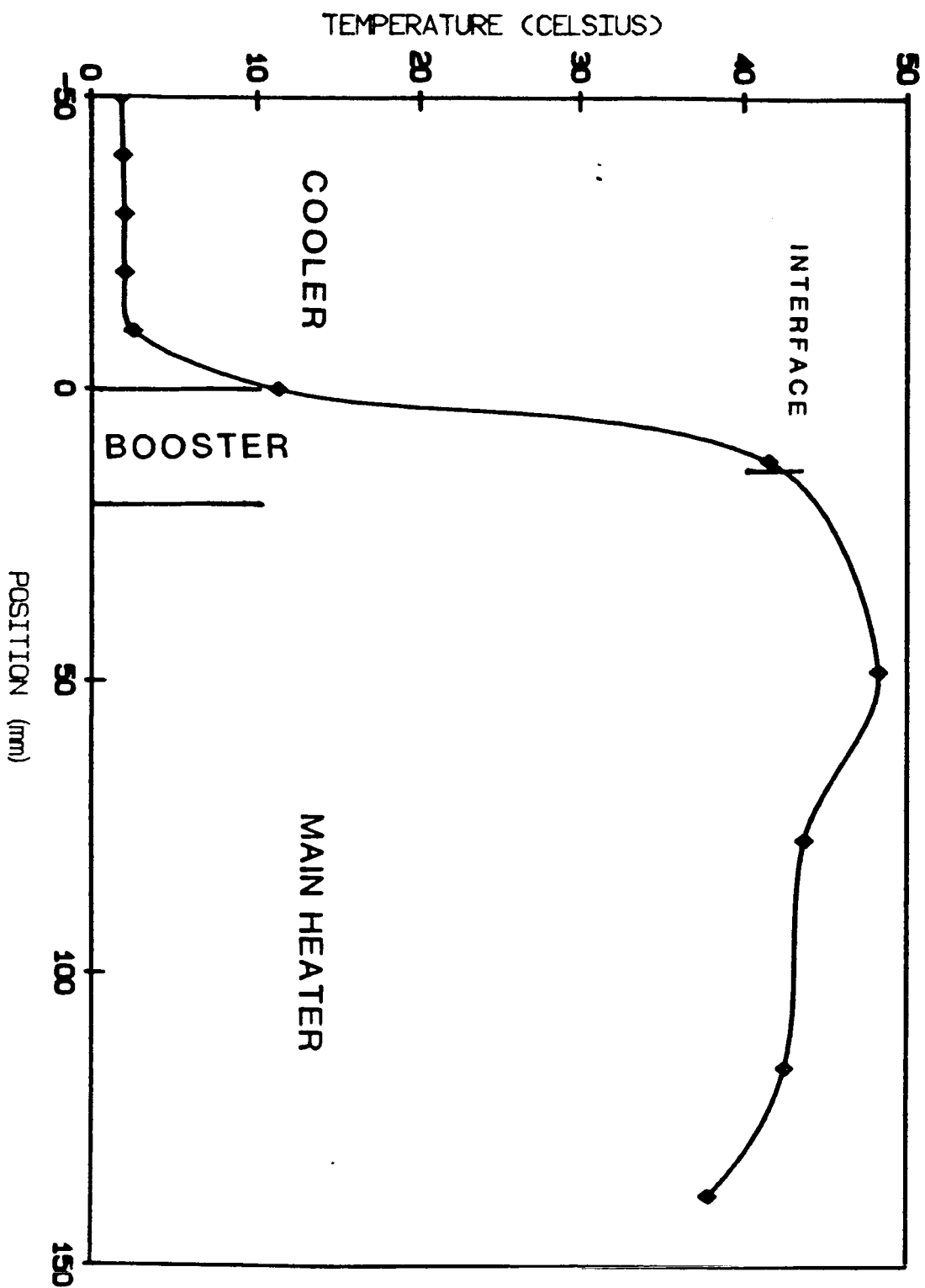
11 32.4 $\bar{T} = 32.7 \pm 0.3$
--

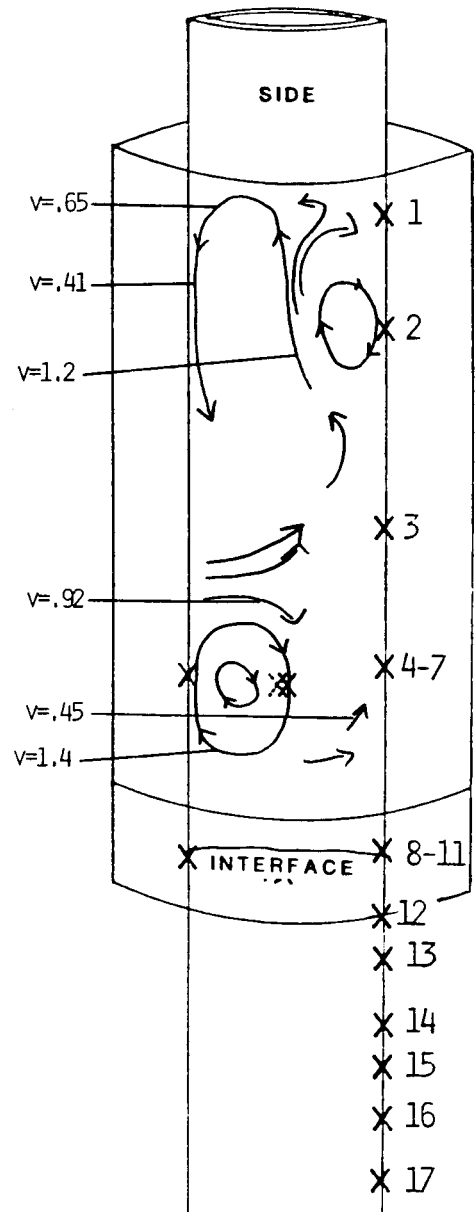
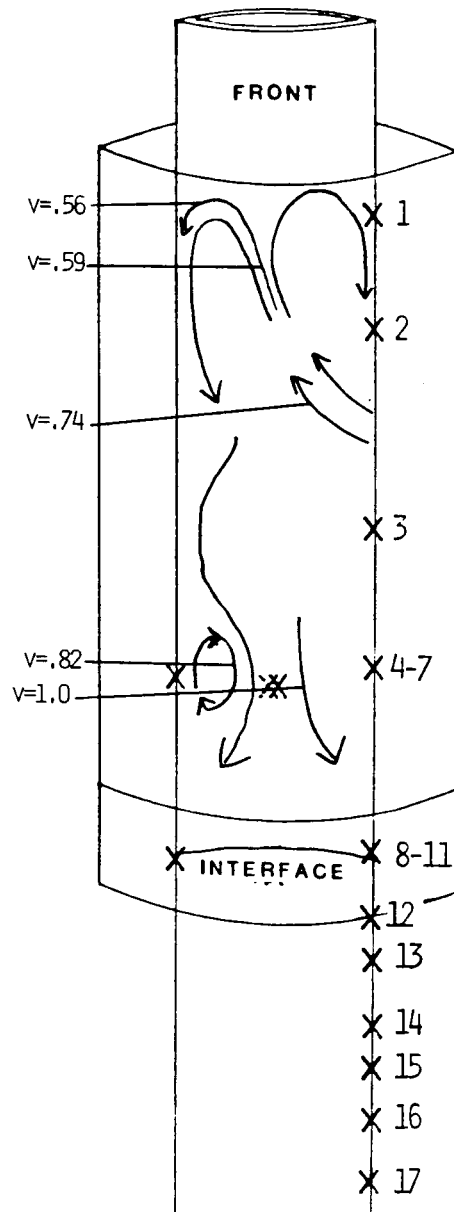
TC# Temp (°C)

12 7.8
13 2.0
14 1.6
15 1.6
16 1.6
17 1.5

bath temp = 1.5

Figure 6a. Temperature of the outer wall of the Pyrex sample ampoule vs. vertical position for run I-52. The location of the melt-solid interface was 13.6 mm above the bottom of the booster heater. The temperature of the cooling bath was 1.5 °C.





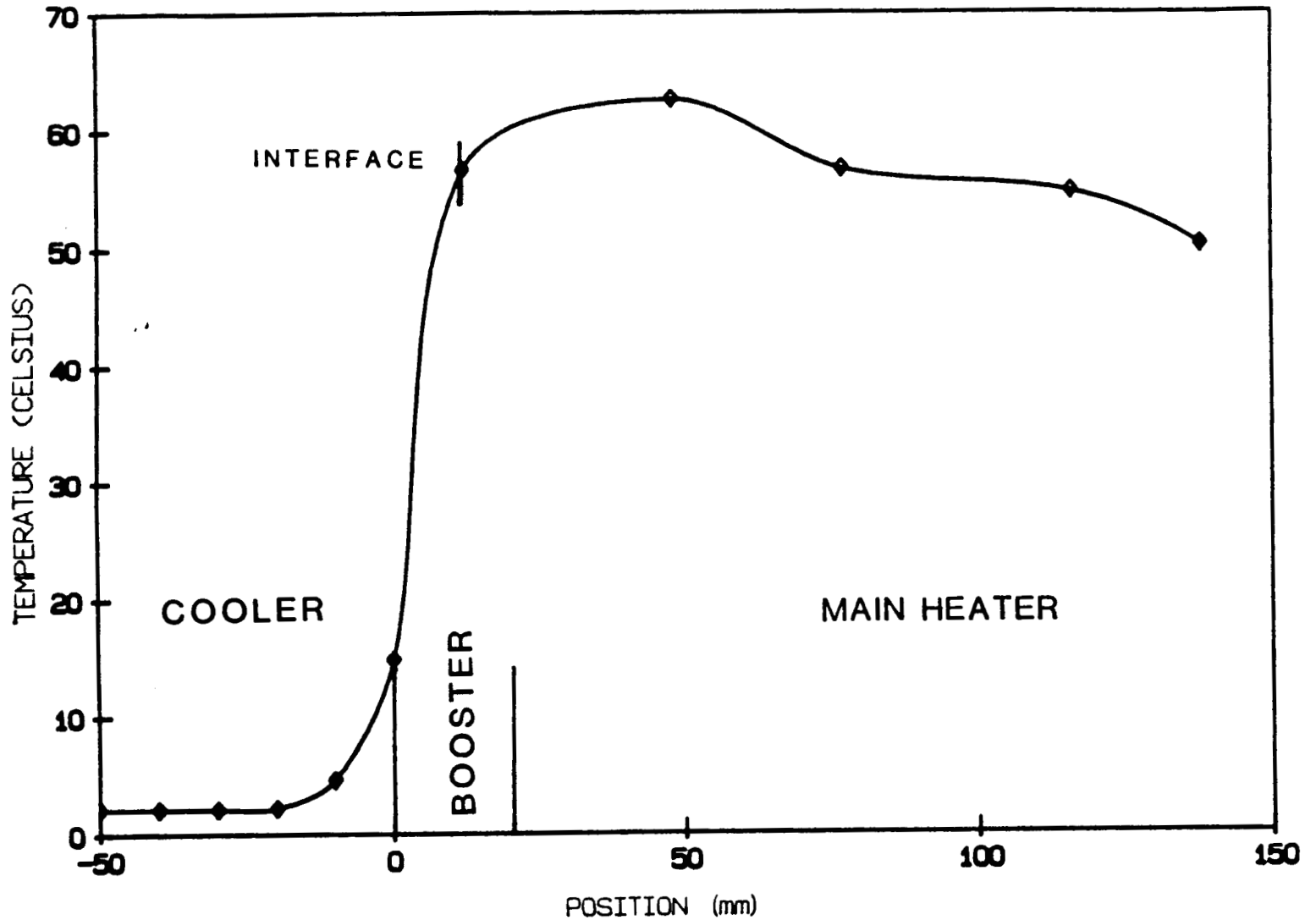


Figure 7a. Temperature of the outer wall of the Pyrex sample ampoule vs. vertical position for run I-62. The location of the melt-solid interface was 13.2 mm above the bottom of the booster heater. The temperature of the cooling bath was 1.9 °C.

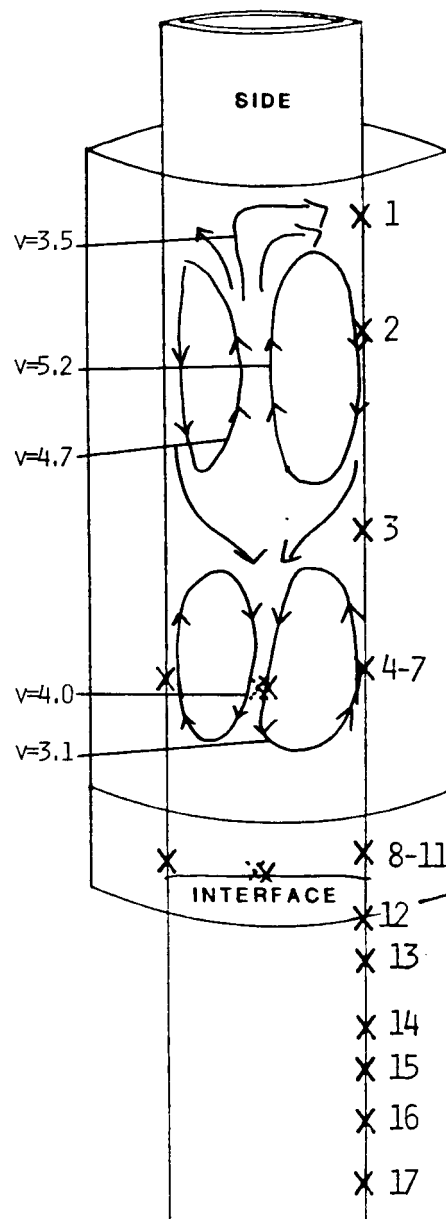
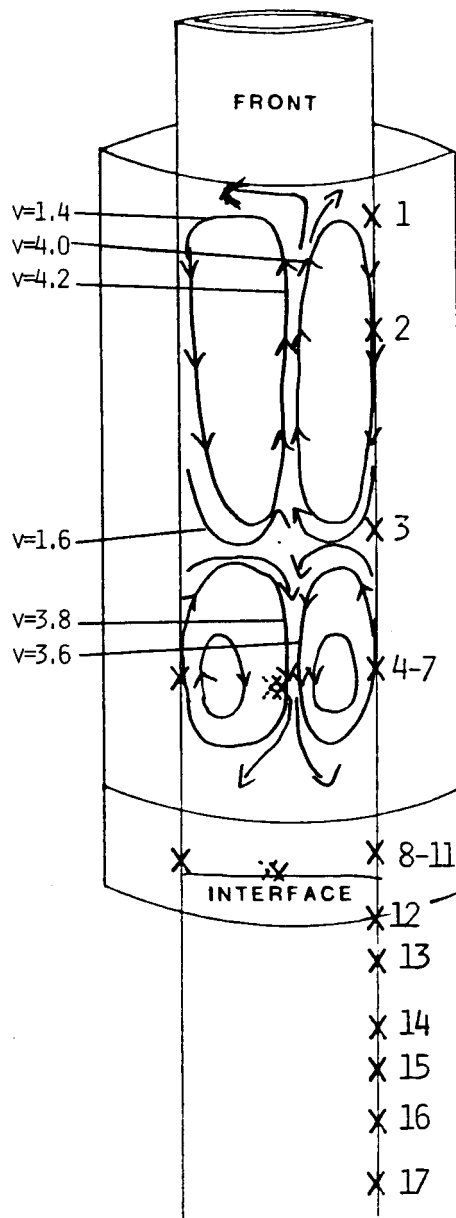
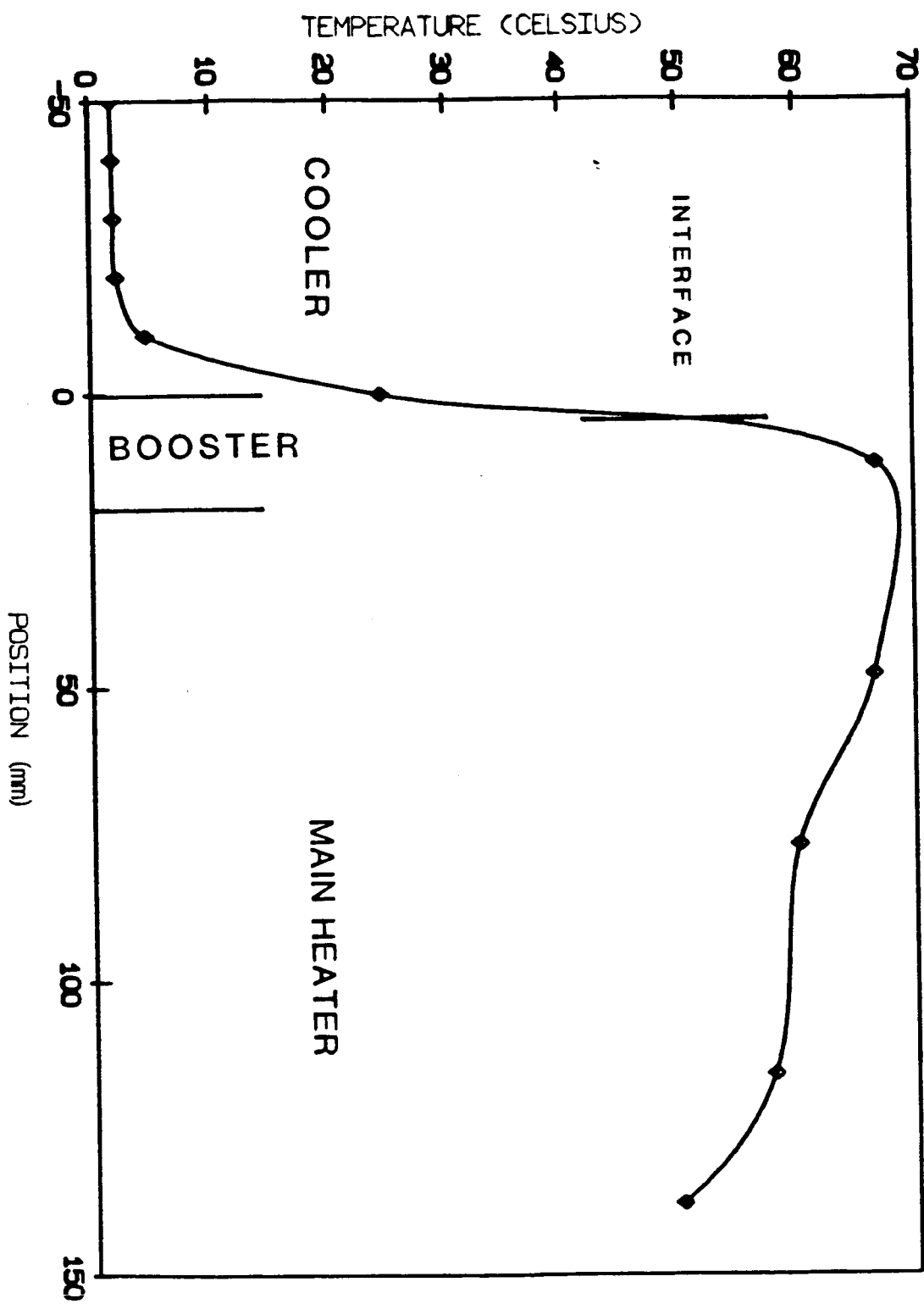


Figure 8a. Temperature of the outer wall of the Pyrex sample ampoule vs. vertical position for run I-55. The location of the melt-solid interface was 4.7 mm above the bottom of the booster heater. The temperature of the cooling bath was 1.3 °C



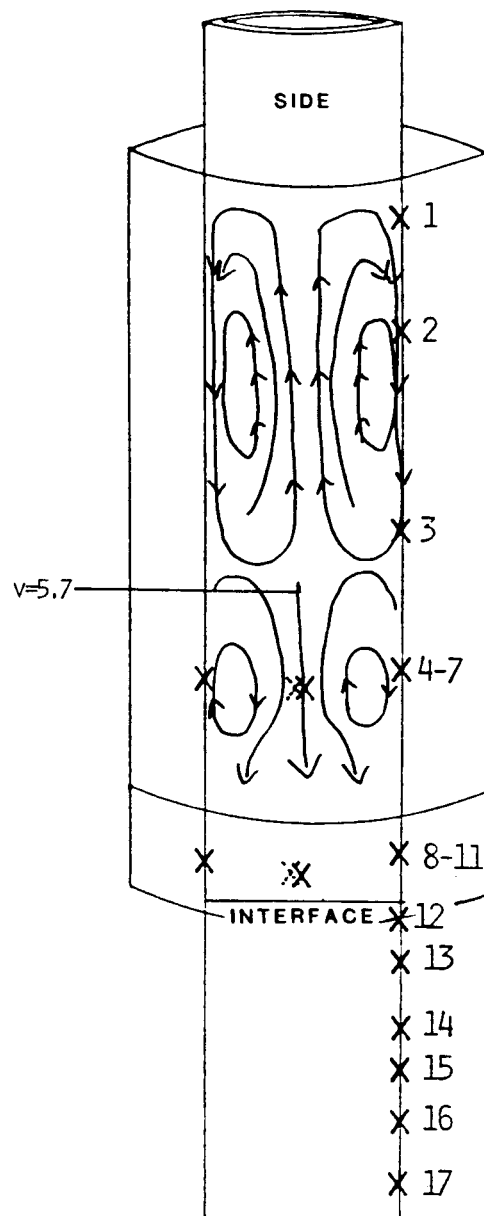
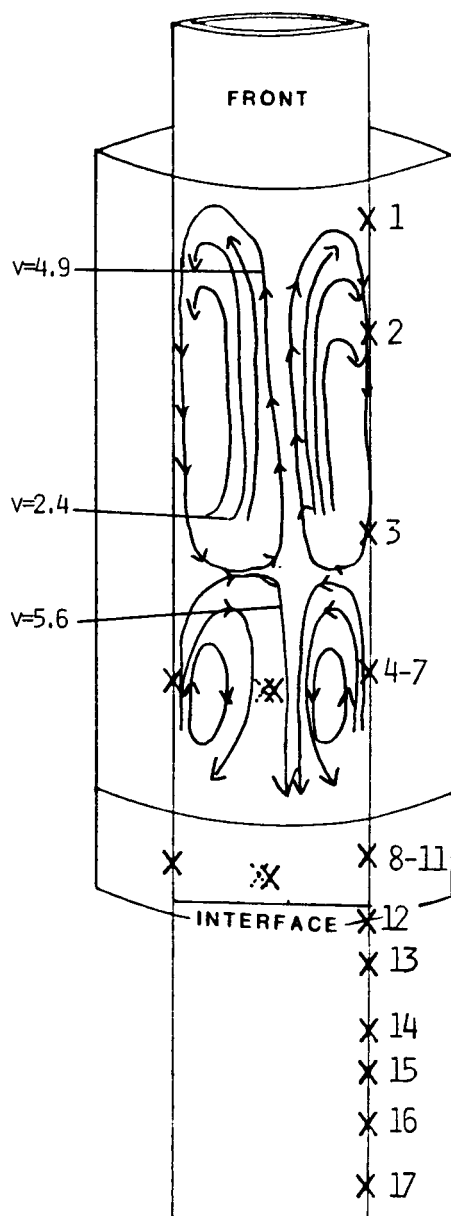
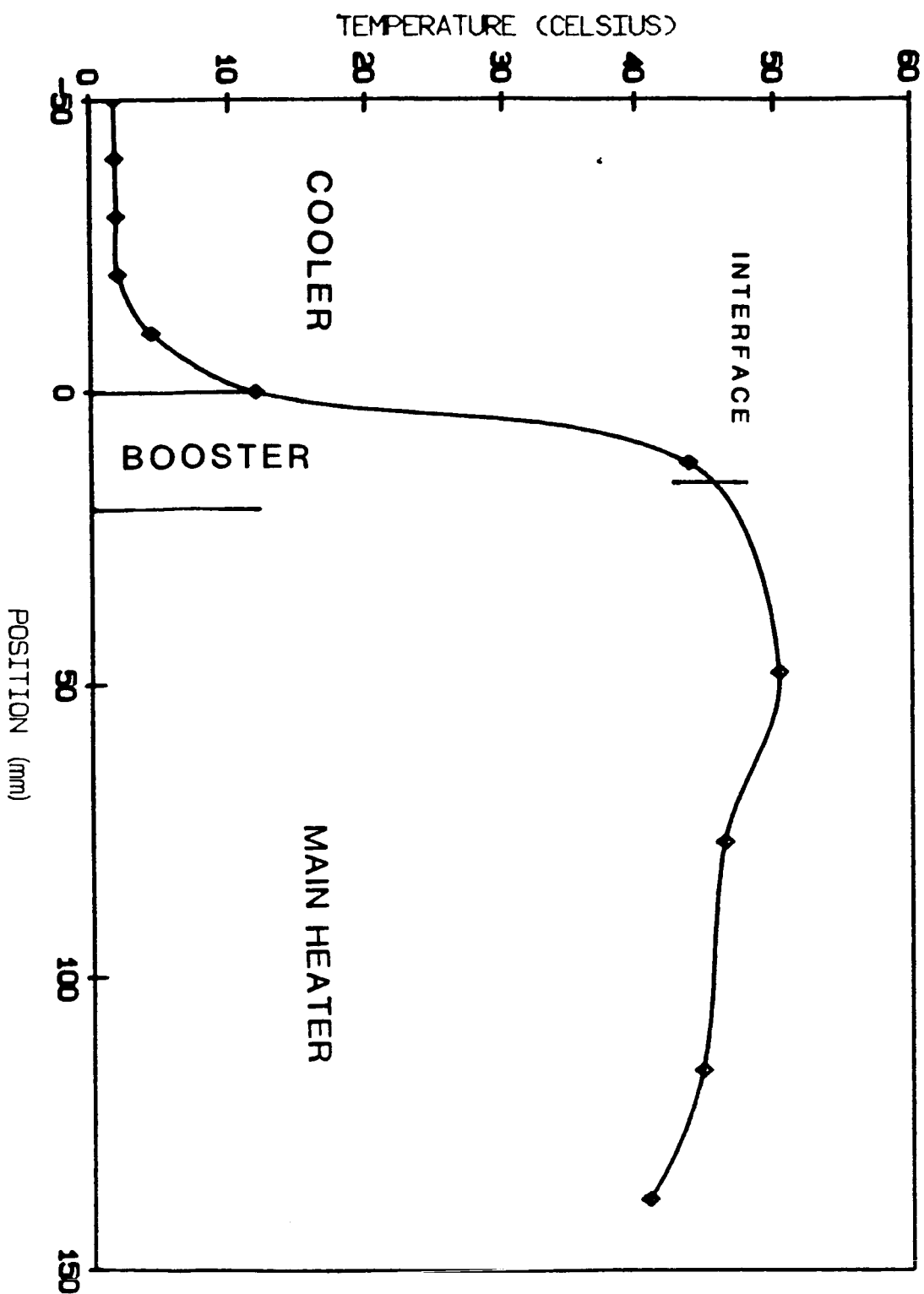
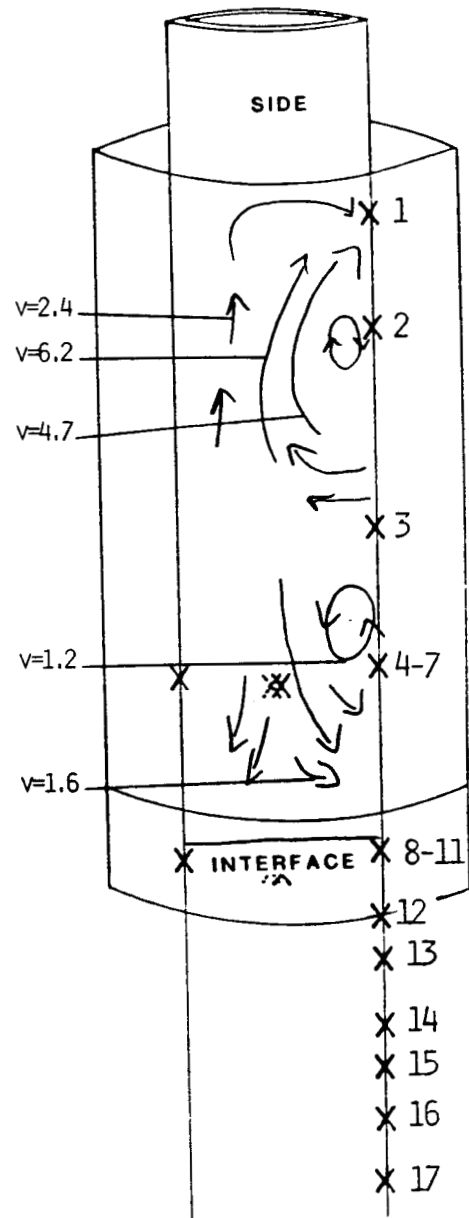
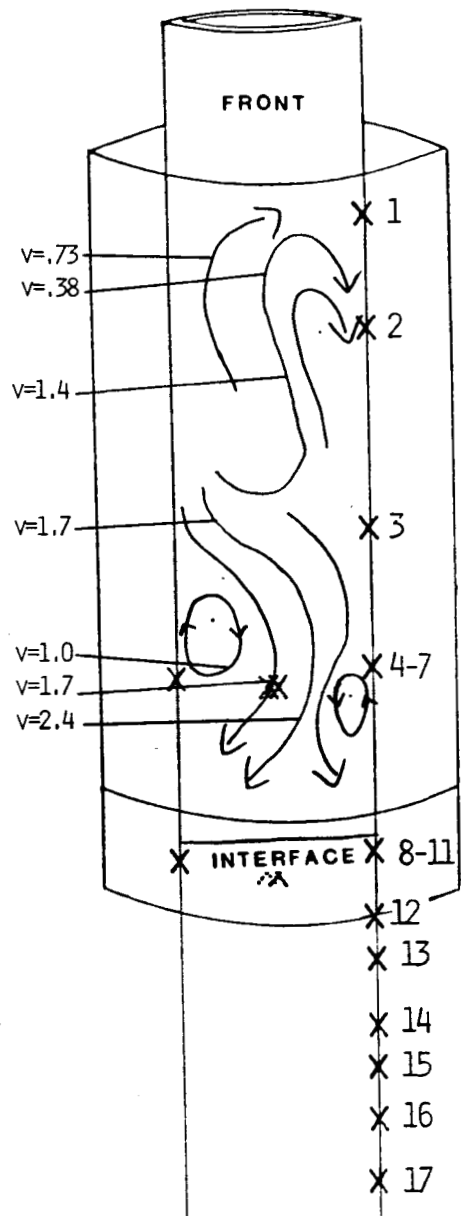


Figure 9a. Temperature of the outer wall of the Pyrex sample ampoule vs. vertical position for run I-66. The location of the melt-solid interface was 15.9 mm above the bottom of the booster heater. The temperature of the cooling bath was 1.5 °C.





1. Convection and Heat Transfer in the Bridgman-Stockbarger Technique
(Hilary Potts, Greg Neugebauer and William R. Wilcox)

The objective of this research was to determine the influence of the heater conditions on convection and heat transfer in the Bridgman-Stockbarger technique. At the termination of this contract on September 30, 1986, two papers had been submitted for publication, one M.S. thesis had been completed, and research for a second M.S. thesis had been completed. Since then, one paper has been published (Appendix A) and the second thesis completed (Appendix C).

Experiments were performed in several different transparent apparatuses using organic compounds as working materials. Fluid motion was revealed by particles floating in the melt. Temperatures were measured at several locations using fine thermocouples.

In the first set of experiments, described in Appendices A and B, heating and cooling were accomplished with agitated baths separated by a polymer diaphragm. Temperature varied only slightly throughout the baths. Convection occurred in the melt, as predicted by the computer models of Professor Carlson at Clarkson and Professor Brown at MIT. However the convection was non-axisymmetric and non-steady, unlike the theoretical predictions. This was attributed to a slight lack of symmetry and to fluctuations in the heating bath. The convection in the melt, while gentle, nonetheless significantly increased heat transfer in the melt and altered the interface shape and position. This is a reflection of the moderately large Prandtl number of organic liquids.

In order to investigate more thoroughly the effect of heating conditions on convection, an unique apparatus was constructed. As described in detail in Appendix C, long vertical heating wires were embedded in a plastic resin which

surrounded the ampoule. A short heater constructed in this manner was placed between the long heater and the cooling bath. With this apparatus the vertical and circumferential variation of heater temperature could be set over a wide range, without convective heat transfer between the heater and the ampoule.

When no power was applied to the short heater, there was negligible convection in the melt near the solid-liquid interface. This was because the temperature increased steadily with height, producing very small radial temperature gradients. This was manifested by achievement of a nearly planar solid-liquid interface regardless of its position in the ampoule.

As power was increased to the short heater, convection in the melt near the interface steadily increased. Careful adjustment of the distribution of power to the heating wires was required to achieve axi-symmetric convective in the melt. Slight tilting of the apparatus or small circumferential variations in temperature caused the convection to become non symmetric.

2. Mathematical Model of Heat Conduction in the
Bridgman-Stockbarger Technique
(Rogerio Balart and Theodore Papatheodorou)

This research was carried out by a doctoral student, Rogerio Balart, under the direction of Professor Papatheodorou. Papatheodorou moved from Clarkson to Greece last summer. Since then Mr. Balart's research has been directed by Dean Mark Ablowitz and he has been paid from Ablowitz's funds. A report of results obtained before Papatheodorou's departure is in Appendix D.

The original objective of this research was to develop computer programs for convective heat transfer for high Prandtl number melts in the Bridgman-Stockbarger technique. This is a very difficult problem because of the close coupling between heat transfer and bouyancy-driven convection. The computer programs of Brown and Carlson are useful only for very small Prandtl number, for which the heat transfer is influenced only slightly by the convection.

By the termination of the contract Balart had succeeded in developing a general analytical solution for two-dimensional conductive heat transfer (Appendix D). In order to obtain numerical values for temperature, computer calculations are required, but very much less than for a finite difference or finite element numerical solution.

Mr. Balart's assignment for the remainder of his Ph.D. thesis is to develop analytical and/or numerical methods for convection. He may, for example, determine the heater profile conditions required for the onset of convection.

3. Melt Behavior during Solidification in Space (Rahda Sen Jayaraj and William R. Wilcox)

Prior research by American, European and Soviet investigators has shown that ingots solidified in space frequently have smaller diameters than their ampoules. This has been attributed to non-wetting of the ampoule by the melt, causing the melt to pull away from the ampoule wall prior to solidification. The objective of our research was to test this explanation. Two papers and a portion of a Ph.D. thesis resulted from this work.

As described in Appendix E, experiments were performed in four KC-135 flights. Several types of ampoules were filled with non-wetting liquids. The ampoules were attached to a video camera, which was periodically shaken and released during the low g portions of the flight.

In cylindrical ampoules, the air either formed one or more large bubbles along the ampoule wall or served to separate the liquid into columns. There was a maximum stable bubble size, which was confirmed by the theoretical treatment given in Appendix F.

In triangular ampoules, the liquid pulled away from the corners and contacted the walls only over finite widths. The contact width was correctly predicted by theory, which also predicts a critical contact angle beyond which contact would be infinitesimally thin.

These results do not explain the results of solidification in space. In order to explain the flight results, solidification experiments must be performed in space in a transparent furnace, so that we can see exactly what is occurring.

4. Twinning of Dodecandicarboxylic Acid (Rahda Sen Jayaraj and William R. Wilcox)

The objective of this research was to elucidate the causes of twinning during crystal growth. The research completed the Ph.D. thesis mentioned in section 3, and yielded the paper in Appendix G.

A search was initiated for a material whose twins are readily identified in transmitted polarized light. Dodecanedioic acid proved very useful. Thin films were prepared and directionally solidified under the microscope. Twins began in polycrystalline regions, indicating a nucleation mechanism. They terminated by intersecting one another or grain boundaries.

The average number of twins increased with increasing freezing rate and increasing temperature gradient. Zone refining reduced twin formation to near zero. The tendency of impurities to cause twins increased as their molecular size and shape approached those of the host crystal. Since one expects the distribution coefficient to approach 1 (as molecular size and shape become identical, this corresponds to increased twin formation as the distribution coefficient approaches 1. Note that these observations do not correspond to any relation between twin formation and constitutional supercooling.

(Constitutional supercooling increases with increasing freezing rate, decreasing temperature gradient, and decreasing distribution coefficient.)

A crude model which is consistent with the results follows. Twins are formed during nucleation of new grains, which increases as the freezing rate increases. Thermal stress, which increases as temperature gradient increases, causes more twins to form in the nucleation process. Impurities lower the twin energy and so favor twin formation. The impurities most able to substitute for the host molecules are those with similar size and shape.

P. 27

CONVECTION IN THE VERTICAL BRIDGMAN-STOCKBARGER TECHNIQUE

Gregory T. NEUGEBAUER and William R. WILCOX

Department of Chemical Engineering and Center for Advanced Materials Processing, Potsdam, New York 13676, USA.

The influence of operating parameters on convection in the Bridgman-Stockbarger technique was studied with a transparent furnace and melt. The convective field was very sensitive to the thermal profile of the furnace. Convection was nearly nonexistent near the interface in the vertically stabilized thermal configuration (temperature increasing with height). With the addition of a short booster heater between the main heater and the cooler, a destabilized temperature gradient was produced near the interface and significant convection was produced throughout the entire melt. Convective velocities increased as power to the booster heater was increased. Convection was usually asymmetrical. Only by careful adjustment of the heating conditions could a symmetrical flow field be produced.

W-77

LR

1. Introduction

The need in recent years to produce more homogeneous crystals has made directional solidification a topic of intensive research. Early theoretical studies were on the effects of heat transfer on the shape of the melt/solid interface; an important parameter in controlling thermal stress, grain selection, and component segregation [1,2]. Most models assume that heat transfer within the melt occurs only by conduction. While this may be a valid assumption for low Prandtl number fluids, the effects of convection on crystal composition are by no means negligible. The microscopic distribution of components at the interface is often extremely sensitive to small changes in convective flow patterns. Because the response of most electronic devices is strongly related to their composition, convective transport in melt growth systems has been actively investigated in recent years [3-10].

Workers at MIT and Clarkson developed two-dimensional numerical models to study convection [7,9]. Since a symmetrical convective field is an a priori assumption in any two-dimensional model, these investigations cannot provide insight into the three-dimensional characteristics of a flow field contained in a less than perfectly symmetrical temperature field.

Recent experimental investigations done here with low melting, low thermal conductivity materials showed strongly asymmetrical convection [10]. It was proposed that this type of flow behavior may be fairly common, as evidenced by compositional striations and azimuthal composition variations observed in many single crystals. Our goal in the present work was to more precisely characterize the relationship between the temperature field of the furnace and the

MODELLING DIRECTIONAL SOLIDIFICATION

NAS8-34891

Final Report

1 June 1982 to 30 September 1985

Clarkson University

Potsdam, New York 13676

Principal Investigator: Dr. William R. Wilcox, Professor and
Chairman of Chemical Engineering
315-268-6650

Co-Investigator: Dr. Theodore S. Papatheodorou, formerly
Associate Professor of Mathematics and
Computer Science

Graduate Student Research Assistants:

Mr. R. Balart, Doctoral Candidate in Mathematics
and Computer Science

Ms. Rahda Sen Jayaraj, Doctoral Candidate in Chemical
Engineering (Completed May 1985)

Mr. Greg Neugebauer, M.S. Candidate in Chemical
Engineering (Completed May 1986)

Ms. Hilary Potts, M.S. Candidate in Chemical
Engineering (Completed May 1984)

Ms. Lorraine Ruggiano, Doctoral Candidate in Chemical
Engineering

CR-179325

M/88-70725

MODELLING DIRECTIONAL SOLIDIFICATION

NAS8-34891

Final Report

1 June 1982 to 30 September 1985

Clarkson University

Potsdam, New York 13676

Principal Investigator: Dr. William R. Wilcox, Professor and
Chairman of Chemical Engineering
315-268-6650

Co-Investigator: Dr. Theodore S. Papatheodorou, formerly
Associate Professor of Mathematics and
Computer Science

Graduate Student Research Assistants:

Mr. R. Balart, Doctoral Candidate in Mathematics
and Computer Science

Ms. Rahda Sen Jayaraj, Doctoral Candidate in Chemical
Engineering

Mr. Greg Neugebauer, M.S. Candidate in Chemical
Engineering

Ms. Lorraine Ruggiano, Doctoral Candidate in Chemical
Engineering

CONTENTS

	Page
Summary.....	1
1. Convection and heat transfer in the Bridgman-Stockbarger technique.....	3
2. Mathematical model of heat conduction in the Bridgman-Stockbarger technique.....	5
3. Melt behavior during solidification in space.....	6
4. Influence of solidification parameters on twinning.....	7
<u>Appendices (Manuscripts, papers and thesis)</u>	
A. Thermal fields in the Bridgman-Stockbarger technique	
B. Chaotic asymmetric convection in the Bridgman-Stockbarger technique	
C. Influence of heater configuration on convection in the Bridgman- Stockbarger technique	
D. A quasi-analytical solution to the steady state Bridgman-Stockbarger model	
E. Behavior of a non-wetting melt in free fall: experimental	
F. Behavior of a non-wetting melt in free fall: theoretical	
G. Twinning of dodecanedicarboxylic acid	

Acknowledgement

This report is the results of work carried out under NASA Contract NAS8-34891. This research effort was sponsored by NASA Headquarters Microgravity Science and Applications Division. Also, the authors would like to thank the Applications Payload Projects Office of the Spacelab Payload Projects Office, Marshall Space Flight Center, AL for their invaluable assistance in programming the total research effort over several years.

SUMMARY

The overall objective of this research was to elucidate phenomena of importance to directional solidification in space. We used a combination of theory, laboratory experiments, and experiments in the KC135. The research has produced 5 papers, a completed Ph.D. thesis, progress toward another Ph.D. thesis, a completed M.S. thesis, the major part of another M.S. thesis, and the beginning of a Ph.D. project. The latter M.S. thesis is included here as an appendix. It will yield one paper. When the second Ph.D. thesis is complete it will result in several papers.

Conclusions of our research are as follows:

1. In the vertical Bridgman-Stockbarger technique (BS), convection is often non axi-symmetric and may not be steady, even when very gentle. (See Appendix B).
2. Convection in BS depends critically on the vertical and circumferential temperature variations in the heater. For example, the convection near the solid-liquid interface increases as the vertical temperature gradient becomes more negative. (See Appendix C).
3. When the temperature increases with height in BS there may be negligible convection near the freezing interface and the interface remains planar over a wide range of vertical positions. (See Appendix C).
4. In moderate Prandtl number melts the temperature field and the interface shape in BS are sensitive to convection. (See Appendix A).
5. The two-dimensional temperature field in BS with conduction only may be computed rapidly using our new methods. (See Appendix D).

6. In space, a liquid which partially fills a non-wetted ampoule either separates into columns or traps a gas bubble on the wall. The gas bubble is unstable beyond a critical size which decreases as the contact angle increases.
7. In a triangular ampoule the liquid contacts the walls only over finite widths which decrease as the contact angle increases.
8. In dodecanedioc acid (DDA) the number of twins increases with increasing temperature gradient, increasing freezing rate, and increasing impurity content when the impurity molecules are similar in size and shape to DDA.

1. Convection and Heat Transfer in the Bridgman-Stockbarger Technique
(Hilary Potts, Greg Neugebauer and William R. Wilcox)

The objective of this research was to determine the influence of the heater conditions on convection and heat transfer in the Bridgman-Stockbarger technique. At the termination of this contract on September 30, 1986, two papers had been submitted for publication, one M.S. thesis had been completed, and research for a second M.S. thesis had been completed. Since then, one paper has been published (Appendix A) and the second thesis completed (Appendix C).

Experiments were performed in several different transparent apparatuses using organic compounds as working materials. Fluid motion was revealed by particles floating in the melt. Temperatures were measured at several locations using fine thermocouples.

In the first set of experiments, described in Appendices A and B, heating and cooling were accomplished with agitated baths separated by a polymer diaphragm. Temperature varied only slightly throughout the baths. Convection occurred in the melt, as predicted by the computer models of Professor Carlson at Clarkson and Professor Brown at MIT. However the convection was non-axisymmetric and non-steady, unlike the theoretical predictions. This was attributed to a slight lack of symmetry and to fluctuations in the heating bath. The convection in the melt, while gentle, nonetheless significantly increased heat transfer in the melt and altered the interface shape and position. This is a reflection of the moderately large Prandtl number of organic liquids.

In order to investigate more thoroughly the effect of heating conditions on convection, an unique apparatus was constructed. As described in detail in Appendix C, long vertical heating wires were embedded in a plastic resin which

surrounded the ampoule. A short heater constructed in this manner was placed between the long heater and the cooling bath. With this apparatus the vertical and circumferential variation of heater temperature could be set over a wide range, without convective heat transfer between the heater and the ampoule.

When no power was applied to the short heater, there was negligible convection in the melt near the solid-liquid interface. This was because the temperature increased steadily with height, producing very small radial temperature gradients. This was manifested by achievement of a nearly planar solid-liquid interface regardless of its position in the ampoule.

As power was increased to the short heater, convection in the melt near the interface steadily increased. Careful adjustment of the distribution of power to the heating wires was required to achieve axi-symmetric convection in the melt. Slight tilting of the apparatus or small circumferential variations in temperature caused the convection to become non symmetric.

2. Mathematical Model of Heat Conduction in the
Bridgman-Stockbarger Technique
(Rogerio Balart and Theodore Papatheodorou)

This research was carried out by a doctoral student, Rogerio Balart, under the direction of Professor Papatheodorou. Papatheodorou moved from Clarkson to Greece last summer. Since then Mr. Balart's research has been directed by Dean Mark Ablowitz and he has been paid from Ablowitz's funds. A report of results obtained before Papatheodorou's departure is in Appendix D.

The original objective of this research was to develop computer programs for convective heat transfer for high Prandtl number melts in the Bridgman-Stockbarger technique. This is a very difficult problem because of the close coupling between heat transfer and buoyancy-driven convection. The computer programs of Brown and Carlson are useful only for very small Prandtl number, for which the heat transfer is influenced only slightly by the convection.

By the termination of the contract Balart had succeeded in developing a general analytical solution for two-dimensional conductive heat transfer (Appendix D). In order to obtain numerical values for temperature, computer calculations are required, but very much less than for a finite difference or finite element numerical solution.

Mr. Balart's assignment for the remainder of his Ph.D. thesis is to develop analytical and/or numerical methods for convection. He may, for example, determine the heater profile conditions required for the onset of convection.

3. Melt Behavior during Solidification in Space (Rahda Sen Jayaraj and William R. Wilcox)

Prior research by American, European and Soviet investigators has shown that ingots solidified in space frequently have smaller diameters than their ampoules. This has been attributed to non-wetting of the ampoule by the melt, causing the melt to pull away from the ampoule wall prior to solidification. The objective of our research was to test this explanation. Two papers and a portion of a Ph.D. thesis resulted from this work.

As described in Appendix E, experiments were performed in four KC-135 flights. Several types of ampoules were filled with non-wetting liquids. The ampoules were attached to a video camera, which was periodically shaken and released during the low g portions of the flight.

In cylindrical ampoules, the air either formed one or more large bubbles along the ampoule wall or served to separate the liquid into columns. There was a maximum stable bubble size, which was confirmed by the theoretical treatment given in Appendix F.

In triangular ampoules, the liquid pulled away from the corners and contacted the walls only over finite widths. The contact width was correctly predicted by theory, which also predicts a critical contact angle beyond which contact would be infinitesimally thin.

These results do not explain the results of solidification in space. In order to explain the flight results, solidification experiments must be performed in space in a transparent furnace, so that we can see exactly what is occurring.

4. Twinning of Dodecandicarboxylic Acid (Rahda Sen Jayaraj and William R. Wilcox)

The objective of this research was to elucidate the causes of twinning during crystal growth. The research completed the Ph.D. thesis mentioned in section 3, and yielded the paper in Appendix G.

A search was initiated for a material whose twins are readily identified in transmitted polarized light. Dodecanedioic acid proved very useful. Thin films were prepared and directionally solidified under the microscope. Twins began in polycrystalline regions, indicating a nucleation mechanism. They terminated by intersecting one another or grain boundaries.

The average number of twins increased with increasing freezing rate and increasing temperature gradient. Zone refining reduced twin formation to near zero. The tendency of impurities to cause twins increased as their molecular size and shape approached those of the host crystal. Since one expects the distribution coefficient to approach 1 (as molecular size and shape become identical, this corresponds to increased twin formation as the distribution coefficient approaches 1. Note that these observations do not correspond to any relation between twin formation and constitutional supercooling. (Constitutional supercooling increases with increasing freezing rate, decreasing temperature gradient, and decreasing distribution coefficient.)

A crude model which is consistent with the results follows. Twins are formed during nucleation of new grains, which increases as the freezing rate increases. Thermal stress, which increases as temperature gradient increases, causes more twins to form in the nucleation process. Impurities lower the twin energy and so favor twin formation. The impurities most able to substitute for the host molecules are those with similar size and shape.

THERMAL FIELDS IN THE BRIDGMAN-STOCKBARGER TECHNIQUE

Hilary POTTS and William R. WILCOX

Department of Chemical Engineering, Clarkson University, Potsdam, New York 13676, USA

Received 17 August 1984; manuscript received in final form 14 May 1985

Temperature measurements were made throughout a naphthalene melt and solid in a simulated Bridgman-Stockbarger apparatus. Heating and cooling were provided by agitated baths separated by a polymer diaphragm. While agitation was sufficient to give uniform temperatures in the baths, the level of agitation in the heater strongly influenced the results. Unlike theoretical results for high thermal conductivity materials, natural convection in the melt had a strong influence on interface position and on the temperature distribution. Isotherms were relatively flat in the solid and both curved and erratic in the melt. The interface became more convex as it was moved higher into the heating bath by raising either the heating bath or cooling bath temperatures. Using a one-dimensional model, the Biot number in the cooler was determined to be 0.03, that for the solid in the heater 0.008, and for the molten region in the heater 0.3. Biot numbers for two or three dimensional models would be significantly different.

1. Introduction

Chang and Wilcox [1] pioneered the use of analytical methods to predict the influence of changes in operating parameters and material parameters on changes in interface shape and position in the Bridgman-Stockbarger technique. A simple two-dimensional cylindrical model was employed, in which convection in the melt was neglected, and assuming constant properties, an infinitely long cylindrical sample with no ampoule, constant temperatures in the heater and cooler with a step function change between them, and a constant heat transfer coefficient h between the sample and its surroundings. From this model they predicted that the interface shape is very sensitive to its position, and that its position is determined by the heater and cooler temperatures. Lowering either of these temperatures moves the interface upwards from the cooler into the heater. A planar interface is expected only when it is at the boundary between the heater and the cooler. It becomes more convex as it is moved into the heater and concave if it is moved into the cooler. The sensitivity to heater and cooler temperatures increases as the radius R is increased, h is increased, and the material thermal conductivity k is decreased (i.e. for small Biot number, $H = hR/k$).

Chang and Wilcox also performed a one-dimensional analysis to determine the influence of ampoule lowering rate and the influence of proximity to the end of the cylinder on interface position. In such a one-dimensional analysis the temperature is assumed to vary only with axial position z and not with radius r . This is a reasonable assumption when the Biot number H is small.

Since Chang and Wilcox, many others have studied the influence of removing simplifying assumptions and of additional variables, always neglecting convection. Most of these have been one-dimensional analyses. Recently Chang and Brown [2] and Chin and Carlson [3] used numerical methods to study heat transfer in high thermal conductivity materials with convection. They concluded that under usual Bridgman-Stockbarger conditions with large k the convection has little influence on the interface shape or thermal field. (A very large influence on impurity segregation and homogeneity is expected.)

In an older study, Tien [4] numerically analyzed heat transfer with convection for a low k material. He used experimentally measured wall temperatures. With low k the convection has some influence on the temperature field in the melt and on the interface shape.

We report here the results of measurements of

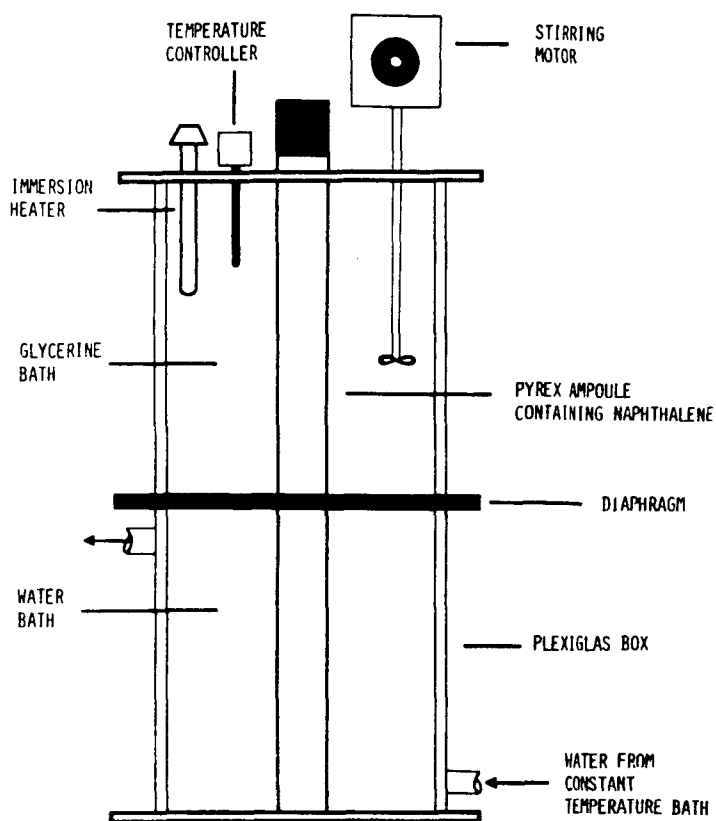


Fig. 1. Apparatus

the three-dimensional temperature field in the Bridgman-Stockbarger technique with low k and moderately large R .

2. Experimental

The details of the experiments are given elsewhere [5]. Fig. 1 shows the apparatus, which is like that used by Tien [4], except that our diaphragm was thicker and made of a sandwich of 1.57 mm thick Teflon inside 1.57 mm thick silicone rubber sheets. The ampoule was Pyrex, 2 cm ID by 40 cm long with a 1 mm wall thickness, and contained naphthalene with a melting point of approximately 80°C.

Five copper-constantan thermocouples located throughout the lower bath detected no tempera-

ture variations, and a maximum difference of 1°C from the constant temperature bath. To make the temperature in the upper bath uniform, sufficient stirring was required that air bubbles were entrained in the glycerine. Stirring below this level produced asymmetric heating, with the interface lower on the side of the ampoule nearest the heater. Figs. 2 and 3 show interface shapes for these two levels of stirring for different heating bath temperatures T_h and cooling bath temperatures T_c ($\Delta T = T_h - T_c$). Therefore for all subsequent runs the higher stirring level was used.

In the cold region (below the diaphragm), temperature were measured by copper-constantan thermocouples. The 0.127 mm Teflon-coated wires were inserted through diametrically opposed holes in the Pyrex tube. Thermocouple junctions were located radially at the center, 5 mm out from the

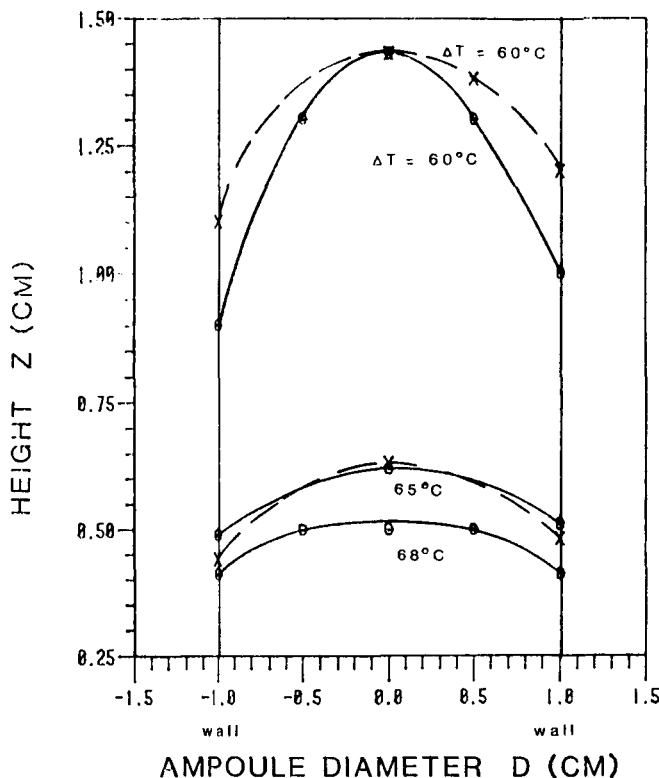


Fig. 2. Interface shapes for low stirring in upper bath (— × —) and for high stirring (— ○ —), with a cooler temperature T_c of 22°C and several temperature differences ΔT between heater temperature T_h and T_c .

center, and at the tube wall; they were placed axially at 1 cm intervals. In the melt a thermocouple probe was used, consisting of the above wire in a 3 mm OD Pyrex pipette. When moved near the solid-liquid interface it did not appreciably alter the interface shape. No temperature measurements were taken between the diaphragm and the solid-liquid interface.

Heating bath temperatures ranged from 82 to 90°C and cooling bath temperatures from 22 to 32°C . Under these conditions the interface was always convex, as shown in figs. 2 and 3. At $T_c = 50^\circ\text{C}$ and $T_h = 90^\circ\text{C}$ the interface was within the diaphragm and presumably planar. At $T_c = 75^\circ\text{C}$ and $T_h = 90^\circ\text{C}$ it was within the cooler and was concave.

After 8 h or more from start-up, temperature readings were taken at 30 min intervals. After several additional hours, when the temperatures no longer changed by 0.3°C over an hour, data

were recorded. Each experimental condition was re-run one to three times. The standard deviations for temperature at particular locations ranged from 0.14 to 0.29°C , with 10 to 30 observations for each.

As described in a companion paper [6], convection in the melt was observed for low stirring in the heating bath. Melt velocities near the solid-liquid interface ranged from 0.08 to 0.84 mm/s, and showed no correlation with T_c , T_h or ΔT .

3. Results

Figs. 4 and 5 show typical results for temperature versus height along the center of the ampule. From such plots, interfacial temperature gradients were calculated and isotherms interpolated. Figs. 6 and 7 show typical isotherms, while fig. 8 shows

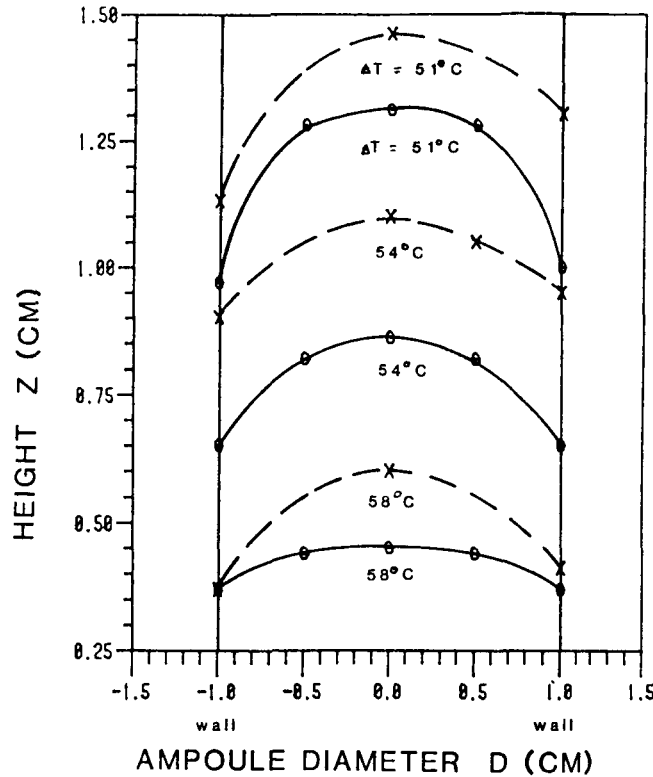


Fig. 3. Interface shapes for low stirring (---) and high stirring (—) in upper bath for $T_c = 31^\circ\text{C}$ versus ΔT .

the interfacial temperature gradient $\partial T/\partial z$ versus ΔT . No dependence of $\partial T/\partial z$ on interface position was observed.

Fig. 9 shows the dependence of average interface position \bar{z} , versus E (the ratio of the amount by which the heating bath temperature T_h exceeds the melting point $T_m = 80^\circ\text{C}$ to the amount by which the cooler temperature T_c is below T_m).

Fig. 10 shows D (the ratio of the amount of temperature change above the diaphragm center to that below) versus

$$E = (T_h - T_m)/(T_m - T_c).$$

Here the diaphragm temperature T_d was obtained by interpolation in the T versus z plots.

4. Analysis and discussion

To interpret these results it is useful to use a one-dimensional analysis, as in ref. [1]. We neglect

the diaphragm and assume the ampoule is infinitely long, which is good since the temperatures in the solid and melt reach T_c and T_h long before the ends of the ampoule. First we neglect differences in properties and assume the Biot number $H = hR/k$ is different in the heater and in the cooler, but constant within each. Following prior workers, we find that the general solution to the differential equation is

$$T - T_a = a_+ \exp[(2H)^{1/2} z/R] + a_- \exp[-(2H)^{1/2} z/R], \quad (1)$$

where $T_a = T_h$ or T_c is the ambient (bath) temperature and a_+ and a_- are constants to be determined from the boundary conditions,

$$T = T_h \quad \text{at} \quad z = \infty, \quad (2)$$

$$T = T_c \quad \text{at} \quad z = -\infty, \quad (3)$$

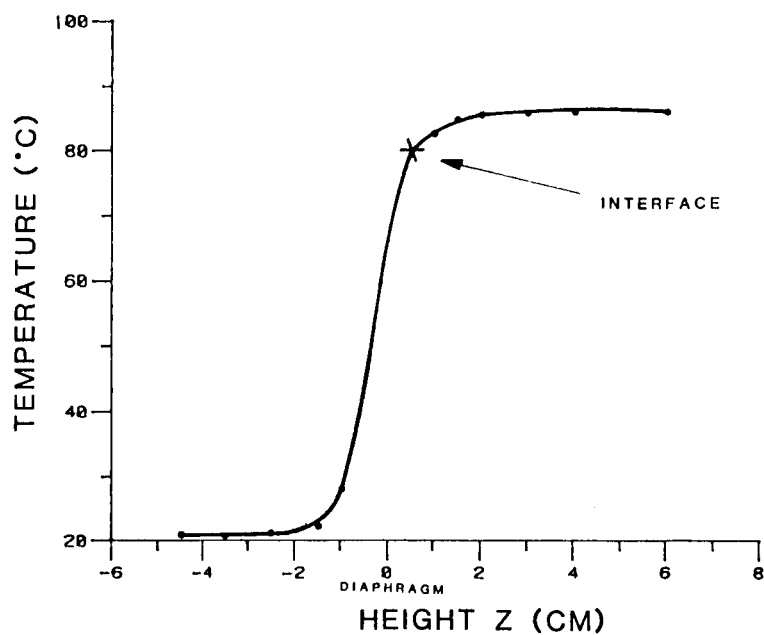


Fig. 4. Temperature T versus height z along the center of the ampoule ($r = 0$) for $T_c = 22^\circ\text{C}$ and $T_h = 87^\circ\text{C}$. Here $z = 0$ is defined as the center of the 4.7 mm thick diaphragm.

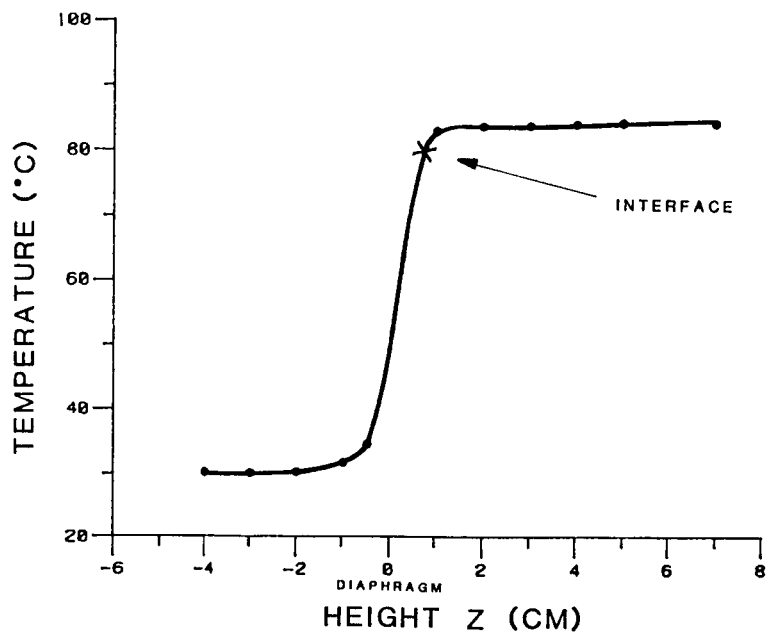


Fig. 5. T versus z at $r = 0$ for $T_c = 31^\circ\text{C}$, $T_h = 85^\circ\text{C}$.

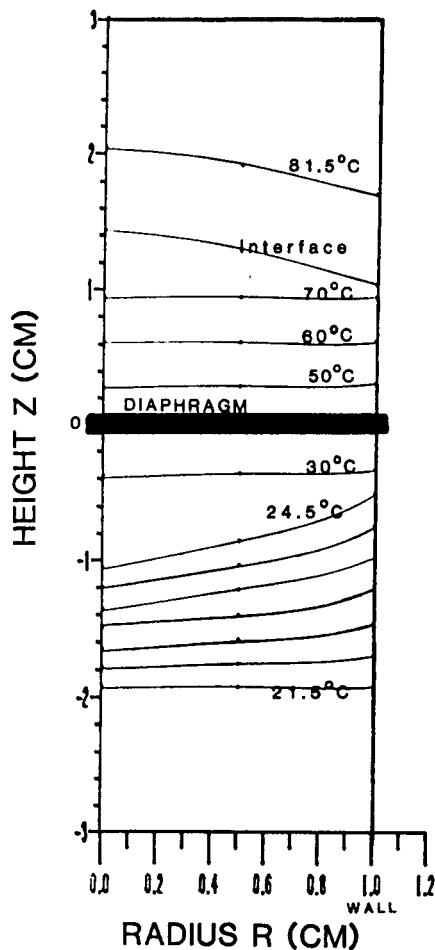


Fig. 6. Interpolated isotherms for $T_c = 22^\circ\text{C}$, $T_h = 82^\circ\text{C}$. Every 0.5°C from 21.5 to 24.5°C .

and T and dT/dz are continuous wherever two regions meet.

From the foregoing we find

$$D = (T_h - T_d)/(T_d - T_c) = (H_c/H_h)^{1/2}, \quad (4)$$

where the subscripts c and h denote values in the cooler and heater, respectively. Note that this predicts that

$$D = (T_h - T_d)/(T_d - T_c)$$

is independent of

$$E = (T_h - T_m)/(T_m - T_c),$$

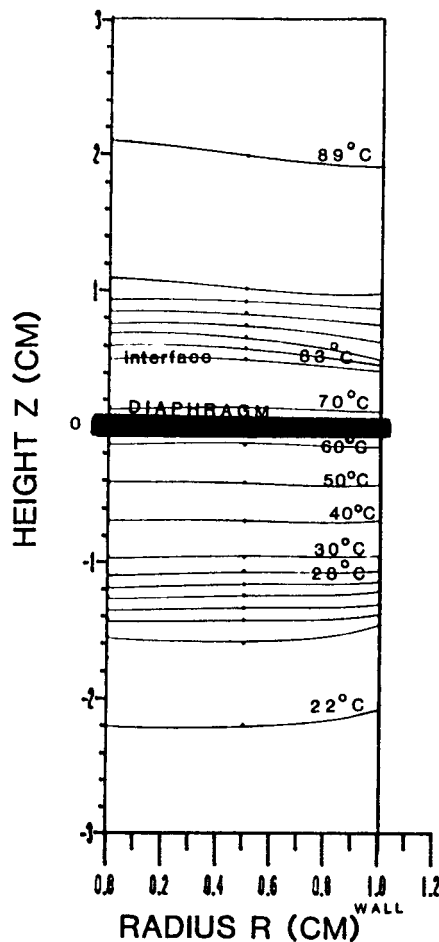


Fig. 7. Isotherms for $T_c = 22^\circ\text{C}$ and $T_h = 90^\circ\text{C}$. Every 1°C from 22 to 28°C and 83 to 89°C .

which fig. 10 shows was untrue. The implication is that H_h increased as T_h and T_c were increased. As fig. 9 shows, increasing T_h and T_c moved the interface down, so that more of the material was molten.

To understand why H_h might depend on interface position z_i , consider the three resistances to radial heat transfer between the material in the ampoule and the bath outside it. First there is the ampoule wall. Its resistance is independent of whether the material is melted or not. Second is convective heat transfer between the outside of the ampoule wall and the bath. While this might be somewhat lower near the diaphragm and far from

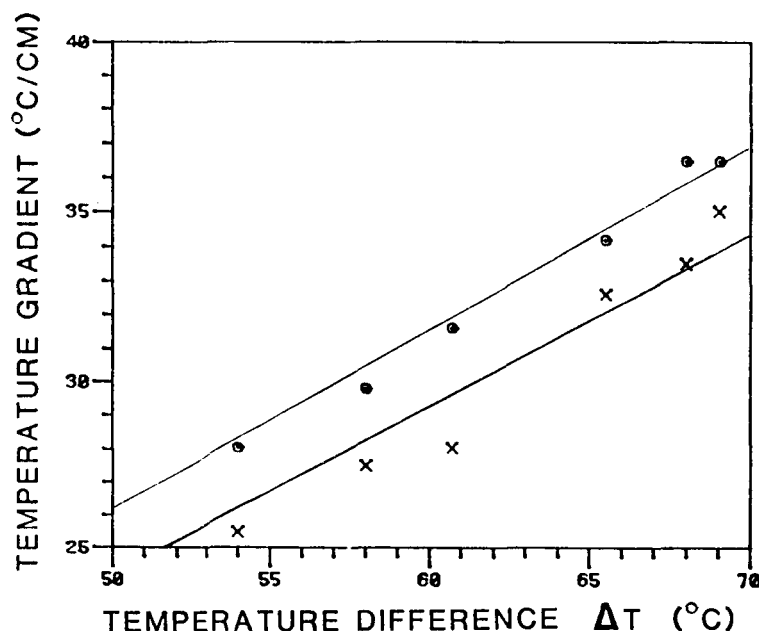


Fig. 8. Interfacial temperature gradient $(\partial T/\partial z)_i$ at center (x) and at wall (o). Values of $(\partial T/\partial z)_i$ are good to about 2°C/cm.

the stirrer, this should not be a large effect and should not depend appreciably on the heater and cooler temperatures. Third is heat transfer between the entire material within the ampoule and the inside wall of the ampoule. When the material is solid, this occurs by conduction only. When it is molten, convection makes a large contribution for low thermal conductivity materials. In addition, convection in the melt increases the effective thermal conductivity k , which tends to lower H_h . This k is a measure of axial heat transfer. Since H_h increased, apparently the influence of convection on radial heat transfer was larger than that on axial heat transfer.

We can estimate the ratio of convective to conduction contributions to heat transfer by a Peclet number $V\rho C_p R/k$, where V is the convective velocities near the interface, ρ is the density of naphthalene, C_p its mass heat capacity and k its thermal conductivity. From the measured convective velocities we calculate thereby a Peclet number of 1200 to 12,000. Thus we would expect h , k and H for the molten region to be quite different from those for the solid material in the heater. We

denote these with subscripts m and s, respectively.

We now apply our one-dimensional analysis to a cylinder with three regions, that in the cooler (c), solid in the heater (s), and melt in the heater (m). This yields the following relationship between E and D :

$$E = (T_h - T_m)/(T_m - T_c) = f/(1 + D - f), \quad (5)$$

where

$$f = 0.5 \left\{ \left[D + (H_c/H_s)^{1/2} \right] A^{1/2} + \left[D - (H_c/H_s)^{1/2} \right] / A^{1/2} \right\}, \quad (6)$$

$$A = \frac{[-D + (H_c/H_s)^{1/2}][1 + (H_s/H_m)^{1/2}]}{[D + (H_c/H_s)^{1/2}][1 - (H_s/H_m)^{1/2}]}. \quad (7)$$

By trial and error the values $(H_c/H_s)^{1/2} = 2.0$ and $(H_s/H_m)^{1/2} = 0.15$ were found to best fit the data of fig. 10. The solid curve shown in fig. 10 is eq. (5) with these Biot number ratios.

The product $(H_c/H_s)^{1/2}(H_s/H_m)^{1/2} = (H_c/H_m)^{1/2} = 0.31$ compares well with the value of 1/3 obtained from eq. (4) and the observation

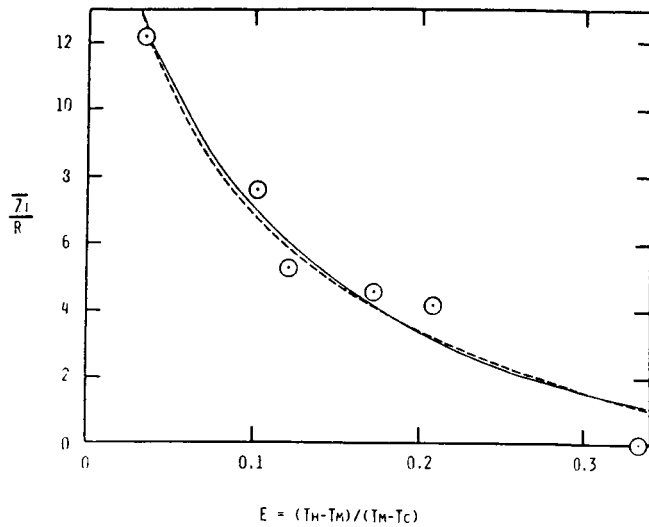


Fig. 9. Average interface position \bar{z}_i versus ratio of temperature change above interface to that below. Values of \bar{z}_i/R are good to within about 0.5. (—) Fit via eq. (8) using D from E and solid curve on fig. 10, and with $(H_c/H_s)^{1/2} = 2.0$ and $(H_s/H_m)^{1/2} = 0.15$, $H_s = 0.0076$. (---) Fit via eq. (9) with $H_s = H_m = H_h = 0.016$ and $H_c = 0.080$.

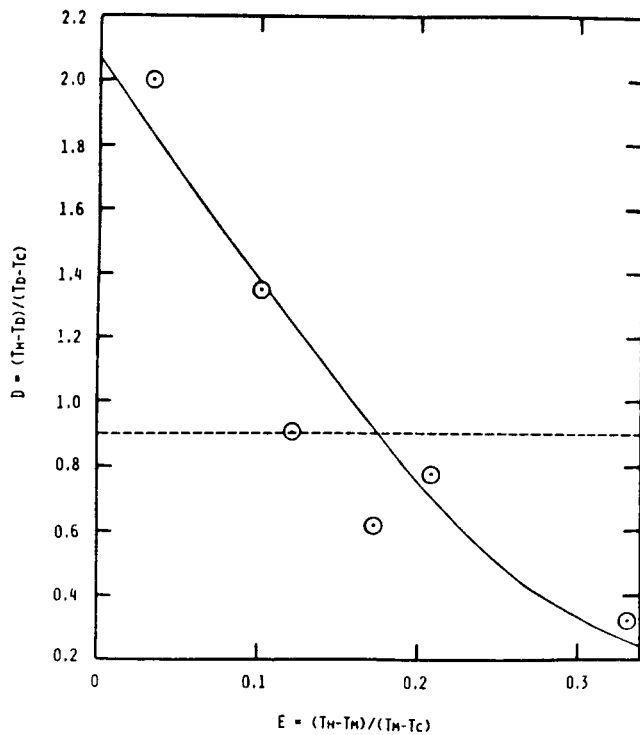


Fig. 10. Ratio of temperature change above diaphragm center to that below versus ratio of temperature change above interface to that below. Values of D are good to within about 0.1. (—) Fit via eq. (5) (for $H_s \neq H_m$) with $(H_c/H_s)^{1/2} = 2.0$ and $(H_s/H_m)^{1/2} = 0.15$. (---) Fit via eq. (4) (for $H_s = H_m = H_h$) with $(H_c/H_h)^{1/2} = 0.9$.

that the interface is within the diaphragm for $T_h = 90^\circ\text{C}$ and $T_c = 50^\circ\text{C}$.

The same one-dimensional analysis as above may be used to find for the interface position:

$$z_i = -R \ln \left[A / (2H_s)^{1/2} \right]. \quad (8)$$

We obtain the best fit to the data of fig. 9 using $H_s = 0.0076$ with the values of H_c/H_s and H_s/H_m found above. The solid curve in fig. 9 shows this fit. Together the above values yield $H_c = 0.031$ and $H_m = 0.033$.

Alternatively we can fit the data of fig. 9 using the one-dimensional model for $H_s = H_m = H_h$, for which:

$$z_i = - \left[R / (2H_h)^{1/2} \right] \ln \left\{ \frac{E \left[1 + (H_c/H_h)^{1/2} \right]}{(1+E)(H_c/H_h)^{1/2}} \right\}. \quad (9)$$

The best fit is shown as the dashed line in fig. 9, with $H_h = 0.016$, $(H_c/H_h)^{1/2} = 0.44$ and $H_c = 0.080$. On the other hand, application of eq. 4 to fig. 10 yields a very poor fit with $D = (H_c/H_h)^{1/2} = 0.9$. Thus \bar{z}_i versus E data can be fit equally well for a $H_s = H_m = H_h$ model as for a $H_s \neq H_m$ model, while E versus D data can only be fit by assuming $H_s \neq H_m$.

Note that the Biot numbers determined above are for a one-dimensional viewpoint in which at any value of z we consider an average temperature for that section and heat transfer to the surroundings from the average solid. In a two-dimensional viewpoint the Biot number would be for heat transfer from the solid only at the ampoule wall to the surroundings. That is, the one-dimensional Biot number includes some radial heat transfer through the material in the ampoule, whereas the two-dimensional Biot number does not. Consequently for a solid material in the ampoule the two-dimensional Biot number is larger, and much larger for small thermal conductivity materials. The reverse is true for the melt, because convection greatly increases the effective value of k in the one-dimensional model, while the true k for the melt would be used in a two-dimensional analysis. It can be inferred from the results presented here that two- or three-dimensional models for low k materials must take into account convective heat transfer in the melt.

Some additional observations follow. Figs. 2

and 3 show that higher stirring in the heating bath increases the interface curvature when the interface is far from the diaphragm. This reflects the greater heat transfer to the bath, thereby causing an increased radial temperature gradient inside the ampoule. The interface in general is also moved downward, as would be expected from an increased H_s and H_m in eq. (8).

The isotherms in the solid in figs. 6 and 7 are remarkably flat. Those in the melt are both curved and erratic, probably due to the convective heat transfer in the melt.

Recent experiments at Clarkson have shown that the intensity of convection in the BS technique depends critically on the way the ampoule is heated [7]. A uniform temperature in the heater, as in the present experiments and in the usual theories (e.g., refs. [2-4]), gives convection. A small "tickler heater" placed near the solid-liquid interface can produce a maximum in temperature in it and increase the amount of convection. On the other hand, the wound resistance heater usually used for BS growth produces a maximum in temperature about half way up it. In this situation the convection can become negligible below the maximum near the interface and vigorous above the maximum high in the ampoule (where it has little influence on impurity segregation).

Acknowledgements

This research was supported by NASA contract NAS8-34891. We are grateful to Tim Tyler and to Hari Narayanan for their assistance with the apparatus and the experiments.

References

- [1] C.E. Chang and W.R. Wilcox, *J. Crystal Growth* 21 (1974) 135.
- [2] C.J. Chang and R.A. Brown, *J. Crystal Growth* 63 (1983) 343.
- [3] L.Y. Chin and F.M. Carlson, *J. Crystal Growth* 62 (1983) 561.
- [4] L.C. Tien, PhD Thesis, University of Michigan, Ann Arbor, MI (1968).
- [5] H. Potts, MS Thesis, Clarkson University, Potsdam, NY (1984).
- [6] H. Potts and W.R. Wilcox, to be published.
- [7] G. Neugebauer, Clarkson University, Potsdam, NY, private communication, 1985.

APPENDIX B

(Accepted by J. Crystal Growth)

CHAOTIC ASYMMETRIC CONVECTION IN THE BRIDGMAN-STOCKBARGER TECHNIQUE

Hilary Potts and William R. Wilcox
Department of Chemical Engineering, Clarkson University
Potsdam, New York 13676, USA

Abstract

Convection was observed in naphthalene in a vertical Bridgman-Stockbarger arrangement. Differing from the assumptions of the theorists, the flow was neither steady nor axi-symmetric because of the heating and cooling conditions employed. It is suggested that such irregular convection may be common and cause compositional striations and azimuthal composition variations.

1. Introduction

A great many simplifying assumptions have been made in the many attempts to model transport phenomena in the Bridgman-Stockbarger technique. One-dimensional models neglect radial heat transfer. Two-dimensional cylindrical models assume axi-symmetry and often neglect convection in the melt as well. Workers at MIT [1] and at Clarkson [2] have developed two-dimensional models including axi-symmetric steady convection for high thermal conductivity materials. Tien [3] considered axi-symmetric heat transfer with steady convection for low k materials. The degree of convection expected for the usual Bridgman-Stockbarger configuration with the heater on top does not significantly influence heat transfer in high k materials, but can have a very large effect for low k materials. Convection is expected to strongly influence segregation and compositional homogeneity in all materials.

As indicated above, when convection in the melt has been considered, it has been assumed to be axi-symmetric and steady (not varying with time). We report here on experimental results that indicate these assumptions are not always realized. To achieve steady axi-symmetric flow may require great care in equipment design, especially for low-melting materials with a small thermal conductivity.

2. Experiments

The experimental apparatus is described in a companion paper. Details are given elsewhere [4]. The convection was revealed by tracer particles in the melt, observed by videotaping. The particles were ceramic micro-balloons from the Emerson Corporation. Nearly neutrally buoyant micro-balloons were pre-selected by suspending them in molten naphthalene and removing those that settled or rose. The videotapes were converted to a form useful here by

placing a transparent grid over the television monitor. Particles were tracked thereby for 5 minute periods. Because the entire ampoule was lighted, the front to back positions of the particles relative to the camera are unknown.

3. Results and Discussion

Results are shown in the figures for different cooler/heater combinations (T_c/T_h). For a convex interface in the heater, theory [1-3] predicts that flow arises along the wall and falls in the center. What we observed, in general, is flow falling near the right wall and rising along the left wall (near the heater in the bath). Even when the stirring in the bath was turned higher, asymmetric convection persisted. Furthermore the flow, while very gentle, was also erratic. Sometimes a particle moved in the opposite direction to the predominant right to left flow along the interface. Flow paths varied from particle to particle. Only occasionally did a particle move in a closed loop. Sometimes a particle moved along in a roughly helical path.

Segregation results reported in the literature show both impurity striations marking the instantaneous interface shape and non-axisymmetric compositions or doping [5-8]. Sensitive temperature measurements in a naphthalene Bridgman-Stockbarger melt revealed irregular temperature fluctuations on the order of 1°C [9]. (The heater around the top of the ampoule consisted of a surrounding Pyrex type wound with nichrome wire, while the bottom of the ampoule hung out in the air.) Steady axisymmetric convection cannot produce such results. Chaotic asymmetric convection can. Note that the flow observed here was not turbulent, which implies eddies of a wide range of scales within one another. Convection in the vertical Bridgman-Stockbarger technique with the water on top is gentle, i.e. laminar. But not steady. The best descriptive word seems to us to be "chaotic."

Recent experiments have been performed at Clarkson using a heater cast from plastic around the ampoule, so that heat transfer to the ampoule walls was by conduction rather than convection [10]. While it was almost impossible to produce completely axisymmetric flow, the convection was steady. Thus we conclude that the origin of the chaotic convection in low melting BS melts is irregular convective heat transfer between the ampoule walls and the heat source, as in the present experiments and in the work of Ref. 9. This would not be expected in high melting materials where heat transfer between the ampoule and the furnace walls is dominated by radiation. Low thermal conductivity melts may also be more subject to chaotic convection than high thermal conductivity melts where external heat transfer fluctuations tend to be damped out in the material before they can influence the convection.

Acknowledgement

This research was supported by NASA under Contract NAS8-34891.

References

- [1] C.J. Chang and R.A. Brown, J. Crystal Growth 63 (1983)343.
- [2] L.Y. Chin and F.M. Carlson, J. Crystal Growth 62 (1983)561.
- [3] L.C. Tien and J.O. Wilkes, Heat Transfer 1970, Vol. 1, U. Grigull and E. Hahne, editors, American Elsevier, NY (1970).
- [4] H. Potts, M.S. Thesis, Clarkson University (1984).
- [5] B.E. Bartlett, P. Capper, J.E. Harris and M.J.T. Quelch, J. Crystal Growth 46(1979) 623.
- [6] D.E. Holmes and H.C. Gatos, J. Electrochem. Soc., 128(1981) 429.
- [7] W.F.H. Micklethwaite, Ch. 3 in Vol. 18 of Semiconductor and Semimetals, Academic Press, NY (1981).
- [8] A.G. Petrosyan, Crystal Res. Technol. 18(1983)1107.
- [9] W.R. Wilcox, Private Communication, Aerospace Corp. (1967).
- [10] G. Neugebauer, Private Communication, Clarkson University (1985).

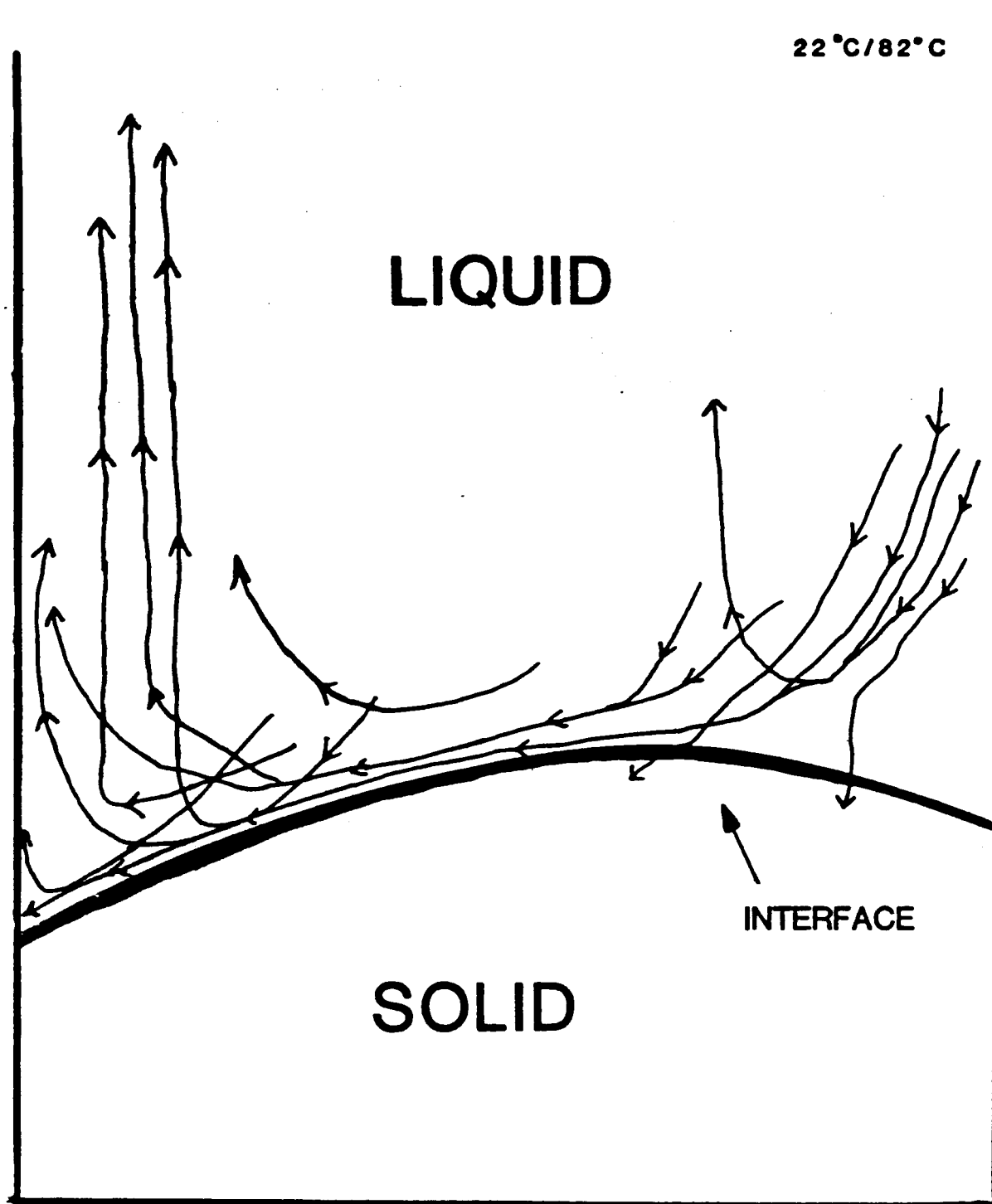


Figure 1. Particle trajectories over a 5 minute period for a cooling bath temperature T_c of 22°C and a heating bath temperature T_h of 82°C.

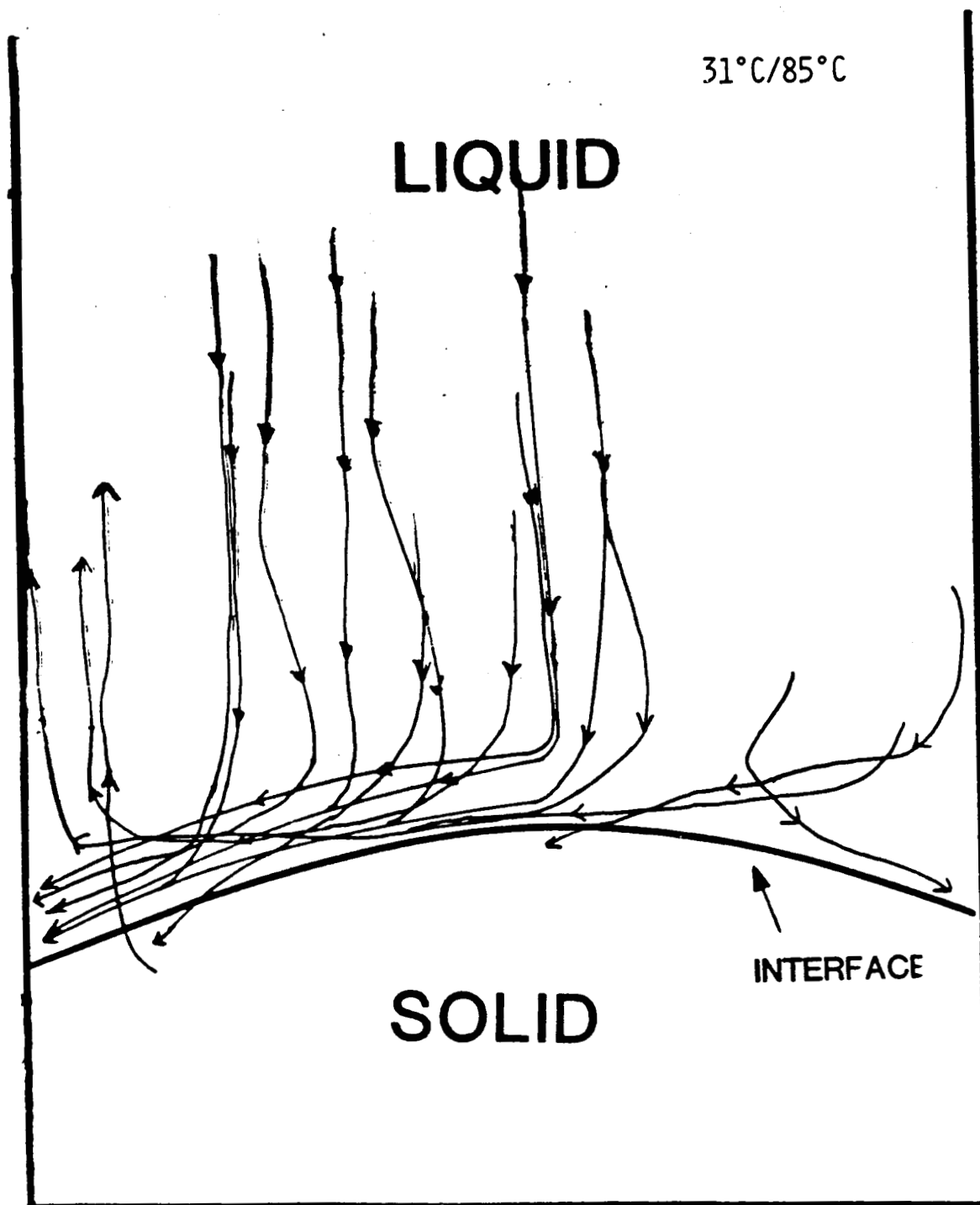


Figure 3. Particle trajectories for $T_c = 31^\circ\text{C}$ and $T_h = 85^\circ\text{C}$.

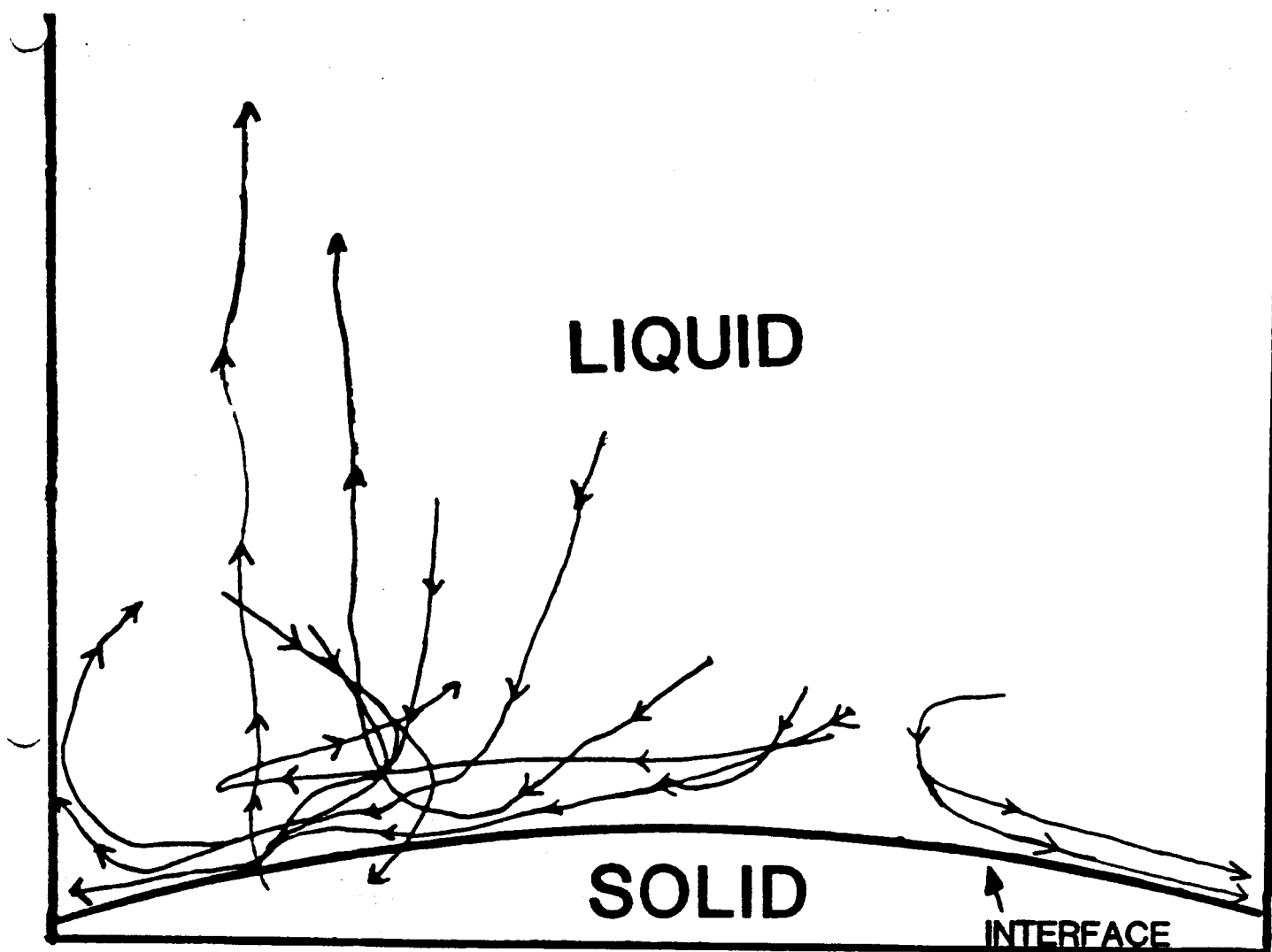


Figure 4. Particle trajectories for $T_c = 22^{\circ}\text{C}$ and $T_h = 90^{\circ}\text{C}$.

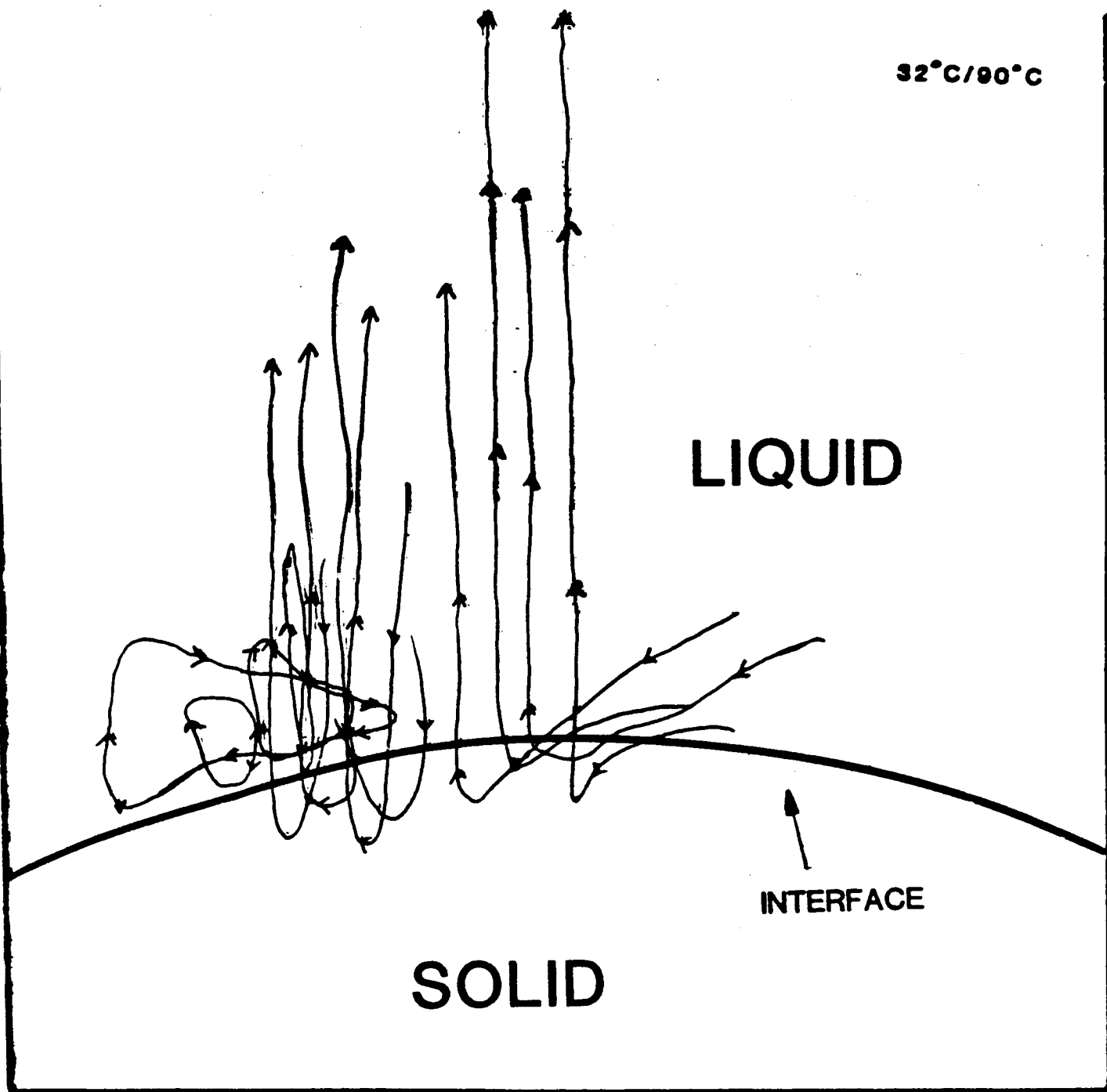
32°C/90°C

LIQUID

INTERFACE

SOLID

Figure 5. Particle Trajectories for $T_c = 32^\circ\text{C}$ and $T_h = 90^\circ\text{C}$.



APPENDIX C
CLARKSON UNIVERSITY

Convection In The Bridgman-Stockbarger Technique

A Thesis

by

Greg Neugebauer

Department of Chemical Engineering

Submitted in partial fulfillment of the requirements
for the degree of
Master of Science
(Chemical Engineering)

31 March 1986

Accepted by the Graduate School

Date

Dean

Abstract

The influence of operating parameters on convection in the Bridgman-Stockbarger technique was studied by observing the convective flow in a model Bridgman system using a transparent furnace and melt. The characteristics of the convective field were very sensitive to small variations in the thermal profile of the furnace. Convection was nearly nonexistent near the interface in the vertically stabilized thermal configuration. With the addition of a short booster heater between the main heater and the cooler, a destabilized temperature gradient was produced near the interface and significant convection was produced throughout the entire melt. Convective velocities increased as power to the booster heater was increased. Convection was usually asymmetrical. However under very carefully controlled conditions a symmetrical flow field could be produced.

TABLE OF CONTENTS

CONTENTS	PAGE
ACKNOWLEDGMENT	i
DEDICATION	ii
ABSTRACT	iii
TABLE OF CONTENTS	iv
LIST OF FIGURES	v
LIST OF TABLES	ix
CHAPTER I. INTRODUCTION	1
CHAPTER II. LITERATURE REVIEW	3
CHAPTER III. EXPERIMENTAL METHODS	40
CHAPTER IV. EXPERIMENTAL RESULTS	54
CHAPTER V. DISCUSSION	105
REFERENCES	114
NOMENCLATURE	116

LIST OF FIGURES

<u>Figure</u>		<u>Page</u>
2.1	Dimensionless isotherms for a stationary rod.	4
2.2	Dimensionless isotherms for a moving rod.	6
2.3	Dimensionless isotherms as influenced by insulation.	6
2.4	Effect of a conductive ampoule on thermal profile.	8
2.5	Effect of a large decrease in thermal conductivity upon solidification on sample's thermal profile.	9
2.6	Dimensionless isotherms for a moving rod.	9
2.7	Composition vs. axial position.	11
2.8	Growth rate vs. axial position.	11
2.9	Interface position vs. demarcation event.	13
2.10	Schematic of furnace with booster heater.	14
2.11	Effect of booster on sample's thermal profile.	14
2.12	Tien's apparatus.	16
2.13	Effect of translation rate on interfacial shape and position (Tien).	18
2.14	Tien's computed streamlines.	19
2.15	Schematic of Chang and Brown's system.	21
2.16	Effect of Rayleigh number on flow field as calculated by Chang and Brown.	21
2.17	Maximum stream function vs. Rayleigh number (Chang and Brown).	23
2.18	Effect of Rayleigh number on dopant concentration fields as computed by Chang and Brown.	24
2.19	Interfacial dopant concentration vs. Rayleigh number.	24
2.20	Effect of interfacial curvature on dopant concentration field (Chang and Brown).	25
2.21	Chang and Brown's computed results for effect of Ra on flow in the destabilized system.	27
2.22	Dopant concentration field for Figure 2.21.	27

<u>Figure</u>		<u>page</u>
2.23	Interfacial dopant concentration vs. Ra for the conditions of Figure 2.21.	27
2.24	Comparison of percentage radial segregation in Chang and Brown's stabilized and destabilized systems.	27
2.25	Geometry of system of Carlson et al.	29
2.26	Effect of interfacial curvature on computed streamlines and isotherms (Carlson et al.).	30
2.27	Effect of interfacial curvature and insulation thickness on computed streamlines and isotherms (Carlson et al.).	30
2.28	Effect of interfacial curvature and Gr on computed streamlines and isotherms (Carlson et al.).	31
2.29	Effect of interfacial curvature and Bi on computed streamlines and isotherms (Carlson et al.).	32
2.30	Effect of interfacial curvature and Pr on computed streamlines and isotherms (Carlson et al.).	33
2.31	Schematic of Potts's set-up.	36
2.32	Convection observed by Potts.	37
2.33	Convection observed by Potts.	38
2.34	Convection observed by Potts.	39
3.1	Photograph of two-zone furnace.	41
3.2	Photograph of three-zone furnace, A4.8.	41
3.3	Photograph of three-zone furnace, A6.7.	42
3.4	Schematic of two-zone furnace.	47
3.5	Schematic of three-zone furnace, A4.8.	48
3.6	Schematic of three-zone furnace, A6.7.	49
4.1a	Plot of temperature vs. position for run I-44.	56
4.1b	Photographs of convective field for run I-44.	57
4.1c	Schematic of convective field for run I-44.	58
4.2a	Plot of temperature vs. position for run I-47.	59
4.2b	Photographs of convective field for run I-47.	60

<u>Figure</u>		<u>Page</u>
4.2c	Schematic of convective field for run I-47.	61
4.3a	Plot of temperature vs. position for run I-49.	62
4.3b	Photographs of convective field for run I-49.	63
4.3c	Schematic of convective field for run I-49.	64
4.4a	Plot of temperature vs. position for run I-52.	65
4.4b	Photographs of convective field for run I-52.	66
4.4c	Schematic of convective field for run I-52.	67
4.5a	Plot of temperature vs. position for run I-21.	68
4.5b	Photographs of convective field for run I-21.	69
4.5c	Schematic of convective field for run I-21.	70
4.6a	Plot of temperature vs. position for run I-62.	71
4.6b	Photographs of convective field for run I-62.	72
4.6c	Schematic of convective field for run I-62.	73
4.7a	Plot of temperature vs. position for run I-55.	74
4.7b	Photographs of convective field for run I-55.	75
4.7c	Schematic of convective field for run I-55.	76
4.8a	Plot of temperature vs. position for run I-66.	77
4.8b	Photographs of convective field for run I-66.	78
4.8c	Schematic of convective field for run I-66.	79
4.9a	Plot of temperature vs. position for run I-71.	80
4.9b	Photographs of convective field for run I-71.	81
4.9c	Schematic of convective field for run I-71.	82
4.10a	Plot of temperature vs. position for run II-12.	84
4.10b	Photographs of convective field for run II-12.	85
4.10c	Schematic of convective field for run II-12.	86
4.11a	Plot of temperature vs. position for run II-11.	87
4.11b	Photographs of convective field for run II-11.	88

<u>Figure</u>		<u>Page</u>
4.11c	Schematic of convective field for run II-11.	89
4.12a	Plot of temperature vs. position for run II-10.	90
4.12b	Photographs of convective field for run II-10.	91
4.12c	Schematic of convective field for run II-10.	92
4.13a	Plot of temperature vs. position for run II-7A.	93
4.13b	Photographs of convective field for run II-7A.	94
4.13c	Schematic of convective field for run II-7A.	95
4.14a	Plot of temperature vs. position for run II-7B.	96
4.14b	Photographs of convective field for run II-7B.	97
4.14c	Schematic of convective field for run II-7B.	98
4.15a	Plot of temperature vs. position for run II-8.	99
4.15b	Photographs of convective field for run II-8.	100
4.15c	Schematic of convective field for run II-8.	101
4.16a	Plot of temperature vs. position for run II-9.	102
4.16b	Photographs of convective field for run II-9.	103
4.16c	Schematic of convective field for run II-9.	104

LIST OF TABLES

<u>Table</u>		<u>Page</u>
2.1	Physical properties of Ga-doped Ge.	21
3.1	Properties of materials.	43
4.1	Experimental run and corresponding thesis figure number.	55
5.1	Temperature of the sample ampoule's outer wall adjacent to the interface.	109

Chapter I.

Introduction

Bridgman's original technique for growing single crystals consisted of a single furnace through which a cylindrical, pointed-bottom container holding the charge could be lowered. The Bridgman-Stockbarger technique was created when Stockbarger added a second furnace which functioned as a cooler. He separated the upper and lower furnaces with a polished platinum thermal screen designed to promote a steep axial temperature gradient (1-3). This method of directional solidification is used to grow single crystals of metals, organics, dielectric oxides, fluorides, sulfides, and halides (3).

The need in recent years to produce more homogeneous crystals has made directional solidification a topic of intensive research. Early theoretical studies were on the effects of heat transfer on the shape of the melt/solid interface: an important parameter in controlling thermal stress, grain selection, and component segregation (4,5). Most models assume that heat transfer within the melt occurs only by conduction. While this may be a valid assumption for low Prandtl number fluids, the effects of convection on crystal composition are by no means negligible. The microscopic distribution of components at the interface is extremely sensitive to small changes in convective flow patterns (6). Because the response of most electronic devices is strongly related to their composition, convective transport in melt growth systems has been actively investigated in recent years.

In this work, a modified Bridgman-Stockbarger technique was used to experimentally observe the effects of variations in temperature profile, melt aspect ratio, and ampoule tilt angle on convection in

the melt.

This thesis consists of five chapters: Chapter I is an introduction, Chapter II is a literature review, Chapter III is a description of experimental methods, Chapter IV gives the results, and Chapter V presents the conclusions and recommends possible future work.

Chapter II.

Literature Review

The Bridgman-Stockbarger technique has been studied extensively for two different heat transfer regimes: negligible convection and significant convection. Since either regime may occur in practice, both are discussed below.

Conduction

An early theoretical analysis of the Bridgman-Stockbarger technique was done by Chang and Wilcox (4). Chang and Wilcox assumed a situation in which a heater on top is separated by a sharp boundary from a cooler beneath. Both the heater and cooler are at constant temperature. In their analysis of an infinitely long cylinder, they assumed convection in the melt was negligible, the physical properties in the melt and solid were constant and equal, and that there was no crucible. The thermal conditions in the model included heat transfer between the sample and the furnaces. The heat transfer coefficients in the heater and cooler were constant and included all modes of heat transfer. An analytical solution in terms of Bessel functions was obtained for the heat conduction equation.

Figure 2.1 shows the dimensionless isotherms $((T - T_c)/(T_h - T_c))$ obtained by Chang and Wilcox for a stationary rod for Biot numbers ($Bi = hR/k$) of 0.4, 1.0, and 2.0. The isotherms are concave in the cooler and convex in the heater. The planar isotherm lies midway between. Since the interface of a pure material is an isotherm at the melting point of the material, each isotherm in Figure 2.1 represents a possible interface shape and position. Chang and Wilcox also

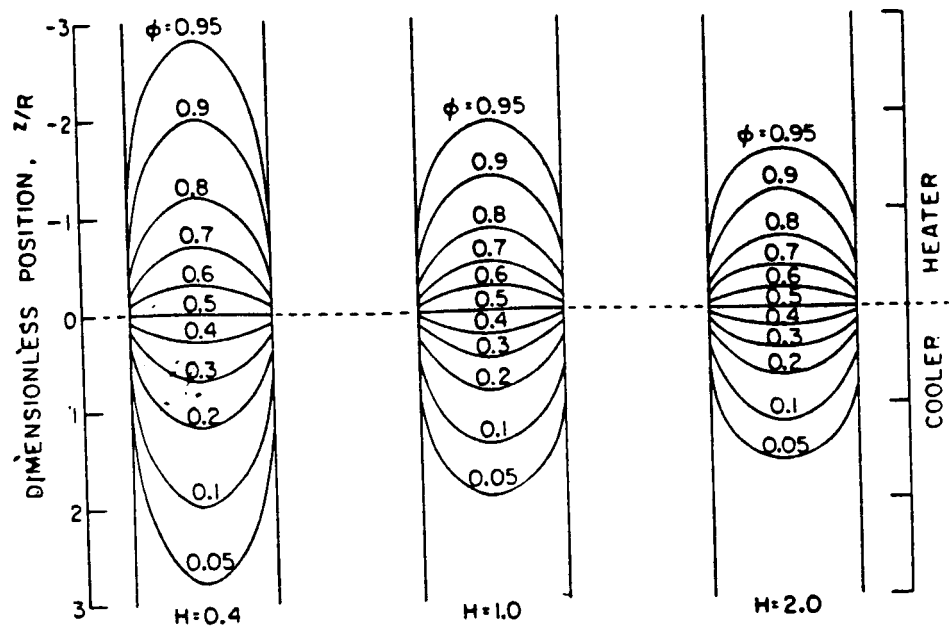


Figure 2.1. Dimensionless isotherms for a stationary rod with no convection and equal properties in the solid and liquid phases (4).

calculated the effect of ampoule translation on the isotherms. As shown in Figure 2.2, increasing the ampoule velocity causes the interface to move into the cooler and become more concave, although the planar isotherm is shifted up and has a larger value.

It was suggested by Chang and Wilcox that the dependence of interface shape on heater temperature could be reduced by inserting a layer of insulation between the heater and the cooler. This would have the effect of forcing heat transfer in the sample to be nearly axial over a longer distance. Since, in the absence of convection, heat flow is perpendicular to an isotherm, an axial heat flux favors a planar interface which reduces thermal stress and improves grain selection (4).

An analysis of the effects of a layer of insulation was done by Fu and Wilcox (5). They considered an infinite rod of constant physical properties surrounded by an isothermal heater on top and an isothermal cooler below. Between the heater and cooler was an adiabatic zone. The dimensionless isotherms for a stationary ampoule with different insulation thickness are shown in Figure 2.3. The isotherms become less curved with increasing insulation thickness.

The effect of the thermal conductivity of the ampoule on interface shape, position and sensitivity was studied by Sen and Wilcox (7). In their theoretical analysis, they considered a finite length ampoule containing a sample of constant physical properties. They showed that the sensitivities of the interface shape and position to the heater temperature is least when the thermal conductivity of the ampoule is the same as the sample.

Naumann investigated the case in which the thermal conductivity of the ampoule is much larger than the sample (8). He derived a

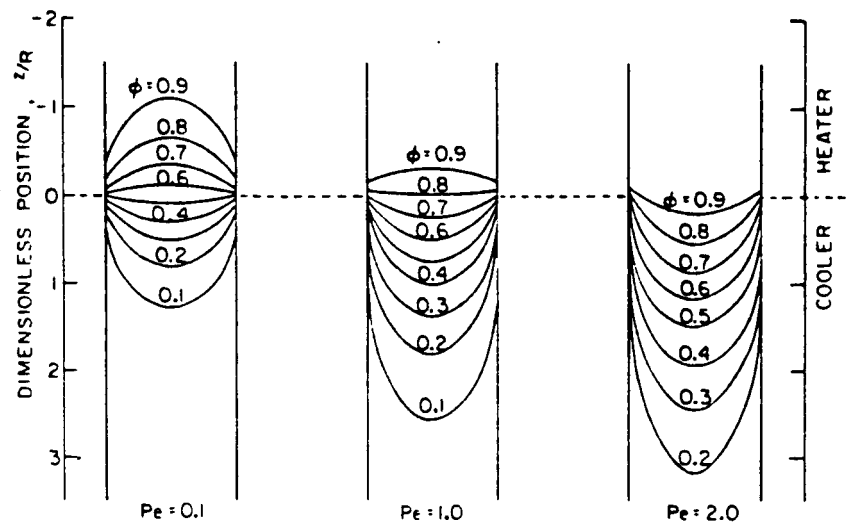


Figure 2.2. Dimensionless isotherms for three different ampoule translation rates (5).

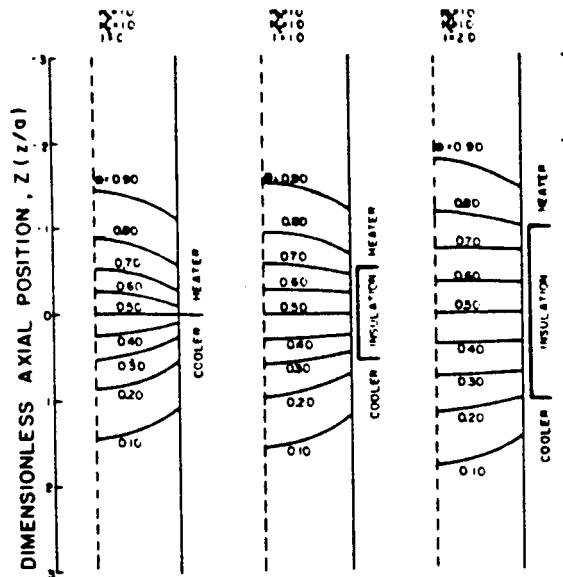


Figure 2.3. Dimensionless isotherms as influenced by insulation thickness (5).

two-dimensional analytical expression for the temperature isotherms in the region of the adiabatic zone when 80% of the axial heat flux is carried through the ampoule and the properties of the solid and liquid are the same. As shown in Figure 2.4, the use of a highly conductive ampoule diminishes the axial temperature gradient. Naumann and Lehoczký (9) extended this analytical analysis to include a large decrease in the thermal conductivity of the sample upon solidification, an effect occurring in the growth of $\text{Hg}_{1-x}\text{Cd}_x\text{Te}$ crystals. In Figure 2.5, it is shown that a large change in thermal conductivity at the solidification interface combined with a highly conductive ampoule results in an increase in radial temperature gradients within the adiabatic zone. This result shows that insertion of an adiabatic zone between a heater and cooler may sometimes have just the opposite effect from that intended, i.e. interfacial curvature is increased rather than decreased.

The effects of increasing the ampoule's translation rate for a given insulation thickness, as calculated by Fu and Wilcox (5), are shown in Figure 2.6. Pursuant to the work of Chang and Wilcox, all isotherms are shifted toward the cooler, and the value of the dimensionless planar isotherm is increased. Fu and Wilcox also showed that the sensitivity of the interface to heater and cooler temperatures decreases almost exponentially with increasing insulation thickness. Adding a layer of insulation does not greatly diminish the axial temperature gradient near a planar interface, an important consideration if one wishes to avoid constitutional supercooling. As pointed out by Sukanek, however, increasing the insulation thickness increases end effects (10,11).

Sukanek was the first to obtain an analytical expression for the

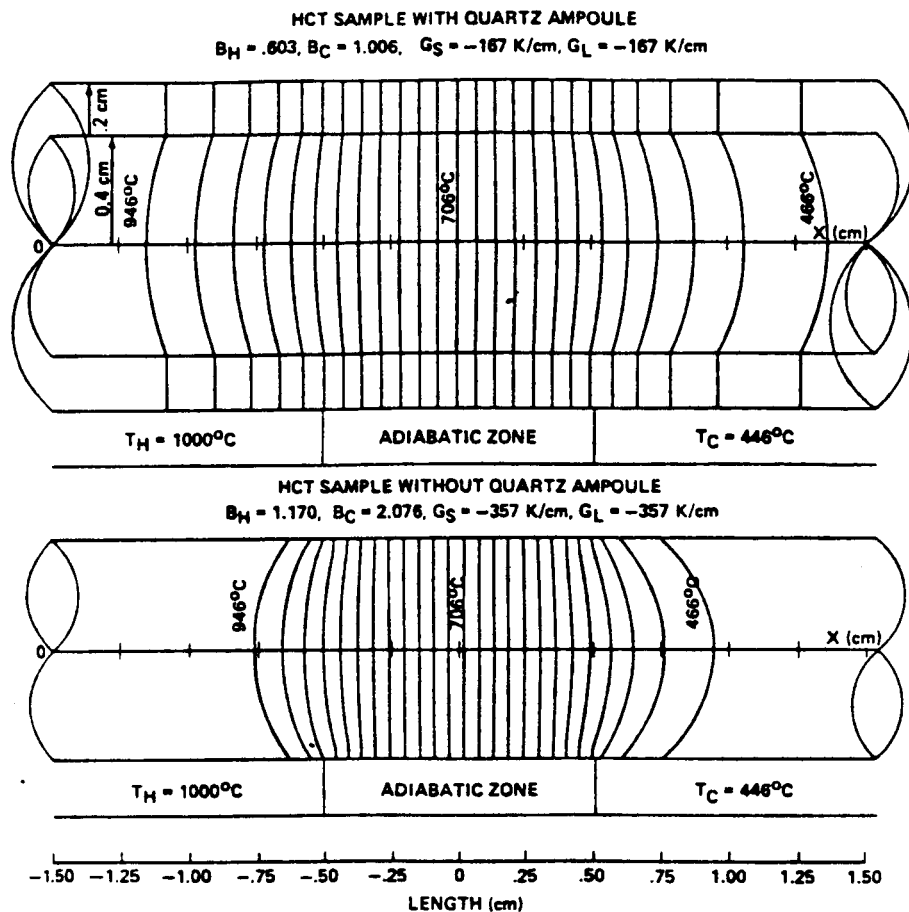


Figure 2.4. The effect of a conductive ampoule which carries 80% of the heat on the thermal profile of a $\text{Hg}_{0.8}\text{Cd}_{0.2}\text{Te}$ sample (8).

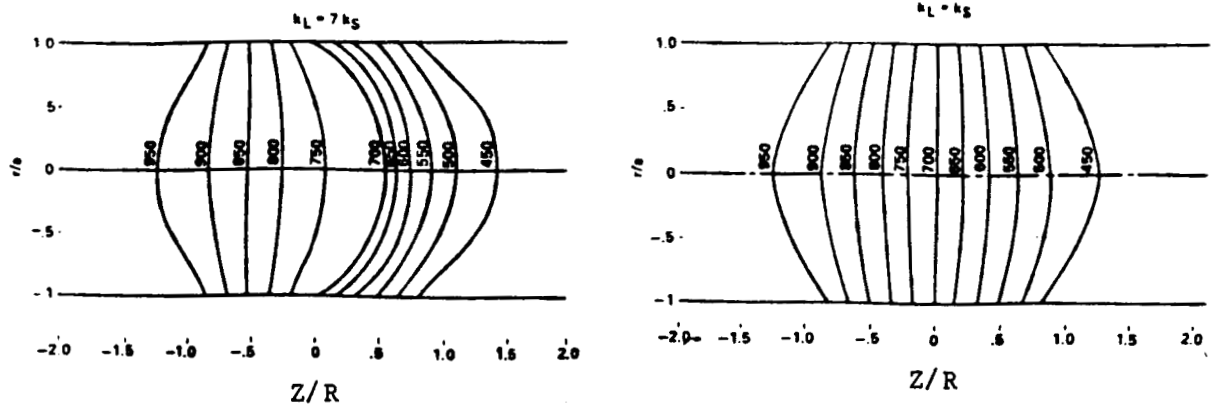


Figure 2.5. The effect of a large decrease in thermal conductivity upon solidification on thermal profile. Note the large curvature of the isotherms when $k_L = 7k_s$ within the insulation zone ($-1.0 < Z/R < 1.0$) (9).

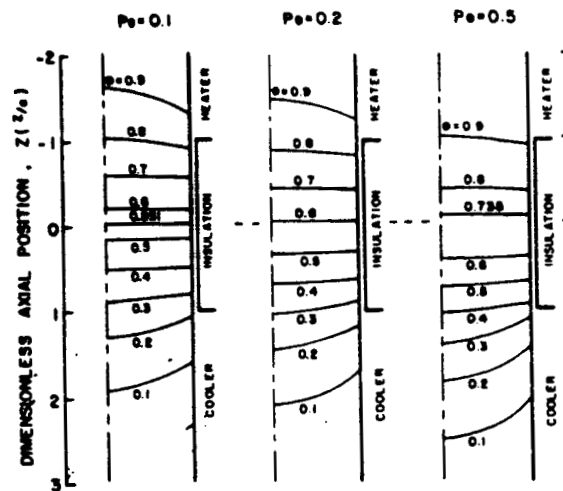


Figure 2.6. Dimensionless isotherms for different translation rates (5).

deviation of freezing rate from translation rate when the interface is near the top or bottom of the ampoule. His analysis, which is valid for low translation rates, small ampoule diameter and/or high thermal conductivities, showed that end effects may extend over considerable portions of the ampoule. Because of end effects, Sukanek predicted that the growth velocity will always be greater than or equal to translation rate. Sukanek's model did not take into account variations in growth rate due to changes in composition, a characteristic of real melt-growth systems. Also, his model assumed that the value of the heat transfer coefficient is the same on the side and the ends of the ampoule. This condition may not necessarily be true in practice (12).

Szofran et al. (12) showed experimentally, for Bridgman grown mercury cadmium telluride, that component segregation can be diffusion controlled. They compared their experiments and results to a modified version of the numerical scheme developed by Clayton et al. (13) which solved for the compositional variation along the length of a solidified ingot. A plot of composition vs. length solidified is shown in Figure 2.7. Also included in Figure 2.7 are the analytical solutions to the initial and final transient regions developed by Smith, Tiller, and Rutter (14). In all cases studied, the modified numerical method (13) matched their experimental results.

Using the measured experimental compositional profiles, Szofran et al. obtained a semi-empirical expression for the instantaneous interfacial translation rate. This rate, normalized by ampoule velocity, is shown in Figure 2.8. In all cases, the ampoule's translation rate exceeded the interfacial translation rate. Interface studies of Bridgman-grown CdTe by Route et al. gave similar results

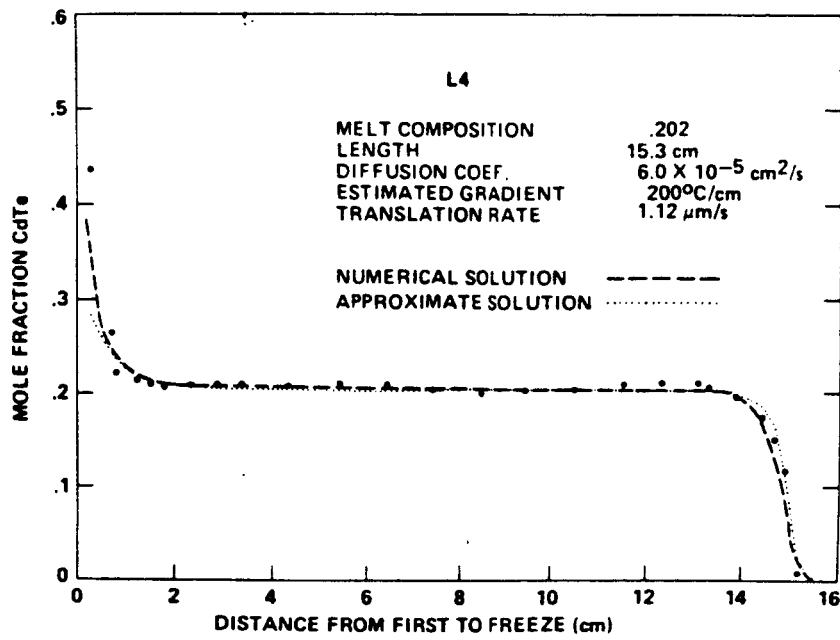


Figure 2.7. Composition vs. axial position. The solid circles indicate experimental measurements (12).

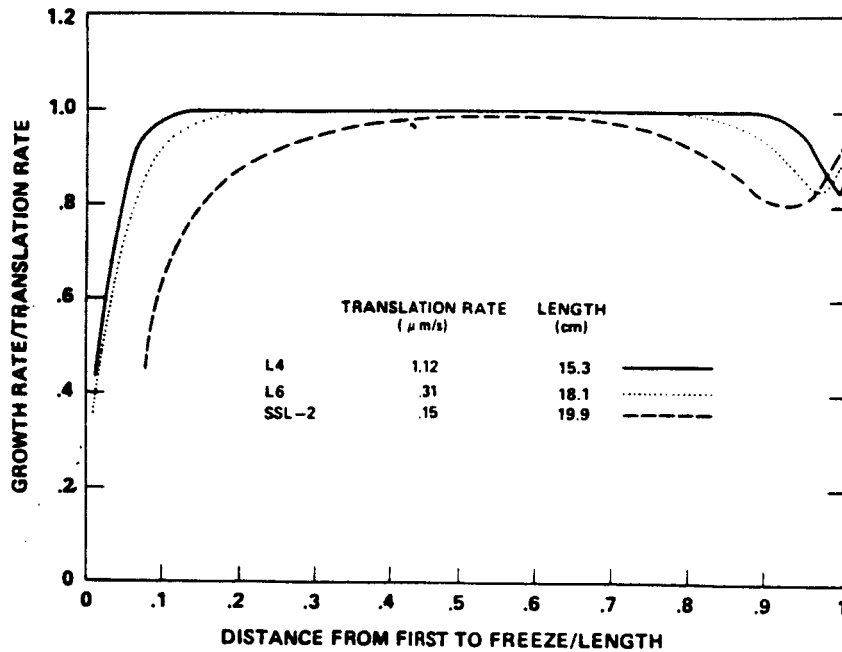


Figure 2.8. Normalized interfacial growth rate vs. normalized position (12).

(15). Using an interface demarcation technique, Route et al. correlated the ampoule's translated distance with the demarcated interface's position. They observed a 35% lag between the freezing rate and the ampoule's translation rate. As shown in Figure 2.9, no lag was observed within the bottom 4 cm long constricted portion of the ampoule.

The configuration of the Bridgman-Stockbarger furnace has sometimes been modified in recent years by adding, between the heater and the adiabatic zone, a short independently controlled furnace called a booster heater (16). This modified version of the Bridgman-Stockbarger furnace is shown schematically in Figure 2.10. With a booster heater it is possible to increase the axial temperature gradient and to provide an additional means of regulating the shape and position of the melt/solid interface.

Using a one-dimensional model, Naumann (16,17) compared the temperature profile in $\text{Pb}_{0.8}\text{Sn}_{0.2}\text{Te}$ for a Bridgman apparatus with and without a booster heater (Figure 2.11). The abscissa is the distance from the center of the adiabatic zone normalized by the sample's radius. If the cooler's temperature is fixed and the temperature of the booster is increased by 400°C , the temperature gradient in the region of the interface is correspondingly increased, and the position of the interface is shifted toward the cooler. If the cooler's temperature is lowered so as to keep the position of the interface fixed at $Z/R = 0$, the interfacial temperature gradient is increased further. These results imply that the modification of using a booster heater has a very significant advantage over Bridgman's original design. The advantage is that a booster heater enables the crystal grower to create a large and controllable temperature gradient without

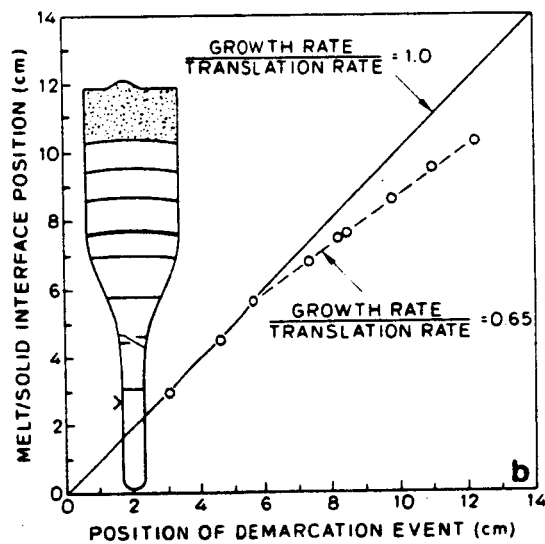


Figure 2.9. Interface position vs. demarcation event. A reduced but uniform growth rate is seen throughout the main body of the crystal (15).

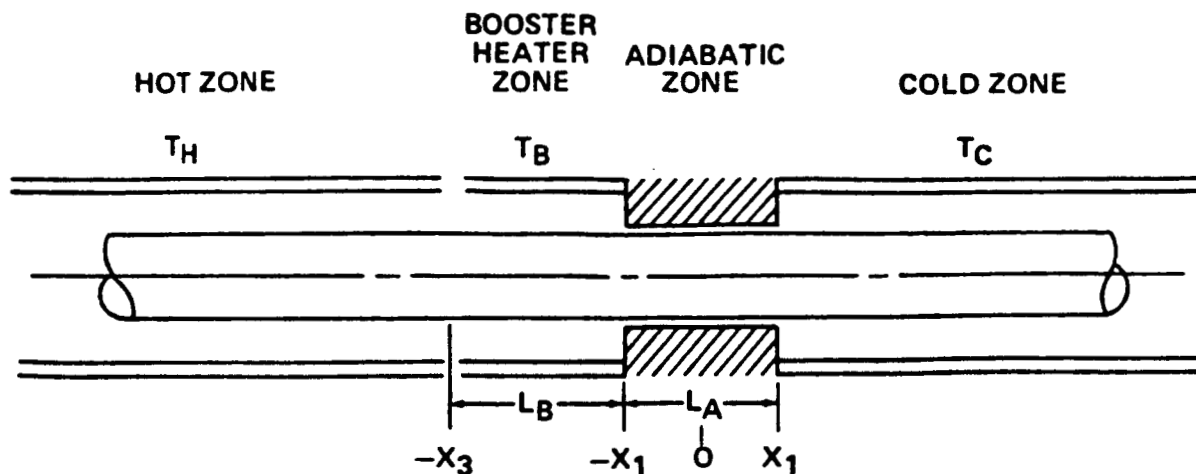


Figure 2.10. Bridgman-Stockbarger furnace with a booster heater (16).

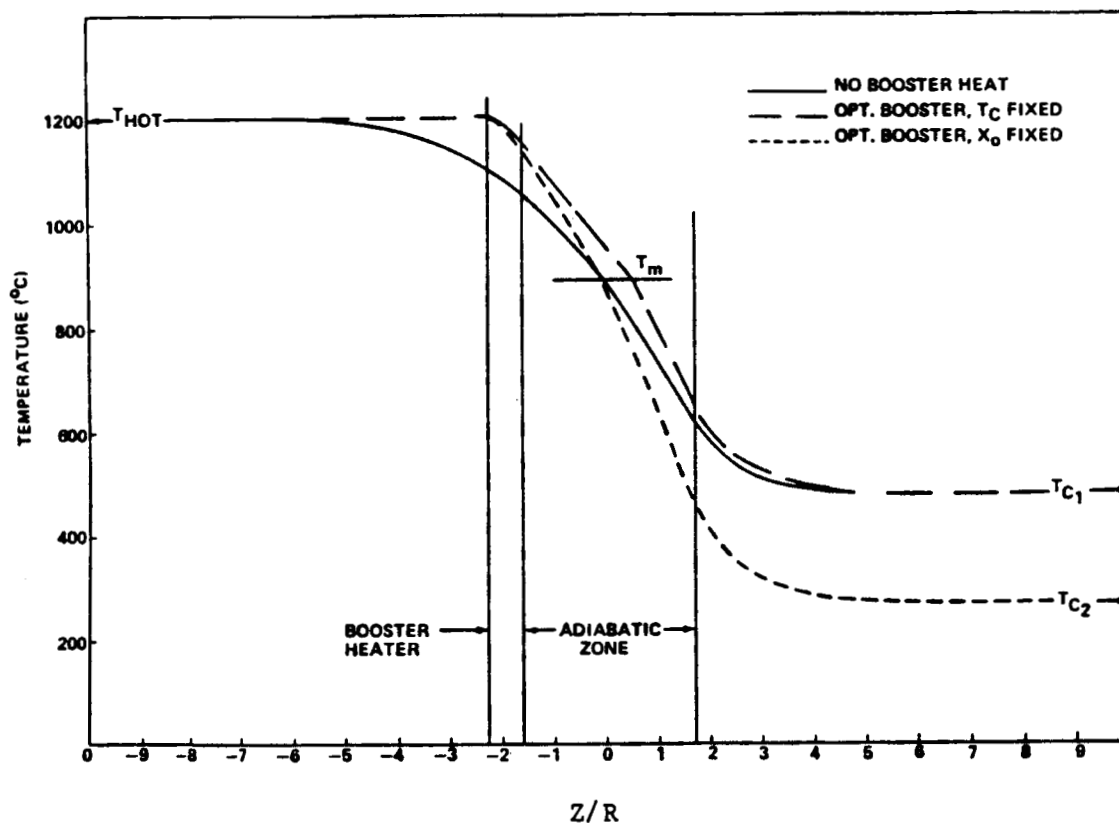


Figure 2.11. Computed thermal profile in $\text{Pb}_{0.8}\text{Sn}_{0.2}\text{Te}$ with and without a booster heater. Two booster cases are shown: T_C fixed, and T_C lowered so as to enable the interface's position to remain fixed (16,17).

unreasonably raising the temperature of the entire melt. This is a most important consideration if one is directionally solidifying materials with very high vapor pressures.

The influence that a booster heater has on convection will be discussed in detail in this thesis.

Convection

Tien and Wilkes were the first to do a two dimensional numerical study of convection in the Bridgman-Stockbarger technique (18,19). The crystal growth coordinate system and boundary conditions are shown below in Figure 2.12. As a model system Tien and Wilkes used naphthalene, because many of its thermo-physical properties had been measured. Naphthalene, like most low molecular weight organic compounds, has a transparent molten phase. The authors also observed convective flows experimentally by using colored Nylon fibers as tracer particles.

Tien and Wilke's system consisted of a vertically mounted, moveable crystal growth tube. The upper portion of the ampoule was heated with a circulating hot bath. The lower portion was cooled with a cold circulating bath. The two circulating baths were separated by a diaphragm. The steady state thermal profile along the inner wall was determined with 30 gauge chromel-alumel thermocouples. In the computations, the temperature at the bottom of the crystal was set equal to the wall temperature of the lower end of the ampoule. Likewise the temperature at the free surface of the melt was approximated by the temperature at the top of the ampoule.

For their numerical analysis Tien and Wilkes used a time-dependent finite-difference method. The boundary condition was the measured inner-wall steady-state temperature profile. By modeling

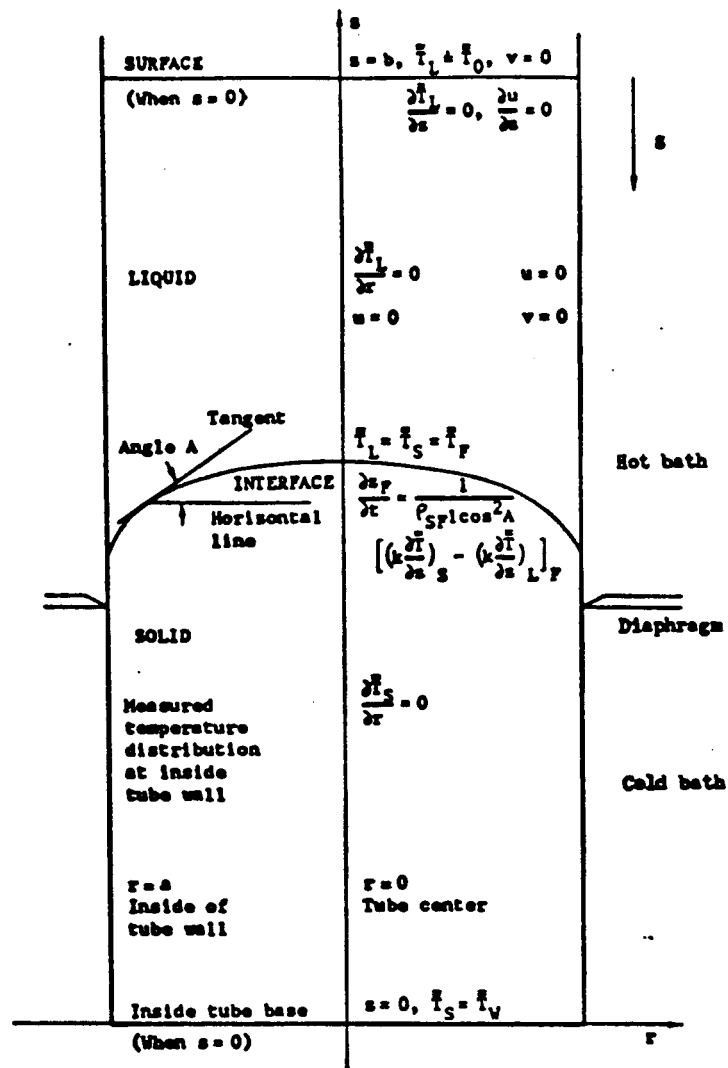


Figure 2.12. Tien's coordinate system, geometry, and boundary conditions (18).

the process as a time-dependent initial value problem, a steady state solution was found at long times.

The computed shape and position of the solid-liquid interface are shown in Figure 2.13 for various translation rates. The interface position at the wall was not computed, it was obtained by experiment. Agreement between theory and experiment for interface position was good for each ampoule translation rate. For the stationary ampoule, it was necessary to use a small grid spacing for accurate convergence. The normalized computed streamlines are displayed in Figure 2.14 for a stationary interface. Tien calculated that the only region of significant convection was near the interface next to the wall. Presumably this was also the region of largest radial temperature gradient. The fluid rose near the wall, descended in the inner melt and returned to the wall across the interface.

In his experiments, Tien revealed the convective flows using colored Nylon tracer fibers. There was good qualitative agreement with theory for flow velocities, both in magnitude and direction. As the interface became less convex, the region of observable convection decreased. Although the natural convection was laminar, it was not quite axisymmetric. The authors attributed this to unavoidable deviations from symmetrical heating and cooling.

Perhaps the most thorough and complex numerical study of the Bridgman-Stockbarger technique was done by Chang and Brown (6). In their analysis, they used a finite element/Newton technique that computed simultaneously the shape of the solidification interface, the velocity and pressure fields in the melt, and the temperature distribution in the melt and crystal. The geometry of the system is shown in Figure 2.15.

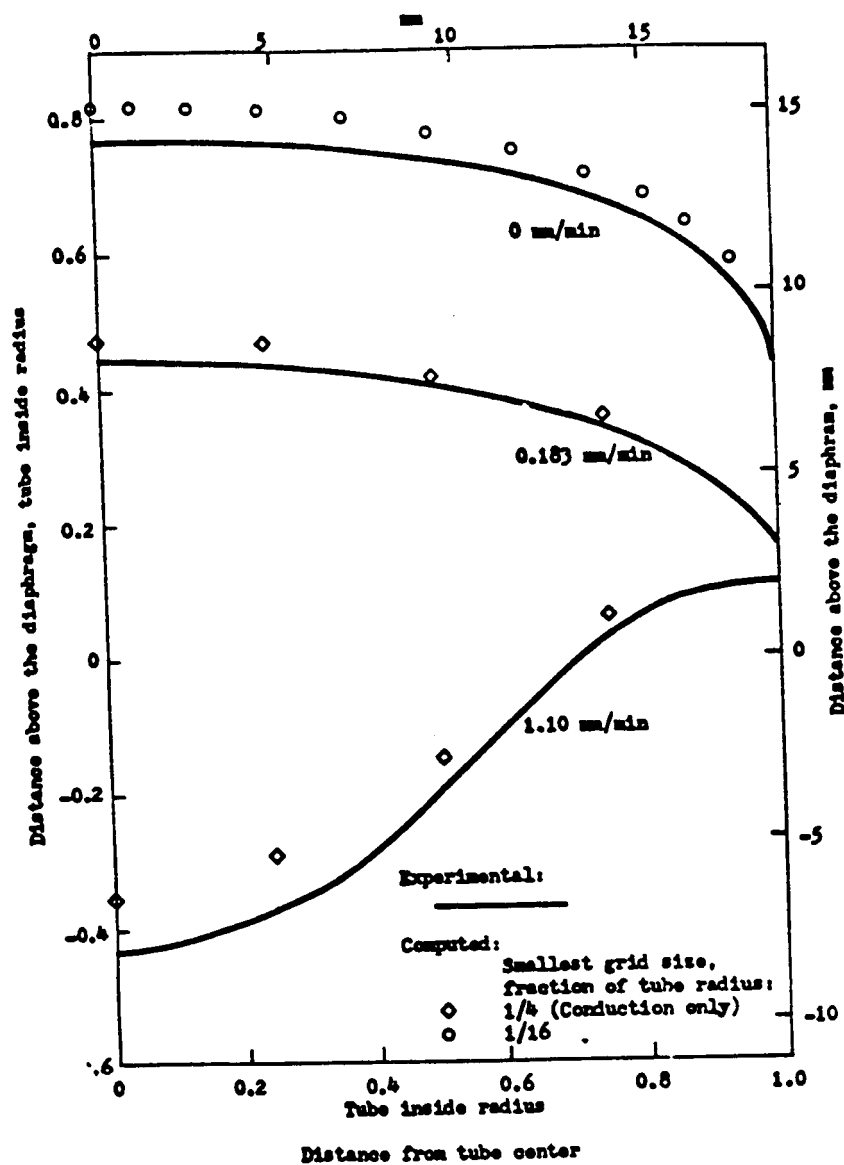


Figure 2.13. Effect of ampoule translation rate on the interface's shape and position.

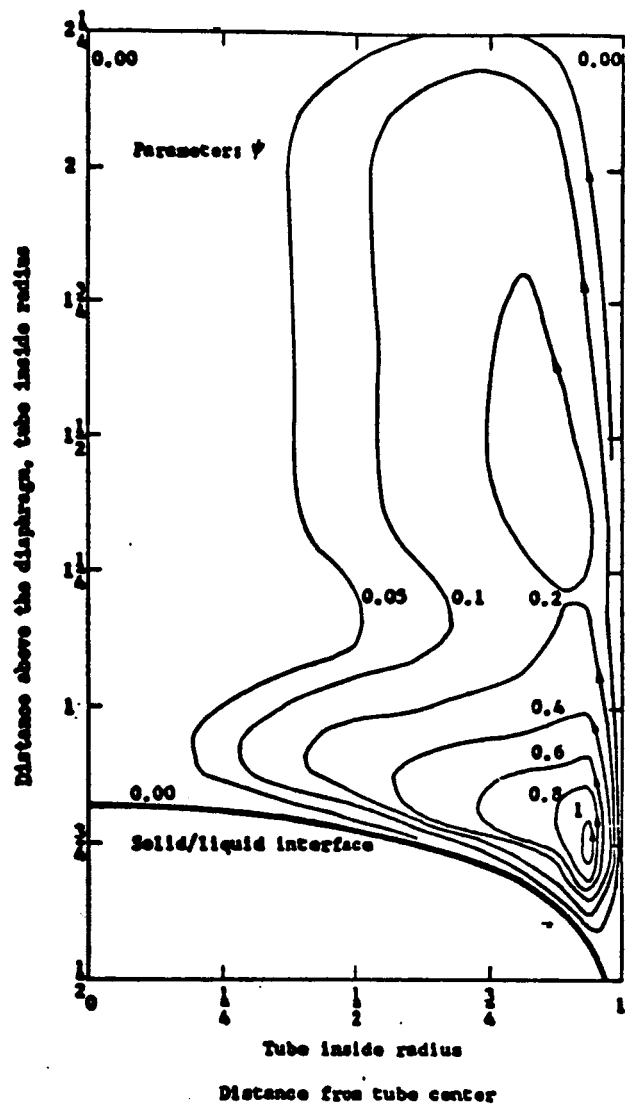
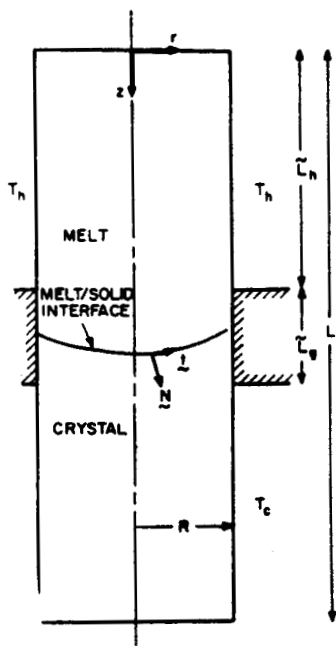


Figure 2.14. Computed streamlines for a stationary ampoule (18).

The model used in the analysis had a constant temperature heating zone on top, a perfectly adiabatic region underneath, and a cooler of constant temperature below. The radius of the ampoule was taken to be 0.5 cm, its overall length was 2.0 cm, the adiabatic region was 0.25 cm long, and the ampoule's translation rate was 16 micron/s. This is an extremely short furnace compared to those used experimentally. The effects of ampoule translation were simulated by adding melt at the top of the furnace and withdrawing crystal from the cooler. For their computations, Chang and Brown used the properties of gallium-doped germanium summarized in Table 2.1.

Chang and Brown assumed that the melt was a Boussinesq fluid. The interface was assumed to be an isotherm at the equilibrium melting point of the material, and the difference in conductive heat flux between the liquid and solid was equal to the latent heat liberated in solidification. The no-slip condition was used for convection at the interface, the ampoule wall, and at the top of the ampoule. The velocity, thermal, and mass transfer fields were assumed to be axi-symmetric. The temperature along the edge of the sample was assumed to be equal to the adjacent heater temperature, i.e. the heat transfer coefficient and the Biot number were infinite. The adiabatic zone was assumed to be a perfect insulator as were the ends of the crystal growth ampoule.

In Figure 2.16 are displayed the effects of increasing Rayleigh number ($Ra = R^3 g \beta (T_h - T_c) / \nu \alpha$) on convection. For low Ra , the flow is rectilinear and reflects only the downward motion of the ampoule. For intermediate values of Ra , a cellular flow pattern is predicted. In agreement with Tien's work, the flow moves upward at the wall and descends near the centerline. At higher Rayleigh numbers



Property	Value
Thermal conductivity of melt (k_L)	0.17 W/K · cm
Thermal conductivity of solid (k_S)	0.17 W/K · cm
Heat capacity of melt (c_{pL})	0.39 J/g · K
Heat capacity of solid (c_{pS})	0.39 J/g · K
Density of melt (ρ_L)	5.6 g/cm ³
Density of solid (ρ_S)	5.6 g/cm ³
Melting temperature (T_m)	958°C
Kinematic viscosity of melt (ν)	1.3×10^{-3} cm ² /s
Heat of fusion (ΔH_S)	506 J/g
Thermal expansion coefficient (β)	0.25×10^{-3} K ⁻¹
Diffusivity of Ga in Ge (\mathcal{D})	1.3×10^{-4} cm ² /s
Segregation coefficient of Ga in Ge (k)	0.1

Table 2.1. Physical properties of gallium-doped germanium (6).

Figure 2.15. Geometry of system studied by Chang and Brown (6).

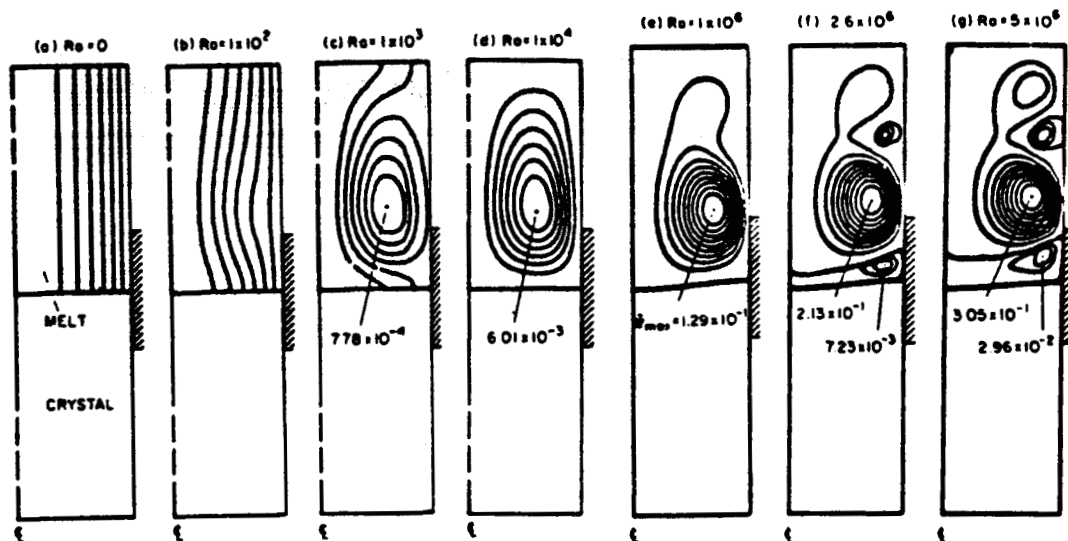


Figure 2.16. Effect of Rayleigh number on flow field. Streamline values are equally spaced with the maximum (or minimum) set equal to zero. Only the right half of the flow field is shown (6).

multicellular flow is predicted. Figure 2.17 shows that the stream function's maximum value increases linearly with Ra over the region of weak cellular flow.

The computed dopant concentration fields corresponding to the flow fields of Figure 2.16 are shown in Figure 2.18. The planar isoconcentration lines for $Ra=0$ correspond to one dimensional diffusion. The weak cellular flows occurring for $Ra=10^3$ produce large radial segregation. Figure 2.19 shows that the radial segregation is a maximum at about $Ra=10^3$. Radial segregation decreases for greater Ra due to the formation of a well-mixed core of melt.

The effect of interfacial curvature alone on segregation is displayed in columns (a) and (d) of Figure 2.20. The curvature of the solid-liquid interface was modified by changing the ratio of the solid to liquid thermal conductivities. Even when $Ra=0$, the curvature of the interface induces large radial segregation. This effect is somewhat larger for a concave interface than for a convex interface.

Up to this point, only the Bridgman-Stockbarger technique employing a heater on top and cooler below has been discussed. In this configuration, the temperature of the melt increases with height. Buoyancy driven convection is not generated by the axial temperature gradient imposed by the system geometry per se but by radial temperature gradients which are generated by heat transfer between the sample and surrounding furnaces. Since the axial temperature gradient in this configuration does not promote convection directly, it is often referred to as the vertically stabilized configuration. If the position of the heating and cooling furnaces is switched, solidification can occur by raising the sample from the heater up into the cooler. In this configuration, the axial

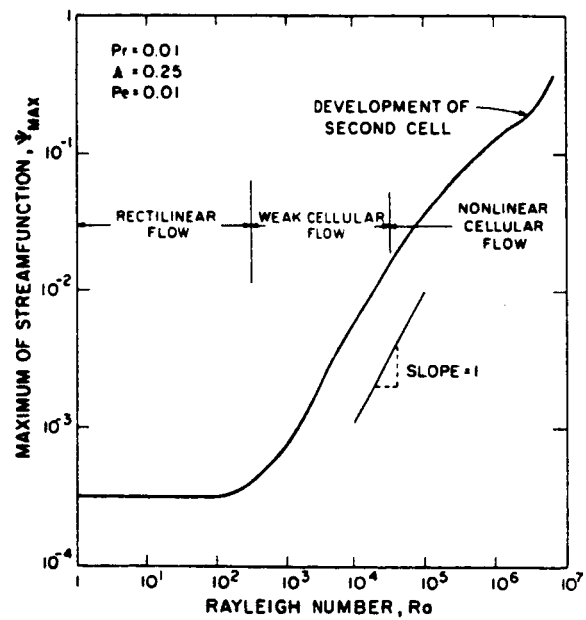


Figure 2.17. Maximum stream function vs. Ra (6).

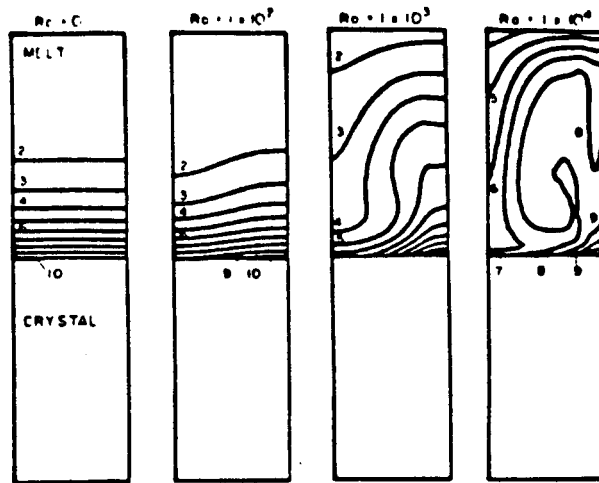


Figure 2.18. Dopant concentration fields for flow field shown in Figure 2.16 (6).

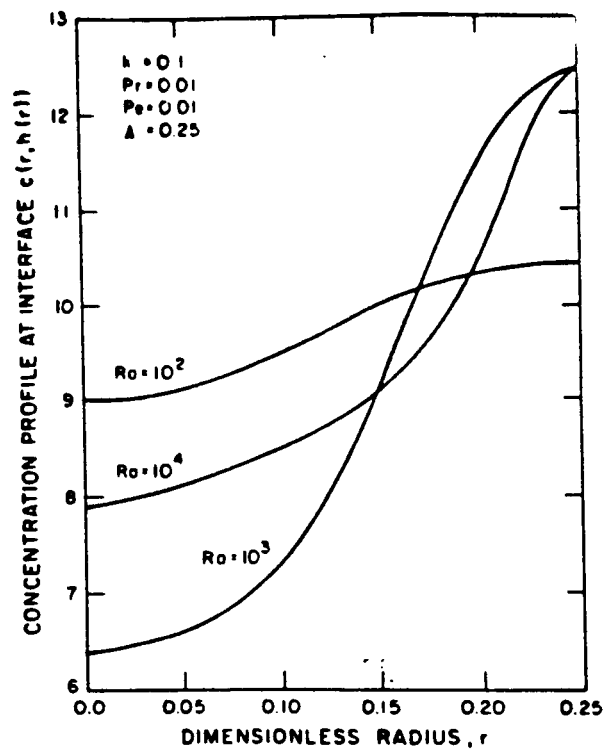


Figure 2.19 Interfacial dopant concentration vs. Ra (6).

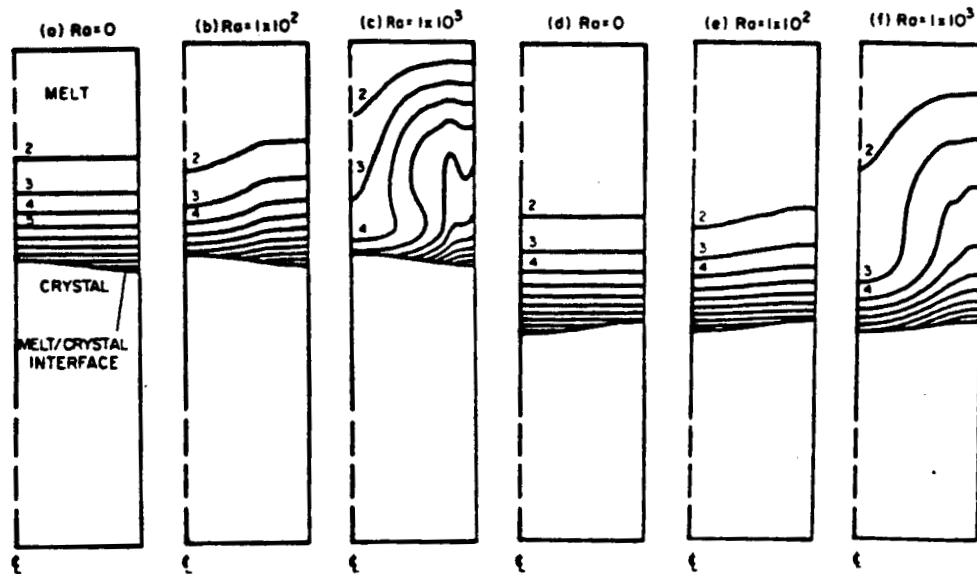


Figure 2.20. Dopant concentration fields as influenced by interfacial curvature and Rayleigh number. Even when $Ra=0$, the isoconcentration lines intersect the melt/crystal interface (6).

temperature gradient is destabilizing because the temperature in the melt decreases with height. Since both the axial and the radial gradients promote buoyancy driven convection, convective velocities are much larger than when the heater is on top.

Chang and Brown also investigated the flow behavior for the destabilized Bridgman system (4). As shown in Figure 2.21, the flow for this system was opposite that of the stabilized system with the heater on top. In the destabilized configuration, the melt moved upward along the wall, across the interface, and down the centerline away from the interface. The concentration fields displayed in Figure 2.22 show the beginning of a well-mixed melt core at $Ra=10^4$. Just as in the stabilized configuration, segregation is greatest for $Ra=10^3$ and thereafter decreases with increasing Rayleigh number, as is shown in Figure 2.23.

In general, convective mixing is greatest when the heater is positioned below the cooler (destabilized system), and radial segregation is therefore smaller. As shown in Figure 2.24, the maximum radial segregation is approximately 20% less for the destabilized system for $Ra=10^3$. However, for $Ra < 100$, the destabilized system promotes greater radial segregation.

Carlson et al. computed convection vs. interfacial curvature, insulation thickness, Grashof number ($Gr = R^3 g \beta (T_h - T_c) / f^2$), Biot number ($Bi = hR/k$), and Prandtl number ($Pr = u C_p / k = f/a$) in the vertical thermally stable Bridgman-Stockbarger technique. The thermophysical properties approximated those of $Pb_x Sn_{1-x} Te$ in a reduced gravity of $0.1g$ (20). The interface shape was not calculated but was arbitrarily chosen to be parabolic, with the interface always intersecting the ampoule at the lower edge of the adiabatic zone

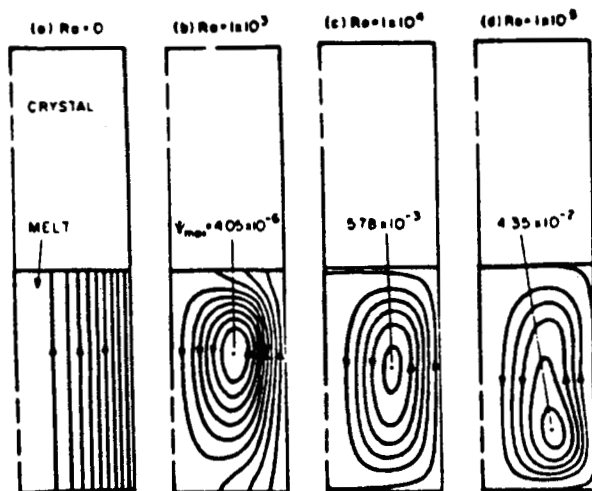


Figure 2.21. Effect of Rayleigh number on flow field for the vertically destabilized Bridgman-Stockbarger system (6).

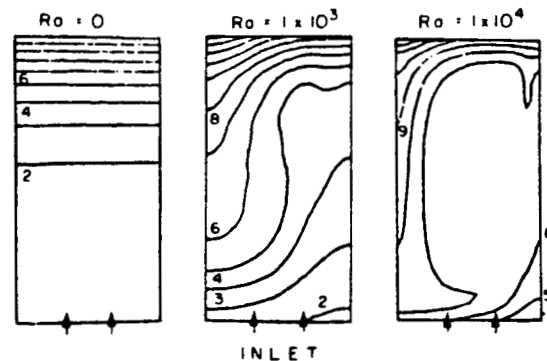


Figure 2.22. Dopant concentration fields for flow field shown in Figure 2.21 (6).

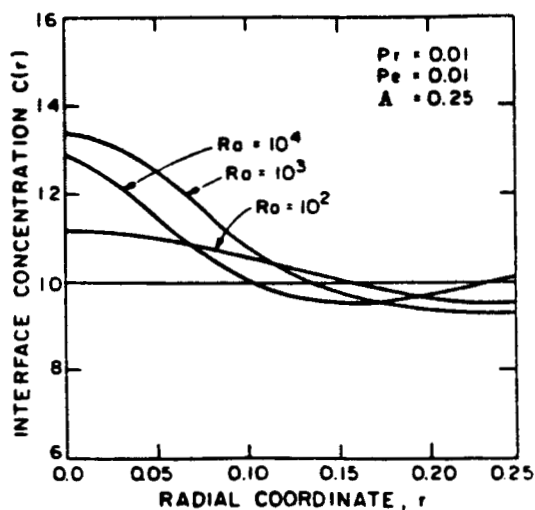


Figure 2.23. Interfacial dopant concentration vs. Ra for the vertically destabilized system (6).

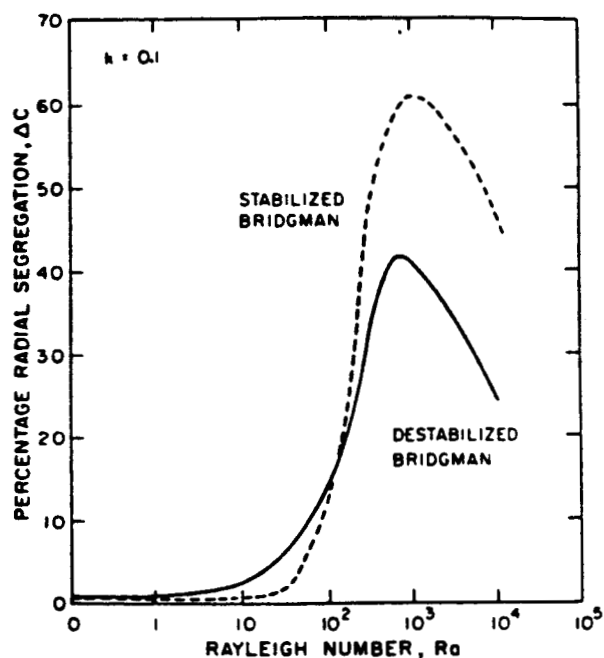


Figure 2.24. Comparison of percentage radial segregation for the stabilized and destabilized systems (6).

(Figure 2.25). The heat transfer coefficients in the heater and cooler were assumed to be constant. The effects of the ampoule were neglected. The Boussinesq approximation was applied to the melt.

Carlson's computed effects of interfacial curvature on convection are summarized in Figure 2.26. When the interface is planar or convex, a single convective cell is observed. In this cell the fluid rises near the wall and descends down the center. As the interface becomes more concave, a secondary flow cell develops whose flow is opposite and always of a lesser magnitude than the upper cell. If the insulation thickness is increased when the interface is concave, convection decreases in the upper cell and increases in the lower one. Adding insulation to a convex interface decreases the level of convection in the melt. These data are shown in Figure 2.27. Increasing the Grashof number (Figure 2.28) increases mixing in the melt. When two cells are present, the lower one is more sensitive to temperature changes. The overall level of mixing decreases with decreasing Biot number (Figure 2.29). Since a small Biot number implies a large thermal conductivity, a small Biot-number fluid is not expected to exhibit the large radial temperature gradients which are necessary to drive convection. The intensity of convection increases with decreasing Prandtl number (Figure 2.30). It is interesting to note that even though convection increases significantly with decreasing Prandtl number, the shape and position of the isotherms are unchanged.

Recently, Potts studied convective flow patterns in a model Bridgman system (2). Using a transparent furnace and a transparent, low melting, organic compound, attempts were made to observe convection using neutrally buoyant tracer particles. Exhaustive

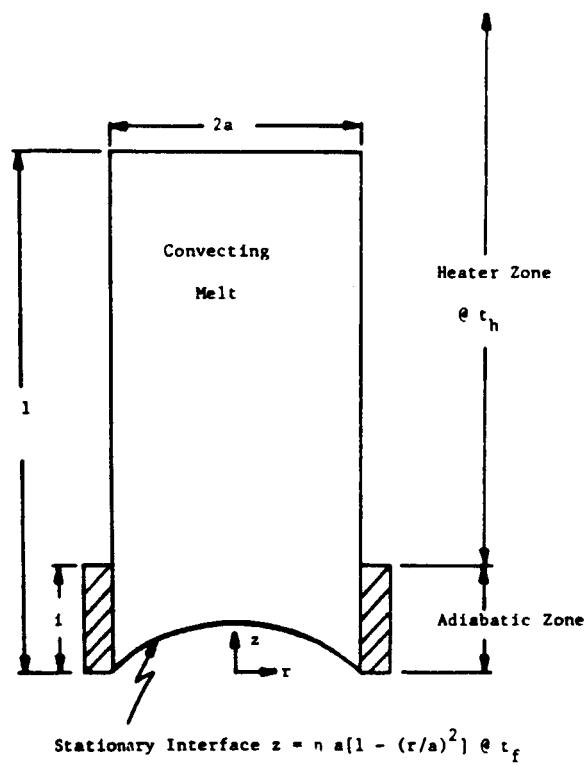


Figure 2.25. Geometry of system studied by Carlson et. al (20).

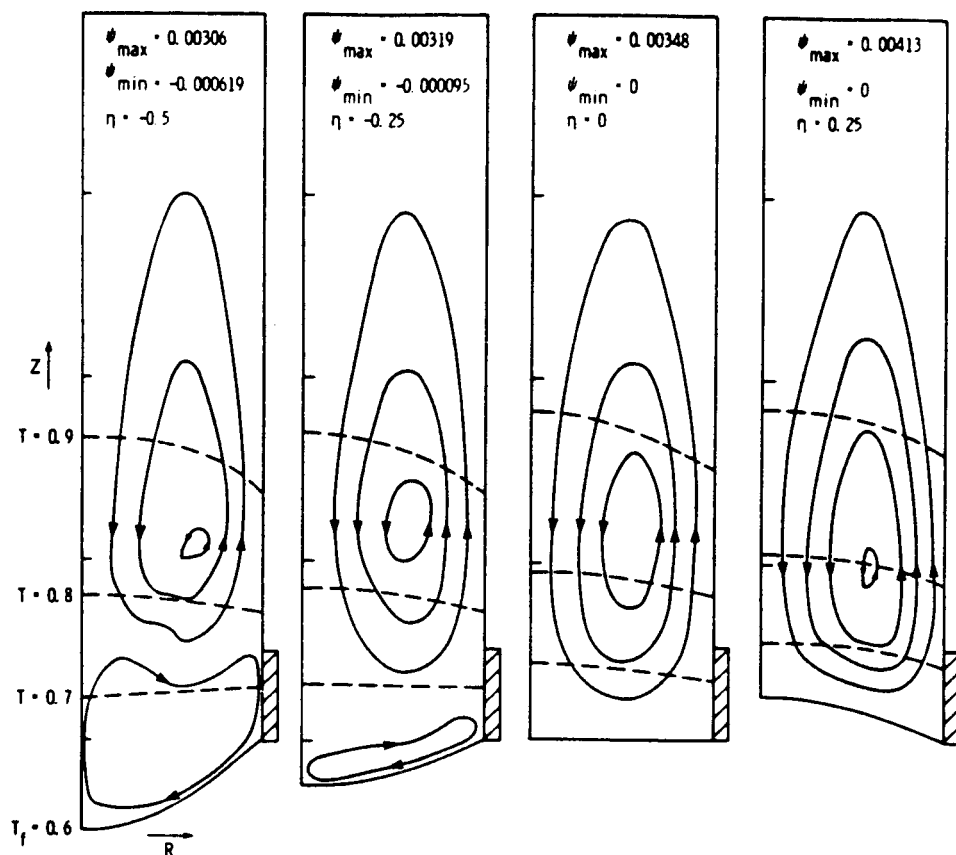


Figure 2.26. Streamlines and isotherms as influenced by interfacial curvature; $Bi=0.5$, $Gr=10000$, and $Pr=0.1$ (20).

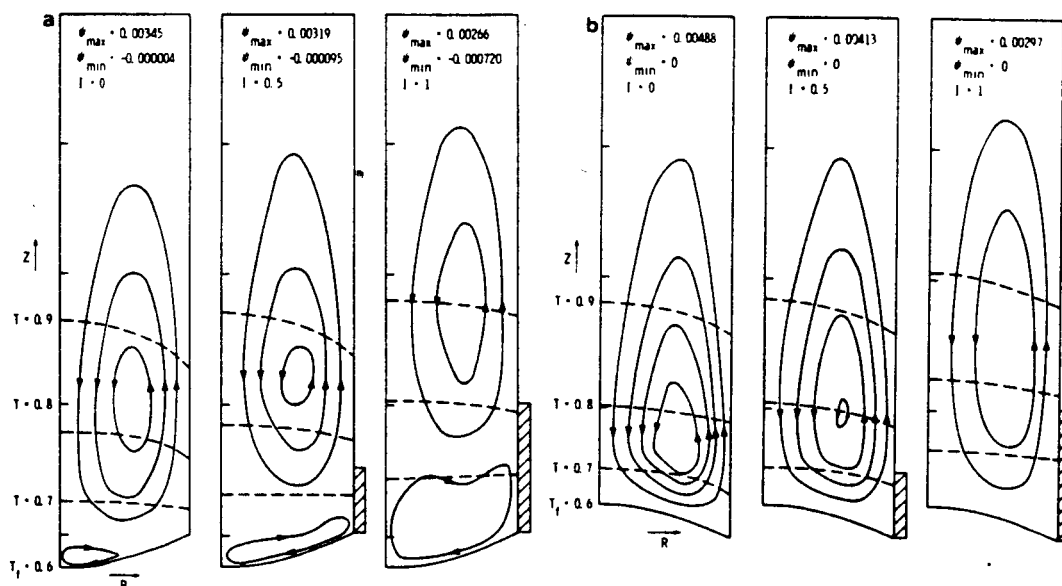


Figure 2.27. Streamlines and isotherms as influenced by insulation thickness and interfacial curvatures; $Bi=0.5$, $Gr=10000$, and $Pr=0.1$ (20).

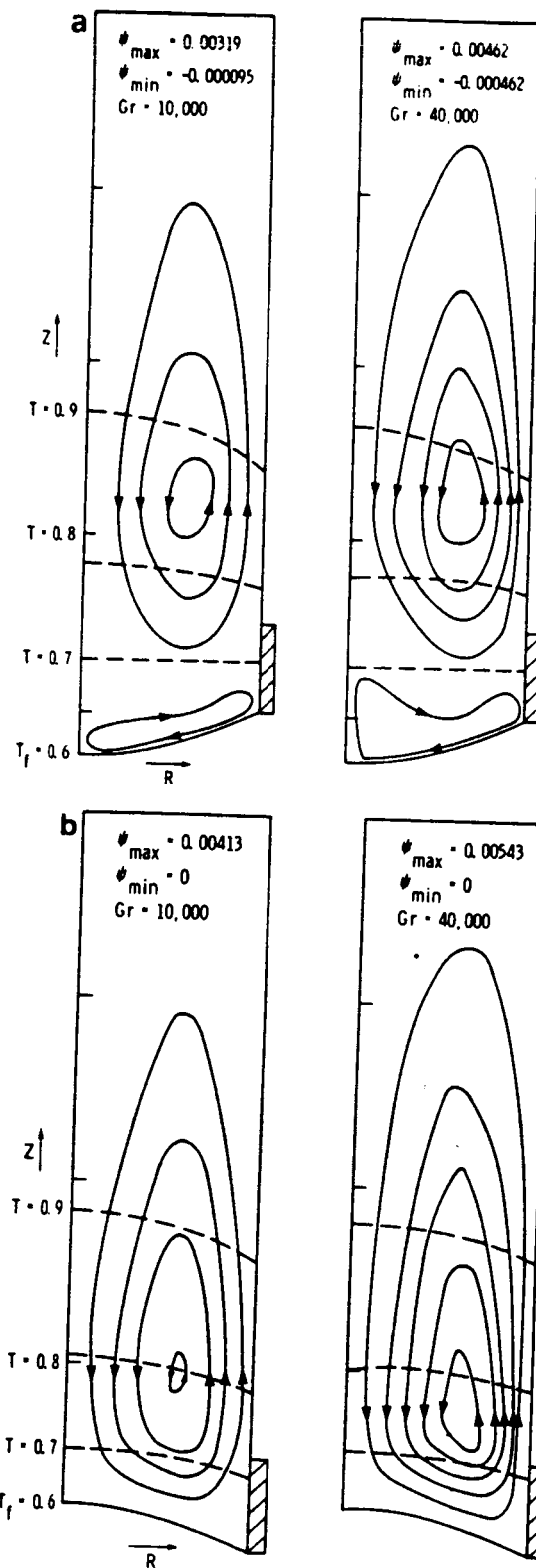


Figure 2.28. Streamlines and isotherms as influenced by Gr and interfacial curvature; Bi=0.5 and Pr=0.1 (20).

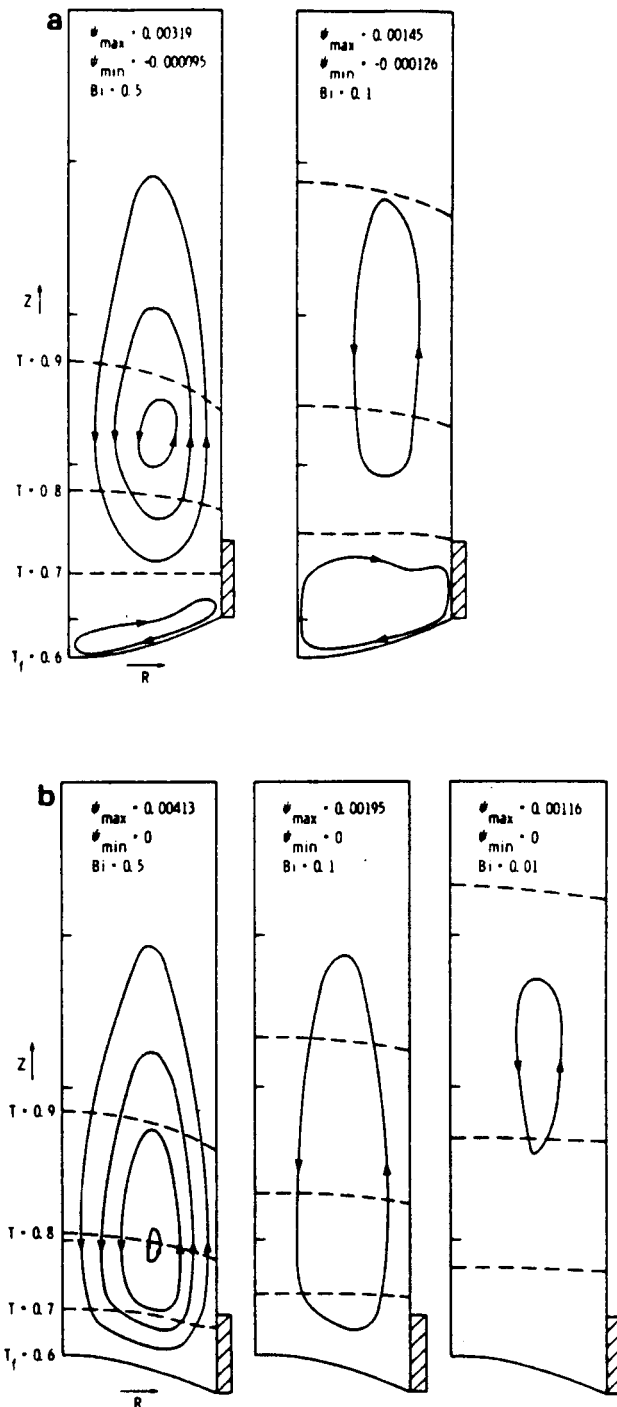


Figure 2.29. Streamlines and isotherms as influenced by Bi and interfacial curvature; $Gr=10000$ and $Pr=0.1$ (20).

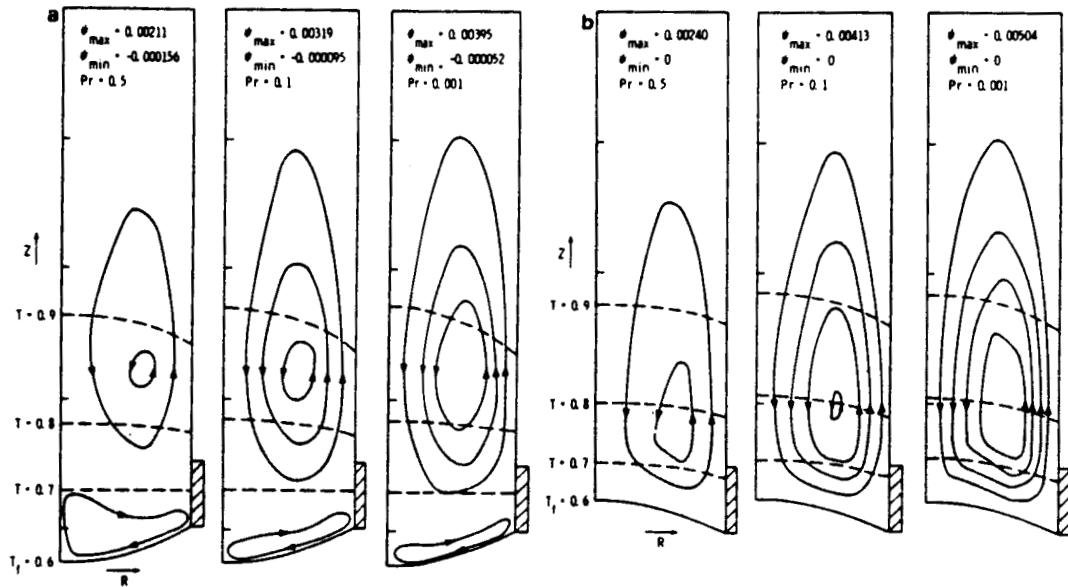


Figure 2.30. Streamlines and isotherms as influenced by Pr and interfacial curvature; $Bi=0.5$ and $Gr=10000$ (20).

attempts to verify the convective behavior reported by Tien were only partially successful.

The Bridgman-Stockbarger apparatus used by Potts, shown in Figure 2.31, was patterned after the set-up studied by Tien (18,19). It consisted of a hot circulating bath on top and a cooler circulating bath beneath. Separating the two baths was a polymer diaphragm. The stationary ampoule was a 1 mm thick Pyrex tube, 40 cm long, and 2 cm ID. Convection in the naphthalene melt was observed using micro-balloons. Particle movement was recorded on videotape. Particle trajectories were traced from their motion on a television monitor over a five minute period. Since the entire ampoule was illuminated and a television monitor presents a two-dimensional image, front to rear motion relative to the camera could not be observed. Some typical convective flow patterns are sketched in Figures 2.32-2.34.

In general, the convection was laminar but neither steady nor axisymmetric. The flow tended to descend the wall farthest from the heater, cross the interface, and ascend the wall closest to the heater. Rarely were particles observed traveling in a closed loop. This behavior persisted even when the stirring was increased in the heating bath.

These results raised several questions. Are small deviations from thermal symmetry or vertical alignment the cause of the chaotic convection? If so, how large a deviation is necessary to cause such flow? Is axisymmetric convection ever really observed? Is truly chaotic convection ever observed? These questions, raised by the work

of Potts, provided the impetus for the present work.

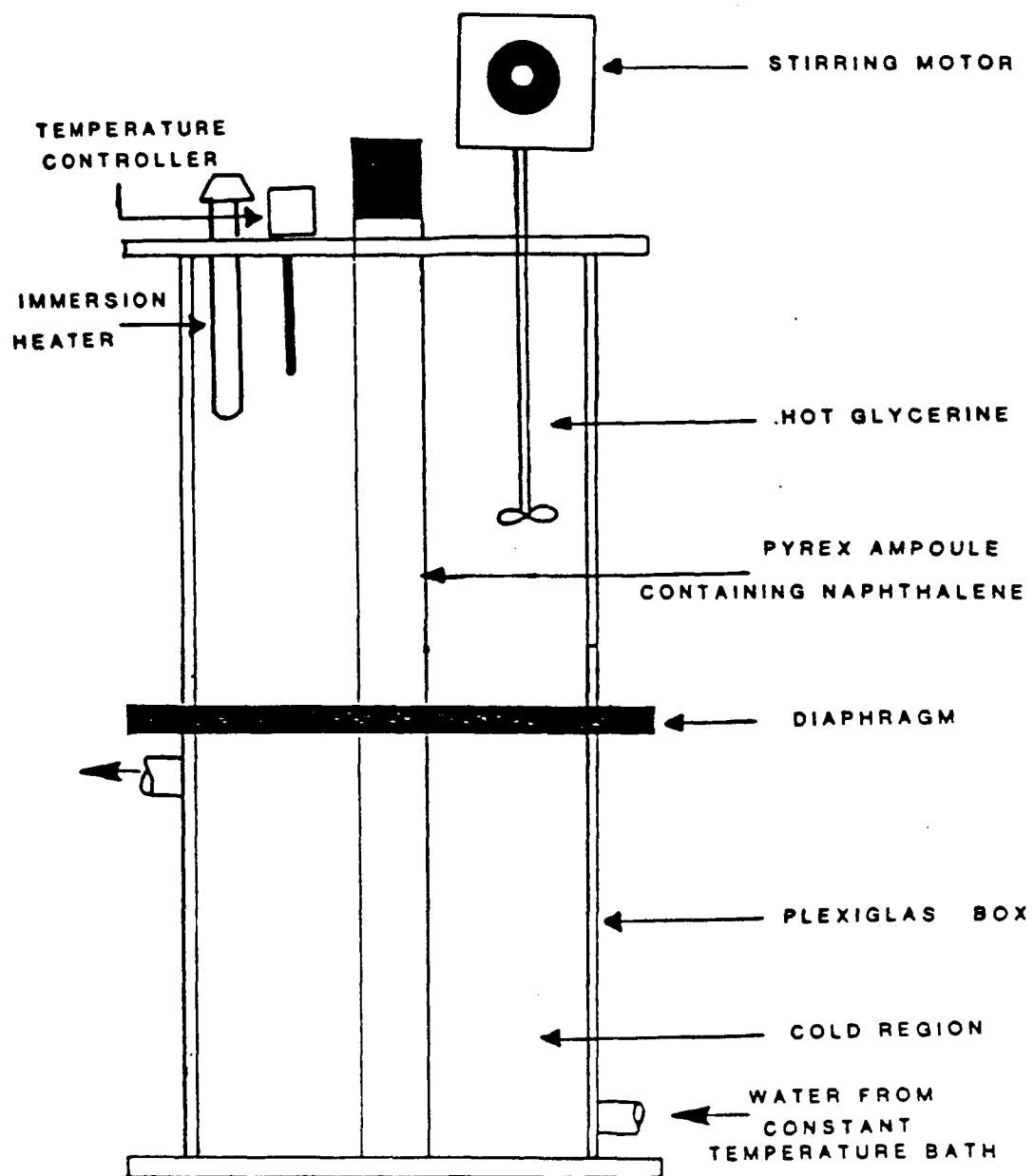


Figure 2.31. Potts's Bridgman-Stockbarger system (2).

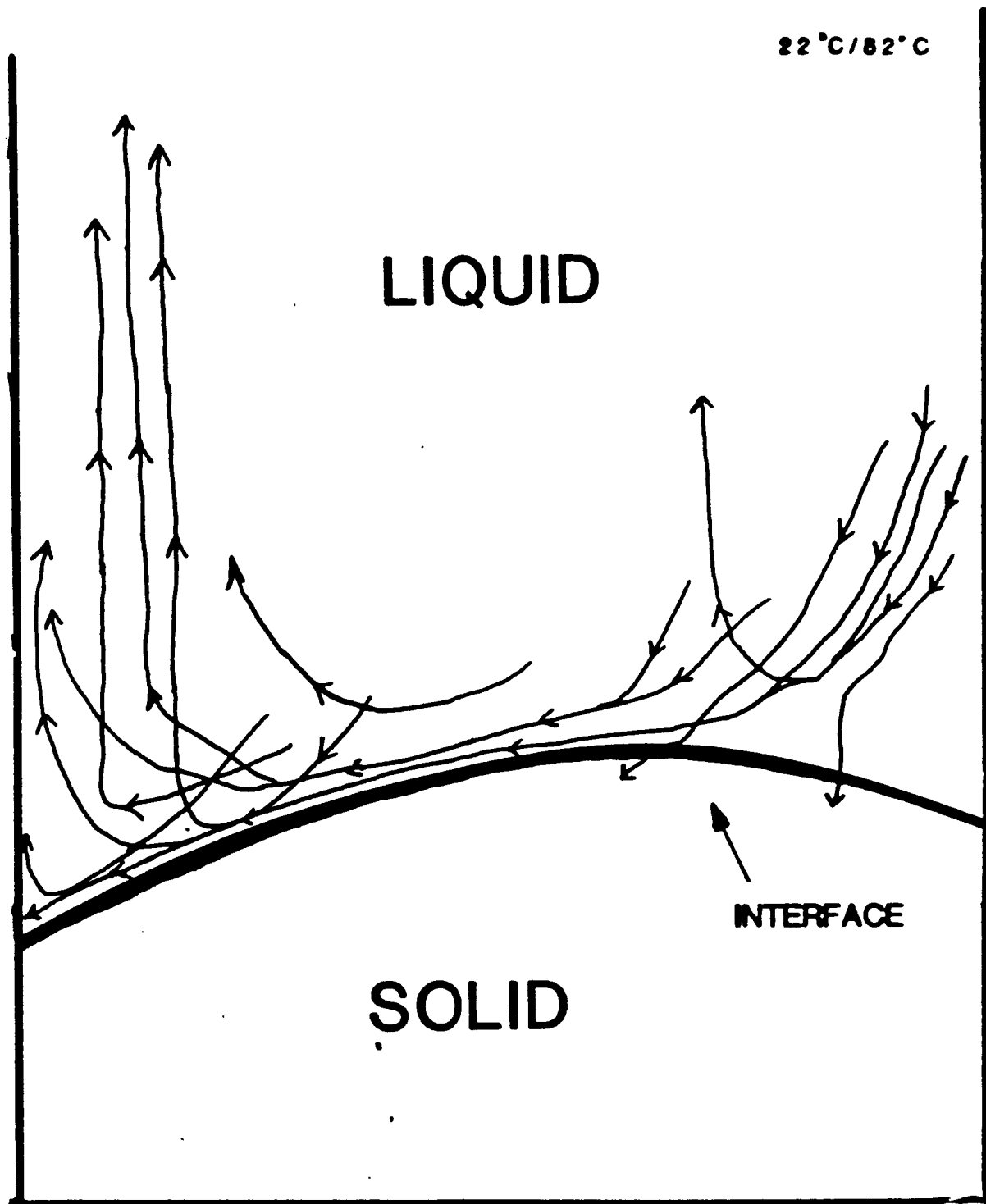


Figure 2.32. Typical convective flow field for $T_{\text{heater}}=82^{\circ}\text{C}$ and $T_{\text{cooler}}=22^{\circ}\text{C}$ (2).

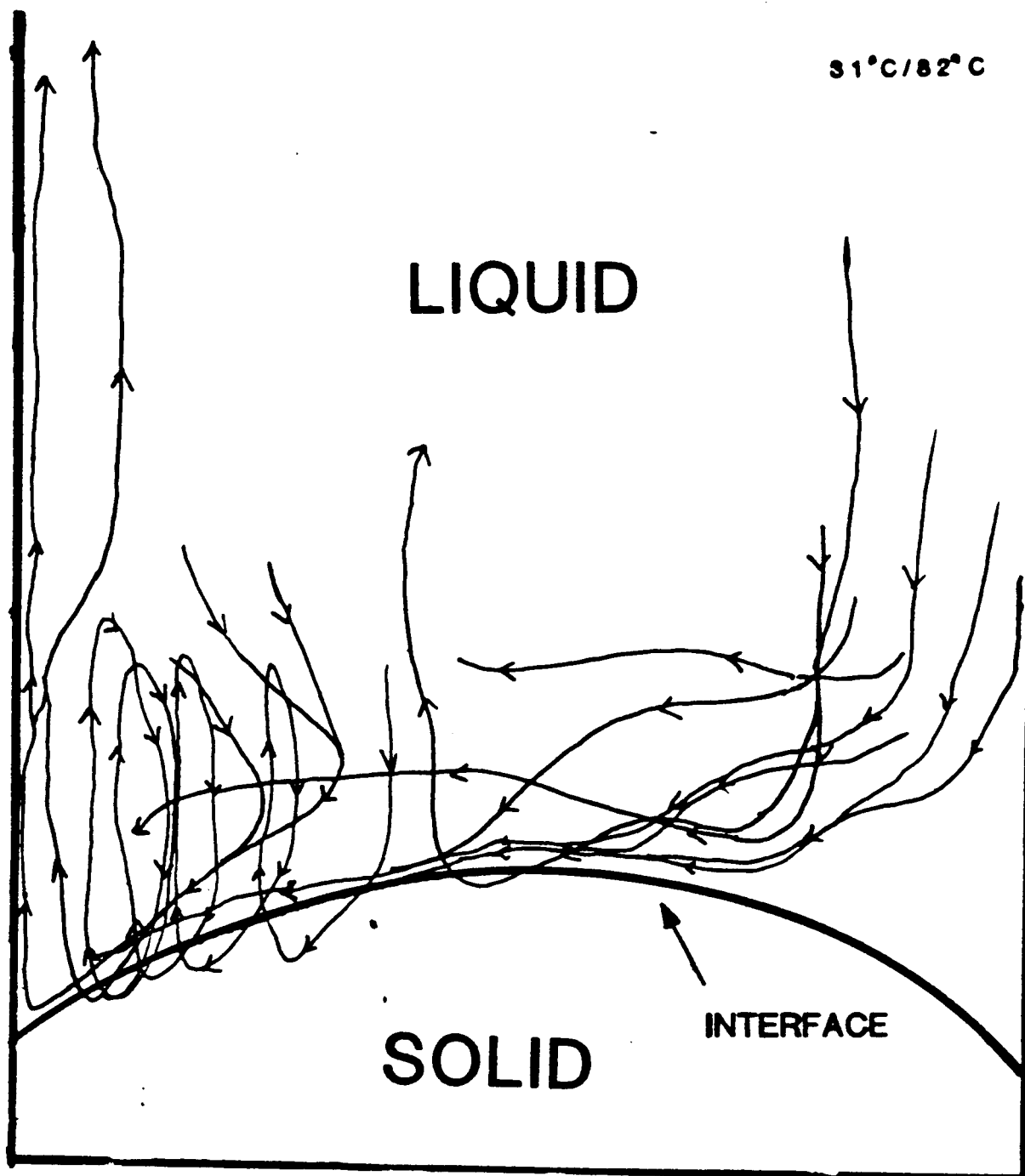


Figure 2.33. Typical convective flow field for $T_{\text{heater}}=82^{\circ}\text{C}$ and $T_{\text{cooler}}=31^{\circ}\text{C}$ (2).

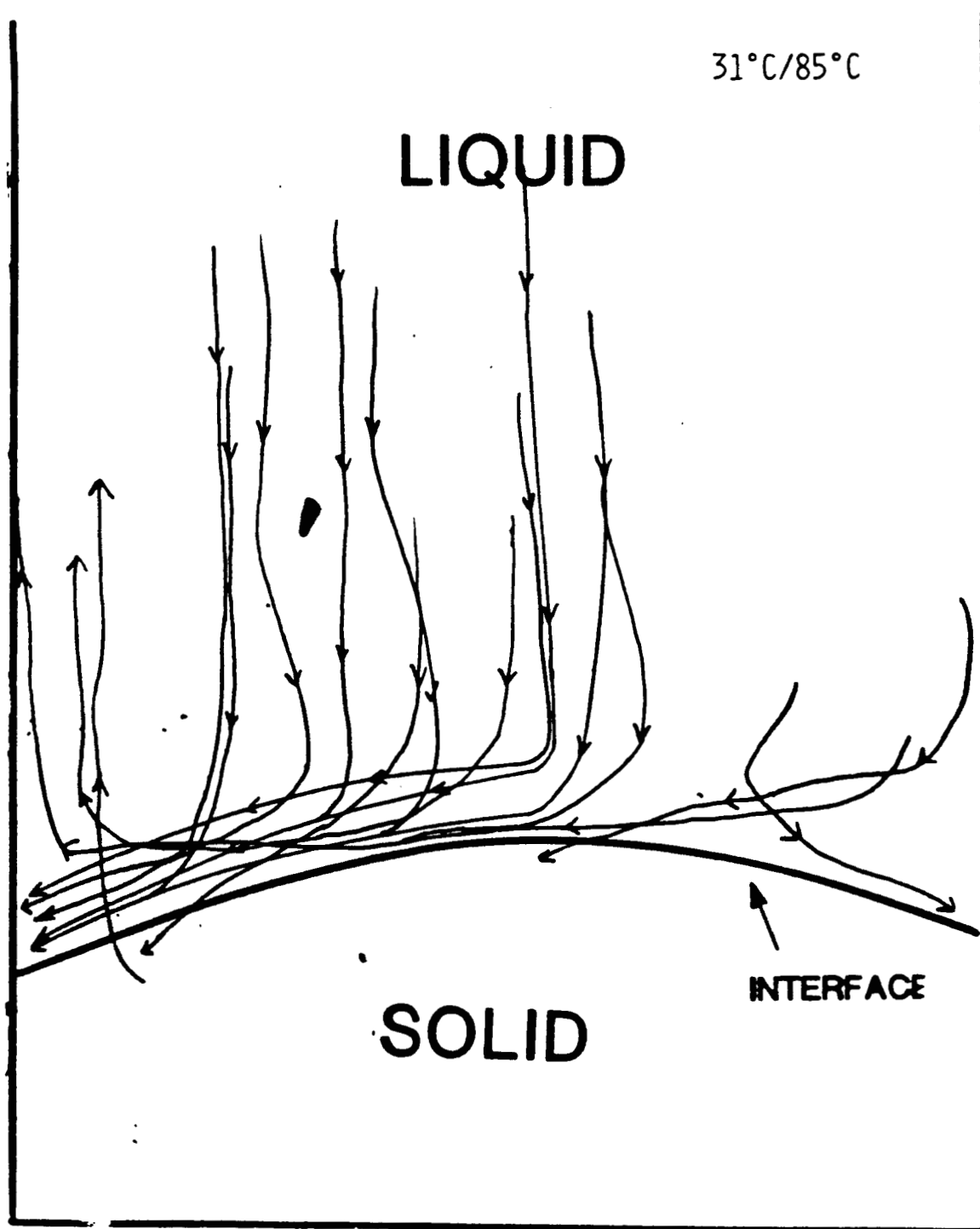


Figure 2.34. Typical convective flow field for $T_{\text{heater}} = 85^{\circ}\text{C}$ and $T_{\text{cooler}} = 31^{\circ}\text{C}$ (2).

Chapter III.

Experimental Methods

Crystals grown by the Bridgman-Stockbarger technique are often metals or semiconductors whose molten phases are opaque. For this reason, the convective flow fields have been observed in transparent, low melting, organic materials (2,18). In the present study, the convective velocity field was revealed by the pathlines traced by the particles suspended in the melt.

1. Materials

Benzophenone and phenyl salicylate (salol) were used as transparent melts in which convection could be observed. These two chemicals were selected because of their low toxicity, low melting point, low price, and high purity of commercial grades. Salol, m.p. 42-43 °C, was obtained from Eastman Kodak Company, Rochester, NY. Benzophenone, m.p. 48-49.5 °C, was obtained 99% pure from Aldrich Chemical Company, Inc., Milwaukee, WI. The physical properties of these materials are summarized in Table 3.1. Sublimated sulfur particles, U.S.P. grade from J.T. Baker Chemical Co. Phillipsburg, NJ., were used to visualize the convection.

As shown in Figures 3.1 to 3.3, each model Bridgman apparatus had a water cooling bath on the bottom and a clear plastic furnace embedded with resistance heating wires on the top. The ampoule containing the sample was a thick-walled Pyrex tube.

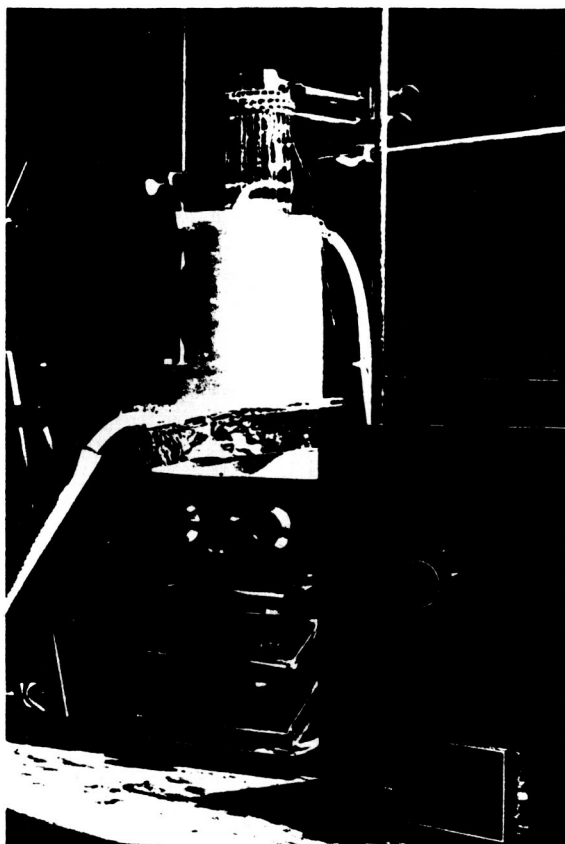


Figure 3.1. Bridgman-Stockbarger apparatus with a simple heating zone on top and a cooling zone below. The aspect ratio (length of heater/diameter of ampoule), $A=4.2$.

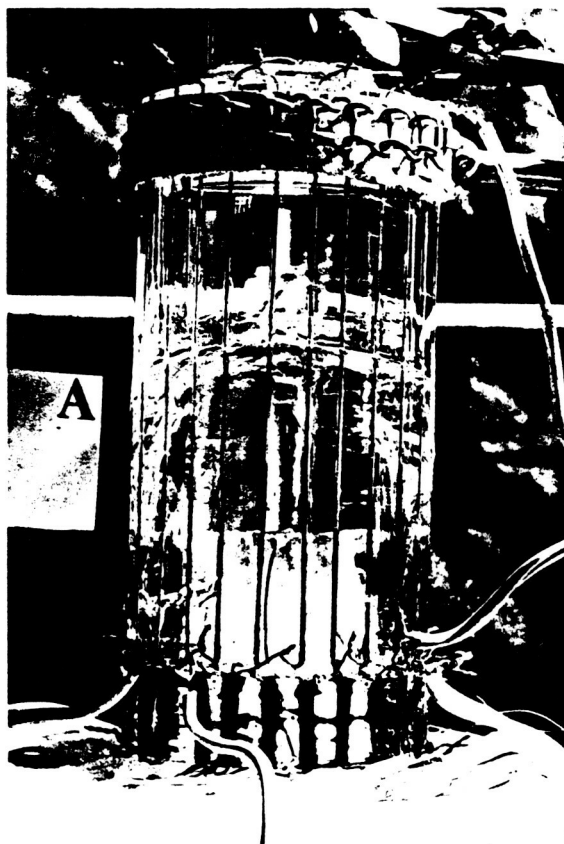


Figure 3.2. Bridgman-Stockbarger apparatus modified with the addition of a short booster heater between the heater and the cooler. Aspect ratio, $A=4.8$.

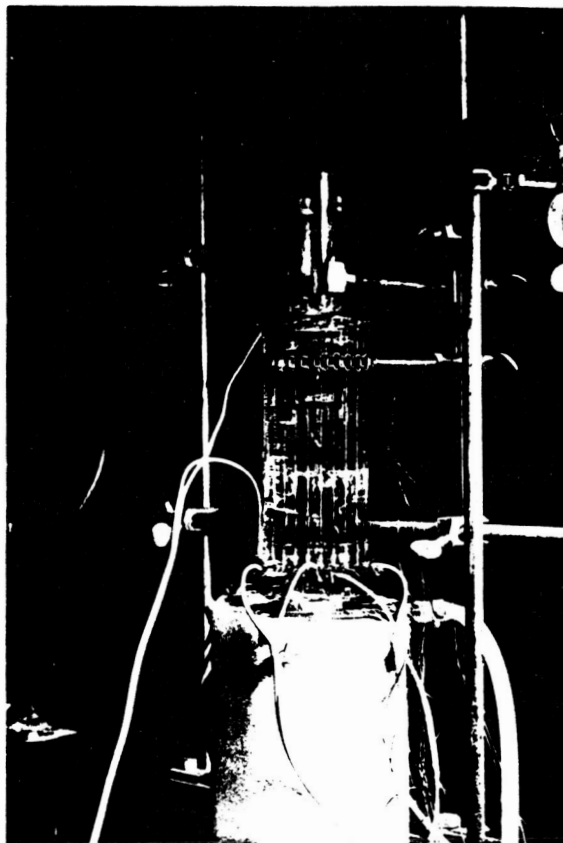


Figure 3.3. Bridgman-Stockbarger apparatus modified with the addition of a short booster heater between the heater and the cooler. Aspect ratio, $A=6.7$.

Table 3.1. Properties of Materials.

Benzophenone ($C_{13}H_{10}O$)

Formula weight: 182.22

Melting point: 48-49.5 °C (21)

Boiling point: 305 °C (21)

T_{tp} : 321.03 ± 0.05 K (24)

P_{tp} : 1.33 Pa (24)

Density (20 °C): 1.146 g/cm³ (21)

Density (54 °C): 1.083 g/cm³ (22)

Latent heat of fusion, H_f : 4040 ± 40 cal/mol (23)

Latent heat of fusion, H_f : 4348 ± 12 cal/mol (24)

Latent heat of sublimation, H_{sub} (@ 321.03 K): 22634 ± 239 cal/mol (24)

Heat capacity (crystal), C_p : $40.42 + 0.4252 \cdot T + 6.27021 \cdot 10^{-4} \cdot T^2$ J/K.mol (24)
80 ≤ T ≤ 290 K

Heat capacity (liquid), C_p : 150.19 + 0.4576 · T (J/K.mol) (24)
280 ≤ T ≤ 350 K

Thermal conductivity:

k_s (10 °C) = 0.244 W/m.K (25)

k_s (20 °C) = 0.236 W/m.K (25)

k_s (30 °C) = 0.229 W/m.K (25)

Refractive index, n_D (19 °C): 1.6077 (21)

Viscosity (26):

u (25 °C) = 13.6 cp

u (55 °C) = 4.67 cp

u (95 °C) = 1.74 cp

$\log(u_1) = 1259.11 \cdot (1/T - 1/402.50)$ cp

Phenyl salicylate, salol ($C_{13}H_{10}O_3$)

Formula weight: 214.22

Melting point: 43 °C (21)

Melting point: 41.09 °C (28)

Melting point: 41.68 °C (29)

Boiling point (@ 12 mm Hg): 173 °C (21)

Viscosity (@ m.p.): 0.746 cp (27)
 Heat capacity, C_p (@ m.p.): 0.391 cal/°C (27)
 Thermal conductivity, k_1 (@ m.p.): 0.00020 cal/(s.cm.K) (27)
 Latent heat of fusion, H_f : 21.28 cal/g (27)
 Latent heat of fusion, H_f : 21.73 cal/g (29)
 Density = $1.2177 - 0.000883 \cdot T$ g/cm³ (28)
 $30.5 \leq T \leq 60.0$ °C
 Surface tension = $45.20 - 0.0976 \cdot T$ dynes/cm (28)
 $30.5 \leq T \leq 60.0$ °C
 Coefficient of thermal expansion, B , (42.1 °C): $7.48 \cdot 10^{-4}$ (28)
 Thermal diffusivity of solid, a (@ m.p.): $1.18 \cdot 10^{-3}$ cm²/s (29)
 Thermal diffusivity of liquid, a (@ m.p.): $0.91 \cdot 10^{-3}$ cm²/s (29)

Pyrex glass

Thermal conductivity:

$$k_s(0 \text{ } ^\circ\text{C}) = 26 \cdot 10^{-4} \text{ cal/cm.s.}^\circ\text{C} \quad (21)$$

$$k_s(100 \text{ } ^\circ\text{C}) = 30 \cdot 10^{-4} \text{ cal/cm.s.}^\circ\text{C} \quad (21)$$

Thermal diffusivity, a (60-100 °C): $7.8 \cdot 10^{-7}$ m²/s (30)

Refractive index: 1.47 (2)

Nichrome Resistance Wire

B&S gauge: 24

Resistance (20 °C): 1.671 ohm/ft (21)

2. Apparatus

The design of the model Bridgman-Stockbarger apparatus used in the present work evolved from that used by Potts (2). As reviewed in Chapter II, the convective flows observed by Potts suggested that the thermal field surrounding the sample was not perfectly axisymmetric. However the nature of her set-up precluded any attempt at controlling or even accurately measuring the azimuthal temperature field. Our goal in redesigning Potts's apparatus was therefore to build a furnace in which the azimuthal temperature field could be both measured and controlled. Consonant with this goal is a solid furnace which heats the sample by conduction.

Three different designs were used. One apparatus consisted of a simple heating zone on top and a cooling zone below. Two others, each with a different aspect ratio, were built with a heater on top, a circulating cooler below, and a short booster heater between. The furnaces and booster heater were constructed of a clear unsaturated polyester casting resin (Chemco Resin Crafts, Dublin, CA). Just inside the outer wall of the plastic resin were mounted vertical equal-spaced, 1mm O.D. capillary tubes which contained nichrome resistance wires. The Pyrex capillary tubes were needed to accurately position the unruly nichrome wires during the casting of the furnace.

The following procedure was used to construct the furnaces. The ampoule in which the organic compound was contained was a Pyrex tube (I.D. = 30 mm and O.D. = 38 mm). To the outer wall of this sample tube were cemented copper-constantan thermocouples (AWG = 36). The mold in which the resin was to be cast was constructed of a 70 mm I.D. thin-walled Pyrex tube with a length equal to that of the resulting furnace. The capillary tubes which contained the nichrome wires were cut a few millimeters shorter than the length of the mold. The empty capillary tubes were attached to the inner wall of the mold using paper clips. The capillary tubes were then attached to the mold using a few drops of casting resin along the length of the tubes. After all of the capillary tubes were glued in place, the paper clips were removed and the nichrome wires were threaded through the tubes. The sample ampoule was placed inside the mold containing the heating wires. In order to contain the casting resin, a thin rubber diaphragm was used to seal one end of the "tube within a tube" annular assembly. The rubber diaphragm was glued in place using silicone sealant. The mold was filled with resin which was allowed to harden for a few

days.

After polymerization of the resin was complete, the outer Pyrex tube, the mold, was removed by hitting it with a hammer causing it to shatter. The nichrome wires were connected to one another and then to a power supply. The three furnaces used in this work are shown in Figures 3.1 to 3.3. Figure 3.1 is a photograph of the furnace consisting of a simple heating zone on the top and a cooling zone on the bottom. Figure 3.2 is a picture of the furnace with the booster heater modification, and Figure 3.3 is a picture of the same type of furnace with a larger aspect ratio. Schematic drawings of each furnace are shown in Figures 3.4 to 3.6 respectively.

3. Experimental Procedure

After assembly of the model Bridgman-Stockbarger apparatus was complete, it was wired for convection studies. The nichrome heating wires were connected to an AC autotransformer (Variac). If a booster heater was to be used, the booster was wired to four separate Variacs; approximately one quarter of the booster heater was controlled by each of these four Variacs. In this way, the azimuthal thermal profile of the furnace in the region of the interface could be controlled by adjusting the voltage of one or more Variacs.

Since rather short pieces of nichrome wire were being used as heating elements in the furnace, two precautionary measures were necessary in order to accurately regulate temperature and to prevent serious damage to the furnace. First, the four Variacs, each connected to a quarter of the booster heater, were not plugged directly into a wall socket, but were all plugged into a four-way outlet, which in turn was connected to another Variac plugged into a wall outlet. In this way, voltage to the booster heater was

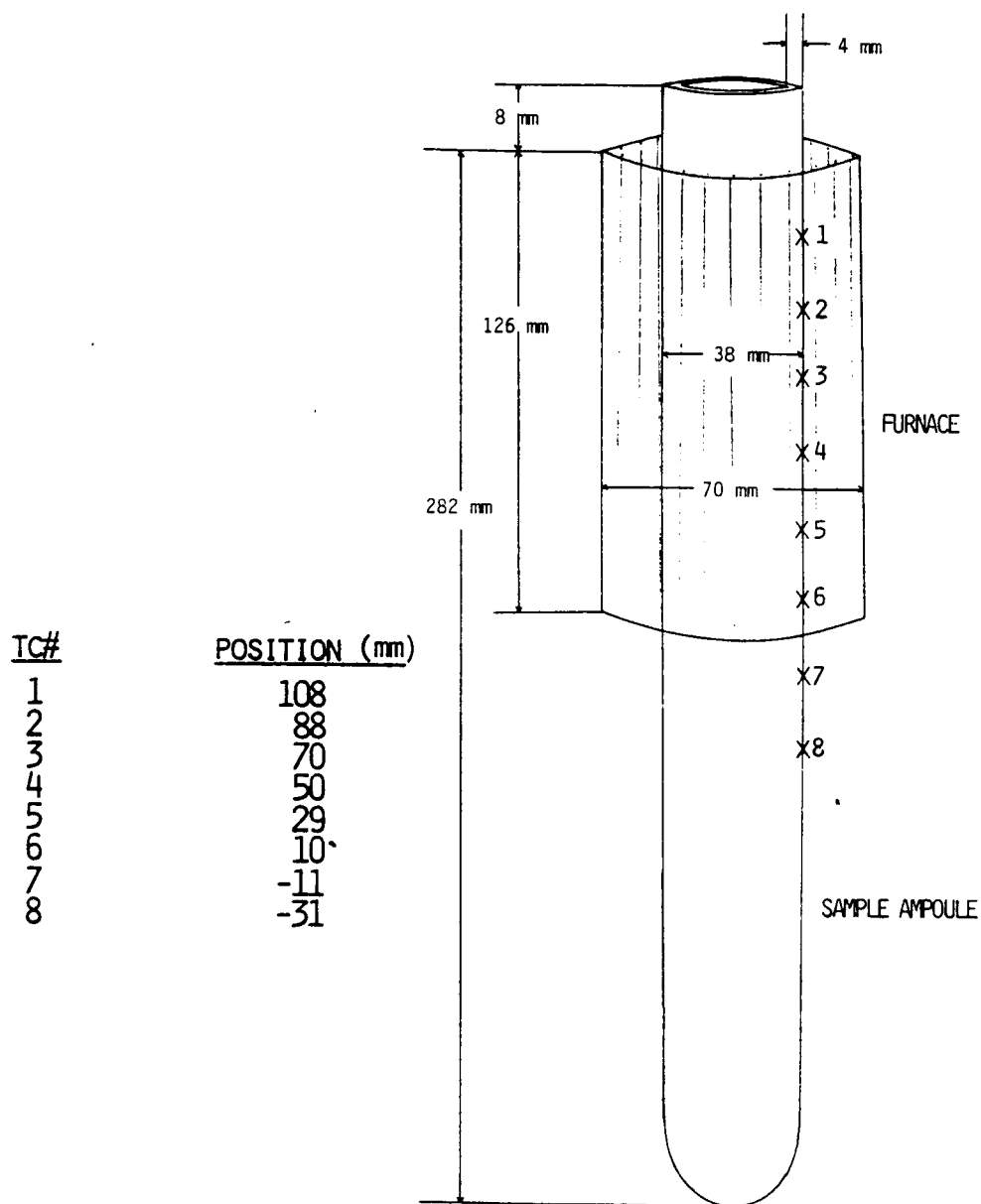


Figure 3.4. Schematic diagram of apparatus pictured in Figure 3.1. "X" denotes the position of a thermocouple (TC). The positions of the thermocouples are measured from the bottom of the furnace. The furnace contains 28 nichrome heating wires spaced 7.8 mm apart.

TC#
1
2
3
4-7
8-11
12
13
14
15
16
17

POSITION (mm)
138
116
77
48
12
0
-10
-20
-30
-40
-50

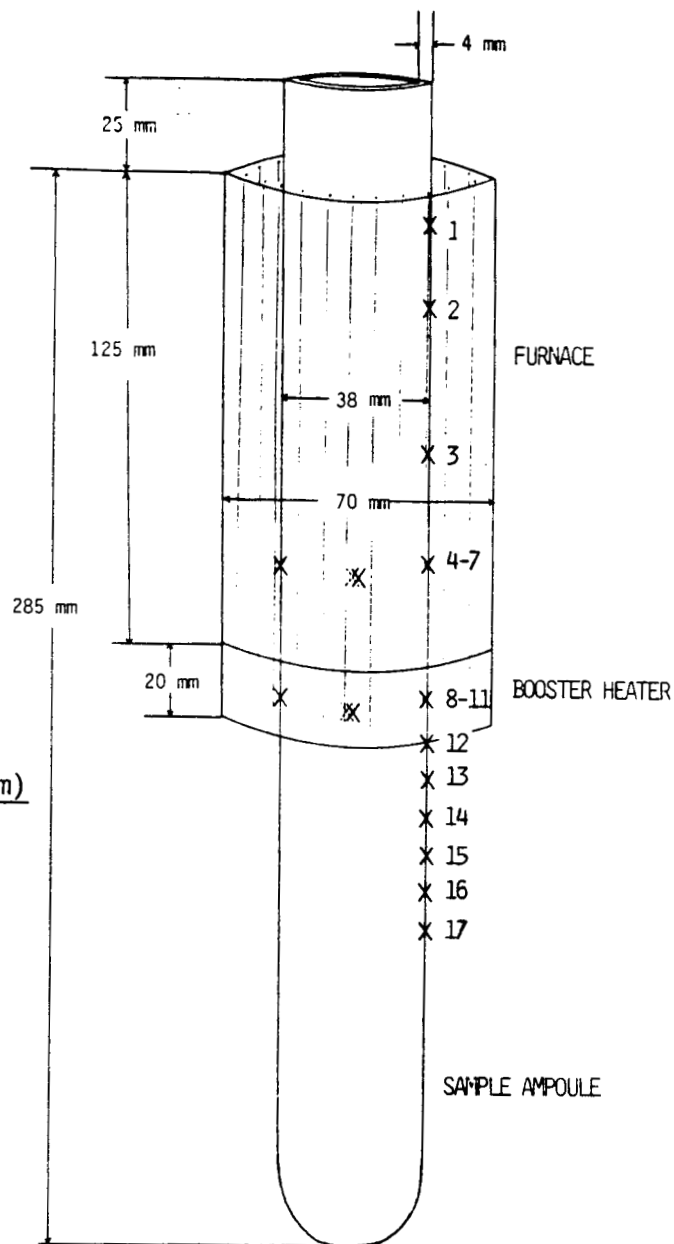


Figure 3.5. Schematic diagram of apparatus pictured in Figure 3.2. "X" denotes the position of a thermocouple (TC). The positions of the thermocouples are measured from the bottom of the booster heater. Thermocouples 4 to 7 and 8 to 11 are circumferentially mounted and are equally spaced. TC# 4 and TC# 8 are mounted on the front of the furnace. Thermocouples 1 to 3 and 12 to 17 are actually positioned on the rear of the furnace but are pictured as being on the side for clarity. The furnace and booster heater contain 27 nichrome heating wires spaced 8.1 mm apart.

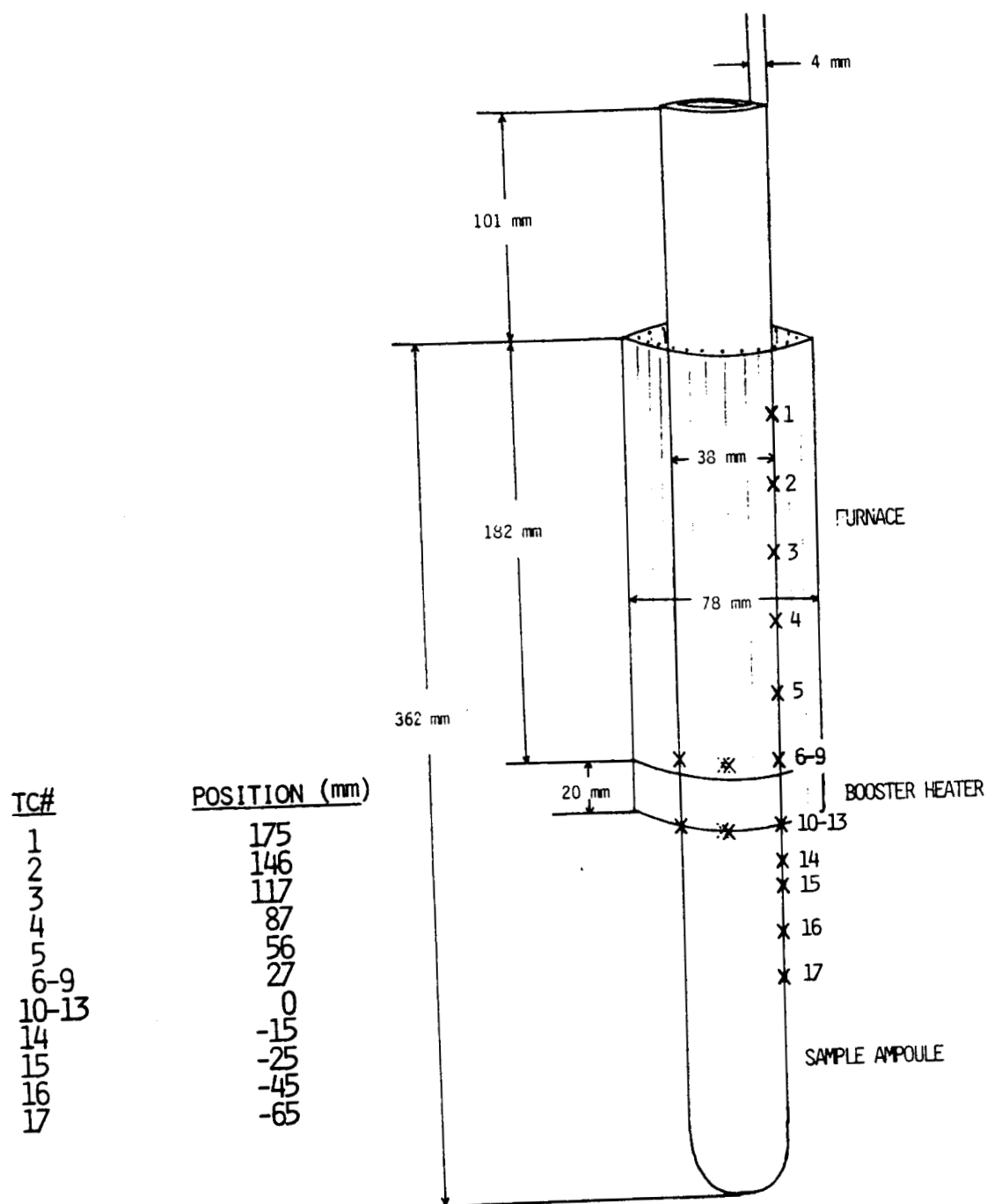


Figure 3.6. Schematic diagram of apparatus pictured in Figure 3.3. "X" denotes the position of a thermocouple (TC). The positions of the thermocouples are measured from the bottom of the booster heater. Thermocouples 6 to 9 and 10 to 13 are circumferentially mounted and are equally spaced. TC# 6 and TC# 10 are mounted on the front of the furnace. Thermocouples 1 to 5 and 14 to 17 are actually positioned on the rear of the furnace but are pictured as being on the side for clarity. The furnace and booster heater contain 25 nichrome heating wires spaced 9.8 mm apart.

stepped-down, enabling the power to each quarter of the booster to be carefully fine-tuned. The second precaution was to replace the 8 ampere fuses in the Variacs (these were the rated fuses) with 3 ampere fuses. This assured that a nichrome wire could not get so hot as to damage the casting resin.

After the heating wires were connected to their respective Variacs, the furnace was clamped to a supporting bracing which was anchored to the wall. Prior to every experiment, the ampoule was checked with a level to insure that there was no tilt. The 2000 ml tempering beaker, which functioned as a cooling bath, was lifted upward on a lab jack until the free surface of the water was approximately 5mm from the bottom of the heater. Since the temperature of the cooling bath was nearly always less than 10°C , the rate of condensation from the atmosphere was usually greater than the rate of evaporation from the cooling bath. Therefore water continuously overflowed from the beaker. During the more arid months, an equilibrium between evaporation and condensation kept the cooling bath filled to a constant level, slightly less than the capacity of the beaker. The tempering beaker sat upon a magnetic stirrer which provided circulation for the water inside the beaker. Cooling was effected using a Neslab EN350 flow-thru cooler coupled with a VWR 1130 heater/pump which circulated the cooling fluid through the jacket of the tempering beaker.

At the commencement of an experiment, the organic compound was melted and poured into the sample tube. The tube was filled to a level just beneath the top of the furnace. The booster, main heater, and cooler were turned on and adjusted to the desired settings. Convection studies were begun after temperatures in the furnace and

cooling bath varied less than 0.2°C over a one hour period, indicating steady-state conditions were reached. Steady-state conditions were reached 8 to 12 hr. after the furnace and cooling bath were turned on.

4. Temperature Measurements

The temperatures in the heater and cooler were measured using Teflon-coated copper-constantan thermocouples (AWG=36, diameter=0.005 inch). The thermocouple junction was made by twisting the ends together and soldering them. The thermocouples were connected through a selector switch to a digital thermometer that read to $\pm 0.1^{\circ}\text{C}$ with an electronic ice point. Each thermocouple was checked by measuring the temperature of a beaker of ice-water and the temperature of a beaker of water at room temperature. When all thermocouples measured the same temperature in each of these fluids, with no more than 0.1°C variation, it was assumed that they worked properly.

Two methods were used to mount the thermocouples in the furnace. The first method was used only for the furnace lacking a booster heater. To mount the thermocouples, a hole was drilled through the plastic wall of the finished furnace. The thermocouple was inserted into the hole and anchored into place using a drop of casting resin. The bore-hole was then sealed using silicone sealant. The second method entailed cementing the thermocouples to the outer wall of the sample tube prior to casting. The thermocouples were thereby anchored in place when the furnace was cast. The former method of mounting the thermocouples was used only once because of the inherent difficulty in accurately positioning the 0.005 inch diameter thermocouple in the center of a 0.625 inch deep, 0.125 inch diameter hole. The latter

method of mounting the thermocouples was superior because of the relative ease with which the end of the wire could be accurately positioned and fastened to the sample tube prior to casting.

The positions of the thermocouples in each of the three furnaces are shown in Figures 3.4 to 3.6.

5. Illumination

In order to visualize convection, it was necessary to illuminate a relatively planar portion of the melt. This was done using the light-cut technique described by Potts (2). A 0.5mW He-Ne laser was used as a light source. Approximately 3 cm from the laser was a cylindrical lens which elongated the beam. Approximately 50 cm from the laser was a second cylindrical lens which focused the beam into a slit. Ninety centimeters from the laser, the light slit entered the top of the apparatus and shined straight down through the melt.

At the top of the furnace, the light slit was shaped like an elongated ellipse, with a major axis of 31 mm and a minor axis of 5 mm. Since a laser is a very bright and non-divergent light source, it illuminated primarily the particles suspended in the melt, and yet did not illuminate the apparatus to any significant degree. This feature made the laser-slit method especially suitable to illuminate the particles in order to photographically record their motion.

6. Convection Studies

The convective streamlines in the melt were visualized by photographically recording the pathlines of the sulfur suspended in the melt. (Under low power magnification, the sulfur particles appeared as irregularly shaped flakes. The 95% confidence interval, with 19 degrees of freedom, for the mean maximum length of a flake was 0.054 ± 0.010 mm.) After steady state conditions were reached, 2 to 3

mg of sublimated sulfur particles were sprinkled into the melt. The upper portion of the melt was mildly agitated with a stirring rod in order to disperse the sulfur. After waiting at least 15 minutes, the pathlines of the particles were recorded by a time exposure photograph. Visual inspection of the melt revealed that approximately 75% of the sulfur remained suspended for 3 hours, and approximately 25% remained suspended for at least 24 hours.

Pictures were taken using a Nikon FM2 camera with a 55 mm Nikon Micro-Nikkor macro lens. Black and white Kodak Tri-X pan film (ASA/ISO speed 400) was used. The shutter was manually operated with a 12 inch remote cable release. Exposures were timed using a stop watch, and ranged from 2 s to over 2 minutes.

The velocities of the particles in the melt were calculated from the length of the streaks on the photograph caused by the motion of the particles, the magnification, and the time of exposure.

Chapter IV.

Experimental Results

Convection in the Bridgman-Stockbarger technique was visualized in three different furnaces: a three zone furnace (heater, booster heater, and cooler) of aspect ratio, $A=4.8$; a second three zone furnace, $A=6.7$; and a simple two zone furnace (heater and cooler). Phenyl salicylate, salol, was the organic compound used as the model melt in all experiments except for the transient observations made in the two zone furnace. Benzophenone was used in those experiments. The convective streamlines were visualized by the streaks on a time exposure photograph caused by the motion of the particles suspended in the melt. Since a very wide range of convective flow velocities was often observed during a single experimental run, two or more photographs of different exposure times were needed to clearly resolve the convective flow. Photographs were usually taken from two different views, front and side, in order to get an indication of the three dimensional structure of the flow.

1. Three Zone Furnace, $A=4.8$

Figures 4.1 to 4.8 show the effects of an increasingly vertically destabilizing temperature gradient on convection. Starting with Figure 4.1, an experimental run in which no power was supplied to the booster heater, the power supply to the main heater was reduced and that to the booster was increased (Figures 4.2 and 4.3). Figures 4.4 to 4.7 show the observed convection when the main heater was turned off completely and power was supplied only to the booster heater.

In order to document the effects of thermal asymmetry on

convection, an asymmetrical thermal field was created by reducing the power supplied to one quadrant of the booster heater by approximately 30%. The right quadrant of the booster (when viewed from the front) was approximately 5 °C cooler than the other three quadrants as measured within the booster at the outer ampoule wall. These results are shown in Figure 4.8. The effects of a 7° deviation from vertical alignment are shown in Figures 4.9a to 4.9c.

Table 4.1 gives the experimental run number for each figure in this thesis. The Roman numeral gives the number of the laboratory notebook and the Arabic numeral gives the page number. Table 4.1 also describes the axial temperature configuration of the furnace and the symmetry of the observed flow field.

Table 4.1. Experimental run and corresponding thesis figure number. A stabilizing or destabilizing temperature profile near the interface is abbreviated as stb. or destb. respectively. A symmetrical or asymmetrical flow field is abbreviated as sym. or asym. respectively.

<u>Run</u>	<u>Figure</u>	<u>Temp. Profile</u>	<u>Convection</u>
I-44	4.1	stb.	asym.
I-47	4.2	stb.	asym.
I-49	4.3	stb.	sym.
I-52	4.4	destb.	asym.
I-21	4.5	destb.	sym.
I-62	4.6	destb.	sym.
I-55	4.7	destb.	sym.
I-66	4.8	destb.	asym.
I-71	4.9	destb.	asym.
II-12	4.10	destb.	sym.
II-11	4.11	destb.	asym.
II-10	4.12	destb.	asym.
II-7a	4.13	stb.	asym.
II-7b	4.14	stb.	sym.
II-8	4.15	stb.	asym.
II-9	4.16	stb.	asym.

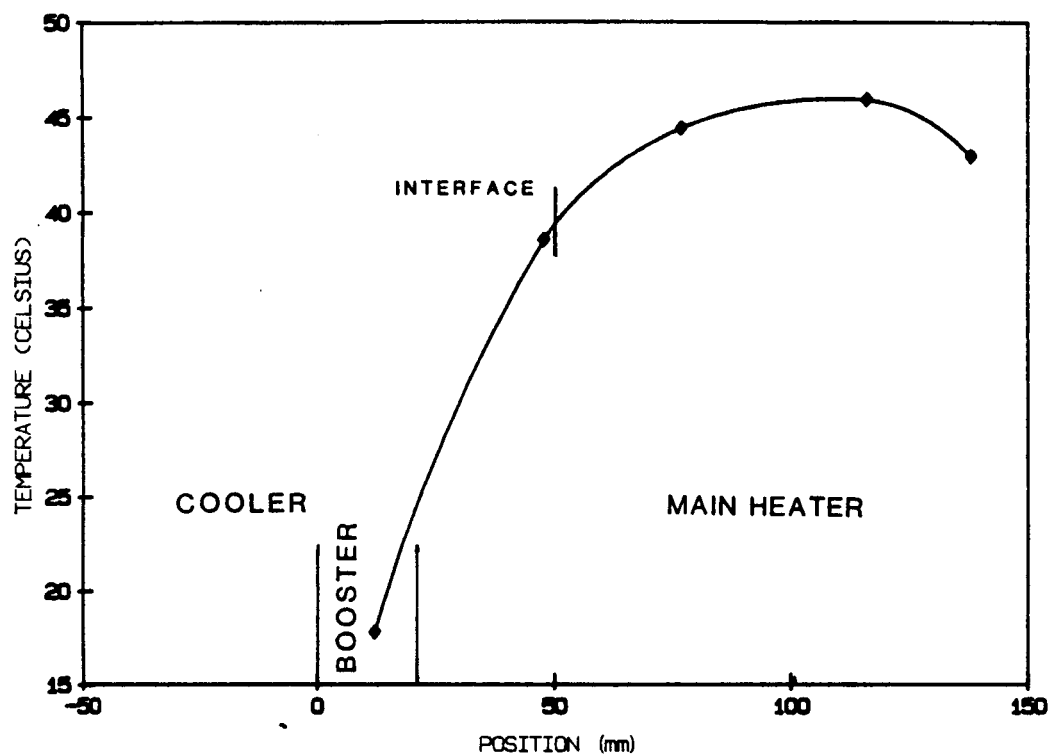


Figure 4.1a. Plot of temperature of the outer wall of the Pyrex sample ampoule vs. vertical position for run I-44. The location of the melt-solid interface was 48.5 mm above the bottom of the booster heater. The temperature of the cooling bath was 1.5 °C.



Figure 4.1b. Photographs of the convective velocity field corresponding to the temperature profile of Figure 4.1a. The photographs are a 4 second (on the left) and a 32 second time exposure of the front view.

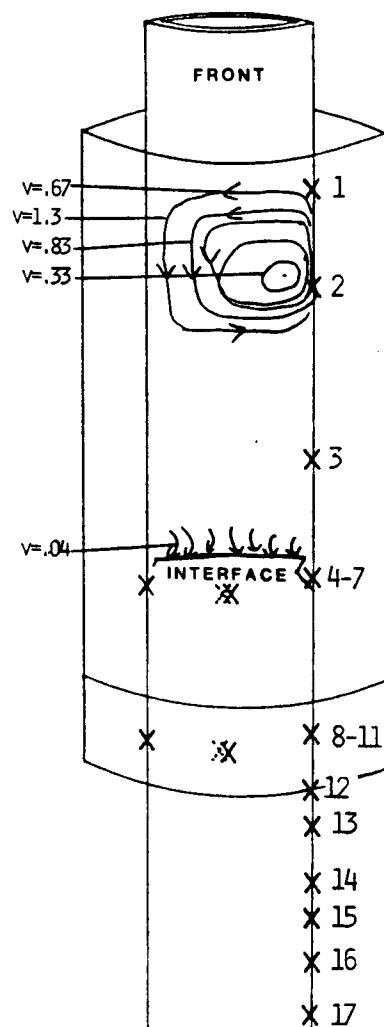


Figure 4.1c. Schematic representation of the convective velocity field shown in Figure 4.1b. Velocities are in mm/s.

<u>TC#</u>	<u>Temp (°C)</u>		<u>TC#</u>	<u>Temp (°C)</u>
1	42.9		12	--
2	45.9		13	--
3	44.4		14	--
--			15	--
4	38.8		16	--
5	38.4		17	--
6	--			
7	38.2	$\bar{T} = 38.5 \pm 0.3$		bath temp = 1.5
--				
8	17.6			
9	17.8			
10	17.2			
11	18.4	$\bar{T} = 17.8 \pm 0.5$		
--				

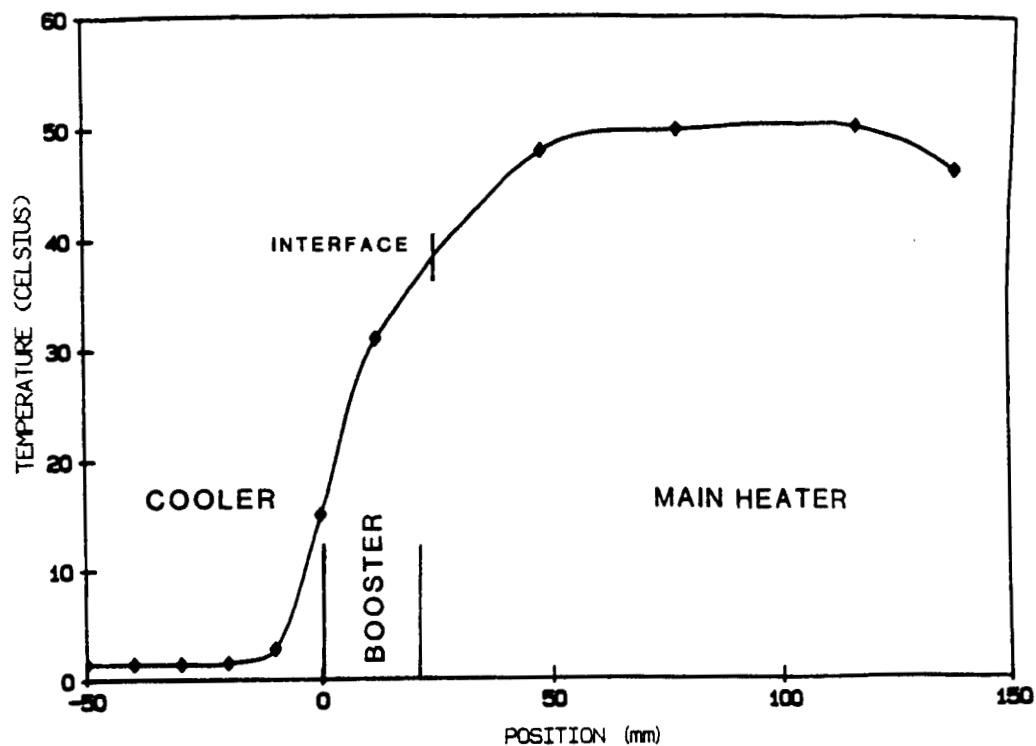


Figure 4.2a. Plot of temperature of the outer wall of the Pyrex sample ampoule vs. vertical position for run I-47. The location of the melt-solid interface was 25.8 mm above the bottom of the booster heater. The temperature of the cooling bath was 1.4 °C.

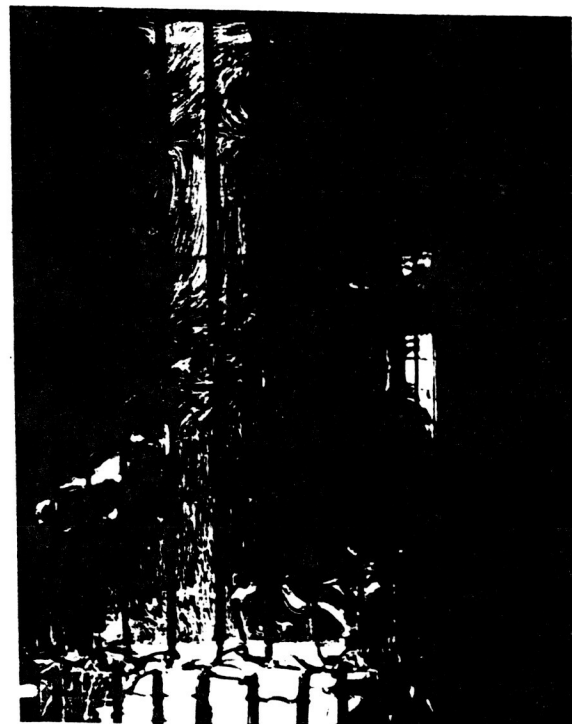
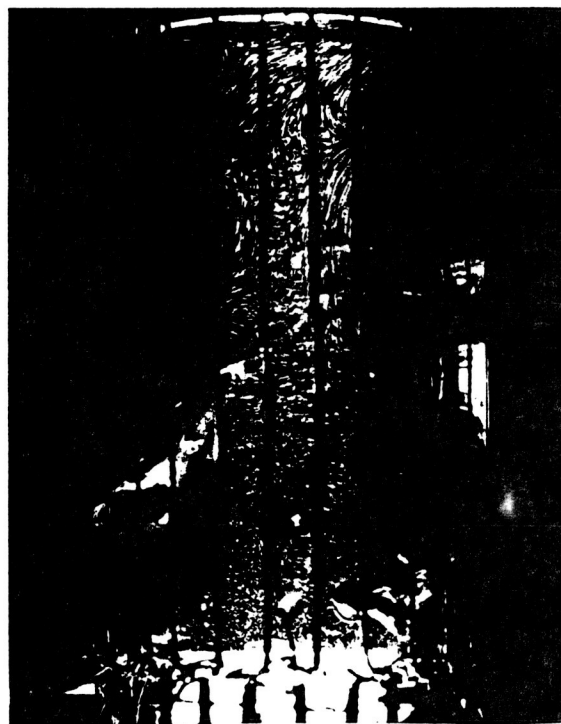
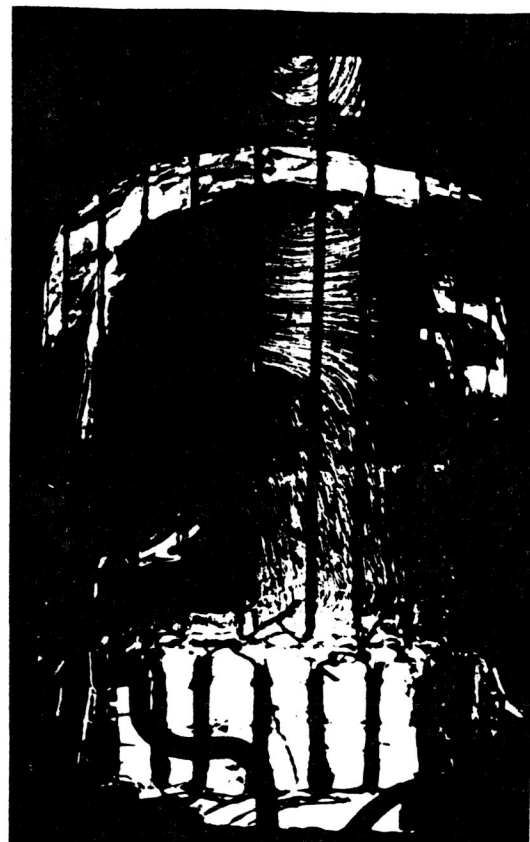
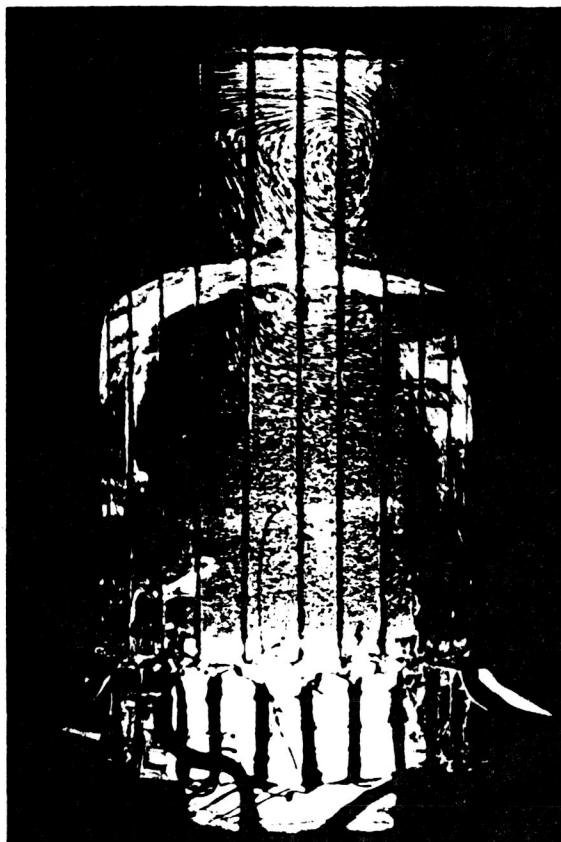


Figure 4.2b. Photographs of the convective velocity field corresponding to the temperature profile of Figure 4.2a. The upper photographs are a 4 second (on the left) and 120 second time exposure of the front view. The lower photographs are a 8 second (left) and 120 second time exposure of the side view.

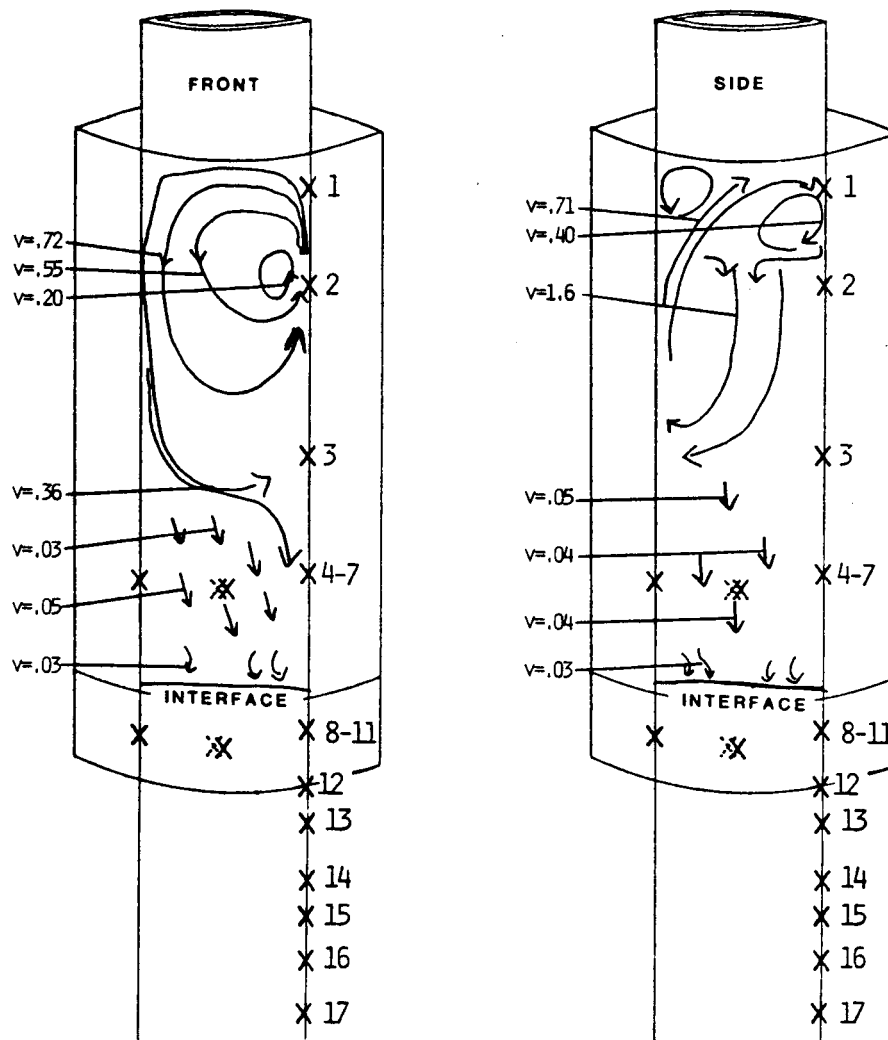


Figure 4.2c. Schematic representation of the convective velocity field shown in Figure 4.2b. Velocities are in mm/s.

TC#	Temp (°C)		TC#	Temp (°C)
1	46.2		12	15.1
2	50.1		13	2.8
3	49.9		14	1.5
--			15	1.4
4	48.1		16	1.4
5	48.2		17	1.4
6	--			
7	47.6	$\bar{T} = 48.0 \pm 0.3$		bath temp = 1.4
--				
8	31.0			
9	30.8			
10	31.2			
11	31.2	$\bar{T} = 31.0 \pm 0.2$		
--				

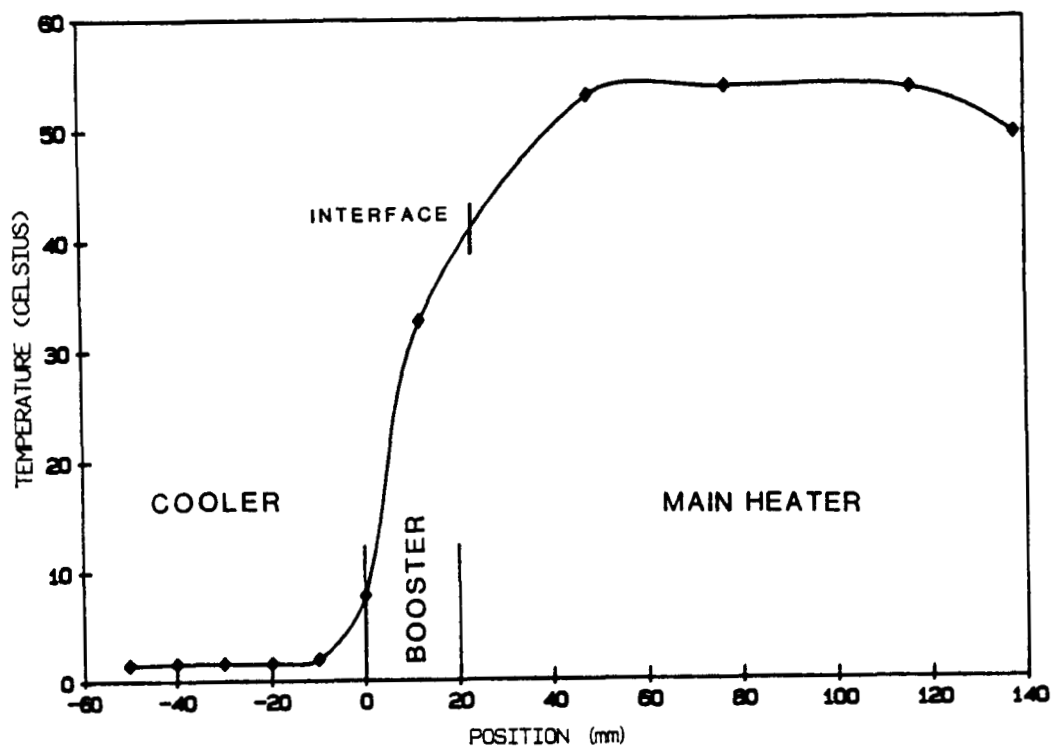


Figure 4.3a. Plot of temperature of the outer wall of the Pyrex sample ampoule vs. vertical position for run I-49. The location of the melt-solid interface is 23.3 mm above the bottom of the booster heater. The temperature of the cooling bath was 1.5 °C.

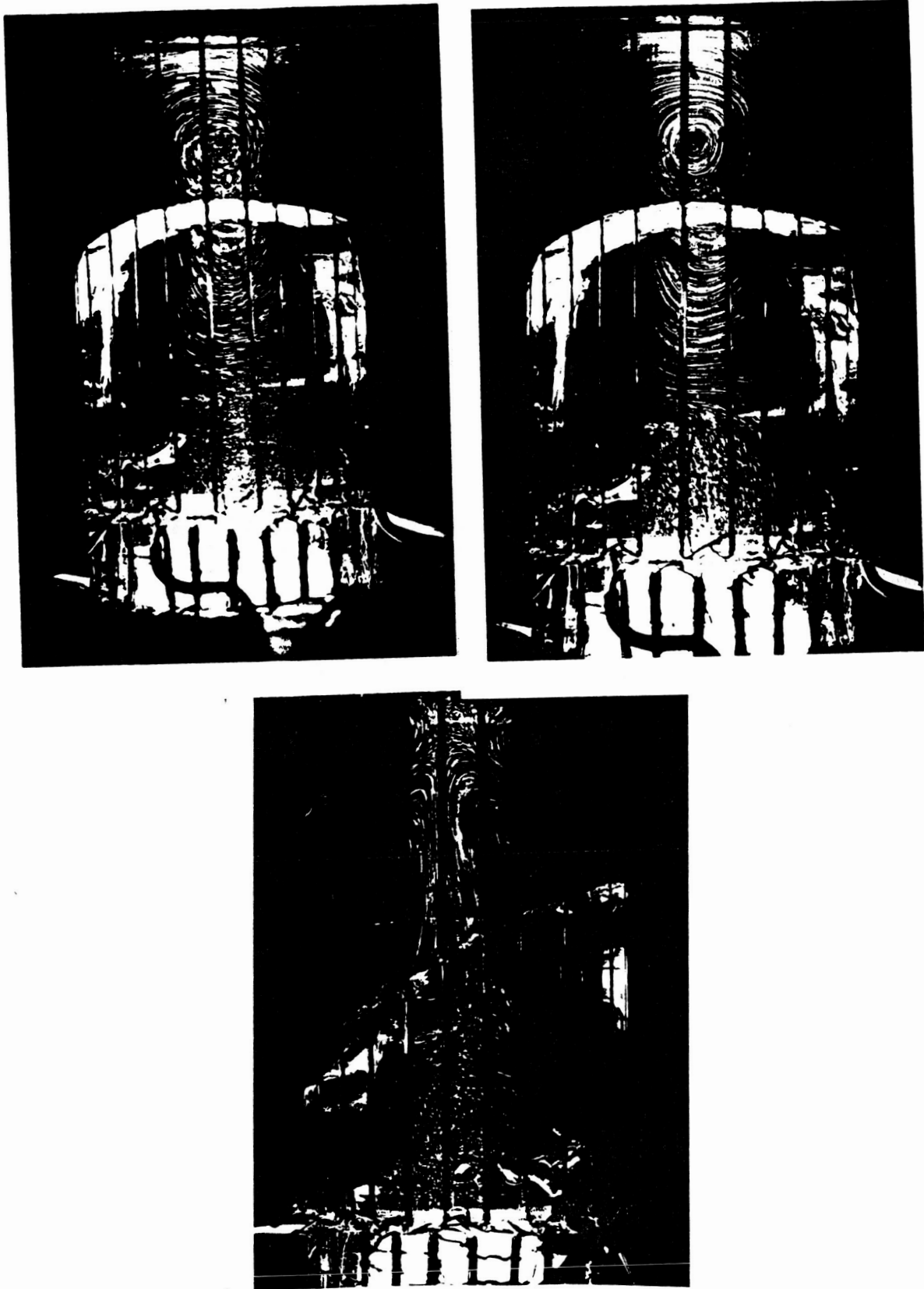


Figure 4.3b. Photographs of the convective velocity field corresponding to the temperature profile of Figure 4.3a. The upper photographs are a 4 second (left) and 30 second time exposure of the front view. The lower photograph is a 16 second time exposure of the side view.

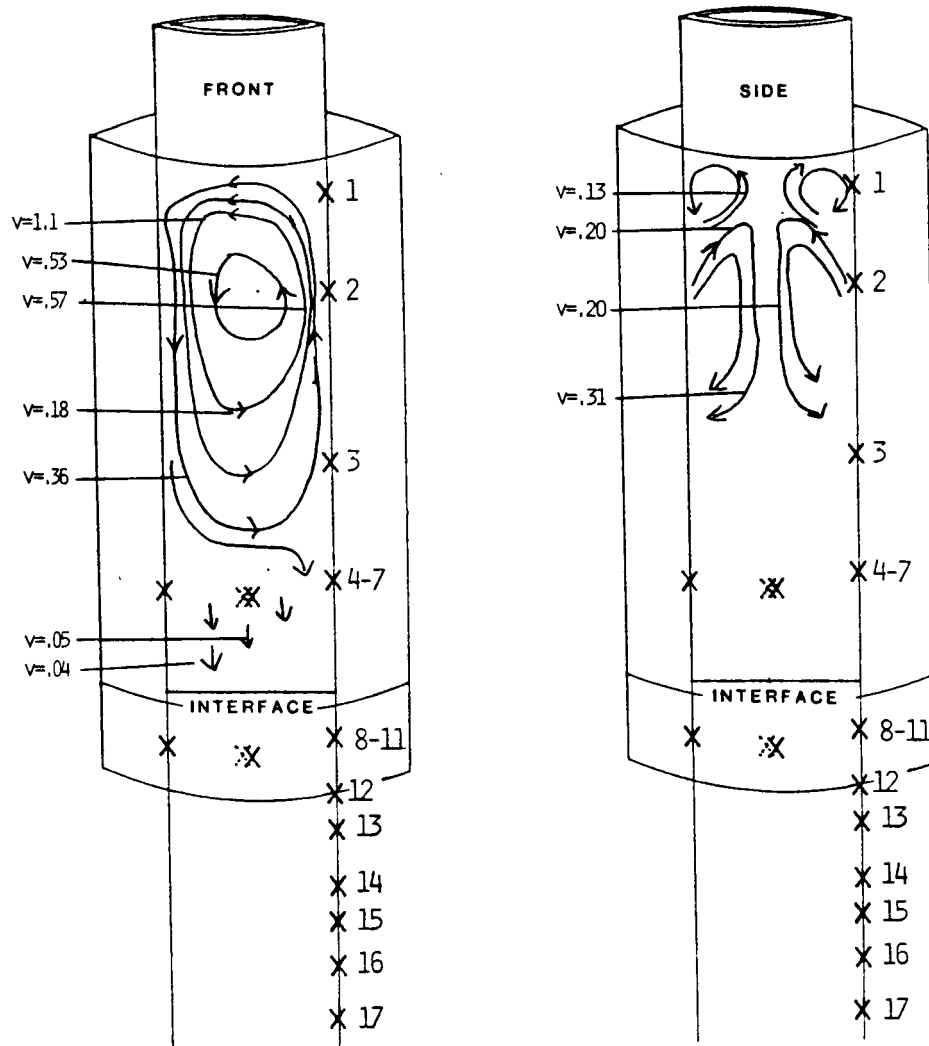


Figure 4.3c. Schematic representation of the convective velocity field shown in Figure 4.3b. Velocities are in mm/s.

TC#	Temp ($^{\circ}$ C)	
1	49.4	
2	53.6	
3	53.8	
--		
4	53.4	
5	53.2	
6	--	
7	52.4	$\bar{T} = 53.0 \pm 0.5$
--		
8	32.6	
9	32.8	
10	33.0	
11	32.4	$\bar{T} = 32.7 \pm 0.3$
--		

TC#	Temp ($^{\circ}$ C)
12	7.8
13	2.0
14	1.6
15	1.6
16	1.6
17	1.5

bath temp = 1.5

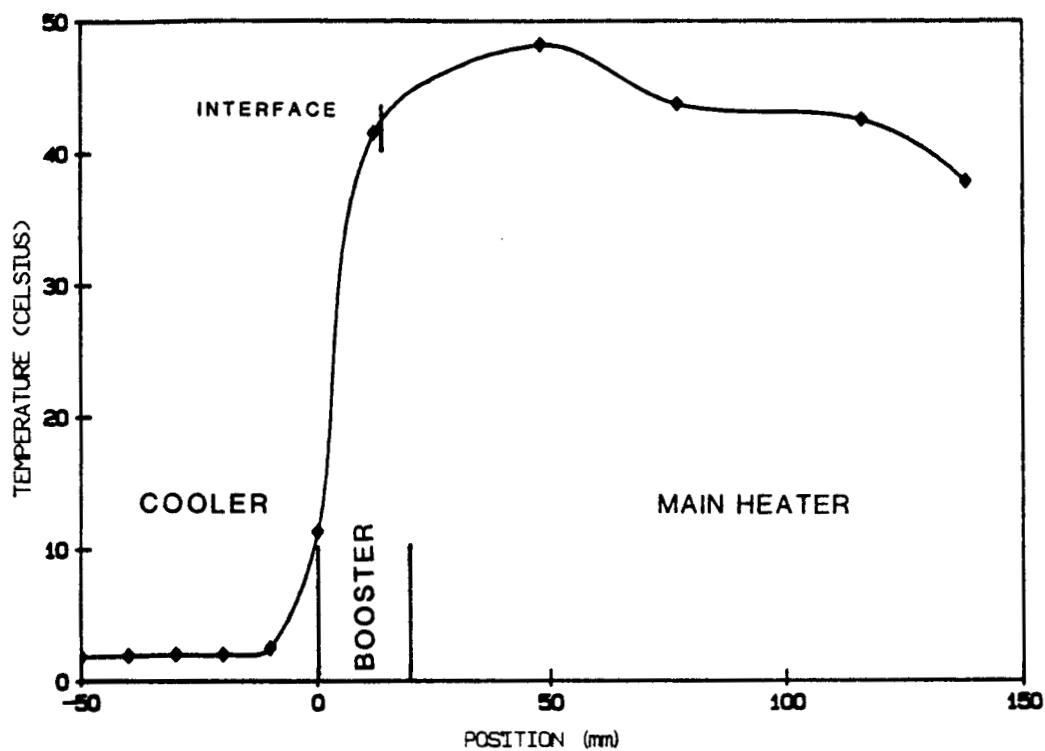


Figure 4.4a. Plot of temperature of the outer wall of the Pyrex sample ampoule vs. vertical position for run I-52. The location of the melt-solid interface was 13.6 mm above the bottom of the booster heater. The temperature of the cooling bath was 1.5 °C.

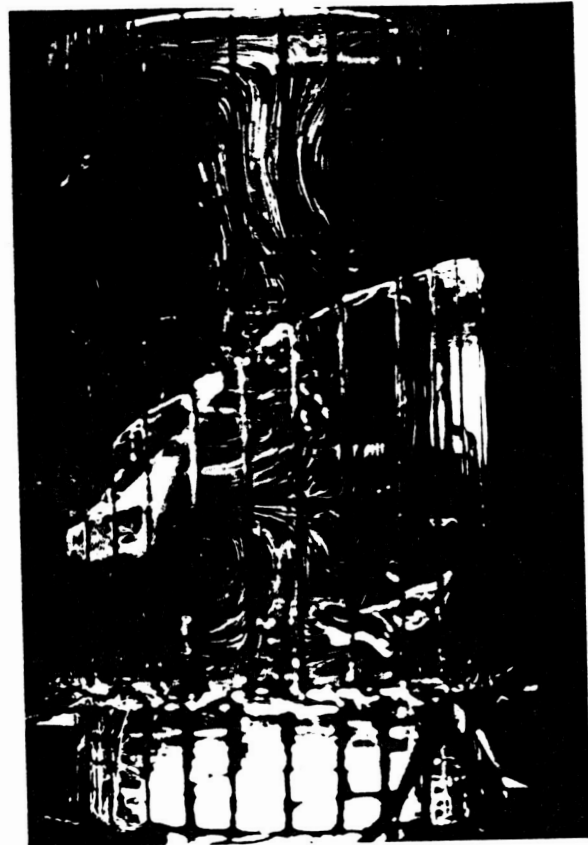
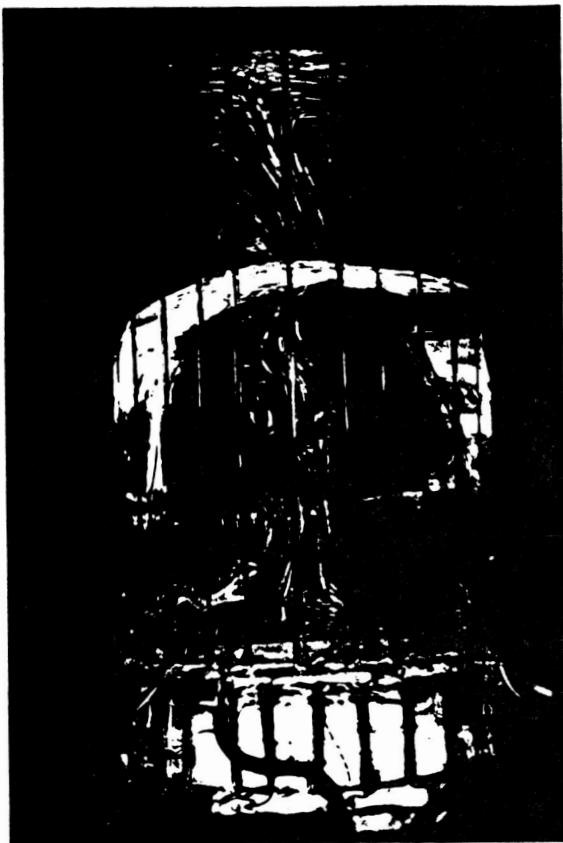


Figure 4.4b. Photographs of the convective velocity field corresponding to the temperature profile of Figure 4.4a. The left and right photographs are 4 second time exposures of front and side views respectively.

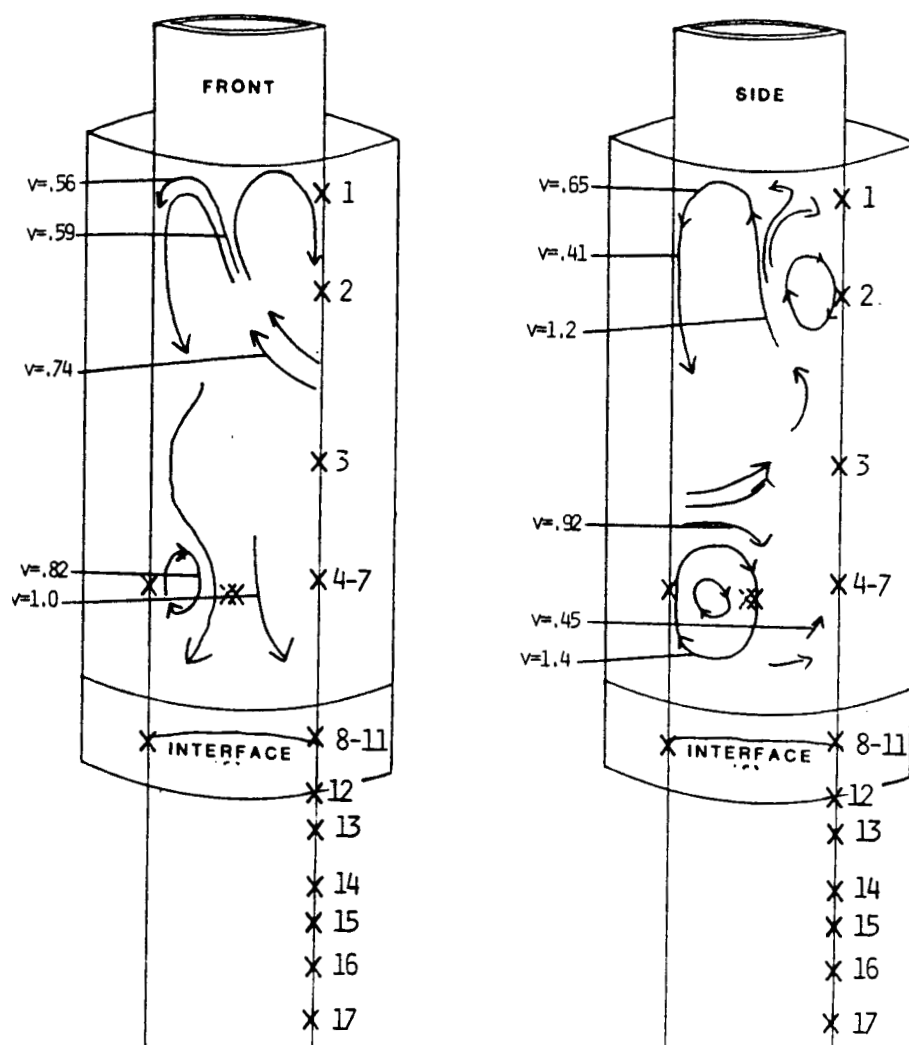


Figure 4.4c. Schematic representation of the convective velocity field shown in Figure 4.4b. Velocities are in mm/s.

TC#	Temp ($^{\circ}\text{C}$)	TC#	Temp ($^{\circ}\text{C}$)
1	37.8	12	11.3
2	42.5	13	2.5
3	43.7	14	2.0
--	--	15	2.0
4	48.8	16	1.9
5	47.8	17	1.8
6	--		
7	48.0	bath temp = 1.5	
	$\bar{T} = 48.2 \pm 0.5$		
--	--		
8	41.2		
9	41.5		
10	41.5		
11	41.7		
	$\bar{T} = 41.5 \pm 0.2$		
--	--		

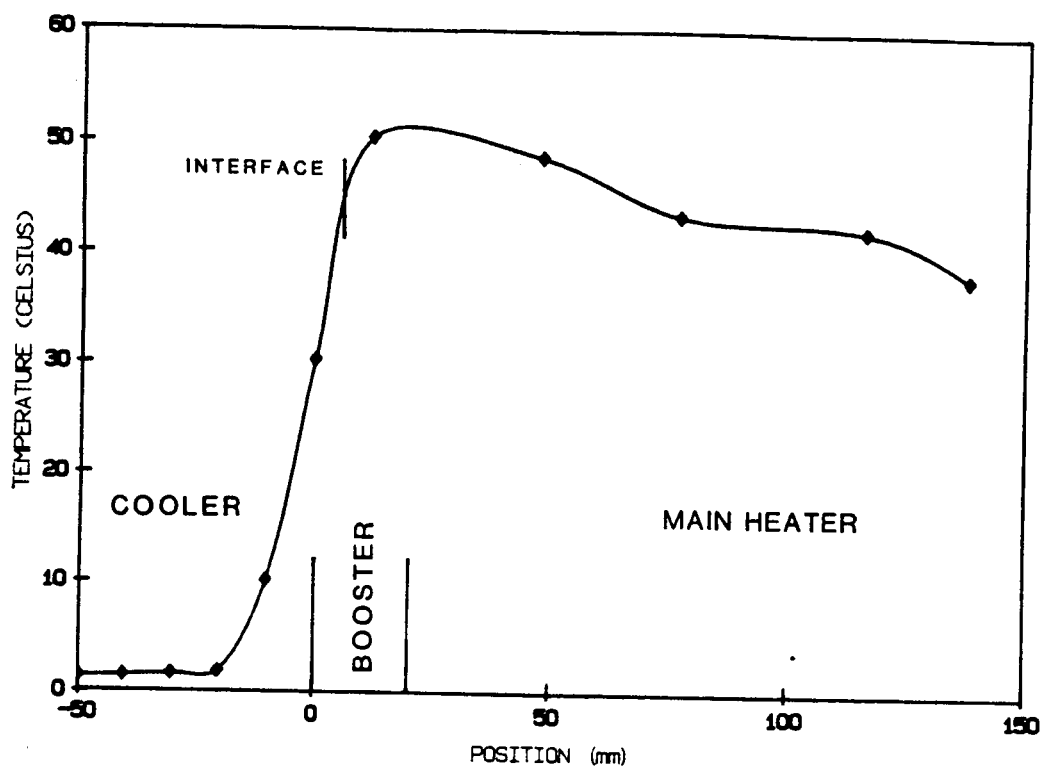


Figure 4.5a. Plot of temperature of the outer wall of the Pyrex sample ampoule vs. vertical position for run I-21. The location of the melt-solid interface was 5.3 mm above the bottom of the booster heater. The temperature of the cooling bath was 1.4 °C.

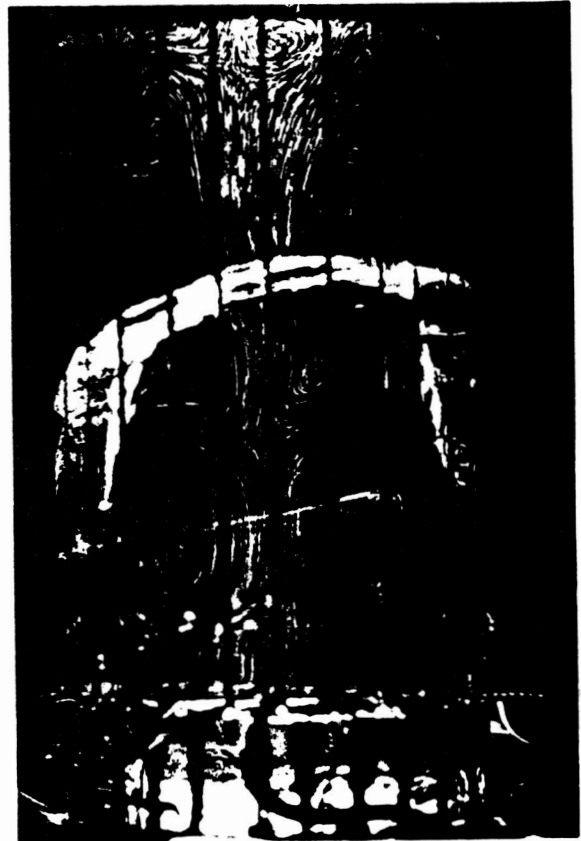


Figure 4.5b. Photographs of the convective velocity field corresponding to the temperature profile of Figure 4.5a. The left and right photographs are 2 and 4 second time exposures of the front view.

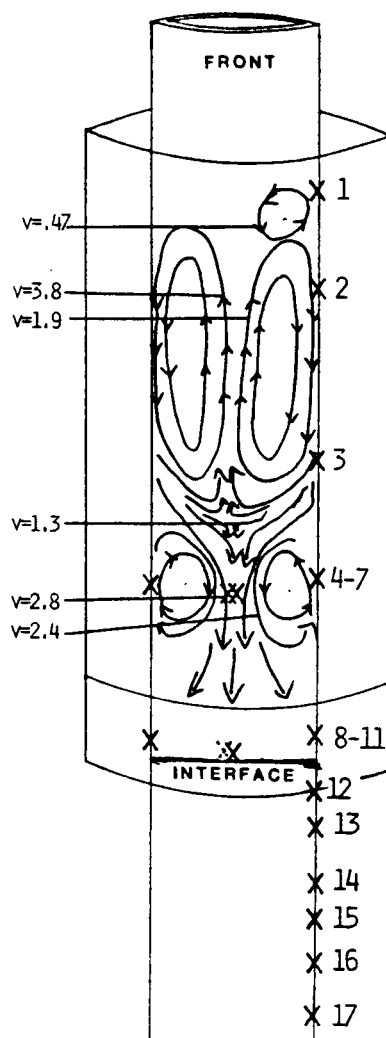


Figure 4.5c. Schematic representation of the convective velocity field shown in Figure 4.5b. Velocities are in mm/s.

TC#	Temp (°C)		TC#	Temp (°C)
1	37.9		12	30.3
2	42.1		13	10.1
3	43.4		14	1.8
--			15	1.6
4	48.8		16	1.4
5	48.4		17	1.3
6	--			
7	48.6	$\bar{T} = 48.6 \pm 0.2$		bath temp = 1.4
--				
8	50.5			
9	50.2			
10	50.8			
11	50.1	$\bar{T} = 50.4 \pm 0.3$		
--				

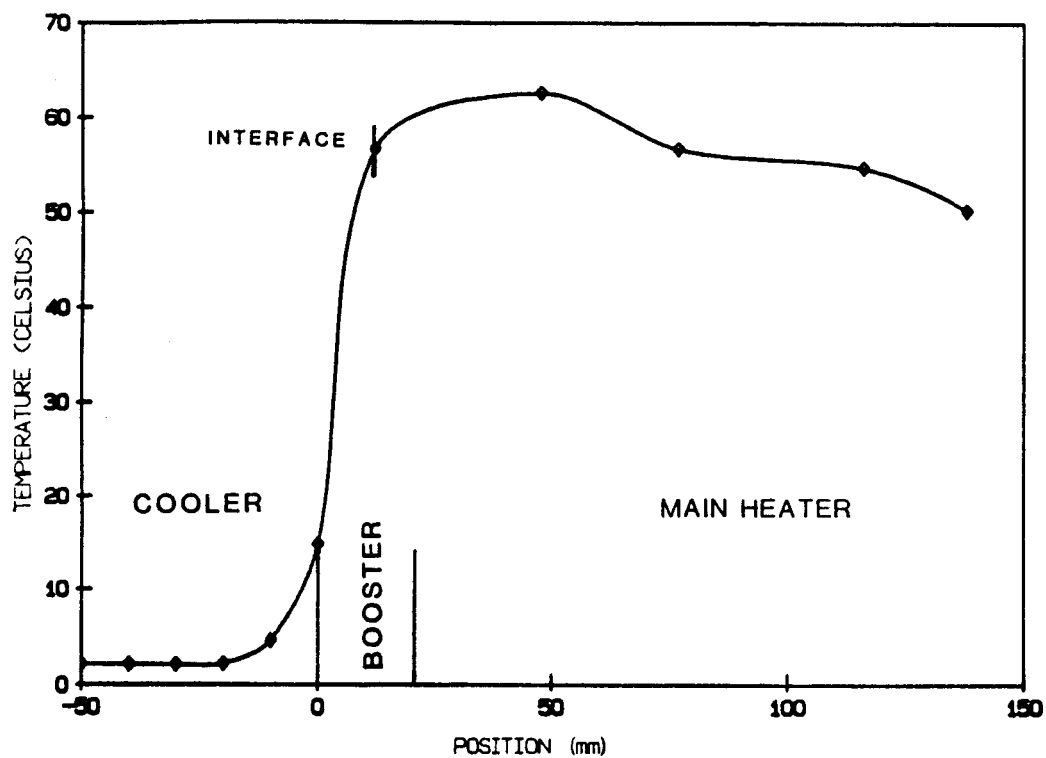


Figure 4.6a. Plot of temperature of the outer wall of the Pyrex sample ampoule vs. vertical position for run I-62. The location of the melt-solid interface was 13.2 mm above the bottom of the booster heater. The temperature of the cooling bath was 1.9 °C.

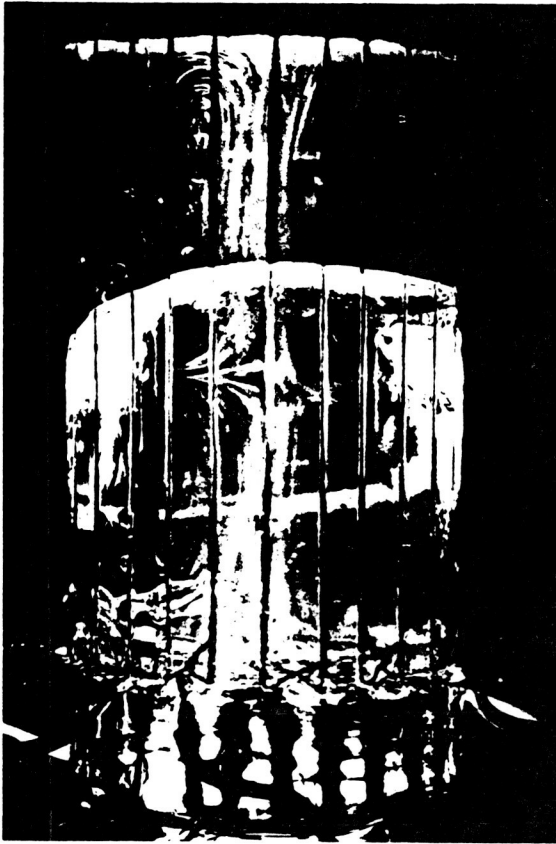


Figure 4.6b. Photographs of the convective velocity field corresponding to the temperature profile of Figure 4.6a. The left and right photographs are 4 second time exposures of the front and side views respectively.

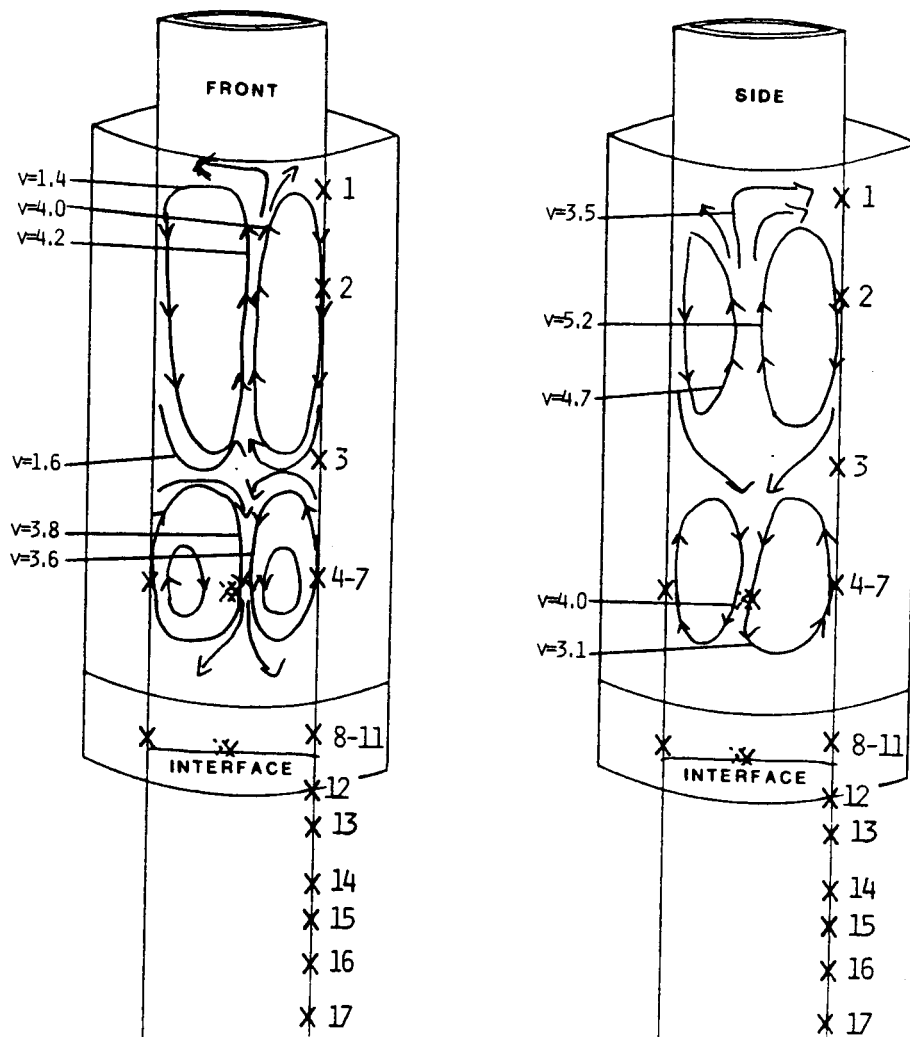


Figure 4.6c. Schematic representation of the convective velocity field shown in Figure 4.6b. Velocities are in mm/s.

TC#	Temp (°C)	TC#	Temp (°C)
1	50.2	12	14.8
2	54.7	13	4.6
3	56.7	14	2.2
--		15	2.1
4	62.6	16	2.1
5	62.5	17	2.1
6	--		
7	62.7	bath temp = 1.9	
	$\bar{T} = 62.6 \pm 0.1$		
--			
8	56.7		
9	56.6		
10	56.5		
11	56.5		
	$\bar{T} = 56.6 \pm 0.1$		
--			

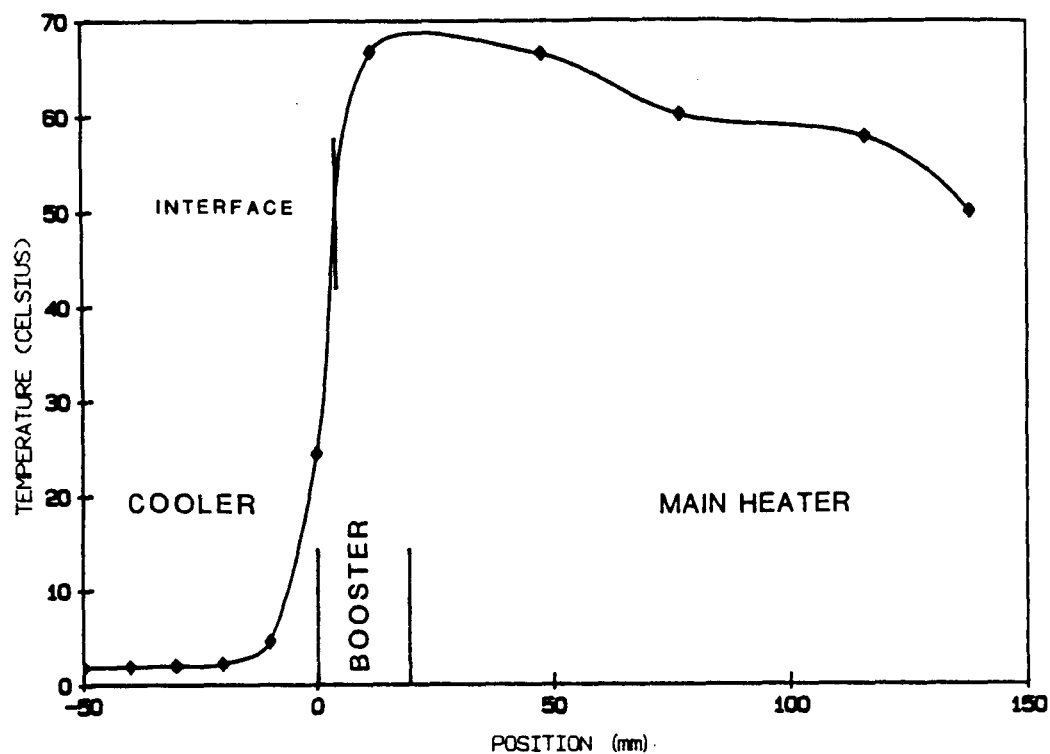


Figure 4.7a. of temperature of the outer wall of the Pyrex sample ampou vertical position for run I-55. The location of the melt-solidiface was 4.7 mm above the bottom of the booster heater. The ature of the cooling bath was 1.3 °C.

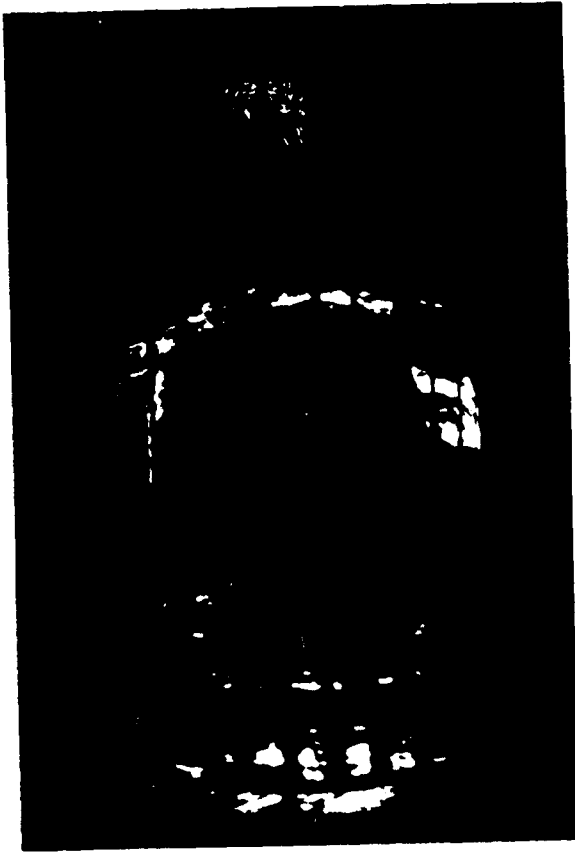


Figure 4.7b. Photographs of the convective velocity field corresponding to the temperature profile of Figure 4.7a. The left and right photographs are 2 second time exposures of the front and side views respectively.

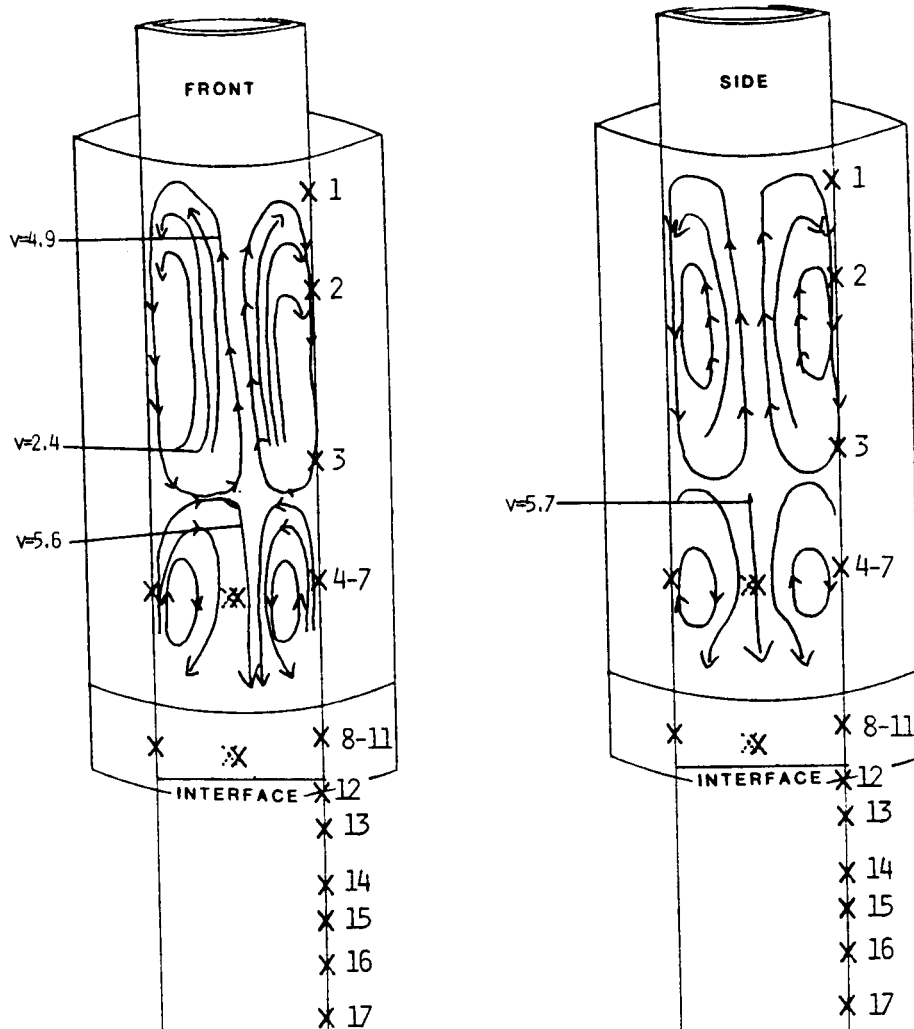


Figure 4.7c. Schematic representation of the convective velocity field shown in Figure 4.7b. Velocities are in mm/s. The poor quality of the photograph of the side view prevented the calculation of many velocities.

TC#	Temp (°C)	TC#	Temp (°C)
1	49.9	12	24.4
2	57.8	13	4.6
3	60.0	14	2.2
--		15	2.0
4	66.7	16	1.9
5	66.1	17	1.8
6	--		
7	66.8	bath temp = 1.3	
	$\bar{T} = 66.5 \pm 0.4$		
--			
8	66.5		
9	66.6		
10	66.7		
11	66.9	$\bar{T} = 66.7 \pm 0.2$	
--			

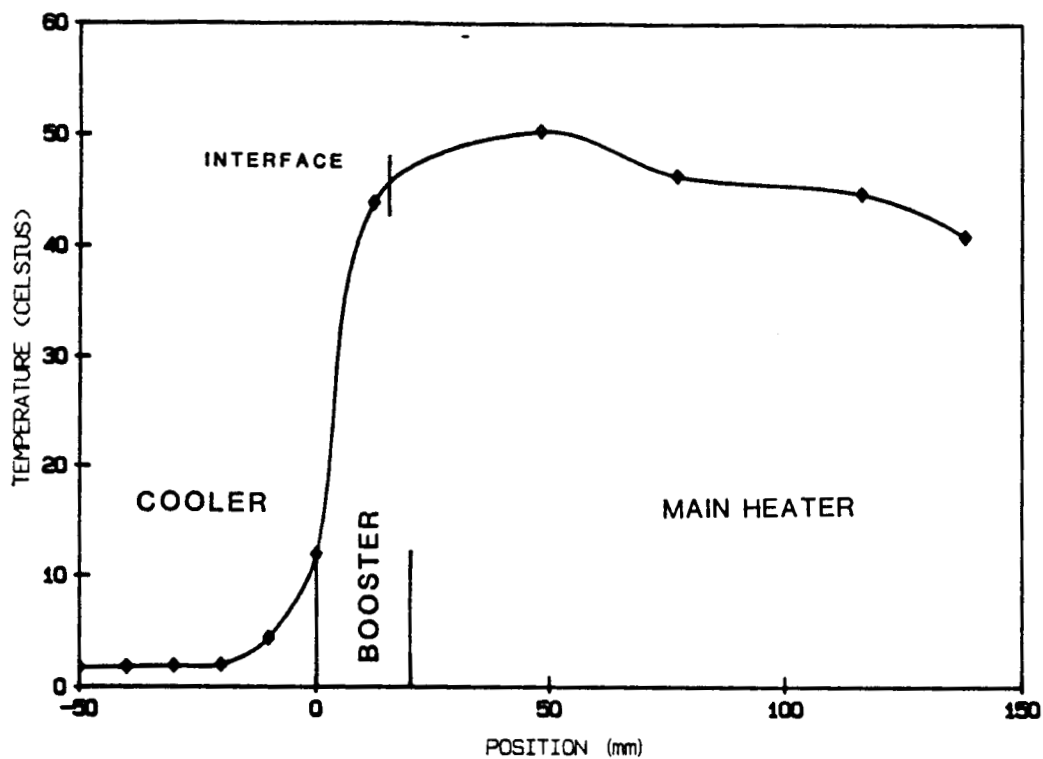


Figure 4.8a. Plot of temperature of the outer wall of the Pyrex sample ampoule vs. vertical position for run I-66. The location of the melt-solid interface was 15.9 mm above the bottom of the booster heater. The temperature of the cooling bath was 1.5 °C.



Figure
conditi^on. Photographs of the convective velocity field under
are 4 f large thermal asymmetry. The left and right photographs
The cool time exposures of the front and side views respectively.
directly ant of the ampoule is to the right in the front view and
e rear in the side view.

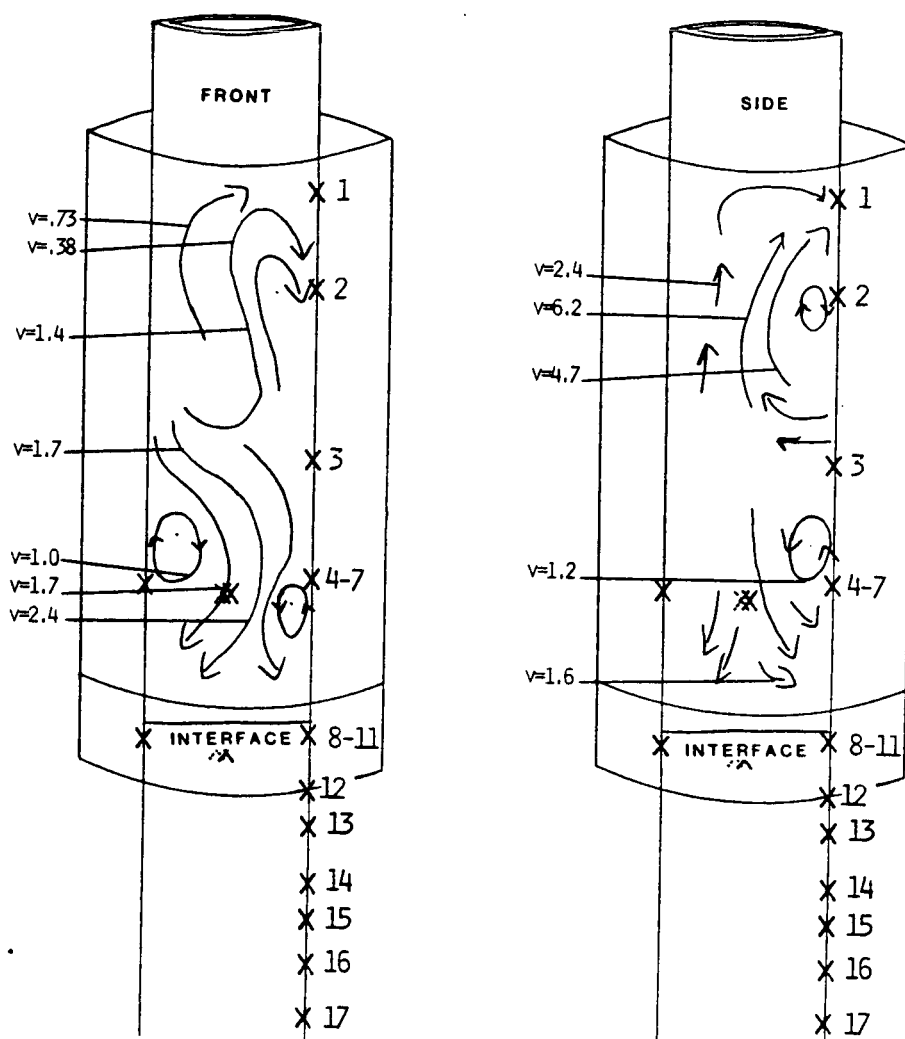


Figure 4.8c. Schematic representation of the convective velocity field shown in Figure 4.8b. The cool quadrant of the ampoule is to the right in the front view and directly to the rear in the side view. Velocities are in mm/s.

TC#	Temp (°C)		TC#	Temp (°C)
1	40.8		12	11.9
2	44.7		13	4.4
3	46.3		14	2.0
--			15	1.9
4	51.0		16	1.8
5	49.0		17	1.7
6	--			
7	51.0	$\bar{T} = 50.3 \pm 1.2$		bath temp = 1.5
--				
8	44.6			
9	40.5			
10	44.7			
11	45.3	$\bar{T} = 43.8 \pm 2.2$		
--				

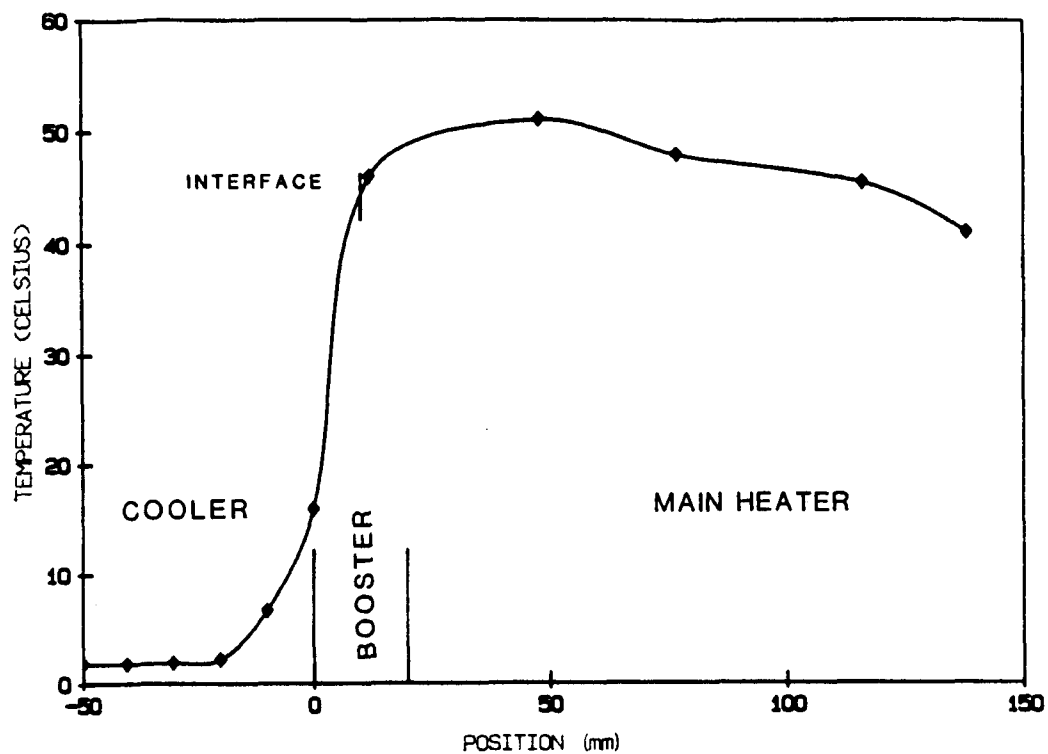


Figure 4.9a. Plot of temperature of the outer wall of the Pyrex sample ampoule vs. axial position for run I-71. The ampoule was tilted 7° from vertical alignment. The location of the melt-solid interface was 11.1 mm above the bottom of the booster heater. The temperature of the cooling bath was 1.5°C .



Figure 4.9b. Photographs of the convective velocity field when the ampoule is tilted 7° . The left and right photographs are 4 second time exposures of the front and side views respectively. The slight tilt of the furnace is clearly seen in the front view. In the side view, the furnace is tilted toward the camera.

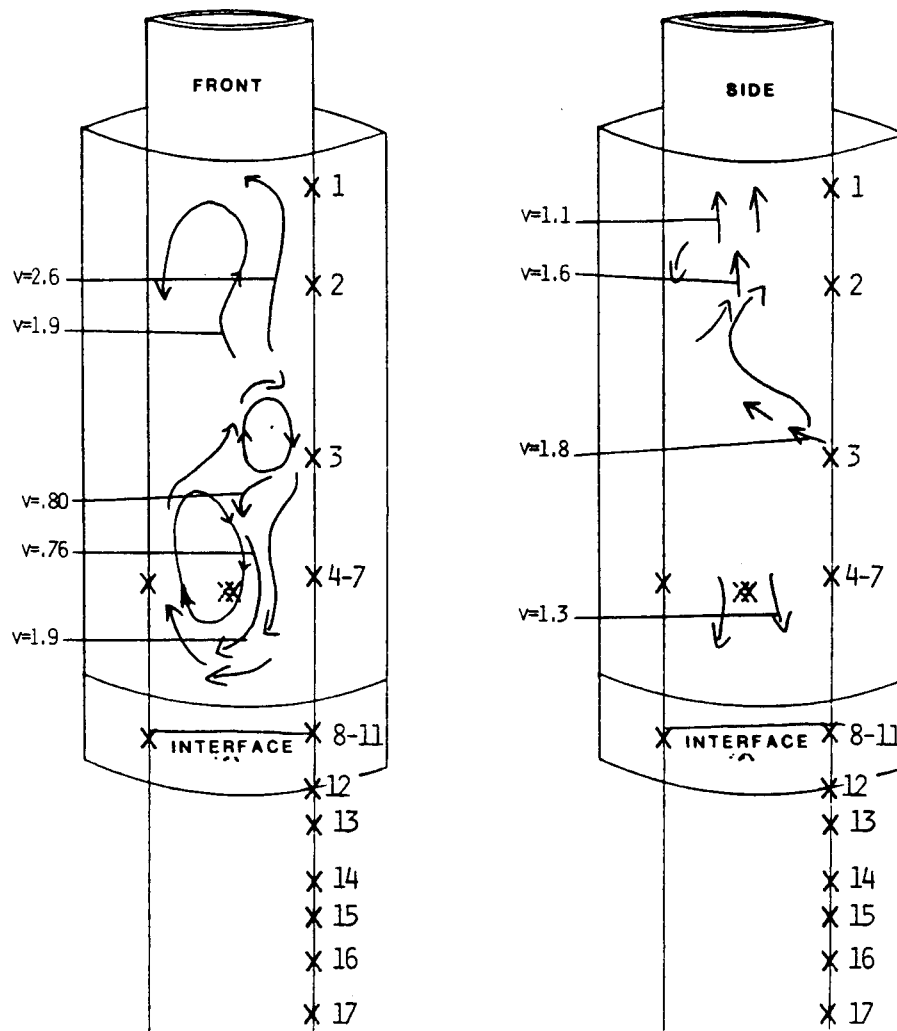


Figure 4.9c. Schematic representation of the convective velocity field shown in Figure 4.9b. Velocities are in mm/s.

TC#	Temp (°C)	TC#	Temp (°C)
1	40.9	12	15.9
2	45.4	13	6.7
3	47.9	14	2.2
--		15	1.9
4	51.5	16	1.8
5	51.5	17	1.8
6	--		
7	50.3	bath temp = 1.5	
	$\bar{T} = 51.1 \pm 0.7$		
--			
8	46.4		
9	46.1		
10	46.6		
11	45.0		
	$\bar{T} = 46.0 \pm 0.7$		
--			

2. Three Zone Furnace, A=6.7

Convection was observed in a slightly longer three zone furnace. In these studies no power was supplied to the furnace. Power was supplied only to the booster heater, in increasing amounts in each subsequent run. The results are summarized in Figures 4.10 to 4.12.

3. Two Zone Furnace

The steady state melt-solid interface in the three-zone furnace experiments was always planar. To see if this was related to the apparent lack of convection near the interface in the vertically stabilized configuration, observations were made during melt-down in which there was a large interfacial curvature. In a two zone furnace in which the benzophenone had completely solidified, power to the furnace was turned on. As the organic compound began to melt, a very convex interface formed. The interface became progressively more planar as the melt/solid interface receded to its equilibrium position. The results of one such run are shown in Figures 4.13 and 4.14. The data and photos for two figures were separated in time by about 50 minutes. The results of a second run are shown in Figures 4.15a to 4.15c. Figure 4.16b is a 120 second time exposure photograph taken during another run. In this figure the interface is only slightly convex.

In general it was found that the lack of convection near the interface in the vertically stabilized configuration had nothing to do with interfacial curvature. For this configuration, convection was absent near the interface when the interface was planar as well as when highly curved.

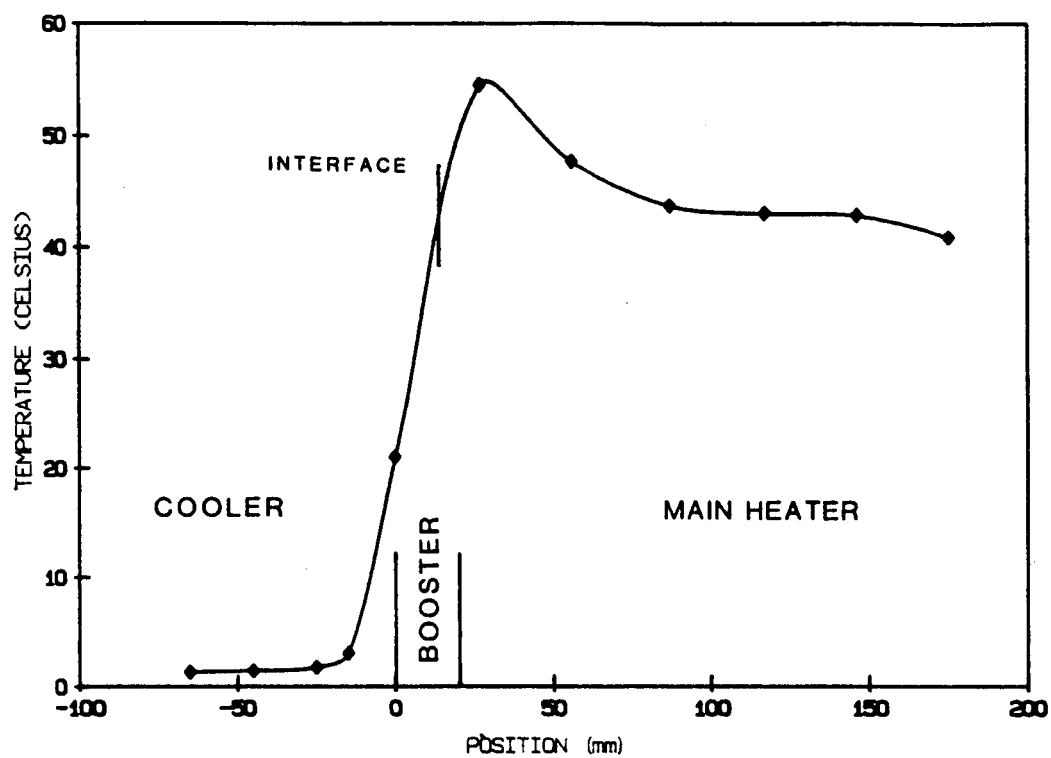


Figure 4.10a. Plot of temperature of the outer wall of the Pyrex sample ampoule vs. vertical position for run II-12. The location of the melt-solid interface was 13.4 mm above the bottom of the booster heater. The temperature of the cooling bath was 1.3 °C.

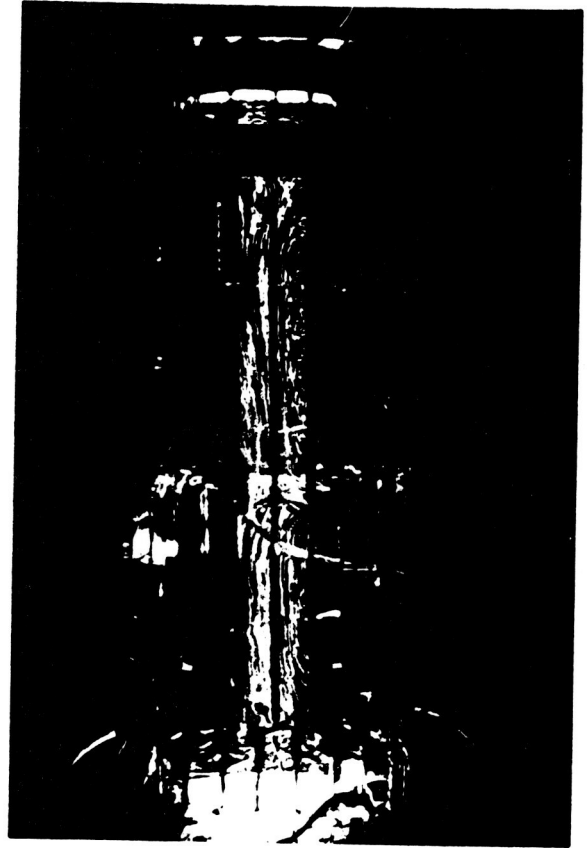
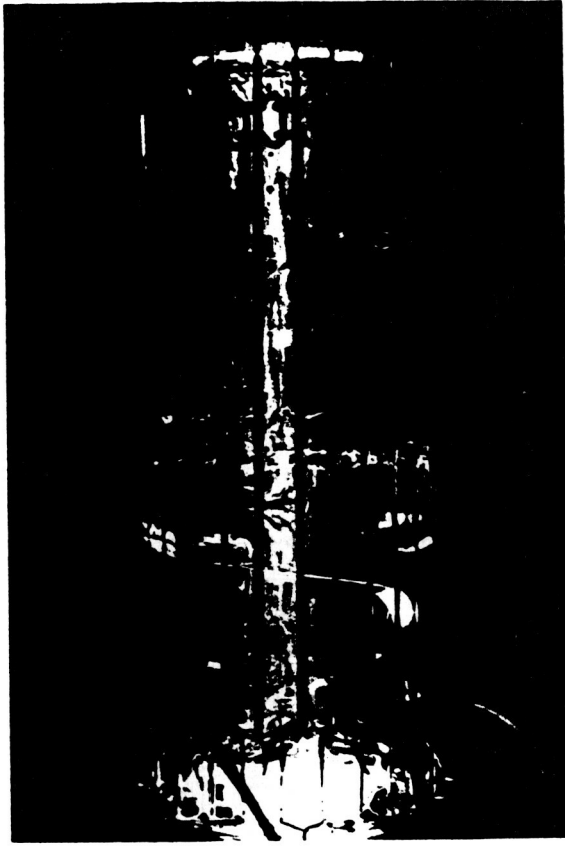


Figure 4.10b. Photographs of the convective velocity field corresponding to the temperature profile of Figure 4.10a. The left photograph is a 4 second time exposures of the front view. The right photograph is a 2 second time exposure of the side view.

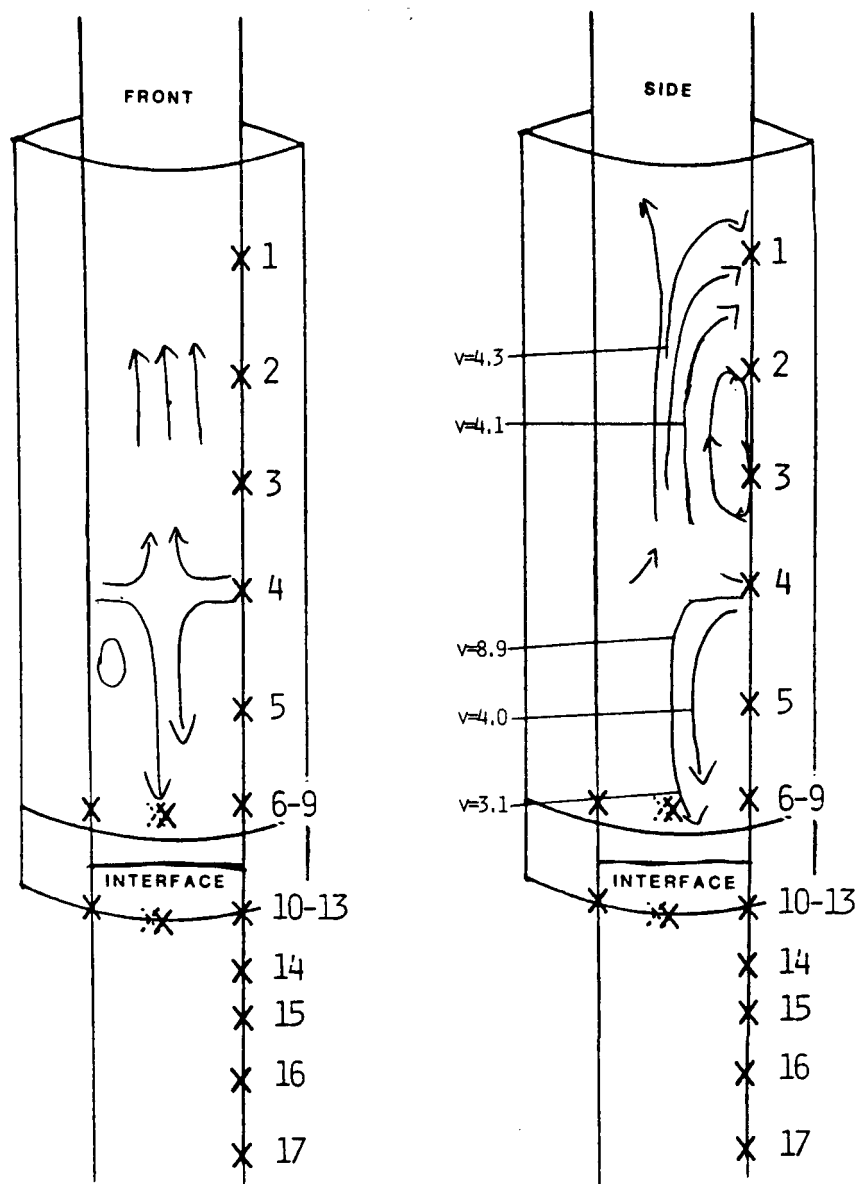


Figure 4.10c. Schematic representation of the convective velocity field shown in Figure 4.10b. Velocities are in mm/s. The poor quality of the photograph of the front view prevented the calculation any velocities.

TC#	Temp (°C)	TC#	Temp (°C)
1	40.7	10	23.4
2	42.7	11	19.6
3	42.9	12	18.4
4	43.6	13	22.6
5	47.6		$\bar{T} = 21.0 \pm 2.4$
--		--	
6	54.6	14	3.0
7	54.4	15	1.7
8	54.7	16	1.4
9	54.3	17	1.3
--			
	$\bar{T} = 54.5 \pm 0.2$		bath temp = 1.3

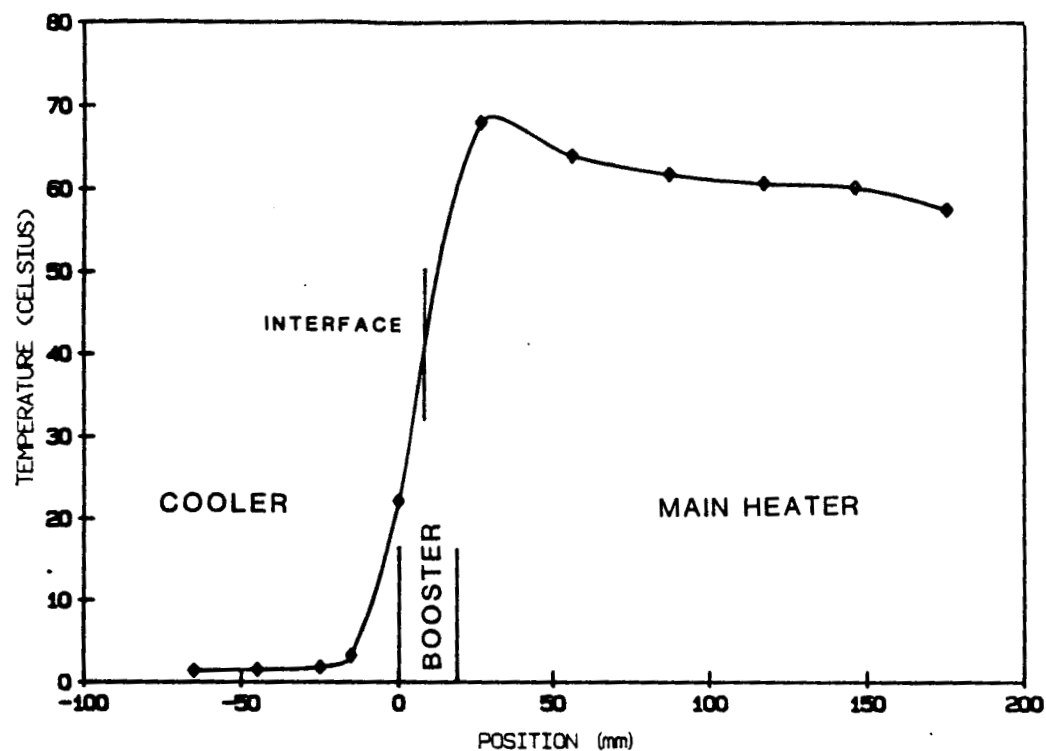


Figure 4.11a. Plot of temperature of the outer wall of the Pyrex sample ampoule vs. vertical position for run II-11. The location of the melt-solid interface was 3.8 mm above the bottom of the booster heater. The temperature of the cooling bath was 1.2 °C.

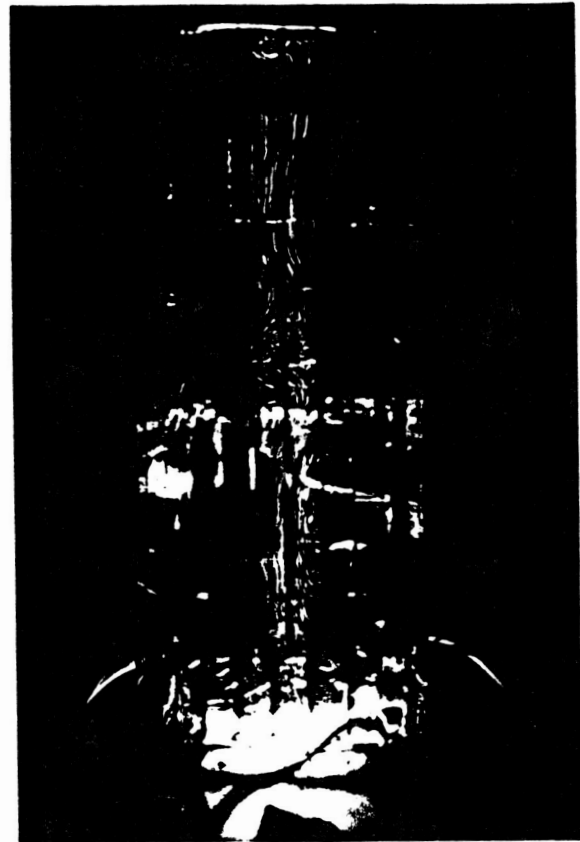
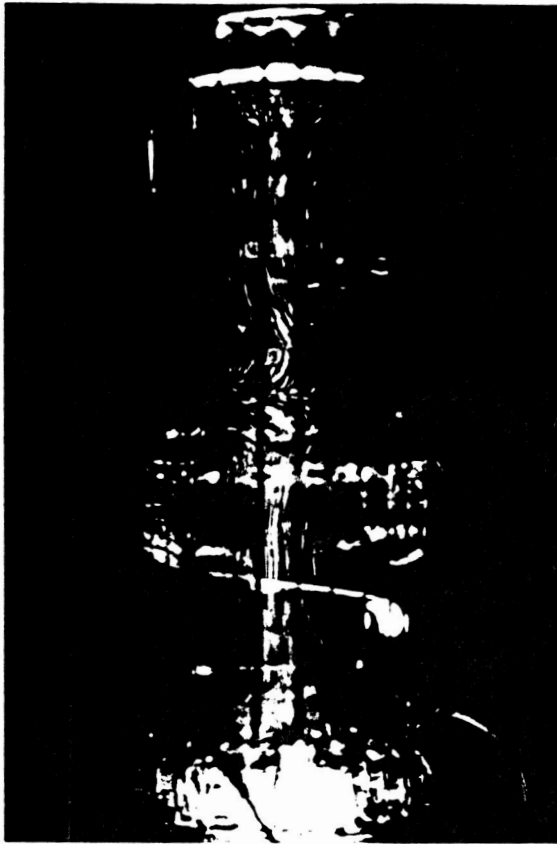


Figure 4.11b. Photographs of the convective velocity field corresponding to the temperature profile of Figure 4.11a. The left and right photographs are 2 second time exposures of the front and side views respectively.

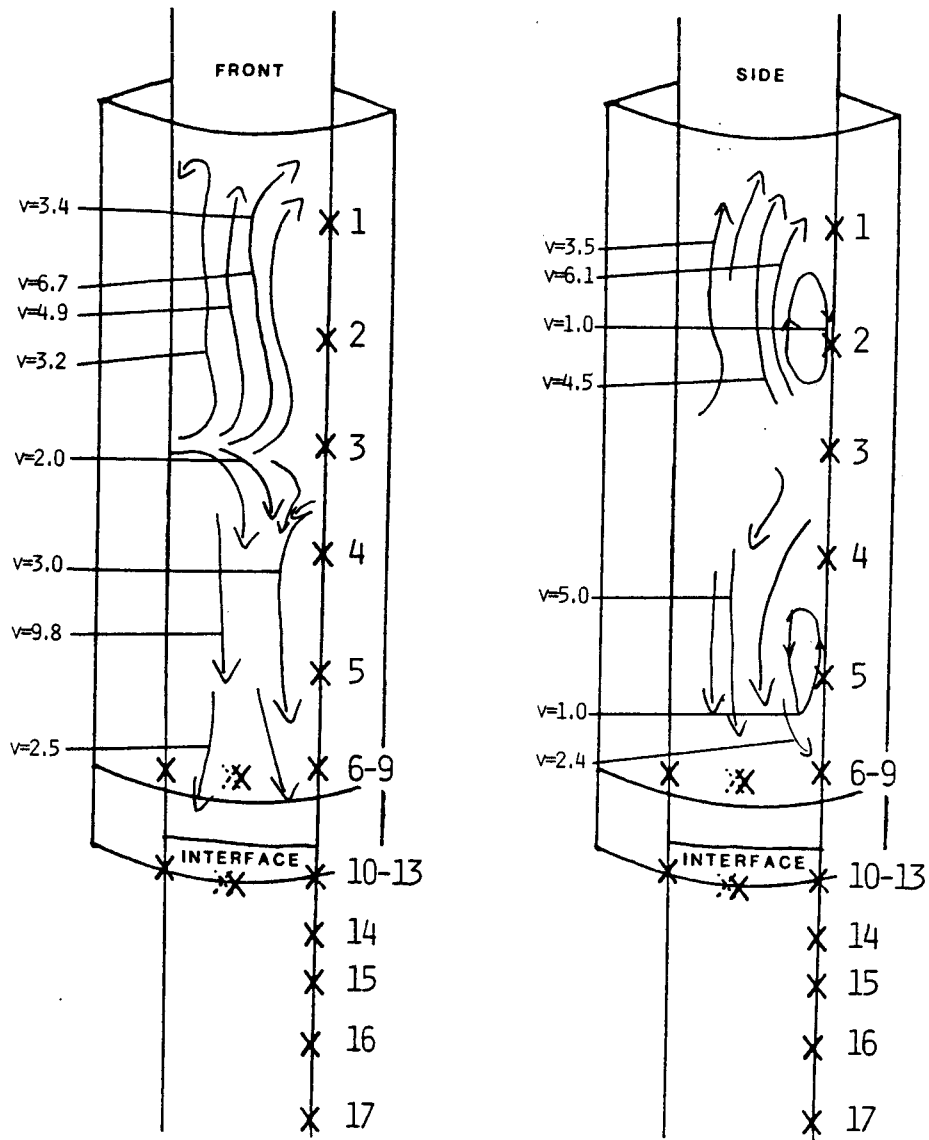


Figure 4.11c. Schematic representation of the convective velocity field shown in Figure 4.11b. Velocities are in mm/s.

TC#	Temp (°C)
1	57.4
2	60.1
3	60.6
4	61.7
5	63.9
--	
6	67.7
7	67.7
8	68.0
9	68.1
--	

$$\bar{T} = 67.9 \pm 0.2$$

TC#	Temp (°C)
10	25.0
11	23.7
12	19.3
13	20.4
--	
14	3.2
15	1.8
16	1.5
17	1.4

$$\bar{T} = 22.1 \pm 2.7$$

bath temp = 1.2

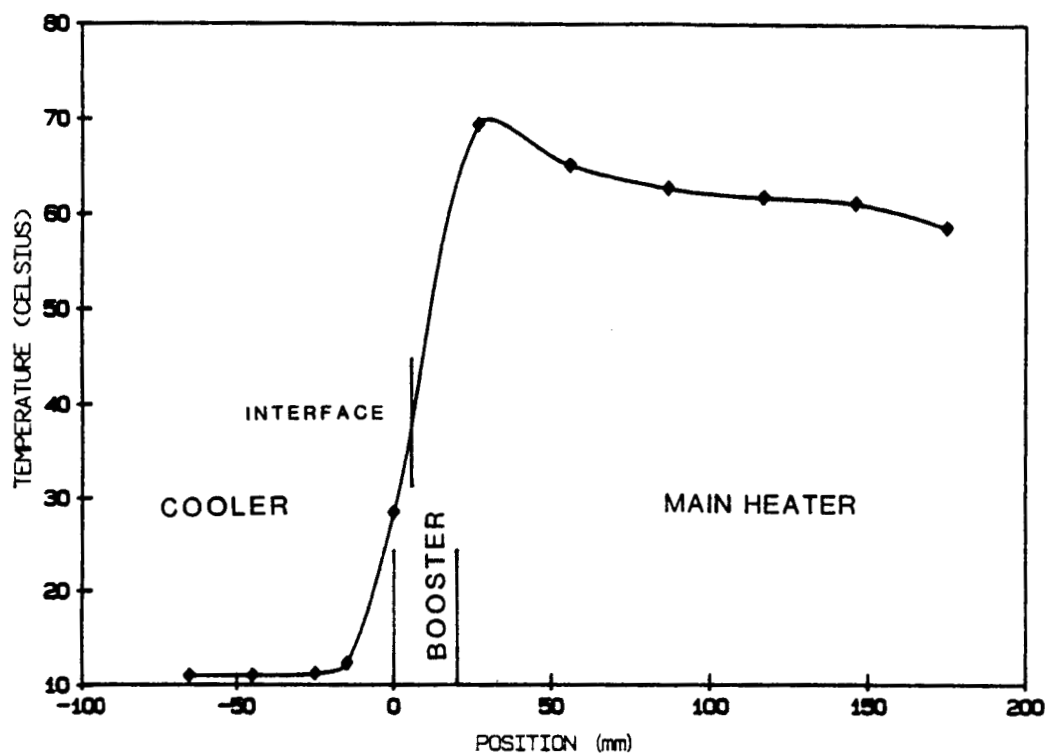


Figure 4.12a. Plot of temperature of the outer wall of the Pyrex sample ampoule vs. vertical position for run II-10. The location of the melt-solid interface was 5.5 mm above the bottom of the booster heater. The temperature of the cooling bath was 9.6 °C.

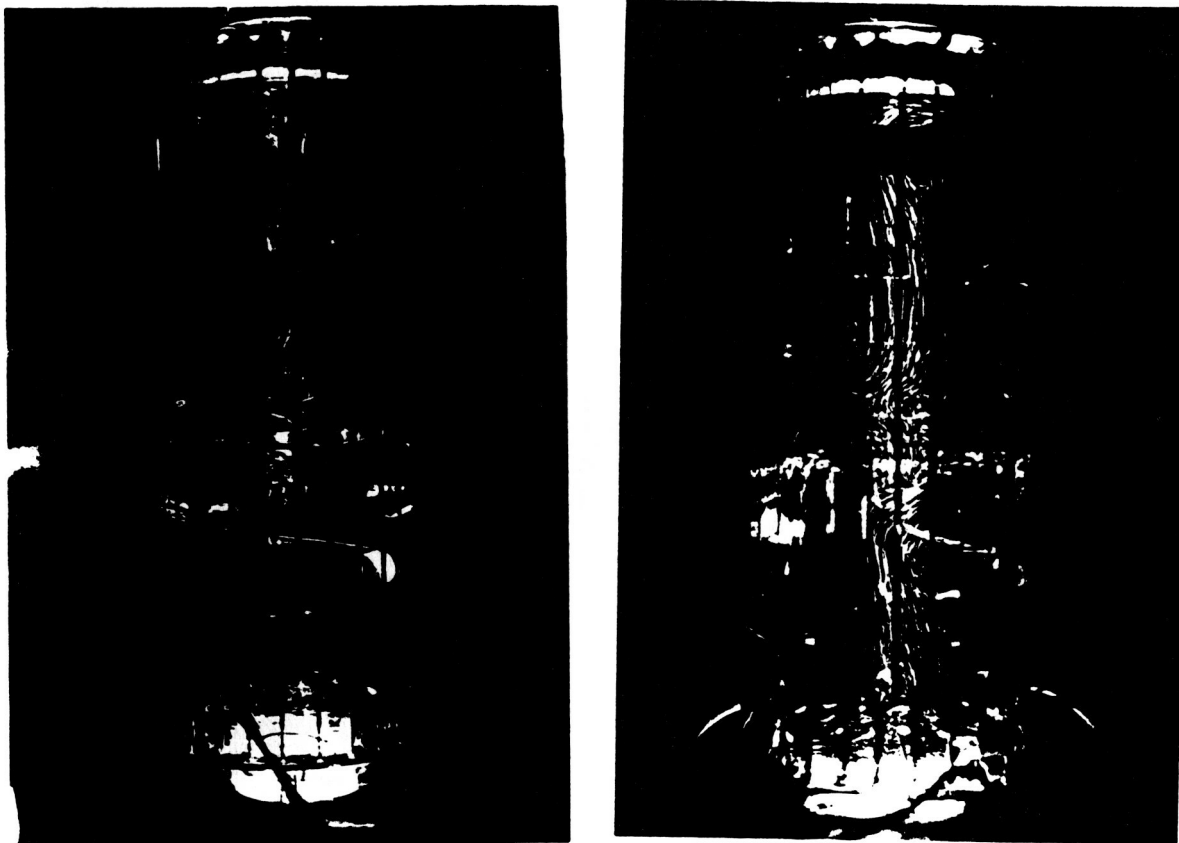


Figure 4.12b. Photographs of the convective velocity field corresponding to the temperature profile of Figure 4.12a. The left and right photographs are 2 second time exposures of the front and side views respectively.

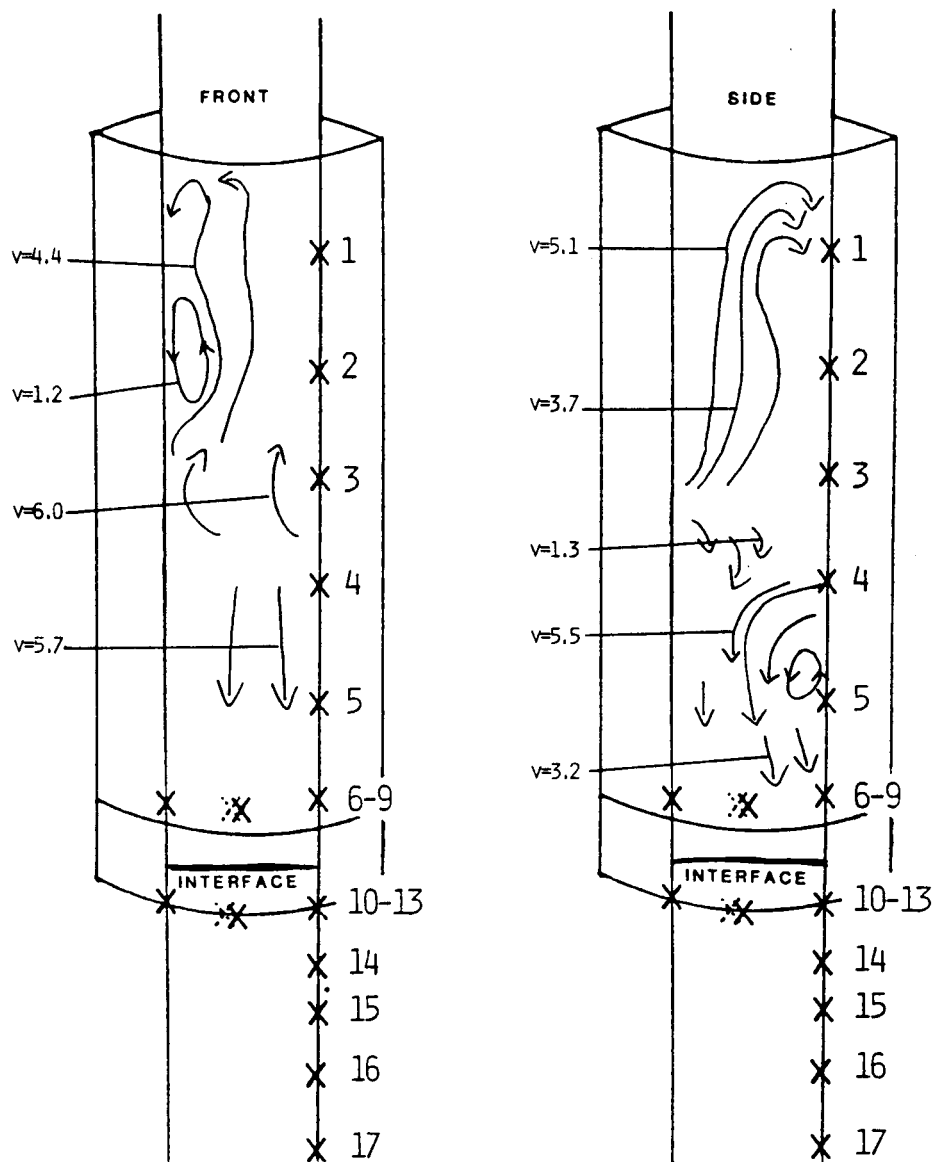


Figure 4.12c. Schematic representation of the convective velocity field shown in Figure 4.12b. Velocities are in mm/s.

TC#	Temp ($^{\circ}\text{C}$)
1	58.5
2	61.1
3	61.7
4	62.6
5	65.1
--	
6	69.4
7	69.2
8	69.5
9	69.6
--	

$\bar{T} = 69.4 \pm 0.2$

TC#	Temp ($^{\circ}\text{C}$)
10	31.3
11	30.1
12	26.2
13	26.2
--	
14	12.3
15	11.2
16	11.0
17	11.0

$\bar{T} = 28.4 \pm 2.6$

bath temp = 9.6

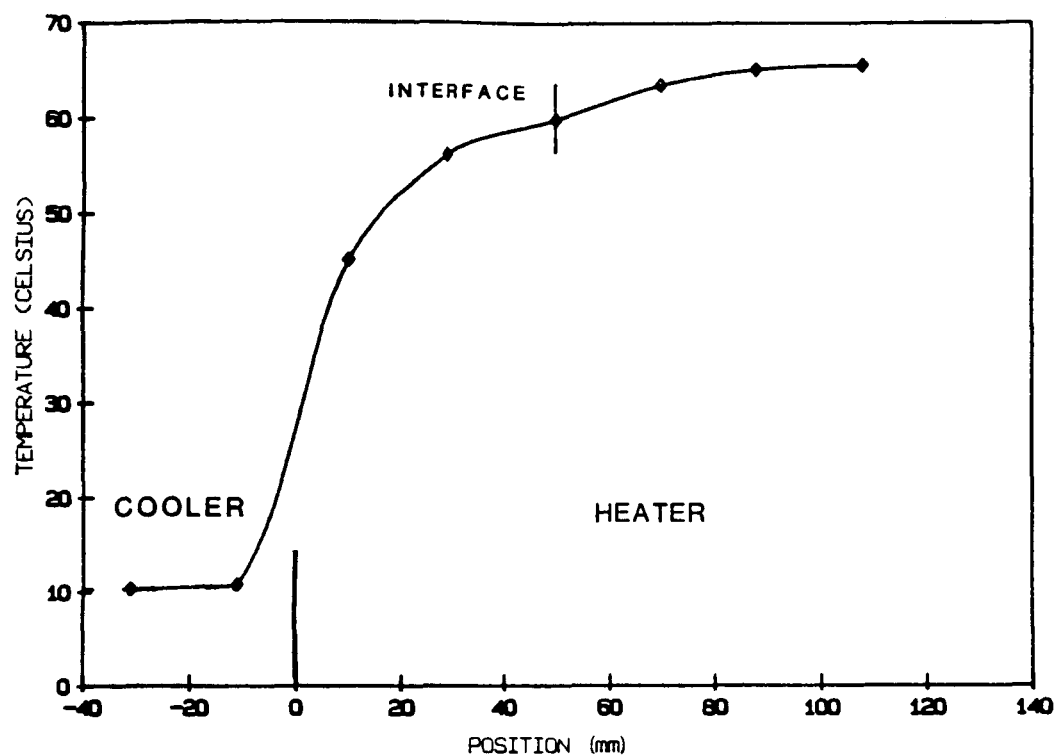


Figure 4.13a. Plot of temperature of the outer wall of the Pyrex sample ampoule vs. vertical position for run II-7A. The location of the melt-solid interface was 50.7 mm above the bottom of the furnace. The temperature of the cooling bath was 10.3 °C.



Figure 4.13b. 16 second time exposure photograph of the convective velocity field corresponding to the temperature profile of Figure 4.13a.

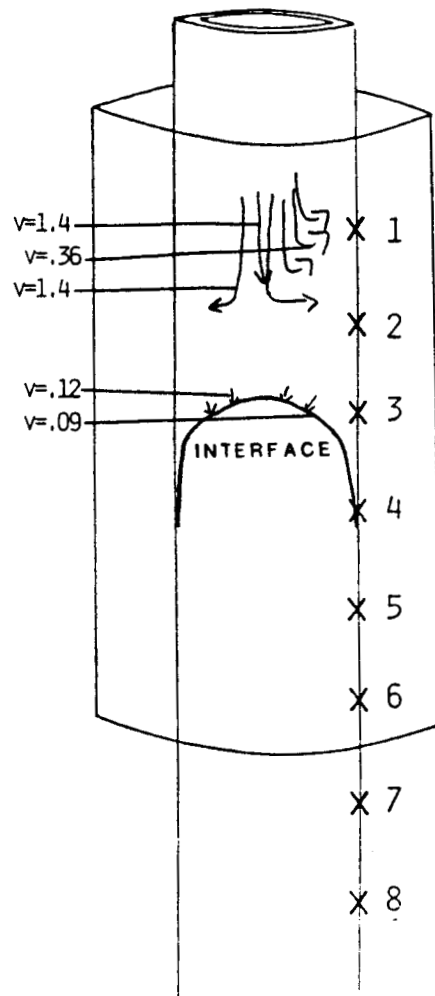


Figure 4.13c. Schematic representation of the convective velocity field shown in Figure 4.13b. Velocities are in mm/s.

TC#	Temp ($^{\circ}$ C)
1	65.5
2	65.1
3	63.5
4	59.8
5	56.1
6	45.1
7	10.8
8	10.3

bath temp = 10.3

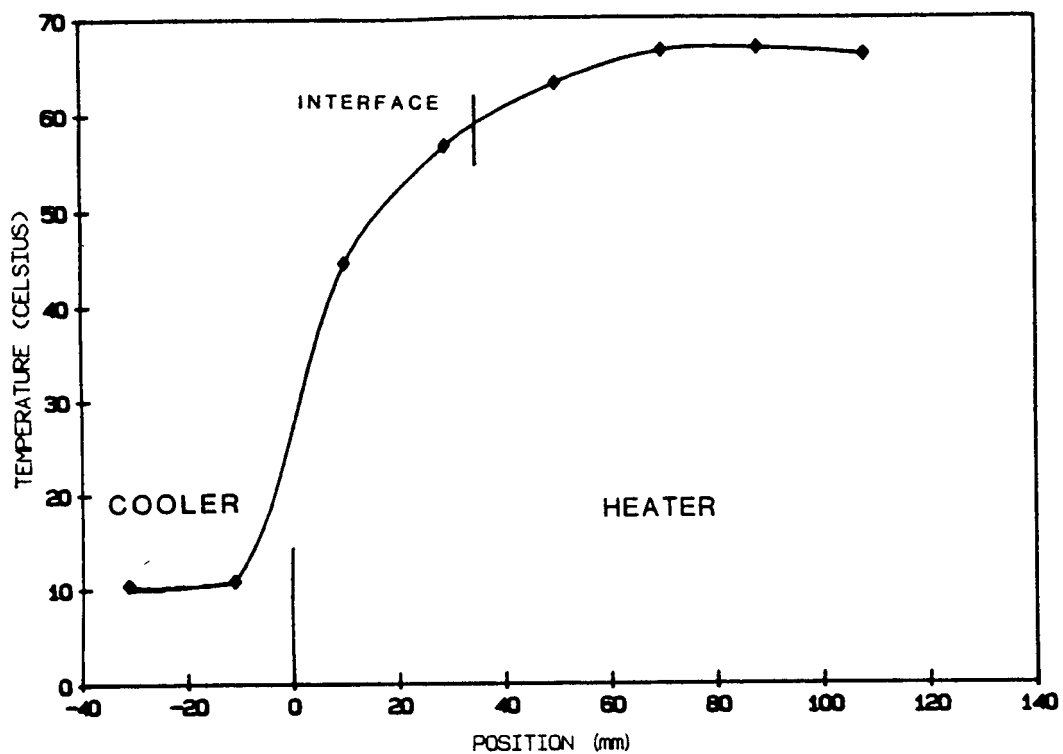


Figure 4.14a. Plot of temperature of the outer wall of the Pyrex sample ampoule vs. vertical position for run II-73. The location of the melt-solid interface was 35.0 mm above the bottom of the furnace. The temperature of the cooling bath was 10.3 °C.



Figure 4.14b. 16 second time exposure photograph of the convective velocity field corresponding to the temperature profile of Figure 4.14a.

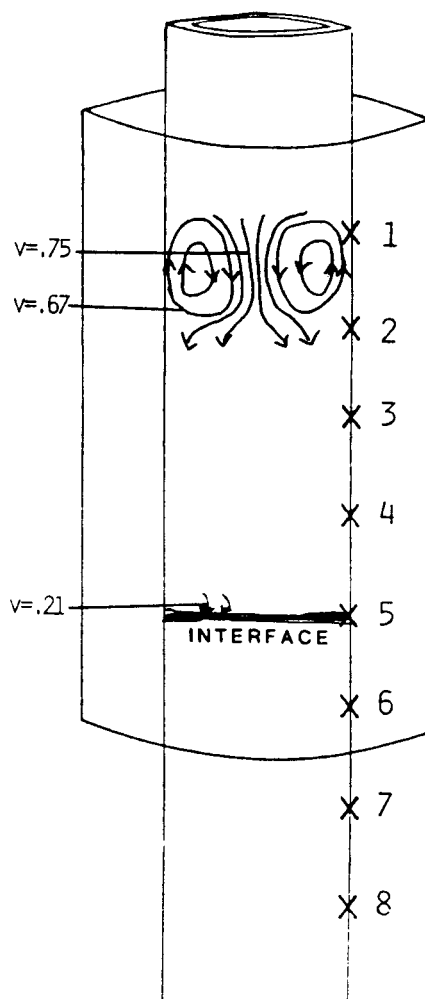


Figure 4.14c. Schematic representation of the convective velocity field shown in Figure 4.14b. Velocities are in mm/s.

TC#	Temp ($^{\circ}$ C)
1	66.1
2	66.8
3	66.5
4	63.1
5	56.6
6	44.5
7	10.8
8	10.4

bath temp = 10.3

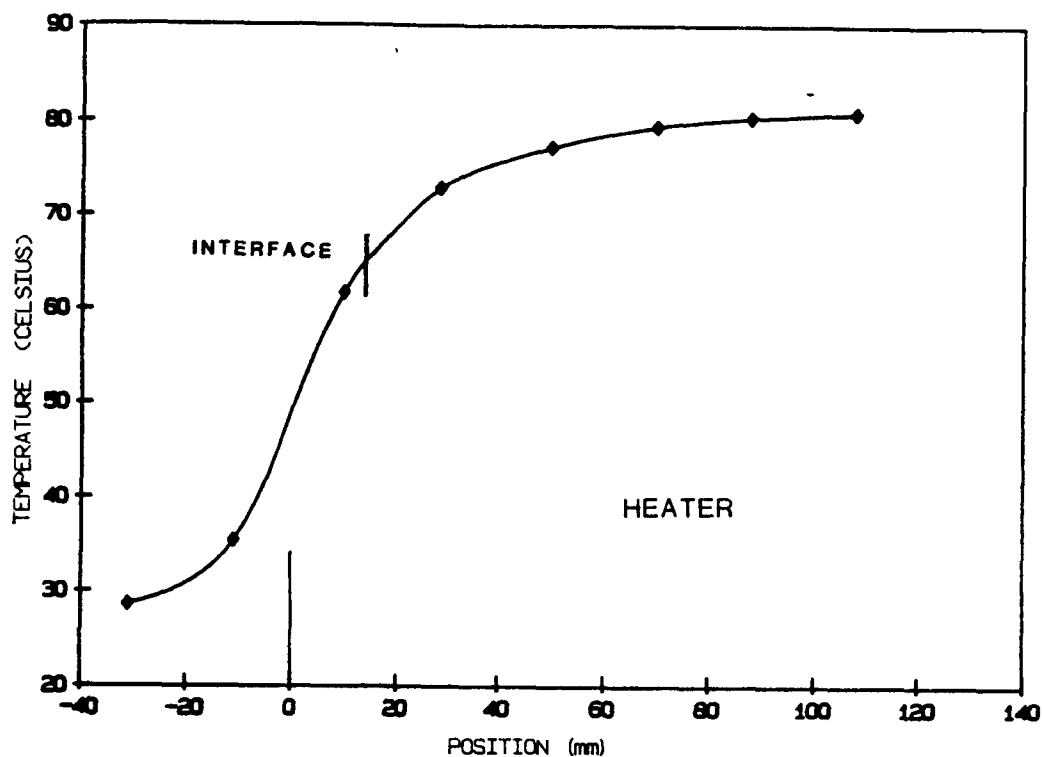


Figure 4.15a. Plot of temperature of the outer wall of the Pyrex sample ampoule vs. vertical position for run II-8. The location of the melt-solid interface was 14.0 mm above the bottom of the furnace. No cooling bath was used. Room temperature was 24.4 °C.

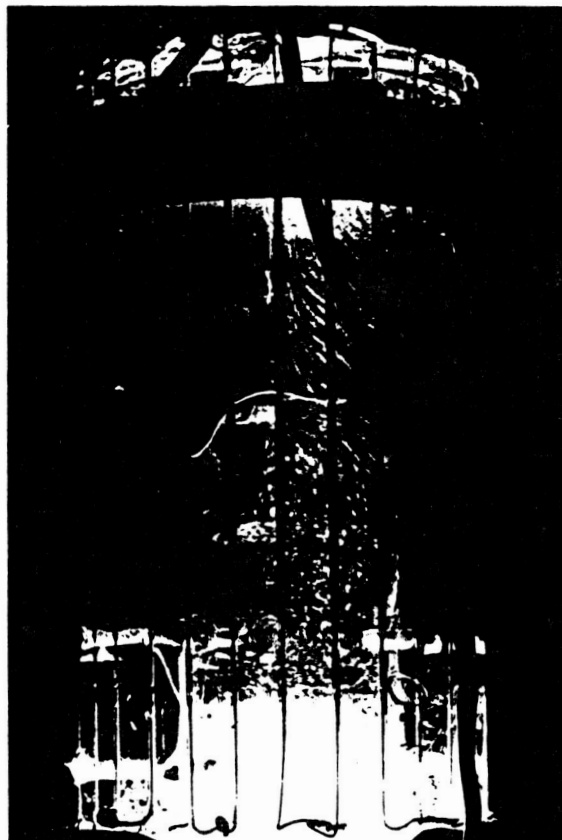


Figure 4.15b. 16 second time exposure photograph of the convective velocity field corresponding to the temperature profile of Figure 4.15

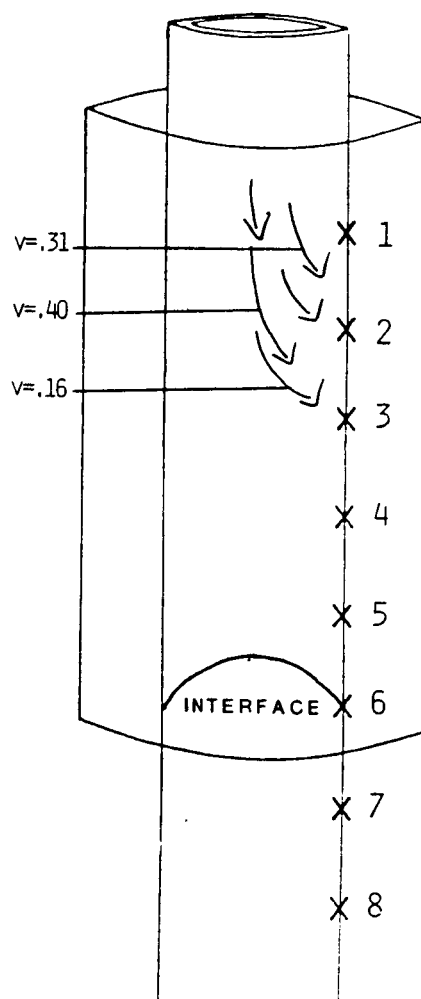


Figure 4.15c. Schematic representation of the convective velocity field shown in Figure 4.15b. Velocities are in mm/s.

<u>TC#</u>	<u>Temp (°C)</u>
1	80.8
2	80.3
3	79.4
4	77.2
5	72.8
6	61.7
7	35.4
8	28.6

no cooling bath
room temp = 24.4

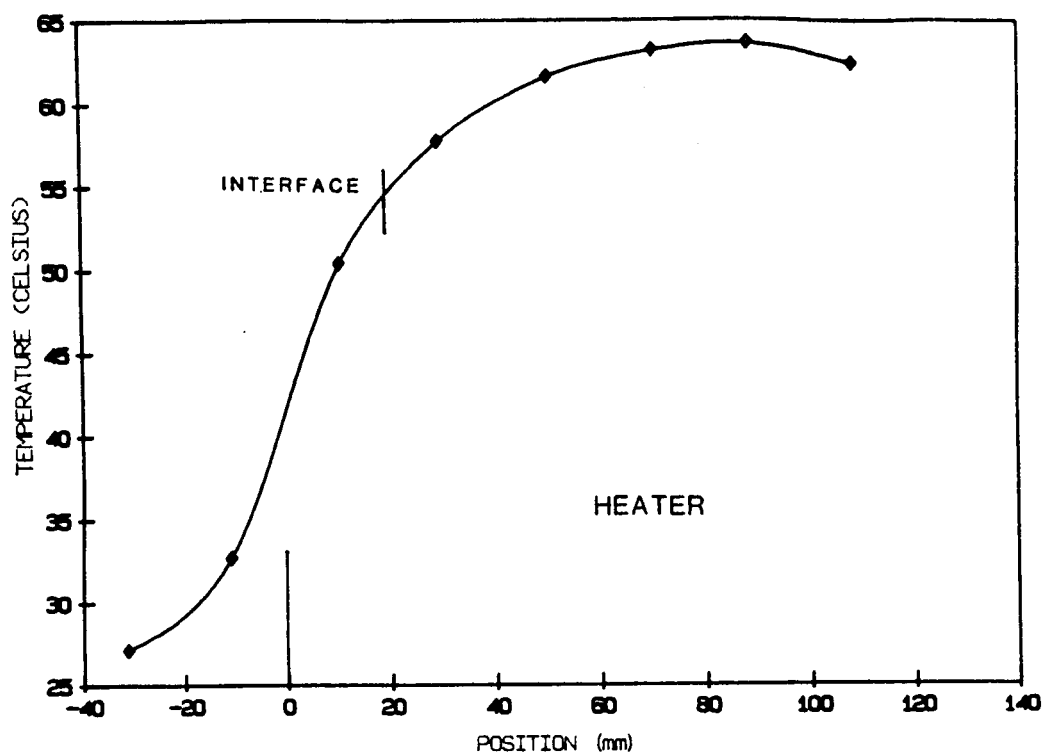


Figure 4.16a. Plot of temperature of the outer wall of the Pyrex sample ampoule vs. vertical position for run II-9. The location of the melt-solid interface was 18.6 mm above the bottom of the furnace. No cooling bath was used. Room temperature was 23.2 °C.

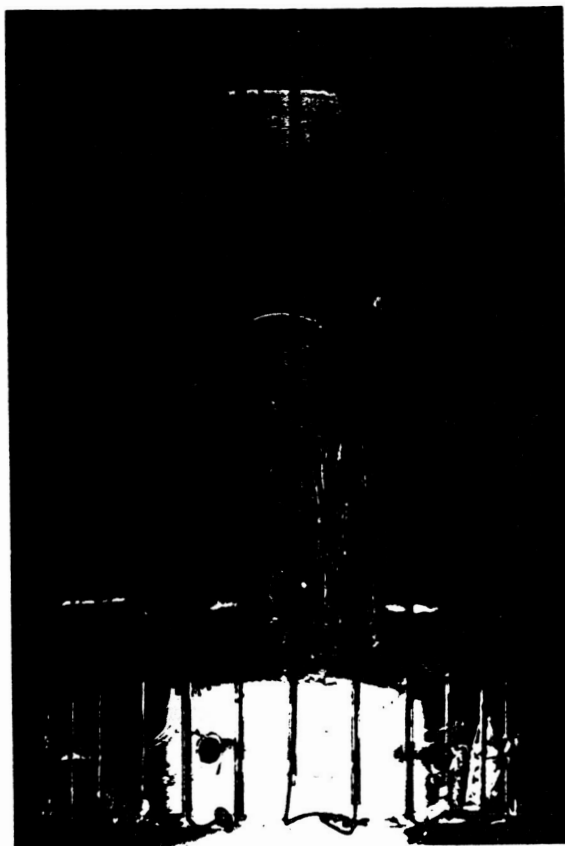


Figure 4.16b. 120 second time exposure photograph of the convective velocity field corresponding to the temperature profile of Figure 4.16a.

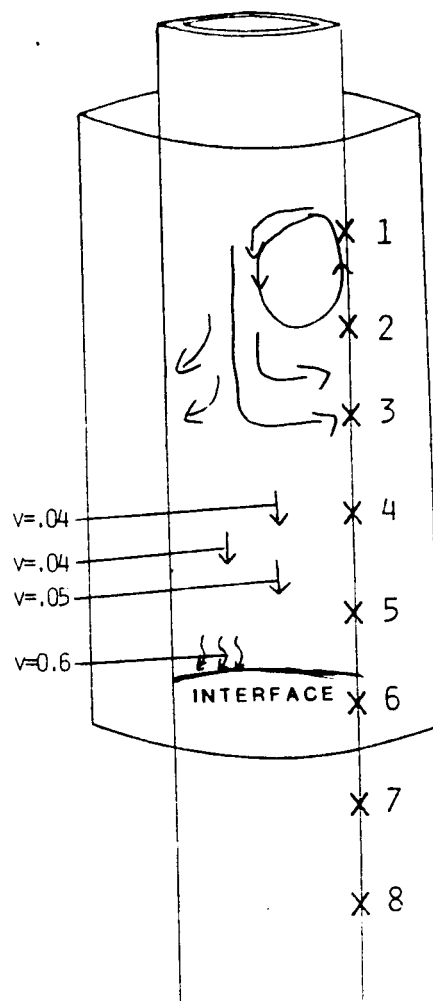


Figure 4.16c. Schematic representation of the convective velocity field shown in Figure 4.16b. Velocities are in mm/s.

TC#	Temp ($^{\circ}$ C)
1	62.4
2	63.6
3	63.2
4	61.6
5	57.7
6	50.4
7	32.7
8	27.1

no cooling bath
room temp = 23.2

Chapter V.

Discussion

Two basic convective flow regimes, characteristic of the temperature profile in the furnace, were observed. A typical convection pattern for the vertically stabilized configuration is shown in Figure 4.2c. The flow field in this figure is divided into two regions. In the upper half of the melt, convective velocities on the order of 1 mm/s were typical. In the lower half of the melt, the suspended sulfur particles moved at a rate of 0.03 to 0.05 mm/s. The movement in the lower half was imperceptible to the eye and could only be visualized with a time exposure photograph at least 30 seconds long. In the vertically destabilized thermal configuration, the flow field was again divided into two regions, upper and lower counter rotational sections. In both the upper and lower areas of the melt, convective velocities were on the order of 1 mm/s.

The long-exposure photographs in Figure 4.2b exemplify the behavior of the convection in the vertically stabilized configuration. When viewed from the front, the flow in the upper portion of the melt consisted of a single circular cell with flow velocities of 1 mm/s being typical. When viewed from the side, the flow bore no relation to the flow observed from the front, although the magnitude of the convective velocities was the same. The temperature versus position figures, 4.1a to 4.16a, show that the temperature of the ampoule at the top of the furnace decreased with height. This destabilizing temperature gradient was probably the major driving force for convection in the upper portion of the melt.

The very slow motion of the sulfur particles in the lower portion of the melt indicated that the convection was nearly nonexistent.

All long exposure photographs of convection in the vertically stabilized configuration showed that the sulfur moved vertically at a rate of 0.03 to 0.05 mm/s in the lower portion of the melt. As noted above, this motion was imperceptible to the eye. The streaks traced by the sulfur particles in this region of the melt are so uniform, both in magnitude and direction, that they probably are an indication of the actual sedimentation velocity of sulfur in an undisturbed melt. Assuming that the sulfur flakes are spheres with an equivalent radius equal to one quarter the maximum flake length, Stoke's law predicts a settling velocity of 0.4 mm/s. The difference between the observed settling velocity and that predicted using Stoke's law merely indicates the difficulty in assigning an equivalent radius to an irregularly shaped flake.

Although the sedimentation of the sulfur was uniformly downward throughout the lower half of the melt, the streaklines show a definite curvature within 1 cm of the interface. This is clearly shown in the long-exposure photographs in Figures 4.1b and 4.2b. Although the streaks are curved, their length, under steady state conditions, correlates with an extremely slow velocity, approximately 0.05 mm/s. Convection this slow near the interface is difficult to resolve photographically due to overexposure of the film.

The second basic flow regime observed in this work was that associated with the thermally destabilized profile created by the booster heater. The major features of this type of flow are summarized in Figure 4.5c. The flow in this figure is divided into two regions. In the lower region the flow rises at the wall and

descends in the center, and in the upper region the flow descends at the wall and rises in the center. As in the destabilized configuration, the flow is complex and usually can't be characterized solely on the basis of one view. The two exceptions are the results shown in Figures 4.6 and 4.7. In these runs, convection was so symmetrical that both views, front and side, presented the same flow field.

Even though the flow patterns in Figures 4.6 and 4.7 are highly symmetrical, a measureable azimuthal thermal asymmetry nevertheless existed in the heater. The question this raises is, how large a thermal asymmetry is necessary to destroy the symmetrical character of the flow? A comparison of Figure 4.4c and Figure 4.7c indicates that very little thermal asymmetry is necessary to completely destroy the symmetrical behavior of the flow.

The azimuthal temperature variation was characterized by the standard deviation of the temperatures measured by the circumferentially mounted thermocouples. The difference in the standard deviation of the temperatures indicated by thermocouples 4 to 7 between Figures 4.4c and 4.7c is only 0.1°C . (Thermocouple 6 failed to operate; therefore the standard deviation of these temperature measurements has only two degrees of freedom.) The standard deviations of the temperatures read by thermocouples 8 to 11 are the same in Figures 4.4c and 4.7c. Even though the magnitude of the azimuthal temperature variations is nearly the same in these two runs (I-52 and I-55), there are great differences in the apparent symmetry of the flow. Since temperature was measured at the outer wall of a 4 mm thick Pyrex ampoule, the measured thermal asymmetry was probably greater than that felt by the melt, because the ampoule

should have dampened out thermal asymmetry by conduction. In any case, no clear boundary emerged from this work about the minimum thermal asymmetry which will produce asymmetrical convection, although it is probably small, on the order of 1 °C as measured at the outer wall of the thick-walled ampoule. No attempt was made to measure the thermal asymmetry at the inner wall of the ampoule.

In the run pictured in Figure 4.8 a thermal asymmetry of several degrees was created. In agreement with the work of Potts (2), the melt rose along the hot portion of the ampoule and descended along the cooler side.

Figures 4.1a to 4.16a are plots of the temperature of the outer wall of the sample ampoule versus vertical position. The location of the melt/solid interface was calculated from the photographs and is noted in these figures. From these plots, the temperature of the outer wall of the ampoule at the point where the interface intersects the inner wall could be read directly. Were there no temperature difference across the ampoule, the temperature at the outer wall would be equal to the melting point of the sample material. As shown in Table 5.1, there was often a significant difference between the outer wall temperature adjacent to the interface and the melting point of the sample material. The melting point of a fresh sample of phenyl salicylate, the sample material of Figures 4.1 to 4.12, was 43.0 to 43.5 °C. The melting point of the phenyl salicylate used in the convective studies which had been in the molten state for over a month was 41.0 to 43.0 °C. Degradation of this organic compound was therefore minimal. The melting point of a distilled sample of benzophenone, the sample material of Figures 4.13 to 4.16, was 49.0 to 49.5 °C. The melting point of the material used in convection studies

which had been molten for a few weeks was 47.9 to 49.3 °C. Again, degradation was minimal.

An interesting feature about the outer wall temperature adjacent to the interface is that no wall temperature was significantly less than the observed experimental melting point, but several were at least 10 °C larger. The latter resulted from the transient experiments used to produce a curved interface. Figure 4.6a is for steady-state conditions, yielding an outer wall temperature 13.7 °C over the experimental melting point range. Significant deviations are noted in Figures 4.5a, 4.7a, and 4.8a as well. These figures correspond to the destabilized configuration, with convection throughout the entire melt.

Table 5.1. The outer wall temperature adjacent to the melt/solid interface and the melting point of the melt sample as measured experimentally in a Mettler capillary melting point apparatus.

<u>Figure</u>	<u>Wall Temp. (°C)</u>	<u>Experimental m. p. (°C)</u>
4.1a	39.4	43.2
4.2a	38.6	"
4.3a	41.0	"
4.4a	42.0	"
4.5a	45.2	"
4.6a	56.7	"
4.7a	51.7	"
4.8a	45.7	"
4.9a	44.3	"
4.10a	43.8	"
4.11a	41.2	"
4.12a	38.2	43.2
4.13a	60.0	49.2
4.14a	58.6	"
4.15a	65.0	"
4.16a	54.2	49.2

These data suggest that the temperature difference across the ampoule is often large. Under conditions in which mixing of the melt is significant, the effective Biot number on the melt side of the tube is increased due to the increased convective heat transfer within the melt. When convective mixing is large, the relatively cool fluid from the upper regions of the furnace descends through the center of the melt and rises along the walls of the ampoule. This cools the inner wall, and when convective mixing is large, this cooling is apparently significant.

Convective mixing is large under the conditions of Figures 4.10 to 4.12 but a significant temperature difference across the ampoule near the interface is not observed. This can be explained in terms of the temperature versus position curves of Figures 4.10a to 4.12a. These figures show that a booster-generated temperature maximum exists in the melt. These figures also show that the melt/solid interface is located well beneath the temperature maximum in the furnace. Interestingly, the temperature difference becomes progressively lower as the interface moves farther from the temperature maximum and closer to the cooler. If the interface were actually in the cooler, one would expect that the inner wall temperature would exceed that of the outer (4). In fact, this effect is seen in the first three entries in Table 5.1.

If this type of apparatus is used to grow crystals from melts containing impurities, constitutional supercooling might be difficult to avoid without the use of a booster heater to maintain a steep axial temperature gradient at the interface. This is an important design consideration if direct loss of heat from the heater to the cooler is a problem. For example, if one tries to increase the temperature

gradient at the interface by lowering the temperature of the cooler, a steep axial temperature gradient will be difficult to maintain if the temperature of the heater has been correspondingly reduced. If a booster heater is not used, the heater should be well insulated from the cooler to avoid direct heat loss.

To see if a steady-state planar interface precluded convection near the interface, observations were done under transient conditions when the interface was highly convex. Presumably when the interface is very curved, a large radial temperature gradient is present. However, no convective velocities over 0.1 mm/s were found near a convex interface. The same extremely weak convection as observed in Figures 4.1b and 4.2b (runs with a stabilizing temperature gradient and planar interface) was observed. Significant convection was always observed near the top of the melt. This most likely was produced by the destabilizing temperature gradient at the top of the ampoule. When a destabilizing temperature gradient near the interface was created with a booster heater, convection existed near the top of the ampoule, but in these cases the origin of the upper convective cell is probably a complex function of power to the booster and cooling from the top of the ampoule.

Benzophenone and salol were effective model melt systems as both were stable at their melting point for weeks. The major conclusions pertaining to the Bridgman-Stockbarger technique are summarized below.

Conclusions:

A. Vertically stabilized thermal configuration.

1. Convection was absent from the melt within one ampoule

diameter of the interface.

2. Significant convection existed in the upper portion of the melt. This was produced by the destabilizing temperature gradient near the top of the ampoule.

3. Negligible convection was observed in the lower portion of the melt even when the melt/solid interface was highly convex.

4. Many of the long-exposure photographs indicated that extremely weak convection was present adjacent to the melt/solid interface in the vertically stabilized configuration.

B. Vertically destabilized thermal configuration.

1. A short booster heater inserted between the main heater and cooler could generate significant convection throughout the entire melt.

2. A highly symmetrical azimuthal temperature profile was required to produce symmetrical convection.

3. Convection in the melt was nearly always asymmetrical as the requisite thermal profile for symmetrical convection could not often be produced.

Were additional work to be done in this area, a few modifications are in order. In a real crystal growth system the ampoule must translate through the furnace. For this reason the heater can not be physically connected to the ampoule, but must heat the ampoule by radiation and by convection and by conduction through a fluid.

Secondly, the destabilizing temperature gradient near the top of the melt was a consequence of furnace design. In future work, it may be desirable to avoid this by adding an additional booster heater near the top of the main heater, by using a longer heater, or by using a heater with closer coils as one moves upward.

Finally, in order to accurately characterize the temperature profile of the furnace, it is important to place the thermocouples sufficiently close together. Figure 4.4a on page 65 shows that a temperature maximum exists above the booster in the main heater even though power to the main heater was turned off. Most likely, had more thermocouples been positioned near the top of the booster, a temperature maximum would have been found there. This would have been more consistent with the temperature vs. position curves in Figures 4.5a, 4.7a, 4.10a, 4.11a, and 4.12a.

References

1. D. C. Stockbarger, Rev. Sci. Instr., 7, 133-136 (1939).
2. H. Potts, M.S. Thesis, Clarkson University, Potsdam, NY. (1984).
3. A. A. Chernov, Modern Crystallography III, Springer-Verlag, New York, 429 (1984).
4. C. E. Chang and W. R. Wilcox, J. Crystal Growth, 21, 134-140 (1974).
5. T. Fu and W. R. Wilcox, J. Crystal Growth, 48, 416-424 (1980).
6. C. J. Chang and R. A. Brown, J. Crystal Growth, 63, 343-364 (1983).
7. S. Sen and W. R. Wilcox, J. Crystal Growth, 28, 36-40 (1975).
8. R. J. Naumann, J. Crystal Growth, 58, 569-584 (1982).
9. R.J. Naumann and S. L. Lehoczky, J. Crystal Growth, 61, 707-710 (1983).
10. P. C. Sukanek, J. Crystal Growth, 58, 208-218 (1982).
11. P. C. Sukanek, J. Crystal Growth, 58, 219-228 (1982).
12. F. R. Szofran, D. Chandra, J.-C. Wang, E. K. Cothran, and S. L. Lehoczky, J. Crystal Growth, 70, 343-348 (1984).
13. J. C. Clayton, M. C. Davidson, D. C. Gillies, and S. L. Lehoczky, J. Crystal Growth, 60, 374 (1982).
14. V. G. Smith, W. A. Tillier, and J. W. Rutter, Can. J. Phys., 33, 723 (1955).
15. R. K. Route, M. Wolf, and R. S. Feigelson, J. Crystal Growth, 70, 379-385 (1984).
16. E. Cothran, An Analytical Approach To Thermal Modeling Of Bridgman-Type Crystal Growth: One-Dimensional Analysis., NASA TM-82487 (1982).
17. R. J. Naumann, J. Crystal Growth, 58, 554-568 (1982).
18. L. C. Tien, Ph. D Thesis, University of Michigan, Ann Arbor, Michigan (1968).
19. L. C. Tien and J. O. Wilkes, J. Heat Transfer, 1, 1-11 (1970).
20. F. M. Carlson, A. L. Fripp, and R. K. Crouch, J. Crystal Growth, 68, 747-756 (1984).

21. R. C. Weast, Ed., CRC Handbook of Chemistry and Physics, 60th Edition, CRC Press, Boca Raton, FL. (1980).
22. R. H. Perry and C. H. Chilton, Eds., Chemical Engineers Handbook, McGraw-Hill Book Company, New York (1973).
23. R. P. Rastogi, R. K. Nigam, R. N. Sharma, and H. L. Girdhar, J. Chem. Phys., 39, 3042-3044 (1963).
24. C. G. De Kruif, J. C. van Miltenburg, and J. G. Blok, J. Chem. Thermodynamics, 15, 129-136 (1983).
25. Von Rolf Wustner, Forsch. Ing.-Wes., 44, 37-41 (1978).
26. D. Van Velzen, Ind. Eng. Chem. Fundam., 11, 20-25 (1972).
27. S. M. Omenyi, Ph.D. Thesis, University of Toronto (1978).
28. R. B. Badachhape, M. K. Gharpurey, and A. B. Biswas, J. Chem. Eng. Data, 10, 143-145 (1965).
29. J. A. De Leeuw Den Bouter and P. M. Heertjes, J. Crystal Growth, 5, 19-25 (1969).
30. J. H. Lienhard, A Heat Transfer Textbook, Prentice-Hall, Inc., Englewood Cliffs, New Jersey (1981).

Nomenclature

a	Thermal diffusivity, m^2/s
A	Aspect ratio, L/D
B	Coefficient of thermal expansion, K^{-1}
Bi	Biot number, hR/k
C_p	Heat capacity, J/Kg.K
f	kinematic viscosity, m^2/s
g	Gravitational acceleration, m/s^2
Gr	Grashof number, $R^3 gB(T_h - T_c)/f^2$
h	Convective heat transfer coefficient, $\text{J/m}^2.\text{K.s}$
k	Thermal conductivity, J/m.K.s
Pe	Peclet number, $Pe = LV/a$
Pr	Prandtl number, $uC_p/k = f/a$
R	Ampoule's inner radius, m
Ra	Rayleigh number, $R^3 gB(T_h - T_c)/fa$
T	Temperature, K
T_c	Cooler temperature, K
T_h	Heater temperature, K
u	Dynamic viscosity, Kg/m.s
V	Velocity, m/s
x	Mole fraction
Z/R	Dimensionless axial position

APPENDIX D
A QUASI-ANALYTICAL SOLUTION TO THE STEADY STATE BRIDGMAN-STOCKBARGER MODEL

R. Balart, T. S. Papatheodorou and I. G. Saridakis

1. INTRODUCTION

Mathematical models for the Bridgman-Stockbarger technique have been used for the determination of the temperature fields and the shape and position of the solid/melt interface by several investigators. For a brief (and by no means exhaustive) review of recent progress, we begin by mentioning the work of Chang and Wilcox [1], who were apparently the first to use analytical methods to study the influence of various parameters on the interface shape and position. From a number of simplifying assumptions that they made, the ones that are of interest to us here are that they neglected the tube wall region. For the remaining two regions (solid and melt), they assumed equal thermal conductivities. Mathematically speaking, as it follows from our analysis, this amounts to having only one (cylindrical) region. They used the analytic solution obtained for this case by Chang [2]. Earlier, Tien [3] developed numerical techniques that used values of the temperature on the wall, measured experimentally. Some limitations of Tien's computer program are pointed out in [1]. Fu and Wilcox [4,5] also investigated Bridgman-Stockbarger growth numerically using a finite difference scheme for the same assumptions of two regions and equal conductivities. Naumann [6] and Jasinski [7] obtained analytical solutions for their respective one dimensional models, and both give a comparative study of their models in [8].

In this report we present a semi-analytical method for solving the steady state problem for the Bridgman-Stockbarger technique, in the absence of gravity, for three regions (melt, solid and glass tube walls) with different thermal conductivities. Our technique is based on an extension to three regions of a method suggested to us by Ablowitz, Kruskal and Segur [9]. More specifically,

we consider the three regions D_M , D_S , and D_G (cf. Figure 1) with thermal conductivities k_1 , k_2 , k_3 respectively and we determine all temperature fields in terms of one sequence of free parameters. Next, this sequence is determined by iterating between the solution of a (small) symmetric system of linear equations and the parameter z_0 , which is the point where the interface meets the interior wall of the ampoule. Our computational experiments have shown that only a small number of iterations are needed to obtain the values of the free parameters and the value of z_0 within about 10^{-6} accuracy. The computer implementation of our method gives sufficiently accurate results in the very short time of about 20-25 seconds (including execution and output time), even though our program is not time and space optimal at this stage.

Using the method presented here, we run a number of computer experiments for different values of operating parameters. Thus, we were able to draw some preliminary conclusions about the influence of these parameters on the position and shape of the interface. These are reported in Section 4. A further investigation is under way in order to understand which parameters must be adjusted (and how they must be adjusted) in order to get a desired interface shape and position, and also to determine how sensitive the system is to small variations in the values of these parameters.

2. MATHEMATICAL MODEL FOR THE BRIDGMAN-STOCKBARGER TECHNIQUE AND ITS SOLUTION

Using appropriate definitions for the physical constants involved, the differential equation for the temperature field in all three regions (Figure 1) is:

$$\frac{\partial^2 T_x}{\partial r^2} + \frac{1}{r} \frac{\partial T_x}{\partial r} + \frac{\partial^2 T_x}{\partial z^2} = 0 \quad (r, z) \in D_x \quad (1)$$

where $x = M, S$ or G (melt, solid, glass). The conditions on the melt/solid interface are:

$$k_1 \nabla T_M = k_2 \nabla T_S \quad (2)$$

$$T_M = T_S \quad (3)$$

while the conditions on the interior $r = \rho$ of the ampoule wall are:

$$T_M = T_G, \quad k_1 \frac{\partial T_M}{\partial r} = k_3 \frac{\partial T_G}{\partial r}, \quad z \geq z_0, \quad (4)$$

$$T_S = T_G, \quad k_2 \frac{\partial T_S}{\partial r} = k_3 \frac{\partial T_G}{\partial r}, \quad z \leq z_0, \quad (5)$$

where (ρ, z_0) is the unknown point on which the melt/solid interface $T = T_f$ meets the wall.

The boundary conditions depend on the case under consideration. For demonstration we use:

$$T_M = T_G = T_H \quad \text{for } z = \ell \quad (6)$$

$$T_S = T_G = T_C \quad \text{for } z = 0. \quad (7)$$

For the exterior of the wall ($\rho = R$) we use the general condition

$$T_G(R, z) = g(z), \quad (8)$$

where g is any well behaved (at least piecewise continuous) function.

Extensions to other conditions, such as $h(T_{\text{wall}} - T_a) = -k(\frac{\partial T}{\partial r})_{\text{wall}}$,

where T_a is the ambient furnace temperature, are also possible. Moreover, using cylindrical symmetry, we also have the condition:

$$\frac{\partial T_x}{\partial r}(0, z) = 0 \quad x = M \text{ or } S. \quad (9)$$

Upon subtracting out T_f and using, for simplicity, the same symbols, we have exactly the same equations and conditions, except that now the melt/solid interface is represented by the isotherm:

$$T_M = T_S = 0. \quad (10)$$

Thus, for the new values we have:

$$T_H > 0, \quad T_C < 0. \quad (11)$$

Now set

$$F(r, z) := \begin{cases} \frac{1}{k_2} T_1(r, z) & (r, z) \in D_M \\ \frac{1}{k_1} T_2(r, z) & (r, z) \in D_S \end{cases} \quad (12)$$

then F satisfies the differential equation (1) and the following conditions in place of (2)-(9)

$$\frac{\partial F}{\partial r} = 0 \quad \text{on } r = 0 \quad (13)$$

$$F = \frac{1}{k_2} T_H \text{ on } z = \ell, \quad F = \frac{1}{k_1} T_C \text{ on } z = 0 \quad (14)$$

$$k_1 k_2 \frac{\partial F}{\partial r} = k_3 \frac{\partial G}{\partial r} \quad \text{on } r = \rho \quad (15)$$

$$k_1 F = G \quad \text{on } r = \rho, \quad z \geq z_0 \quad (16)$$

$$k_2 F = G \quad \text{on } r = \rho, \quad z \leq z_0 \quad (17)$$

$$G = g \quad \text{on } r = R. \quad (18)$$

The conditions (4)-(5) on the melt/solid interface are automatically

satisfied. Therefore, one needs to solve for F on the rectangular region $D = D_M \cup D_S$ and then, determine the melt/solid interface as the curve for which, by (10):

$$F = 0. \quad (19)$$

The transformed problem can be solved by separation of variables. The formulae

$$F(r,z) = \tilde{L}(z) + \sum_{n=1}^{\infty} F_n I_0\left(\frac{n\pi}{\ell} r\right) \sin\left(\frac{n\pi}{\ell} z\right), \quad (20)$$

$$G(r,z) = L(z) + \sum_{n=1}^{\infty} [A_n I_0\left(\frac{n\pi}{\ell} r\right) + B_n K_0\left(\frac{n\pi}{\ell} r\right)] \sin\left(\frac{n\pi}{\ell} z\right),$$

where

$$\begin{aligned} L(z) &= T_H \frac{z}{\ell} + T_C \frac{\ell-z}{\ell} \\ \tilde{L}(z) &= \frac{T_H}{k_2} \frac{z}{\ell} + \frac{T_C}{k_1} \frac{\ell-z}{\ell} \end{aligned} \quad (21)$$

give the general solution to the problem, and satisfy all the conditions except (15), (16), (17), (18) and (19).

Conditions (15) and (18) determine all the sequences of coefficients in (20) in terms of just one unknown sequence, F_n . More specifically, if we write

$$\begin{aligned} g(z) &= L(z) + (g(z)-L(z)) \\ g(z)-L(z) &= \sum_{n=1}^{\infty} \gamma_n \sin\left(\frac{n\pi}{\ell} z\right) \end{aligned} \quad (22)$$

and apply (18), we immediately get

$$I_0(q_n) A_n + K_0(q_n) B_n = \gamma_n \quad (23)$$

where $q_n = \frac{n\pi}{\ell} R$.

Next, application of (15) gives

$$I_1(p_n)A_n - K_1(p_n)B_n = \frac{k_1 k_2}{k_3} I_1(p_n)F_n, \quad (24)$$

where

$$p_n = \frac{n\pi}{\ell} \rho.$$

The system of (23), (24) is easily solved: Denoting the negative determinant of the 2×2 coefficient matrix above by d_n , i.e.,

$$d_n = I_0(q_n)K_1(p_n) + I_1(p_n)K_0(q_n) \quad (25)$$

we obtain

$$\begin{bmatrix} A_n \\ B_n \end{bmatrix} = \frac{1}{d_n} \begin{bmatrix} K_1(p_n)\gamma_n + K_0(q_n) \frac{k_1 k_2}{k_3} I_1(p_n)F_n \\ I_1(p_n)\gamma_n - I_0(q_n) \frac{k_1 k_2}{k_3} I_1(p_n)F_n \end{bmatrix}, \quad (26)$$

which gives an expression for A_n and B_n in terms of a sequence of the known constants γ_n , and a sequence of unknown constants F_n . Substituting into the expression (20) we obtain, for G ,

$$\begin{aligned} G(r, z) = L(z) + \sum_{n=1}^{\infty} \frac{1}{d_n} \{ K_1(p_n)I_0\left(\frac{n\pi}{\ell} r\right) + I_1(p_n)K_0\left(\frac{n\pi}{\ell} r\right) \} \gamma_n \sin\left(\frac{n\pi}{\ell} z\right) \\ + \sum_{n=1}^{\infty} \frac{k_1 k_2}{k_3} \frac{I_1(p_n)}{d_n} \{ K_0(q_n)I_0\left(\frac{n\pi}{\ell} r\right) - I_0(q_n)K_0\left(\frac{n\pi}{\ell} r\right) \} F_n \sin\left(\frac{n\pi}{\ell} z\right). \end{aligned} \quad (27)$$

Now evaluate G at $r = \rho$, and notice that

$$K_1(p_n)I_0(p_n) + I_1(p_n)K_0(p_n) \equiv W\{K_0(p_n), I_0(p_n)\} = \frac{1}{p_n} = \frac{\ell}{n\pi\rho} \quad (28)$$

to get from (27) that

$$G(\rho, z) = L(z) + \sum_{n=1}^{\infty} \delta_n \sin\left(\frac{n\pi}{\ell} z\right) + \frac{k_1 k_2}{k_3} \sum_{n=1}^{\infty} C_n F_n \sin\left(\frac{n\pi}{\ell} z\right), \quad (29)$$

where

$$\delta_n := \frac{\ell}{n\rho} \frac{\gamma_n}{nd_n} \quad (30)$$

and

$$c_n := \frac{I_1(p_n)}{d_n} \{I_0(p_n)K_0(q_n) - I_0(q_n)K_0(p_n)\}. \quad (31)$$

Also for $i = 1, 2$, we find from (20) that

$$k_i F(\rho, z) = k_i \tilde{L}(z) + k_i \sum_{n=1}^{\infty} I_0(p_n) F_n \sin\left(\frac{n\pi}{\ell} z\right). \quad (32)$$

Then for $z \geq z_0$, condition (17) gives

$$\sum_{n=1}^{\infty} [I_0(p_n) - \frac{k_1}{k_3} c_n] F_n \sin\left(\frac{n\pi}{\ell} z\right) = \frac{k_1 - k_2}{k_1 k_2} T_c \frac{\ell - z}{\ell} + \frac{1}{k_2} \sum_{n=1}^{\infty} \delta_n \sin\left(\frac{n\pi}{\ell} z\right). \quad (33)$$

Similarly, for $z \leq z_0$, condition (16) gives

$$\sum_{n=1}^{\infty} [I_0(p_n) - \frac{k_2}{k_3} c_n] F_n [-\sin\left(\frac{n\pi}{\ell} z\right)] = \frac{k_1 - k_2}{k_1 k_2} T_H \frac{z}{\ell} - \frac{1}{k_1} \sum_{n=1}^{\infty} \delta_n \sin\left(\frac{n\pi}{\ell} z\right). \quad (34)$$

If we multiply (33) by k_1 and (34) by k_2 , and we rearrange (34), we obtain:

$$\begin{aligned} \sum_{n=1}^{\infty} [k_1 I_0(p_n) - \frac{k_1 k_2}{k_3} c_n] F_n \sin\left(\frac{n\pi}{\ell} z\right) &= (k_1 - k_2) \frac{T_c}{k_1} \frac{\ell - z}{\ell} \\ &+ \sum_{n=1}^{\infty} \delta_n \sin\left(\frac{n\pi}{\ell} z\right), \quad z \geq z_0 \end{aligned} \quad (35)$$

$$\begin{aligned} \sum_{n=1}^{\infty} [k_1 I_0(p_n) - \frac{k_1 k_2}{k_3} c_n] F_n \sin\left(\frac{n\pi}{\ell} z\right) &= (k_2 - k_1) \frac{T_H}{k_2} \frac{z}{\ell} \\ &+ \sum_{n=1}^{\infty} \delta_n \sin\left(\frac{n\pi}{\ell} z\right), \quad z \leq z_0. \end{aligned} \quad (36)$$

In (35)-(36) the unknowns are F_n , $n = 1, 2, \dots$, and z_0 .

Now consider the function $\psi(z)$ defined as follows:

$$\psi(z) := \begin{cases} k_2 F(\rho, z) - G(\rho, z), & z \geq z_0 \\ k_1 F(\rho, z) - G(\rho, z), & z \leq z_0. \end{cases} \quad (37)$$

From (16) and (17), the function $\psi(z)$ is identically zero. Here we get for its Fourier coefficients that

$$\frac{2}{\ell} \int_0^{\ell} \psi(z) \sin\left(\frac{m\pi}{\ell} z\right) dz = 0, \quad m = 1, 2, \dots \quad (38)$$

But from (29) and (32),

$$\psi(z) = \begin{cases} -(k_1 - k_2) \frac{T_H}{k_2} \frac{z-z_0}{\ell} \sum_{n=1}^{\infty} \beta_n F_n \sin\left(\frac{n\pi}{\ell} z\right) - \sum_{n=1}^{\infty} \delta_n \sin\left(\frac{n\pi}{\ell} z\right), & z \geq z_0 \\ -(k_2 - k_1) \frac{T_H}{k_2} \frac{z}{\ell} + \sum_{n=1}^{\infty} \epsilon_n F_n \sin\left(\frac{n\pi}{\ell} z\right) - \sum_{n=1}^{\infty} \delta_n \sin\left(\frac{n\pi}{\ell} z\right), & z \leq z_0, \end{cases} \quad (39)$$

where

$$\beta_n := k_2 I_0(p_n) - \frac{k_1 k_2}{k_3} C_n, \quad \epsilon_n := k_1 I_0(p_n) - \frac{k_1 k_2}{k_3} C_n. \quad (41)$$

Hence, by (38):

$$0 = \frac{2}{\ell} \left\{ \sum_{n=1}^{\infty} \beta_n F_n \int_{z_0}^{\ell} \sin\left(\frac{n\pi}{\ell} z\right) \sin\left(\frac{m\pi}{\ell} z\right) dz + \sum_{n=1}^{\infty} \epsilon_n F_n \int_0^{z_0} \sin\left(\frac{n\pi}{\ell} z\right) \sin\left(\frac{m\pi}{\ell} z\right) dz \right\} - b(m) - \delta_m \quad (42)$$

where

$$b(m) = \frac{2}{\ell} \left\{ \frac{k_1 - k_2}{k_1} T_C \int_{z_0}^{\ell} \frac{z-z_0}{\ell} \sin\left(\frac{m\pi}{\ell} z\right) dz + \frac{k_2 - k_1}{k_2} \frac{T_H}{\ell} \int_0^{z_0} z \sin\left(\frac{m\pi}{\ell} z\right) dz \right\}. \quad (43)$$

If we now define

$$S_{\alpha}^{\beta}(m, n) := \int_{\alpha}^{\beta} \sin\left(\frac{n\pi}{\ell} z\right) \sin\left(\frac{m\pi}{\ell} z\right) dz \quad (44)$$

equation (42) becomes

$$\frac{2}{\ell} \sum_{n=1}^{\infty} [\beta_n S_{z_0}^{\ell}(m, n) + \epsilon_n S_0^{z_0}(m, n)] F_n = \frac{2}{\ell} b(m) + \delta_m. \quad (45)$$

Noticing that

$$S_0^{z_0}(m, n) + S_{z_0}^{\ell}(m, n) = S_0^{\ell}(m, n) = \begin{cases} \frac{\ell}{2}, & \text{if } n = m \\ 0, & \text{if } n \neq m \end{cases}, \quad (46)$$

equation (45) becomes

$$\sum_{n=1}^{\infty} (\epsilon_n - \beta_n) S_0^{z_0}(m, n) F_n + \beta_m \frac{\ell}{2} F_m = b(m) + \frac{\ell}{2} \delta_m. \quad (47)$$

Equation (47) represents an infinite system of equations with respect to the infinite vector $V := [F_1, \dots, F_n, \dots]^T$, i.e.

$$MV = w, \quad (48)$$

where the components of the right hand side vector w are given by

$$w(m) := b(m) + \frac{\ell}{2} \delta_m \quad (49)$$

and the entries of the coefficient matrix M are

$$\begin{aligned} M(n, m; z_0) &:= (\epsilon_n - \beta_n) S_0^{z_0}(m, n) \quad m \neq n \\ M(n, m; z_0) &:= (\epsilon_m - \beta_m) S_0^{z_0}(m, m) + \beta_m \frac{\ell}{2} \quad m = n. \end{aligned} \quad (50)$$

With the help of (41) and (44) we calculate

$$\begin{aligned} M(n, m; z_0) &= (k_1 - k_2) \left\{ \frac{1}{\pi} \frac{1}{m-n} \sin[(m-n) \frac{\pi z_0}{\ell}] - \frac{1}{\pi} \frac{1}{m+n} \sin[(m+n) \frac{\pi z_0}{\ell}] \right\} \quad m \neq n \\ M(n, m; z_0) &= (k_1 - k_2) \left\{ \frac{z_0}{\ell} - \frac{1}{\pi} \frac{1}{2m} \sin(2m\pi \frac{z_0}{\ell}) \right\} + k_2 - \frac{k_1 k_2}{k_3} \frac{C_m}{I_0(p_m)} \quad m = n, \end{aligned} \quad (51)$$

while from (43) and (49) we get

$$w(m) = \delta_m + 2(k_1 - k_2) \left\{ \left(\frac{T_C}{k_1} - \frac{T_H}{k_2} \right) \frac{1}{2m\pi} \sin\left(\frac{m\pi}{\ell} z_0\right) + \frac{1}{m\ell\pi} \left[\frac{T_C}{k_1} (\ell - z_0) + \frac{T_H}{k_2} z_0 \right] \cos\left(\frac{m\pi}{\ell} z_0\right) \right\}. \quad (52)$$

We remind that δ_m is given by (30) i.e.

$$\delta_m = \frac{\ell}{m\rho} \frac{\gamma_m}{m d_m}, \quad (53)$$

where γ_m and d_m are known by (22) and (25).

Notice that M is symmetric. Since z_0 is not yet known, the matrix M is still unknown. However, condition (19), at $r = \rho$, $z = z_0$, i.e.

$$F(\rho, z_0) = 0 \quad (54)$$

has not been applied yet.

In order to solve system (48) with the constraint (54) we start with an initial guess for z_0 and iterate until (54) is satisfied. Our calculations have shown that, even though (48) is an infinite system, a truncation after a small number of terms (e.g. 60 terms) does not significantly affect the results.

3. SOME IMMEDIATE APPLICATIONS

- a) Previous results follow as a special case of the above. If we follow the usual assumptions ($[1], \dots, [5]$) of equal thermal conductivities, then $k_1 = k_2 := k$. Even if we don't drop the glass domain D_G , the matrix in system (48) is diagonal. In this case the equations are simplified to

$$k(1 - \frac{k}{k_3} \frac{C_m}{I_0(p_m)}) F_m = \frac{\ell}{m\rho} \frac{\gamma_m}{md_m}, \quad m = 1, 2, 3, \dots \quad (55)$$

where γ_m , d_m and C_m are given by (22), (25) and (31) respectively. From (55) one can read the unknown coefficients immediately, hence obtaining a complete analytical solution.

- b) The case of the Rayleigh-Benard problem, where the temperature at the wall has a linear variation was investigated in [10]. It's steady state form can be solved as a special case of the preceeding analysis: Since g is linear in z , with $g(\ell) = T_H$ and $g(0) = T_C$, we get $g(z) = L(z)$. Hence by (22)

$$\gamma_m = 0, \quad m = 1, 2, 3, \dots \quad (56)$$

i.e., one uses the special case of (52) with $\delta_m = 0$.

- c) An even more special solution arises when both a) and b) are considered simultaneously. Then from (55) and (56) we obtain $F_n = 0$, hence, from (20) and (21)

$$F(r, z) = \frac{T_H}{k_2} \frac{z}{\ell} + \frac{T_C}{k_1} \frac{\ell - z}{\ell}$$

which is a trivial solution, indepent of r .

4. COMPUTATIONAL RESULTS

We now report on preliminary computational results for Bridgman-Stockbarger model under the following conditions. A pyrex ampoule of finite length ℓ ($= 40$ cm. in our case) containing liquid naphthalene (cf. Figure 1) is placed in a liquid bath in such a way that the temperature on the base and on the outer ampoule wall $r = R$ from $z=0$ to $z=\alpha$ is kept at a constant value of T_C . Along the outer wall of the ampoule from $z=\alpha$ to $z = \alpha + \Delta\alpha$ (i.e., the insulator region), the temperature assumes a linear variation, and along the top of the ampoule and the outer ampoule wall from $z = \alpha + \Delta\alpha$ to $z=\ell$, the temperature is kept at a constant value of T_H . For the insulator and the glass wall to exist we need, $\Delta\alpha > 0$ and $R-\rho > 0$ ($R-\rho = .1$). The melting temperature for naphthalene is taken to be 80.2°C .

In this situation, the function g of (8), representing the temperature distribution at the outer ampoule wall takes the form

$$g(z) = \begin{cases} T_C & 0 \leq z \leq \alpha \\ T_C + \frac{T_H - T_C}{\Delta\alpha} (z - \alpha) & \alpha \leq z \leq \alpha + \Delta\alpha \\ T_H & \alpha + \Delta\alpha \leq z \leq \ell \end{cases}$$

then, by the use of (22), we calculate

$$\begin{aligned} \gamma_n &= \frac{2}{\ell} \int_0^\ell \{g(z) - L(z)\} \sin\left(\frac{n\pi}{\ell} z\right) dz \\ &= \frac{2(T_H - T_C)}{n^2 \pi^2} \frac{\ell}{\Delta\alpha} \{ \sin\left[\frac{n\pi}{\ell}(\alpha + \Delta\alpha)\right] - \sin\left(\frac{n\pi}{\ell} \alpha\right) \}. \end{aligned}$$

From this and (25), (30), we find the parameters δ_n , $n = 2, 2, \dots$.

A set of different sample values for the user defined parameters T_H , T_C , T_{melt} , k_1 , k_2 , k_3 , α , $\Delta\alpha$, was chosen for these preliminary tests. The respective problems are given in Tables 1-2. The results for each problem are given in Figures 2 to 11.

From these results we can make the following preliminary conclusions, some of which are expected, and some need further exploration. In the following, all user defined parameters are held constant except the ones explicitly mentioned.

- (I) For several values of $\Delta T = T_H - T_C$, all three interface shapes are observed (cf. Figure 8 to Figure 12).
- (II) There exist combinations of temperatures T_H, T_C for which the interface displays a dip near the glass wall. This phenomenon needs further investigation (cf. Figure 7, Figure 8).
- (III) Increasing the ratio k_1/k_2 makes the interface more planar.
- (IV) Decreasing k_3 makes the interface more planar.
- (V) Increasing the thickness of the insulator makes the interface more planar.
- (VI) The point z_0 (on the interior ampoule wall where $T = T_{\text{melt}}$) is different, in general, from the point on the outer ampoule wall where $T = T_{\text{melt}}$.

In closing, we point out that even though our program has not yet been optimized, the technique presented here is shown to be very effective, as its computer implementation displays the following advantages:

1. Fast results (≈ 20 seconds execution and output time, IBM 4341).
2. We can obtain z_0 within $\approx 10^{-6}$ accuracy (and therefore the correct coefficient matrix) with a maximum of 5 iterations, even though we start with the poor initial guess of $z_0 = 0$.

PROBLEM #	T _H (0 _C)	T _C (0 _C)	α (cm)	Δα (cm)	k ₁ watt/cm.K	k ₂ watt/cm.K	k ₃ watt/cm.K	FIGURE #
1	90	32	19.75	.5	1.3E-3	6.5E-4	1.2E-2	2
	90	32	19.75	.5	1.3E-3	1.0E-3	1.2E-2	
	90	32	19.75	.5	1.3E-3	1.3E-3	1.2E-2	
	90	32	19.75	.5	1.3E-3	2.0E-3	1.2E-2	
	90	32	19.75	.5	1.3E-3	2.6E-3	1.2E-2	
	90	32	19.75	.5	1.3E-3	2.8E-3	1.2E-2	
2	90	32	19.75	.5	1.4E-3	2.8E-3	1.2E-2	3
	90	32	19.75	.5	2.0E-3	2.8E-3	1.2E-2	
	90	32	19.75	.5	3.2E-3	2.8E-3	1.2E-2	
	90	32	19.75	.5	4.4E-3	2.8E-3	1.2E-2	
	90	32	19.75	.5	5.6E-3	2.8E-3	1.2E-2	
3	90	32	19.75	.5	1.3E-3	2.8E-3	1.2E-1	4
	90	32	19.75	.5	1.3E-3	2.8E-3	1.2E-2	
	90	32	19.75	.5	1.3E-3	2.8E-3	1.2E-3	
	90	32	19.75	.5	1.3E-3	2.8E-3	1.2E-4	
4	90	32	0	.5	1.3E-3	2.8E-3	1.2E-2	5
	90	32	8	.5	1.3E-3	2.8E-3	1.2E-2	
	90	32	16	.5	1.3E-3	2.8E-3	1.2E-2	
	90	32	24	.5	1.3E-3	2.8E-3	1.2E-2	
	90	32	32	.5	1.3E-3	2.8E-3	1.2E-2	
	90	32	39.5	.5	1.3E-3	2.8E-3	1.2E-2	
5	90	32	19	2.0	1.3E-3	2.8E-3	1.2E-2	6
	90	32	19.5	1.0	1.3E-3	2.8E-3	1.2E-2	
	90	32	19.764	.472	1.3E-3	2.8E-3	1.2E-2	
	90	32	19.9	.2	1.3E-3	2.8E-3	1.2E-2	

TABLE 1

PROBLEM #	T_H (0_C)	T_C (0_C)	α (cm)	$\Delta\alpha$ (cm)	k_1 watt/cm.K	k_2 watt/cm.K	k_3 watt/cm.K	FIGURE #
6.1	90	0	19.75	.5	1.3E-3	2.8E-3	1.2E-2	7
	95	0	19.75	.5	1.3E-3	2.8E-3	1.2E-2	
	110	0	19.75	.5	1.3E-3	2.8E-3	1.2E-2	
	125	0	19.75	.5	1.3E-3	2.8E-3	1.2E-2	
	175	0	19.75	.5	1.3E-3	2.8E-3	1.2E-2	
6.2	90	32	19.75	.5	1.3E-3	2.8E-3	1.2E-2	8
	95	32	19.75	.5	1.3E-3	2.8E-3	1.2E-2	
	110	32	19.75	.5	1.3E-3	2.8E-3	1.2E-2	
	125	32	19.75	.5	1.3E-3	2.8E-3	1.2E-2	
	175	32	19.75	.5	1.3E-3	2.8E-3	1.2E-2	
6.3	90	50	19.75	.5	1.3E-3	2.8E-3	1.2E-2	9
	95	50	19.75	.5	1.3E-3	2.8E-3	1.2E-2	
	110	50	19.75	.5	1.3E-3	2.8E-3	1.2E-2	
	125	50	19.75	.5	1.3E-3	2.8E-3	1.2E-2	
	175	50	19.75	.5	1.3E-3	2.8E-3	1.2E-2	
6.4	90	65	19.75	.5	1.3E-3	2.8E-3	1.2E-2	10
	95	65	19.75	.5	1.3E-3	2.8E-3	1.2E-2	
	110	65	19.75	.5	1.3E-3	2.8E-3	1.2E-2	
	125	65	19.75	.5	1.3E-3	2.8E-3	1.2E-2	
	175	65	19.75	.5	1.3E-3	2.8E-3	1.2E-2	
6.5	90	75	19.75	.5	1.3E-3	2.8E-3	1.2E-2	11
	95	75	19.75	.5	1.3E-3	2.8E-3	1.2E-2	
	110	75	19.75	.5	1.3E-3	2.8E-3	1.2E-2	
	125	75	19.75	.5	1.3E-3	2.8E-3	1.2E-2	
	175	75	19.75	.5	1.3E-3	2.8E-3	1.2E-2	

TABLE 2

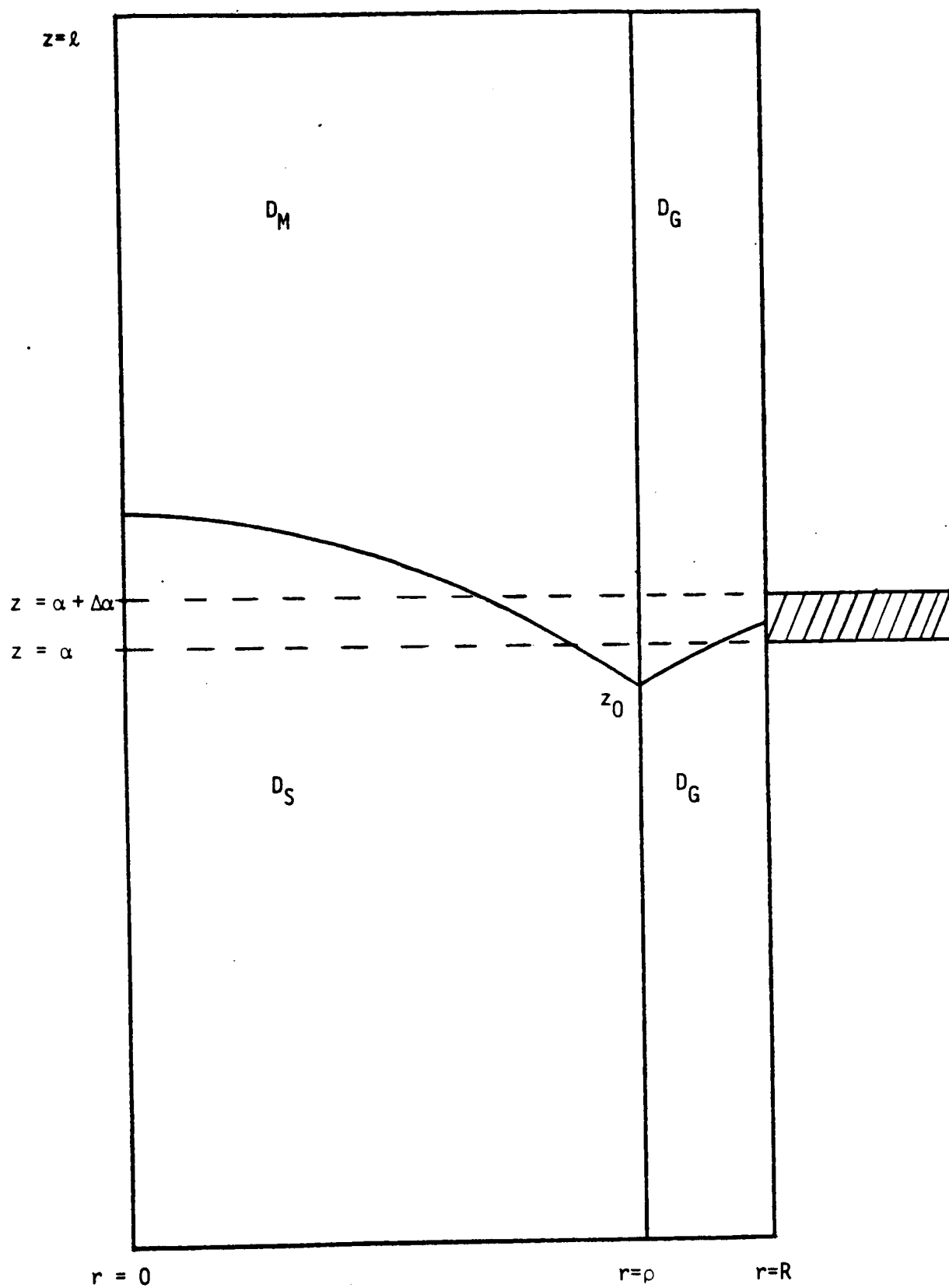


FIGURE 1

FIGURE 2

$$T_H = 90$$

$$T_C = 32$$

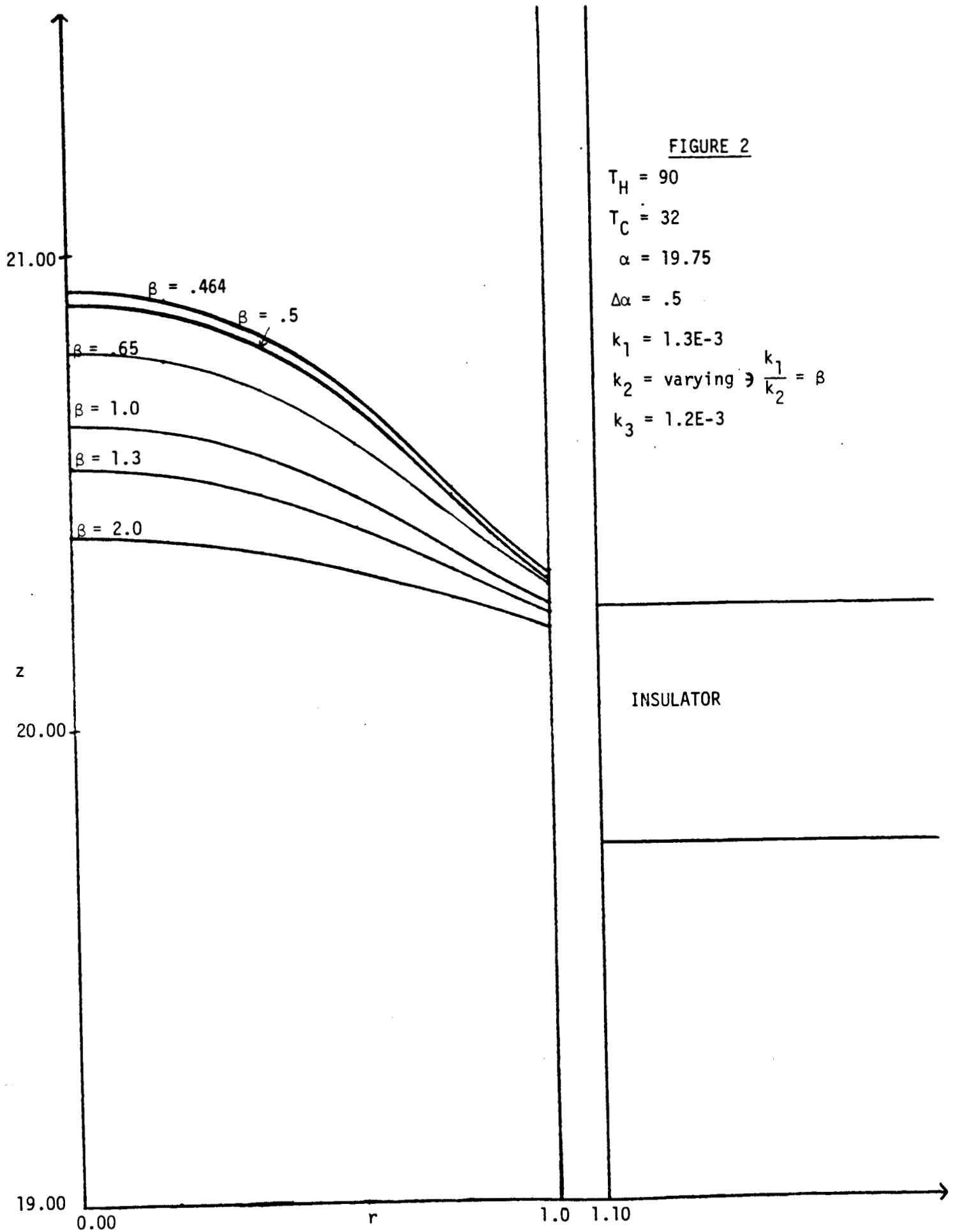
$$\alpha = 19.75$$

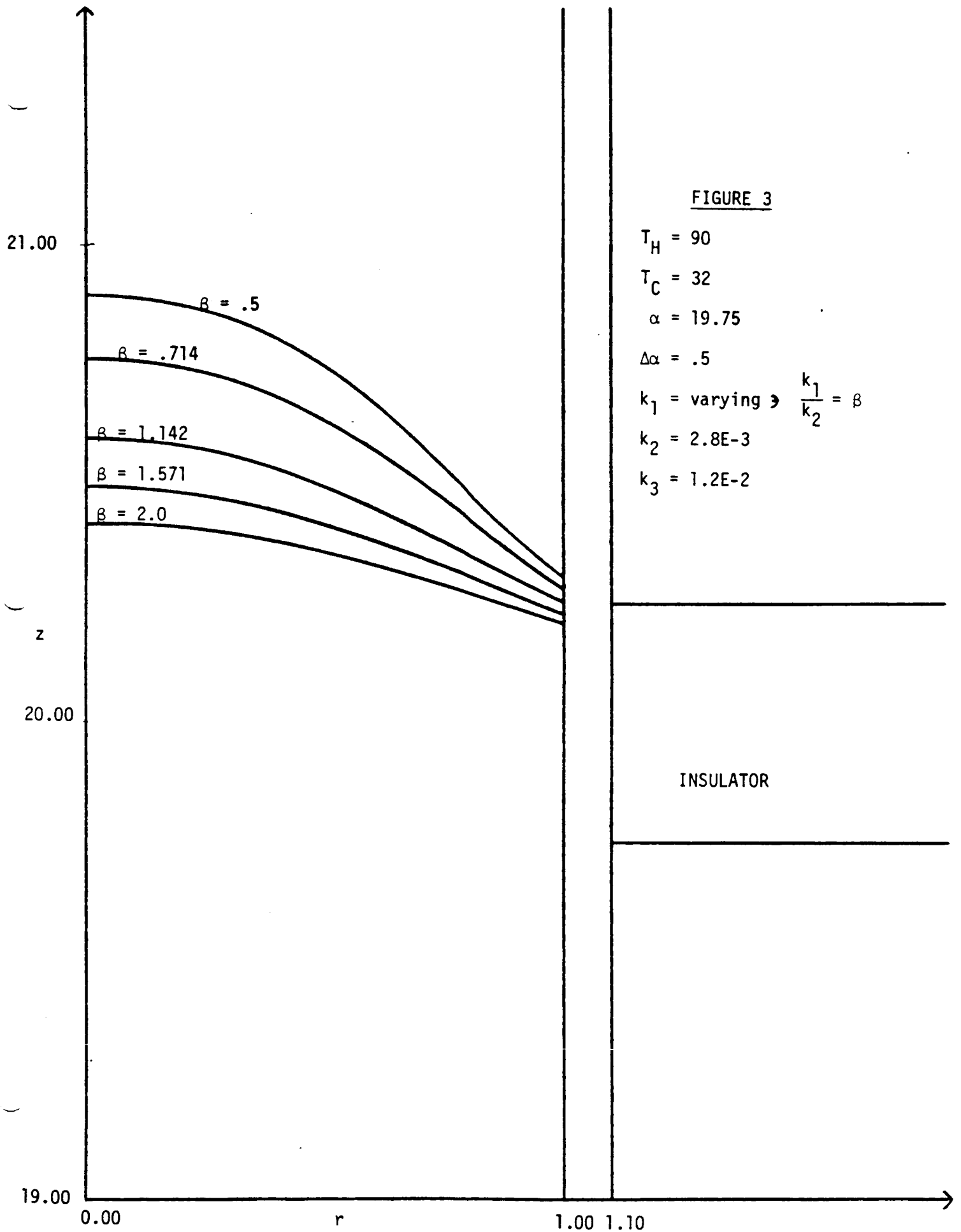
$$\Delta\alpha = .5$$

$$k_1 = 1.3E-3$$

$$k_2 = \text{varying} \Rightarrow \frac{k_1}{k_2} = \beta$$

$$k_3 = 1.2E-3$$





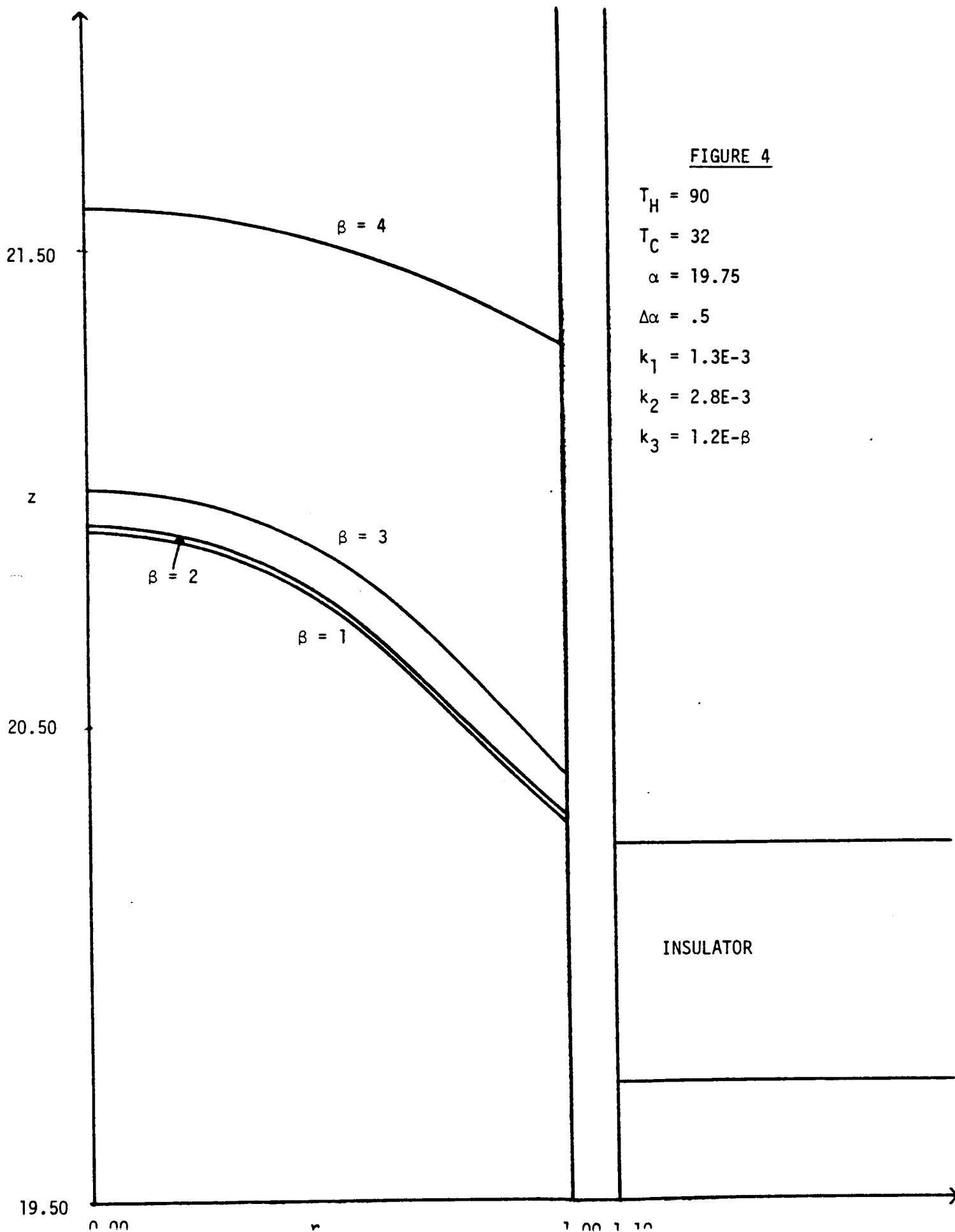


FIGURE 5

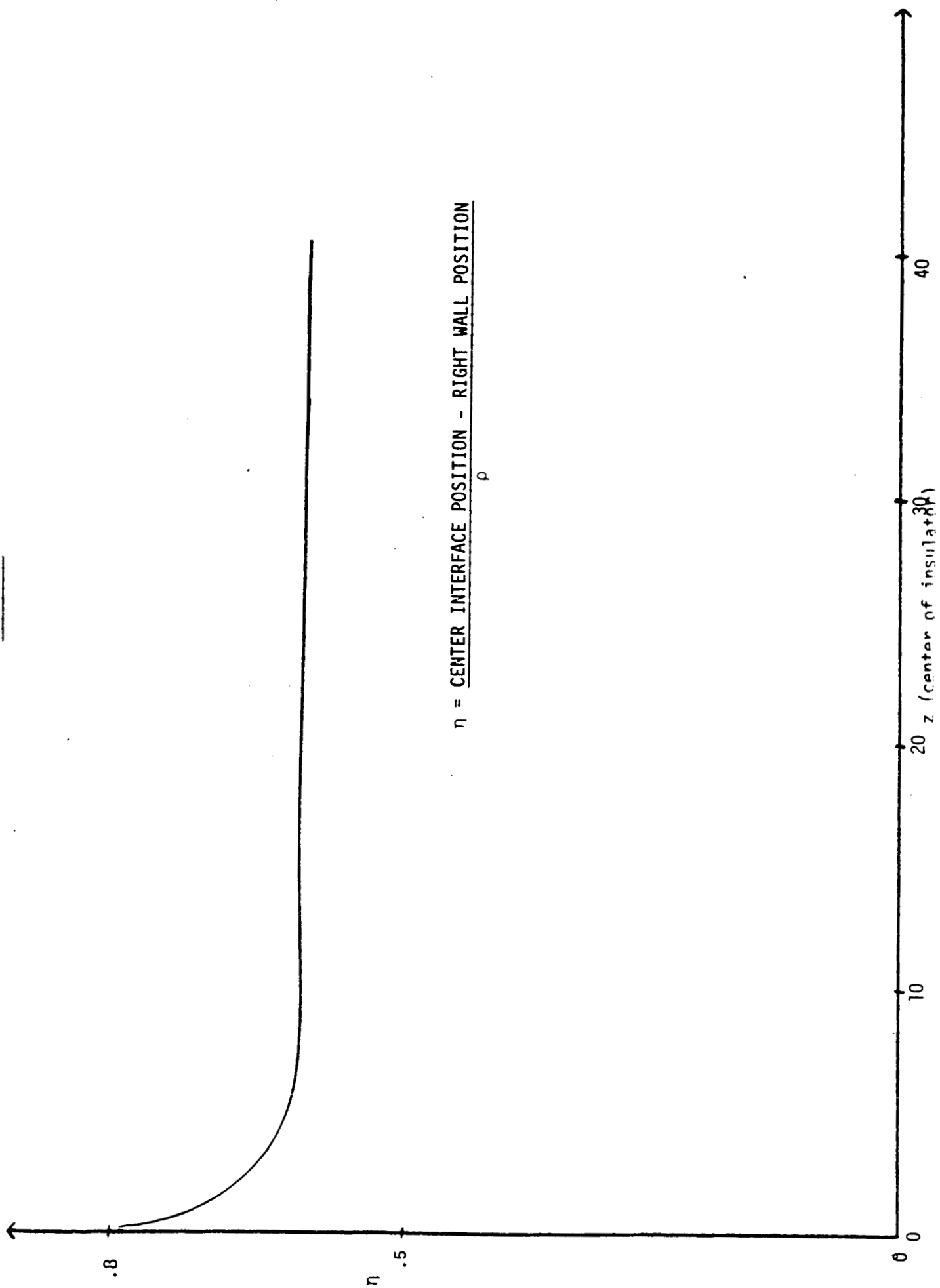
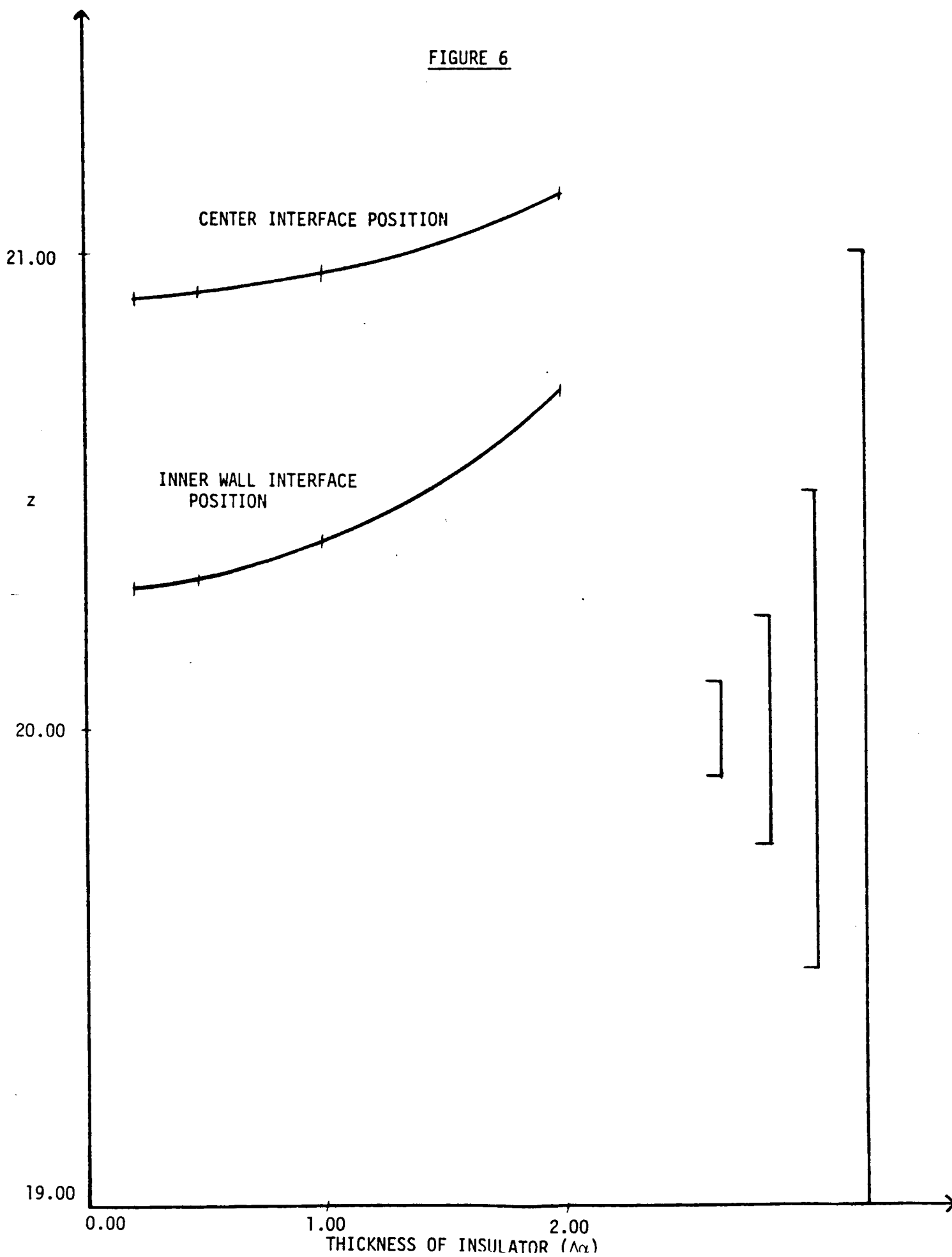
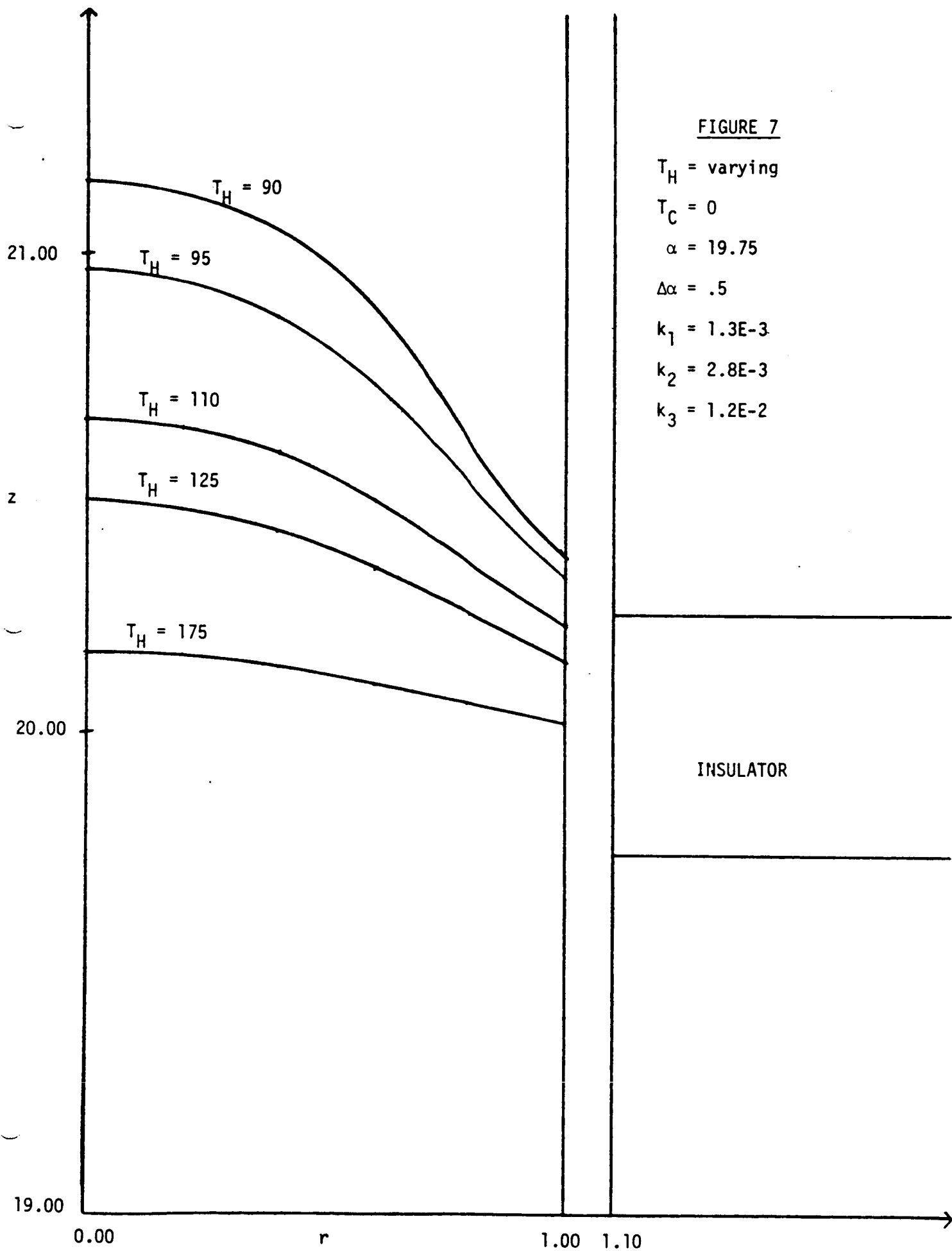
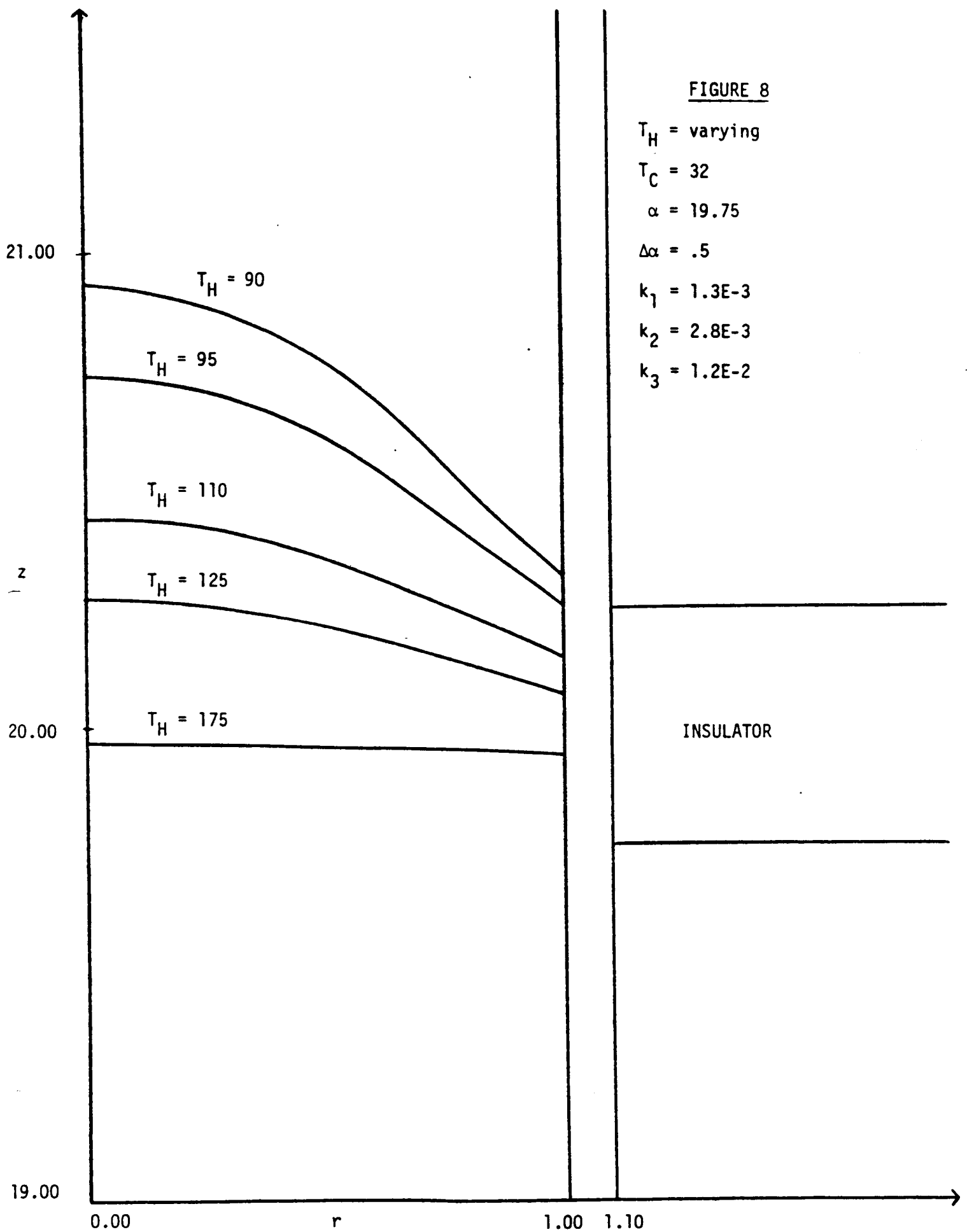


FIGURE 6







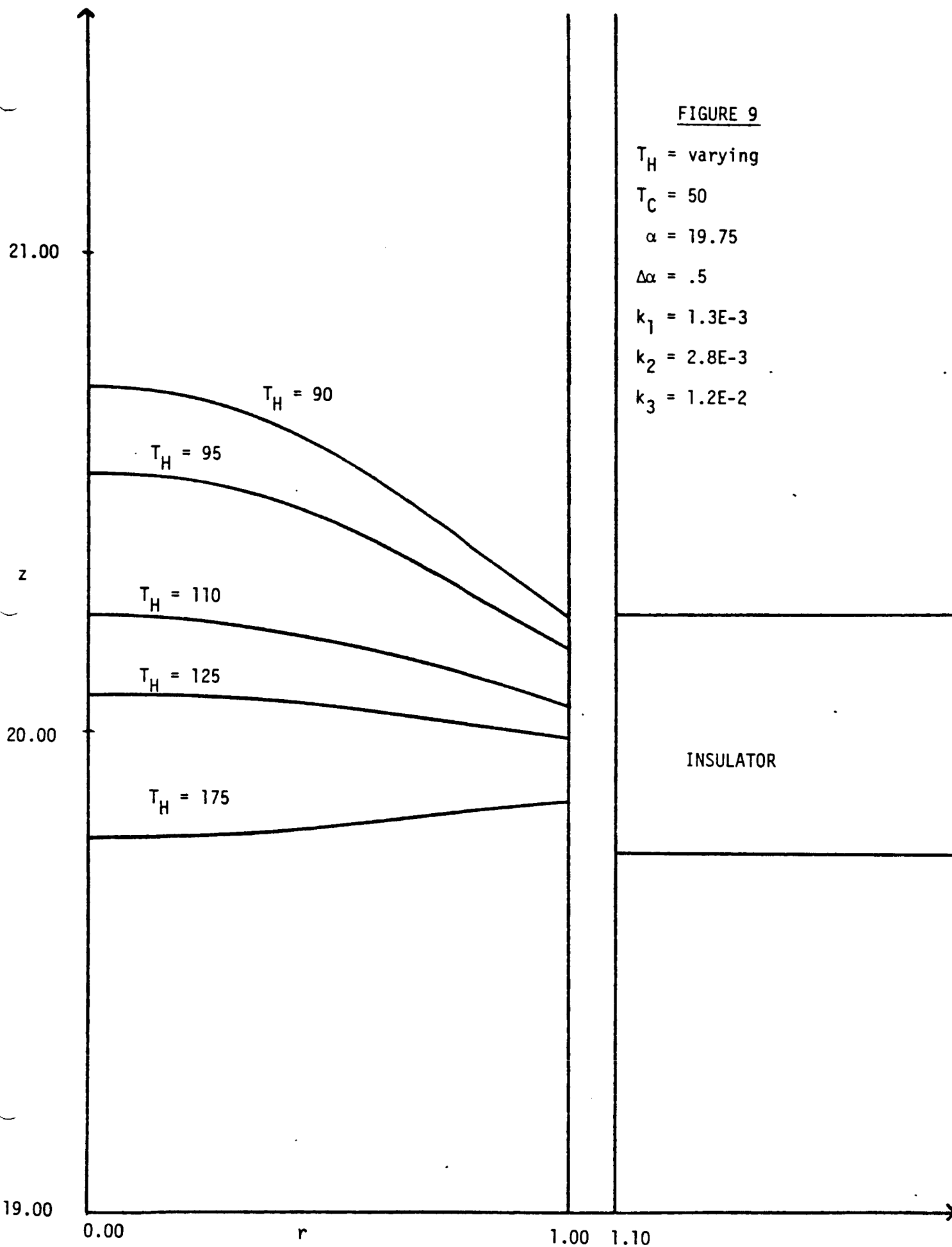


FIGURE 10

$T_H = \text{varying}$

$T_C = 65$

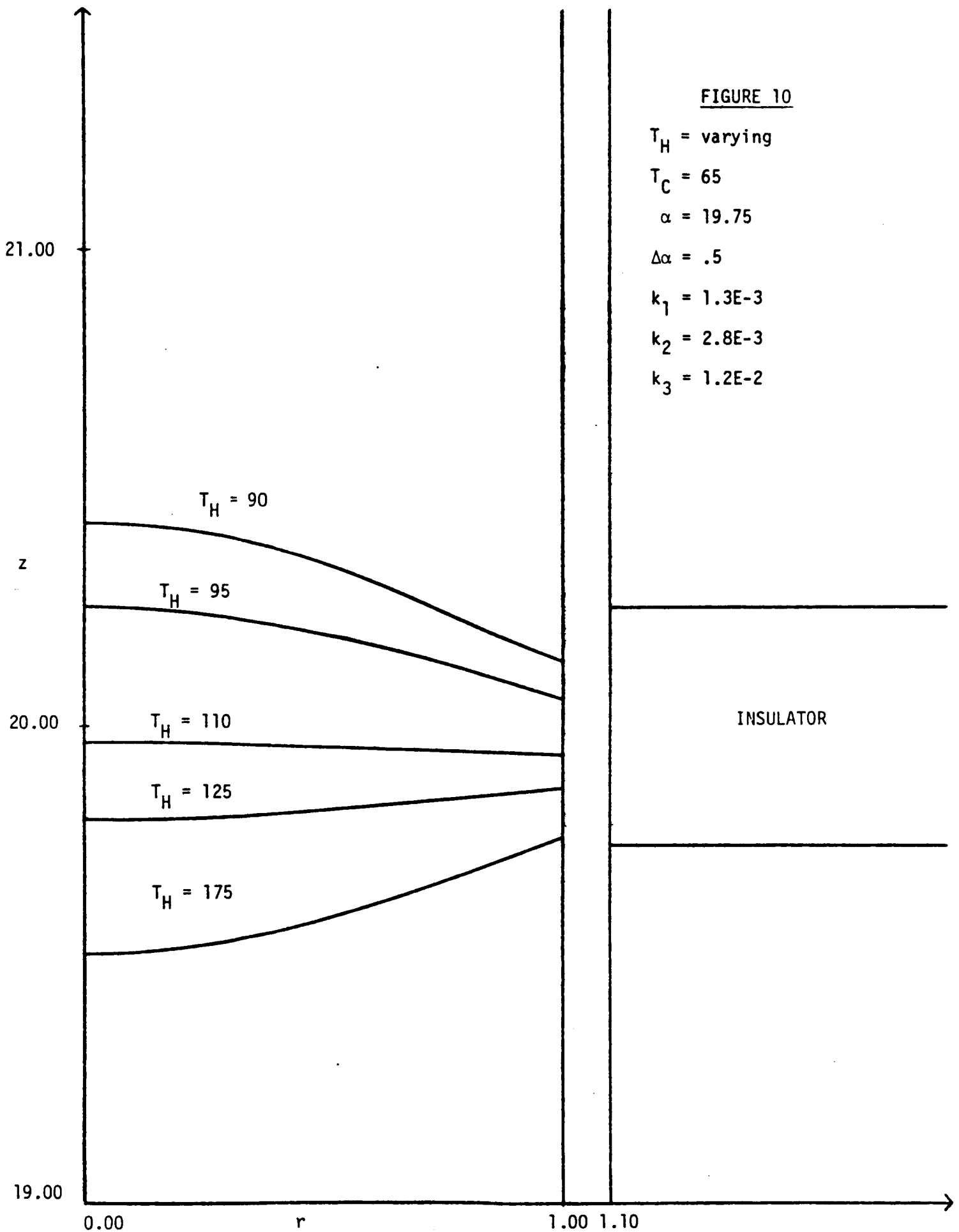
$\alpha = 19.75$

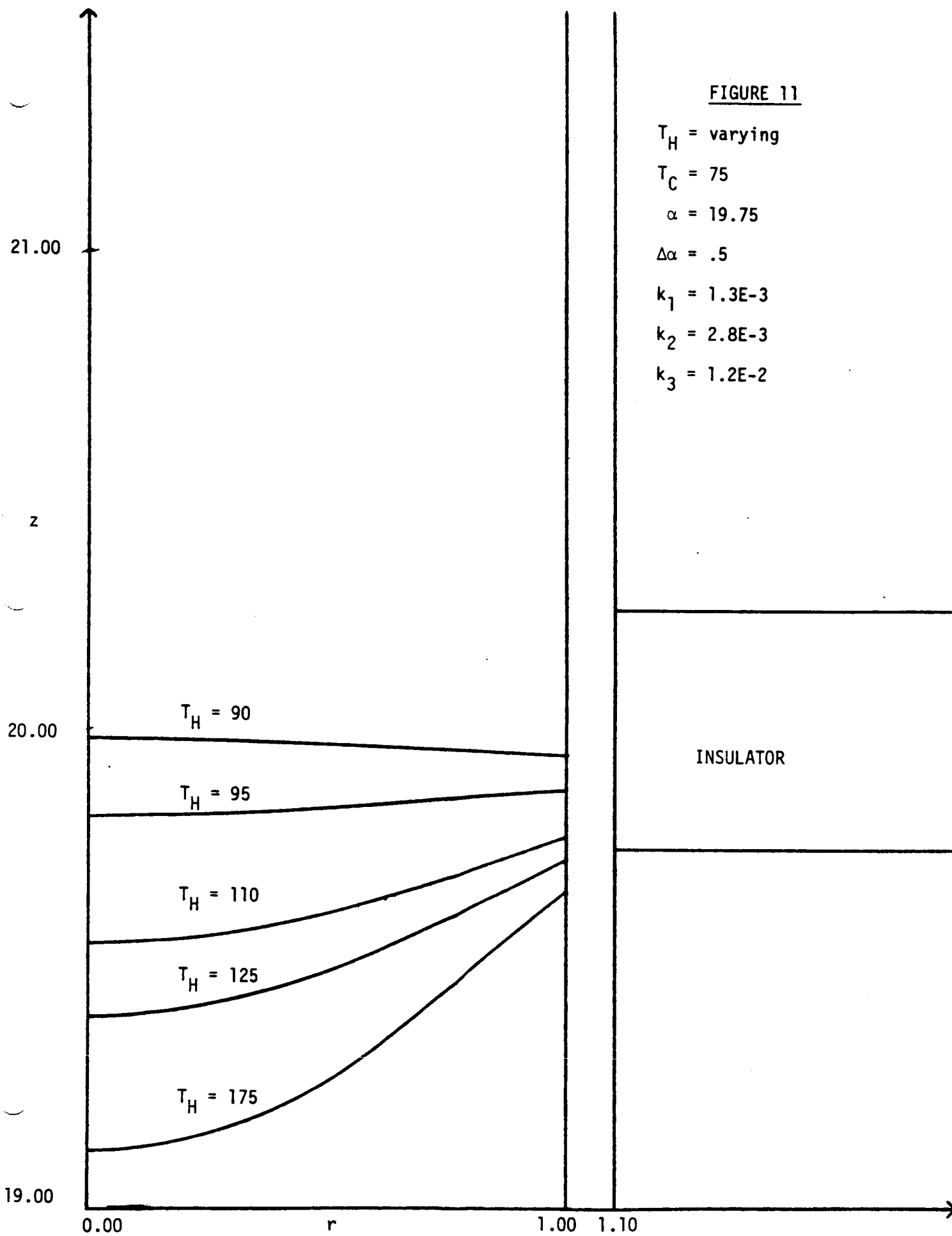
$\Delta\alpha = .5$

$k_1 = 1.3E-3$

$k_2 = 2.8E-3$

$k_3 = 1.2E-2$





REFERENCES

- [1] C.E. Chang and W.R. Wilcox, J. Crystal Growth 21 (1974).
- [2] C.E. Chang, Ph.D. Dissertation, Univ. of Southern California (Los Angeles, 1973).
- [3] L.C. Tien, Ph.D. Dissertation, Univ. of Michigan (Ann Arbor, 1968).
- [4] T.W. Fu and W.R. Wilcox, J. Crystal Growth 48 (1980).
- [5] T.W. Fu and W.R. Wilcox, J. Crystal Growth 51 (1981).
- [6] R.J. Naumann, J. Crystal Growth 58 (1982).
- [7] T. Jasinski, W.M. Roshenow and A.F. Witt, J. Crystal Growth 61 (1983).
- [8] T. Jasinski and R.J. Naumann, J. Crystal Growth 66 (1984).
- [9] M.J. Ablowitz, M. Kruskal, H. Segur, Personal Communications.
- [10] C.S. Chang, R.A. Brown, J. Comp. Phys. 53 (1984).

APPENDIX E
Accepted by J. Crystal Growth

BEHAVIOR OF A NON-WETTING MELT IN FREE FALL: EXPERIMENTAL

RADHA SEN* and WILLIAM R. WILCOX
Department of Chemical Engineering
Clarkson University, Potsdam, NY 13676, USA

ABSTRACT

A liquid metal in a non-wetted ampoule formed either columns separated by gas spaces or gas bubbles on the wall. Separated columns were favored by small amounts of the liquid while only bubbles were found when the liquid almost filled the ampoule. In ampoules with a triangular cross-section the liquid pulled away from the corners. This allowed the liquid to move readily in the presence of residual accelerations, because the air in the ampoule could easily move in the opposite direction to the liquid.

When water wet well an ampoule's walls, air bubbles remained suspended and did not contact the walls. If the air is taken to represent a non-wetting fluid, then it seems possible for a fluid to avoid completely contact with the ampoule wall.

*Present address: University of Minnesota, Minneapolis.

1. Introduction

When metals and semiconductors were directionally solidified in space, the resulting ingots were often somewhat smaller in diameter than the ampoule, usually with a wavy or irregular surface [1-15]. These results were generally explained in a vague way by attributing them to the melt not wetting the ampoule wall. Probably the melt was visualized as pulling away from the crucible wall, with the solidification following the melt surface.

Directional solidification in an ampoule in space has always been carried out in opaque furnaces. Thus no one has actually observed the melt behavior or the solidification. In the research reported here we took the first step by observing liquid behavior in a poorly wetted ampoule. In a subsequent paper we will give theoretical predictions, which are in agreement with the experimental results presented here.

2. Experimental Methods

The experiments were performed in a KC135 aircraft flying out of Ellington Field near NASA's Johnson Space Center outside of Houston. The KC135 is a modified Boeing 707 that does controlled parabolic dives to give approximately 20 seconds of free fall. In a successful flight, 50 free-fall parabolas are performed. The present experiments required three such flights.

The ampoule preparation is described in detail elsewhere [16]. Three types of ampoules were employed; cylindrical, cylindrical with capillary tubes along the wall, and triangular. For the cylindrical ampoules we used transparent polycarbonate tubes 1.9 cm in diameter and about 14 cm long. Eight glass capillary tubes were epoxied around the wall of some of these. The capillaries were 2 mm outside diameter and about 1 cm shorter than the

ampoules. The triangular ampoules were fabricated by cementing three 1.2 x 7.6 cm glass slides together with epoxy along their edges.

Most of the experiments were performed with mercury as the liquid. Mercury's contact angle on glass was about 120° and on polycarbonate 130° . Both the polycarbonate and the triangular glass ampoules were filled 30 to 95% with mercury and the open ends sealed with silver. Silver was chosen to simulate the solid-liquid interface, which is generally thought to be wet well by the corresponding melts.

Some experiments were also carried out with distilled water in polycarbonate ampoules sealed with Corning machineable ceramic plugs, which are wet well by water. During storage prior to flight, the water began to wet the polycarbonate tubes to varying extents and sometimes almost entirely leaked out. The contact angle ranged from near 0 to about 90 degrees.

To avoid leakage of liquids into the aircraft interior, each ampoule was thoroughly sealed in larger polycarbonate tubes.

The liquid behavior was recorded by attaching an ampoule in its polycarbonate tube to a video camera. This assembly was periodically shaken and released (except for the cable connecting the camera to its videotape recorder). The photographs shown here were taken from television displays of these video recordings.

3. Results

Equilibrium was reached within a few seconds of releasing the apparatus during a low g parabola. We report first on equilibrium fluid configurations.

a. Mercury in cylindrical ampoules

Two classes of equilibrium shapes were observed. In one class, two or more columns of mercury were separated by air, as shown in Figure 1.

The second class of configurations consisted of an air bubble at the ampoule wall, as shown in Figure 2. Alternately this can be regarded as a liquid bridge connecting two columns of mercury. Consequently we will refer to this as the bubble/bridge configuration. This configuration became more common as the amount of mercury was increased. The separated column configuration predominated when the ampoule was about 70% or less filled with mercury. Bubble/bridges were not seen in ampoules 30% full or less.

In glass ampoules, trapped air larger than about 1.2 cm^3 in volume tended to form the separated column configuration, while in polycarbonate ampoules bubble/bridges were unstable above about 0.9 cm^3 in volume.

The wetted silver end plugs seemed to have no influence on the liquid behavior, except that some mercury always remained in contact with it, often a small drop.

b. Mercury in ampoules containing capillaries

Unfortunately the liquid could not be seen clearly in the videotapes of these ampoules. It had been hoped that the capillaries would cause the mercury to pull away entirely from the ampoule walls and contact only the capillaries. This appeared to happen rarely and then only over short distances. As with the plain cylindrical ampoules, bubble/bridge and separated column configurations were typical. The separated columns seemed to form much more readily than without capillary tubes and no large bubbles were observed. It is hypothesized that the mercury pulled away at the intersection of the ampoule and capillary walls as shown in Figure 3, but we could not see well enough to verify such behavior.

c. Mercury in triangular ampoules

As shown in Figures 4 and 5, the mercury pulled away from the glass walls along the edges and contacted it along the centers, over about half the width

of each side. Occasionally the mercury column would remain in contact with the silver end plug, as in Figure 5.

d. Transient behavior of mercury

There were three sources of changing accelerations giving rise to transient behavior: going into free fall, shaking of the apparatus, and residual accelerations while the apparatus was floating.

In several experiments the ampoule was held horizontal prior to going into free fall, so that the flat free surface of the mercury ran along the length of the ampoule. When the aircraft went into its low g parabola the surface became wavy and unstable. The instabilities grew until the mercury filled the cross section in some places, connected by bubble/bridges. In a few seconds the larger bubble/bridges broke to form a separated column configuration.

Periodically the ampoules were shaken to try to produce a variety of configurations. In the cylindrical ampoules the air in the bubble/bridges moved fairly readily, with the mercury moving in the opposite direction. However the separated-columns were relatively stable because the mercury and air could move past one another only if the shaking was vigorous enough to break up the liquid. From a separated-column configuration often we could form by gentle shaking a bubble/bridge not touching the walls, i.e. a central neck. However this configuration was unstable and broke to reform separate columns in a few seconds.

Even gentle shaking of the capillary-lined ampoules and the triangular ampoules produced ready movement of the mercury, presumably because return paths were available for the air. In the capillary-lined ampoules the air could move either up the interior of the unsealed capillary tubes or along the air columns hypothesized in Figure 3. In the triangular ampoules the air could move along the edges. After shaking a triangular ampoule, the mercury

often was forced to one end of the ampoule so that it contacted the edges. The mercury instantly moved away from the edges when the ampoule was released.

Smaller manifestations of the ease of movement occurred with a floating ampoule. The configurations were stable in the cylindrical ampoules after a second or two. The mercury continued to move somewhat in the capillary-lined and triangular ampoules, reflecting the small residual accelerations.

e. Influence of a temperature gradient

Nichrome heating wire was wound on the end of an ampoule. In the laboratory this produced a temperature gradient of 3 to 4 K/cm in the mercury when the ampoule was held vertically with the heater on top and with the ampoule completely filled with mercury. In the KC135 experiment this ampoule was about half full of mercury. The only difference in behavior from unheated ampoules was that the bubble/bridge was never observed.

Because surface tensions and contact angles are temperature dependent, we had expected the mercury to move to one end of the heated ampoule, probably the heated end. However in the separated-column configuration in a cylindrical ampoule there is no path for the return flow of the air. It would be interesting to repeat this experiment with a hard vacuum in a cylindrical ampoule and in a triangular ampoule.

f. Behavior of water

As noted earlier, the contact angle for water became small during storage. Without gravity, gases and liquids are equivalent from the viewpoint of equilibrium fluid behavior. Thus we may regard the air as the non-wetting fluid in these experiments, with a large contact angle.

Small air bubbles tended to remain suspended and not contact the walls or coalesce, as shown in Figure 6. In contrast, when mercury drops formed during vigorous shaking, they soon recombined with the bulk mercury. There are

several reasons the air bubbles remained suspended in water so much better than in the mercury. The contact angle of the air was much larger. The difference in density between the fluids was larger with mercury, so it moved more in response to residual accelerations. And the air-water interface was more likely to have been coated with a surfactant which would have retarded coalescence.

Larger air bubbles as in Figure 6 often were separated from contact with the ampoule walls only immediately after shaking. Usually the water drained away so that the bubble contacted the wall in a few seconds. When the amount of water was very small, it usually formed ripples and waves and finally separate drops. If the contact angle of the air was very high it appeared that the water did not drain and the air remained out of contact with the wall, as in Figure 7. However since the free-fall time between shaking was only a few seconds, it is not known if this behavior would have persisted indefinitely.

4. Discussion and Conclusions

The initial motivation for this research was to help explain why directional solidification in space has often produced ingots smaller in diameter than their containing ampoules. We found that mercury in polycarbonate ampoules did not pull away from the ampoule walls. With a gas present in the ampoule the mercury did not move under the influence of a temperature gradient. One would expect the liquid behavior to depend on its contact angle. Thus it is possible, although unlikely, that the contact angle for semiconductor melts is so high that they do pull away from the ampoule wall in the neighborhood of the freezing interface. Unfortunately no contact data are available for the melts solidified in space, although some data are available for similar systems. For example, gallium containing 3.16% As

formed a contact angle of 140 to 153 degrees on graphite at 1125K [17]. A variety of liquid metals had contact angles ranging from 114 to 134 degrees on graphite [18]. The contact angle of aluminum on ceramics was a strong function of temperature, ranging from 66 to 120 degrees [19].

Another possibility is that the residual accelerations in a spacecraft play a role in determining the surfaces of the ingots. In one Spacelab 3 crystal growth experiment, for example, the fluctuating acceleration level was on the order of milligees (0.001 earth gravity), with occasional 0.1g spikes. If an acceleration causes the melt to momentarily pull away from the crucible wall it will receive less heat from the heater and tend to freeze in this position. Since such movement is hindered by a gas in the ampoule, one would expect surface variations to be more pronounced when there is a hard vacuum in the prepared ampoule.

Our experiments on triangular ampoules showed that contact with the ampoule wall is reduced. In a subsequent paper we show that the contact with the wall decreases as the contact angle increases, becoming a line beyond a critical value.

Acknowledgements

This research was supported by NASA under contract NAS8-34891. Wilcox is grateful to the KC135 crew and to Bob Shurney for their help, and to the physiological training personnel at Pease Air Force Base for an interesting experience under their competent direction.

References

- [1] A.F. Witt, H.C. Gatos, M. Lichtensteiger, M.L. Lavine and C.J. Herman, p. 275 in Vol. 1 of "Proceedings Third Space Processing Symposium: Skylab Results," NASA Report M-74-5, Marshall Space Flight Center (1974).
- [2] J.F. Yee, S. Sen, K. Sarma, M.C. Lin and W.R. Wilcox, loc. cit., p. 301.
- [3] J.T. Yue and F.W. Voltmer, p. 375, loc. cit.
- [4] A.O. Ukanwa, p. 425, loc. cit.
- [5] E.A. Hasemeyer, C.V. Lovoy and L.L. Lacy, loc. cit., p. 457.
- [6] H.C. Gatos, A.F. Witt, M. Lichtensteiger and C.J. Herman, Section V of "Apollo-Soyuz Test Project - Composite of MSFC," NASA TM X-73360, Marshall Space Flight Center (1977).
- [7] V.S. Zemskov et al., Section IX, loc. cit.
- [8] A.F. Witt, H.C. Gatos, M. Lichtensteiger, M.C. Lavine and C.J. Herman, J. Electrochem. Soc. 122 (1975) 276.
- [9] I. Gyuro et al., Acta Astronautica 11 (1984) 361.
- [10] V.S. Avduyevsky, S.D. Grishin and L.V. Lescov, Acta Astronautica 9 (1982) 583.
- [11] F.R. Khashimov et al. in "Proceedings of Third European Symposium on Material Science in Space," European Space Association SP-142, Grenoble (1979).
- [12] R.R. Galazka et al., loc. cit.
- [13] E.V. Markov et al., 6th International Conference on Crystal Growth, Moscow (1980).
- [14] W.R. Wilcox, J.F. Yee, M.C. Lin, K. Sarma and S. Sen, p. 27 in "Skylab Science Experiments," American Astronautical Society, Tarzana (1975).
- [15] E. Lendvay et al., J. Crystal Growth 71 (1985) 538.
- [16] R. Sen, Ph.D. Thesis, Clarkson University (1985).
- [17] U. Konig and W. Keck, J. Electrochem. Soc. 130 (1983) 685.
- [18] C.P. Buhsmer and E.A. Heintz, J. Mat. Sci. 4 (1969) 592.
- [19] S.K. Rhee, J. Am. Ceram. Soc. 53 (1970) 386.

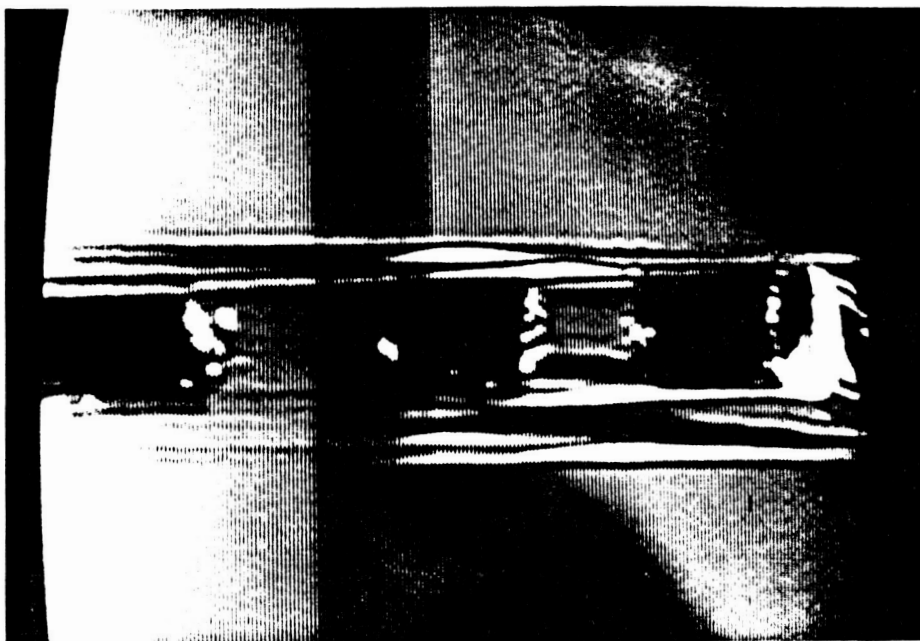


Figure 1. Three columns of mercury separated by air in a cylindrical polycarbonate ampoule.

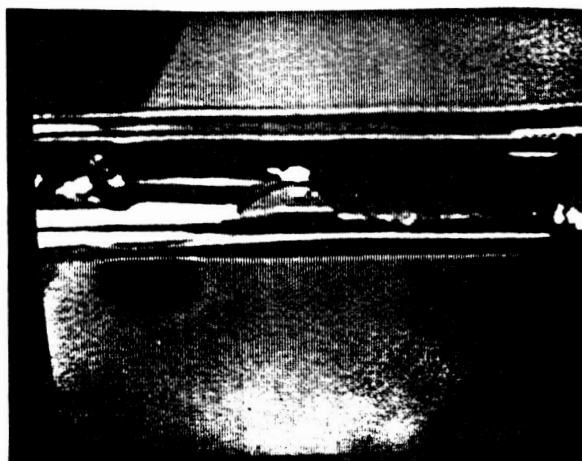


Figure 2. Large air bubble on wall in mercury-filled ampoule.

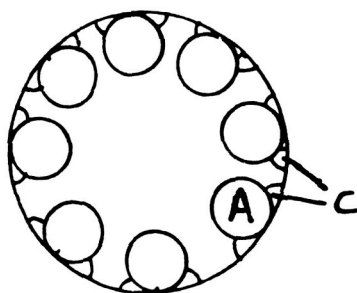


Figure 3. Hypothesized behavior of mercury column in ampoule B containing internal capillaries A. C represents air columns.

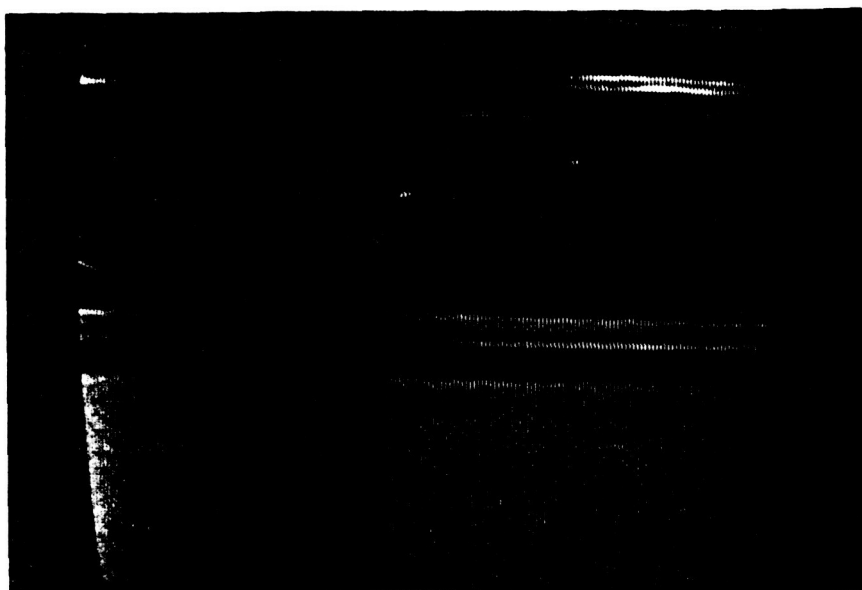


Figure 4. Corner-on view of small column of mercury in a triangular ampoule. The two dark ellipses are the portions in contact with the ampoule walls.

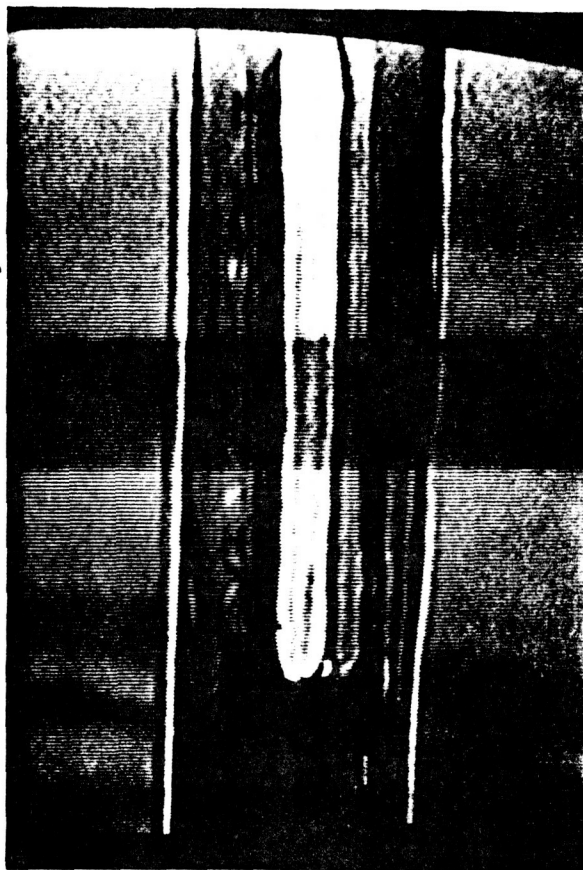


Figure 5. Face-on view of long column of mercury in a triangular ampoule.
The long shiny portion is that in contact with the ampoule wall.



Figure 6. Air bubbles in water.

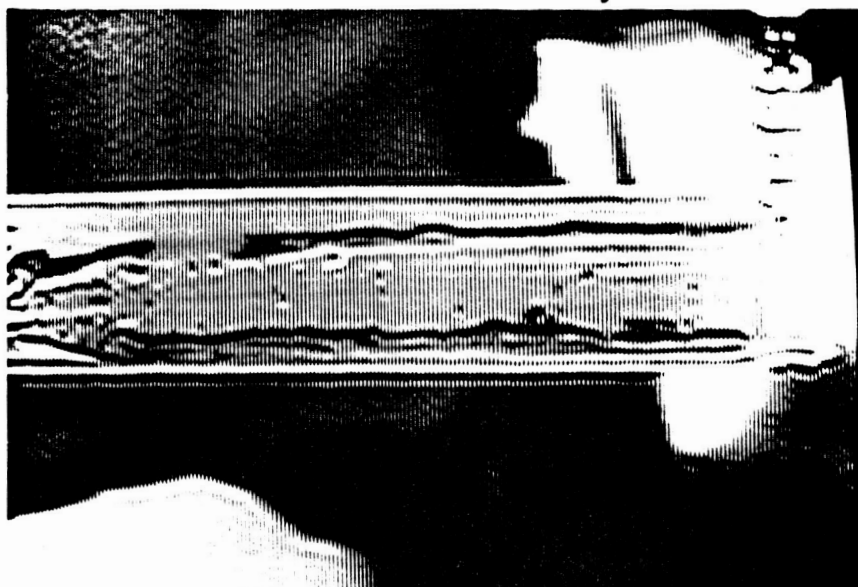


Figure 7. Large air bubble surrounded by wavy film of water.

APPENDIX F
Submitted to J. Crystal Growth

BEHAVIOR OF A NON-WETTING MELT IN FREE FALL: THEORETICAL

RADHA SEN^{*} and WILLIAM R. WILCOX
Department of Chemical Engineering
Clarkson University, Potsdam, NY 13676, USA

ABSTRACT

In a previous paper the experimental equilibrium configurations of a non-wetting liquid in an ampoule were described. Theoretical analyses of these configurations are described here. In a cylindrical ampoule a bubble/bridge configuration is predicted to be stable only up to a critical volume of gas, beyond which separated columns of liquid form. This critical bubble volume decreases as the contact angle of the liquid on the ampoule increases. In a triangular ampoule the liquid contacts the ampoule along the center of the faces and not in the corners. As the contact angle increases beyond 90° , the contact width decreases.

^{*}Present address: University of Minnesota, Minneapolis.

1. Introduction

In a companion paper [1], we reported on experiments performed during parabolic flights of NASA's KC135 aircraft. Cylindrical and triangular ampoules were partially filled with a non-wetting liquid. In cylindrical ampoules the liquid formed columns, either completely separated by gas or connected by a liquid bridge along one wall. Since a bridge can be regarded as a gas bubble on the opposite wall of the ampoule, this is known as the bubble/bridge configuration. The two configurations in cylindrical ampoules are shown schematically in Figure 1.

In ampoules with a triangular cross-section, the liquid pulled away from the corners (the vertices), and contacted the ampoule walls only along their centers.

In the present paper we estimate the total energy of each of the three configurations described above. From these we show that the bubble/bridge configuration becomes unstable with respect to the separated-column configuration above a critical bubble size which depends on the contact angle of the melt on the ampoule wall. Similarly the contact width for minimum energy in the triangular ampoules is shown to be a function of contact angle.

The symbols in the following developments are defined in the table of nomenclature at the end of this paper.

2. Cylindrical Ampoules

Temperature, total volume inside the ampoule, and the volume of the liquid are assumed to be constant. The liquid forms only two columns, either completely separated by gas or connected by a bubble/bridge, and not in contact with the ends of the ampoule. All liquid-gas surfaces are assumed to be hemispherical with constant radius of curvature and known contact angle at the solid/liquid/air interface.

The total interfacial free energy inside the ampoule is:

$$F = A_{1s}\gamma_{1s} + A_{1a}\gamma_{1a} + A_{sa}\gamma_{sa} \quad (1)$$

where A_{1s} , A_{1a} and A_{sa} are the surface areas between liquid (1), air (a) and solid (s). Here γ_{1s} , γ_{1a} and γ_{sa} are the corresponding surface energies. Thus for each configuration the problem is to estimate these surface areas under the given constraints.

For the separated-columns configuration Equation (1) becomes [2]:

$$F = 2\pi a L_{\text{air}} \gamma_{1s} + 4A_{\text{cap}} \gamma_{1a} + [2\pi(L - L_{\text{col}}) + 3\pi a^2] \gamma_{sa} \quad (2)$$

where a is the ampoule radius, A_{cap} is the surface area of each of the four hemispherical end caps on the two columns of liquid, L is the length of the ampoule, L_{col} is the total length of the liquid columns along the axis, and L_{air} is the total length of the air columns in the ampoule measured along the wall. Equation (2) is non-dimensionalized by dividing areas by a^2 , surface energies by γ_{1a} , and the total surface energy by $a^2 \gamma_{1a}$, to obtain:

$$F^* = 2\pi L_{\text{air}} \gamma_{1s} / \gamma_{1a} + 4A_{\text{cap}} + [2\pi(L^* - L_{\text{col}}^*) + 2\pi] \gamma_{sa} / \gamma_{1a} \quad (3)$$

In a similar fashion the total dimensionless surface energy for the bubble/bridge configuration may be shown to be [2]:

$$F^* = [2\pi(L - L_{\text{C+B}}) / a + (A_{\text{sa}})_{\text{bubble}} / a^2 + 3\pi] \gamma_{sa} / \gamma_{1a}$$

$$\begin{aligned}
& + [(A_{la})_{\text{bubble}}/a^2 + 2A_{\text{cap}}/a^2] \\
& + [2\pi L_{C+B}/a + 2R/a + (A_{sa})_{\text{bubble}}/a^2] \gamma_{ls}/\gamma_{la}
\end{aligned} \tag{4}$$

where R is the radius of curvature of the bubble (see Figure 2), L_{C+B} is the sum of the lengths of liquid columns B and C (see Figure 1), $(A_{la})_{\text{bubble}}$ is the liquid/air area of the bubble and $(A_{sa})_{\text{bubble}}$ is the solid/air surface area of the bubble. Numerical integration as shown in Figure 2 is used to obtain $(A_{la})_{\text{bubble}}$ and $(A_{sa})_{\text{bubble}}$.

Numerical calculations were performed corresponding roughly to the experiments [1], with an ampoule radius a of 0.98 cm and $\gamma_{sa} = 78 \text{ erg/cm}^2$ (for silica [3]) for several different contact angles, ampoule lengths, liquid-air surface energies, and volumes of liquid. In each case the value of γ_{ls} was calculated by the relation between contact angle θ and surface energies, $\gamma_{ls} = \gamma_{sa} - \gamma_{la} \cos\theta$. As shown in Fig. 3 the total surface energy of the separated-column configuration is independent of the length of gas separating the columns (provided the liquid does not contact the ends of the ampoule). On the other hand, the total surface energy of the bubble/bridge configuration increases as the size of the bubble increases. Since equilibrium corresponds to the lowest total energy of the system, we expect the bubble/bridge configuration to be stable below the gas bubble volume where the energy curves for the two configurations cross over.

Figure 4 shows that the critical crossover bubble volume is a strong function of contact angle, but is almost independent of the total amount of liquid in the ampoule. The critical bubble volume is plotted vs. contact angle and γ_{la} in Figure 5. The experimental values [1] of 1.2 cm^3 for 110° and 0.9 cm^3 for 130° fall exactly on the top line of Figure 5, which is for a

liquid-air surface energy of 500 erg/cm^2 . The literature [3] gives a value of 484 erg/cm^2 for the surface energy of mercury at 20°C .

3. Triangular Ampoules

Figure 6 shows the triangular ampoule geometry analyzed, with air in the corners and liquid contacting the ampoule walls over width W . The end caps were assumed to be hemispherical, which can only be approximately true.

The total dimensionless surface free energy of the system is:

$$F^* = 3W^*H^*\gamma_{ls}/\gamma_{la} + [4\pi r_{\text{cap}} + (\pi-2\alpha)R^*H^*] + 3(1-W^*)H^*\gamma_{sa}/\gamma_{la} \quad (5)$$

where L is the width of the side walls, $F^* = F/L^2\gamma_{la}$, r_{cap} is the radius of each hemispherical end cap, $R^* = r/L$ is the dimensionless radius of curvature of the liquid-air interface in the corners, $W^* = W/L$ is the dimensionless contact width, and $H^* = H/L$ is the dimensionless length of the liquid along the center.

Numerical computations were performed for conditions similar to the experiments: side width $L = 1.25 \text{ cm}$, ampoule length $H = 10 \text{ cm}$, volume of liquid $= 5 \text{ cm}^3$, $\gamma_{sa} = 78 \text{ erg/cm}^2$, γ_{la} from 200 to 484 erg/cm^2 , and a contact angle ranging from 90 to 160° . Typical results are shown in Figure 7. The equilibrium contact width is that giving the minimum surface energy. Figure 8 shows the equilibrium contact width vs. contact angle and liquid/air surface tension. In the experiments [1] the contact angle was 120 to 130° and the contact width was somewhat over $1/2$, which lies near the bottom curve on Figure 8.

Acknowledgement

This research was supported by NASA under Contract NAS8-34891.

References

- [1] R. Sen and W.R. Wilcox, J. Crystal Growth (in press).
- [2] R. Sen, Ph.D. Thesis, Clarkson University (1985).
- [3] P.C. Hiemenz, ''Principles of Colloid and Surface Chemistry,'' Dekker, NY, pp. 215, 245.

Nomenclature

Cylindrical Ampoule

A_{cap}	Surface area of the end cap (m^2).
A_{la}	Interfacial area between liquid and air (m^2).
A_{ls}	Interfacial area between liquid and solid (m^2).
A_{sa}	Interfacial area between solid and air (m^2).
a	Radius of the cylindrical tube (m).
dx	Thickness of an infinitesimal section of the bubble (cm).
F	Total interfacial free energy inside ampoule (J)
H	Height of the bubble at its center (see Figure 2) (m).
h	Height of the bubble at distance x from its center (see Figure 2) (m).
L	Length of the ampoule (cm).
L_{air}	Total length of the air columns in the separated-columns configuration (m).
L_{C+B}	Sum of the lengths of regions B and C in Figure 1 for bubble/bridge configuration (m).
L_{col}	Length of the liquid column in the separated-columns configuration (m).
R	Radius of curvature of the bubble (m).
γ_{la}	Surface energy between liquid and air (J/m^2).
γ_{ls}	Surface energy between liquid and solid (J/m^2).
γ_{sa}	Surface energy between solid and air (J/m^2).
θ	Contact angle of liquid on the solid in air (radian).
•	Dimensionless

Triangular Ampoule

F	Total interfacial free energy inside ampoule (J).
H	Length of the liquid column to the end caps (m).

L Width of the wall (see Figure 6) (m).
R Radius of curvature at the corners (m).
 r_{cap} Radius of the end cap (m).
W Width of contact on the wall.
 α $(7/6)\pi - \theta$ (radian).

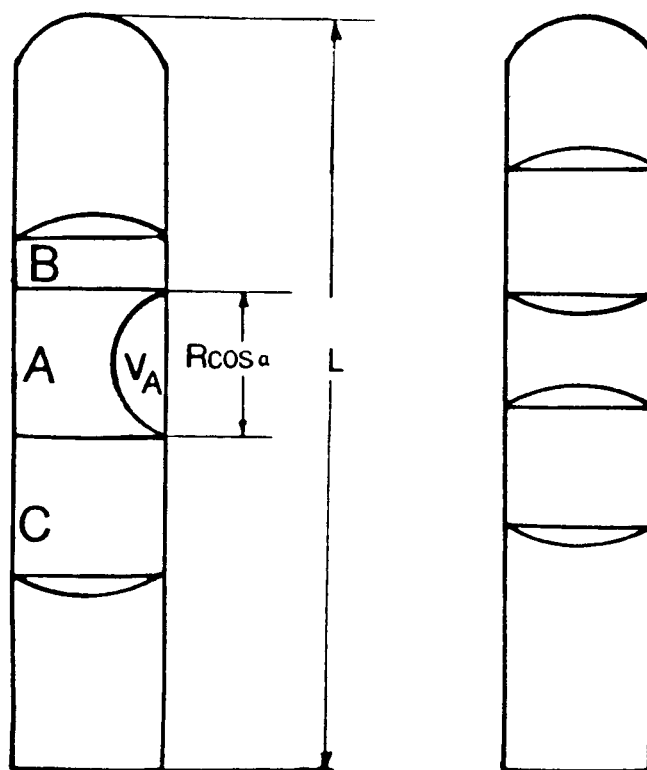


Figure 1. Two equilibrium configurations observed in cylindrical ampoules.

(a) Bubble/bridge configuration. A, B and C mark the three regions referred to in the calculations.

(b) Separated columns configuration.

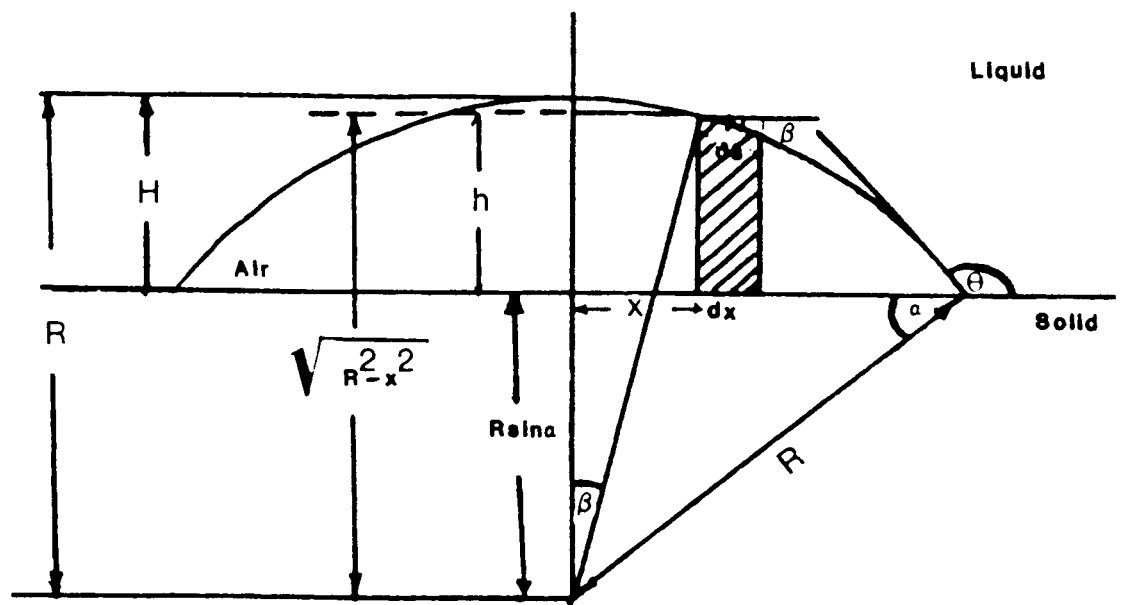


Figure 2. Side view of the bubble/bridge configuration showing the nomenclature and the coordinate system used to numerically calculate the solid/air and liquid/air surface areas.

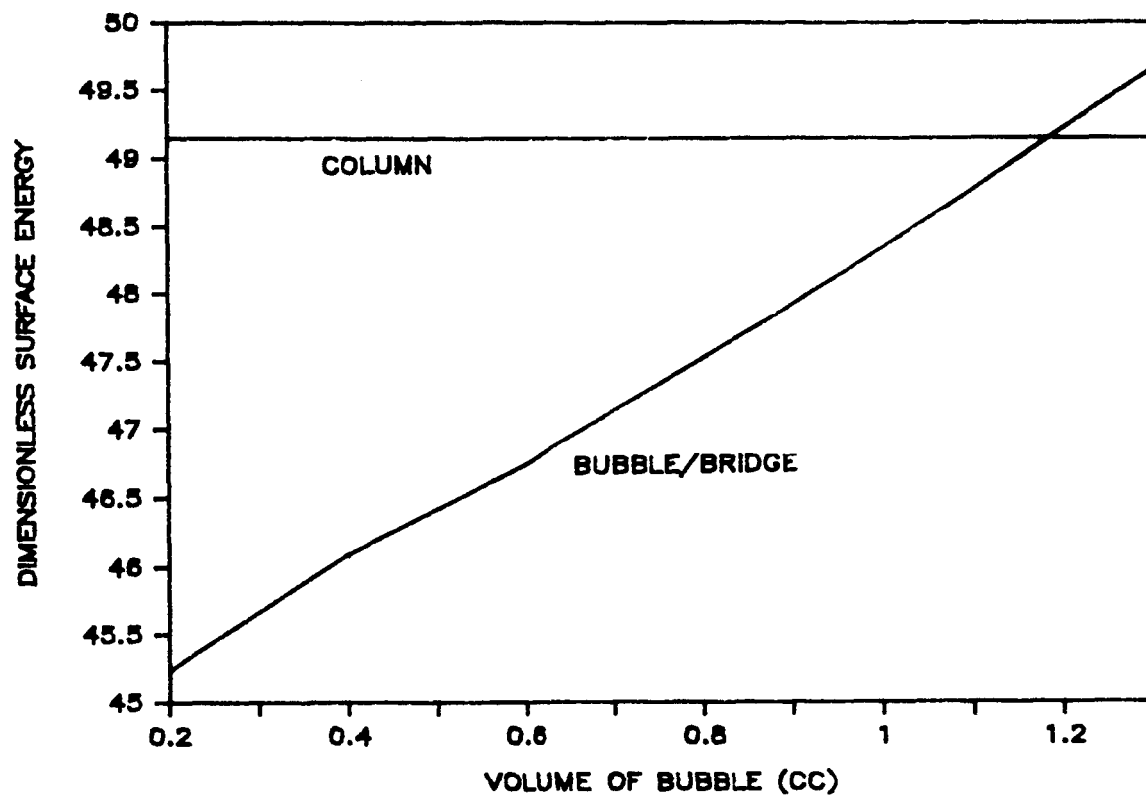


Figure 3. Total dimensionless surface energy F^* for cylindrical ampoule versus volume of air bubble for $\gamma_{la} = 484 \text{ erg/cm}^2$ (mercury [3]), $\gamma_{sa} = 78 \text{ erg/cm}^2$ (silica [3]), contact angle $\theta = 120^\circ$, 0.98 cm radius, 14 cm long and 20 cm^3 of liquid.

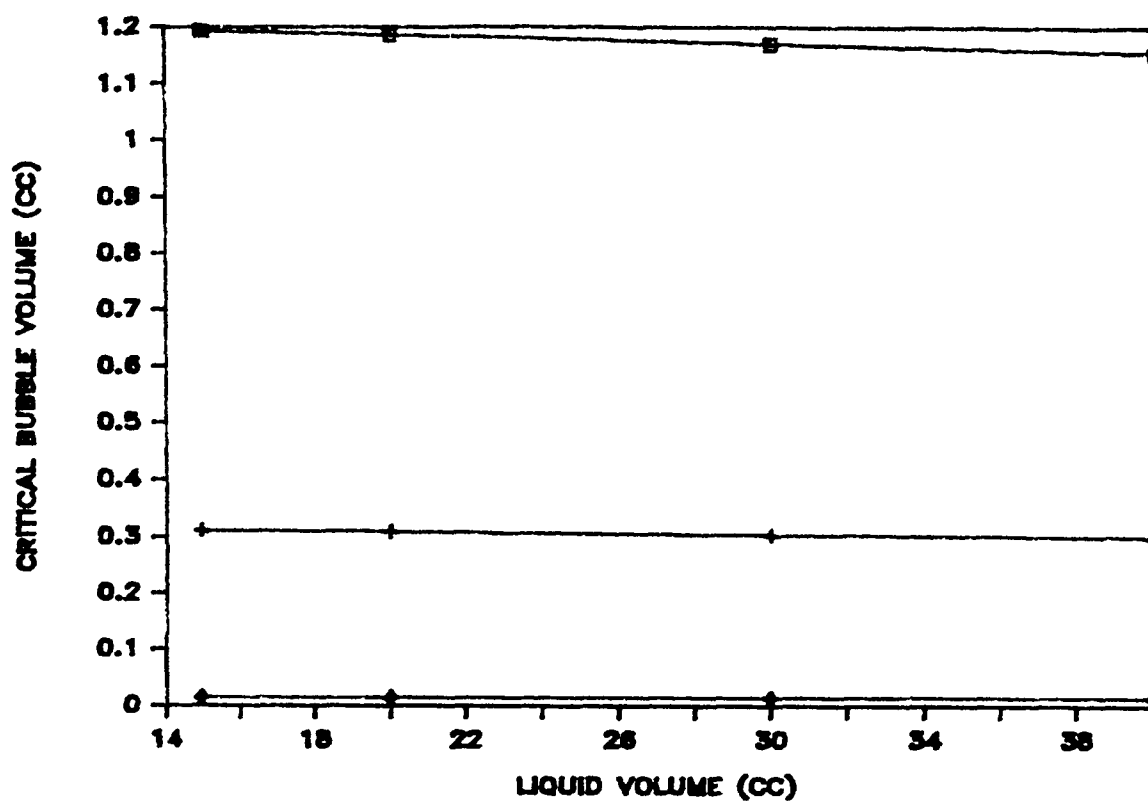


Figure 4. Influence of liquid volume for three different contact angles, γ_{sa}
 $= 78 \text{ erg/cm}^2$, $\gamma_{la} = 484 \text{ erg/cm}^2$, ampoule length = 20 cm. Top,
 120° ; middle, 150° ; bottom 170° .

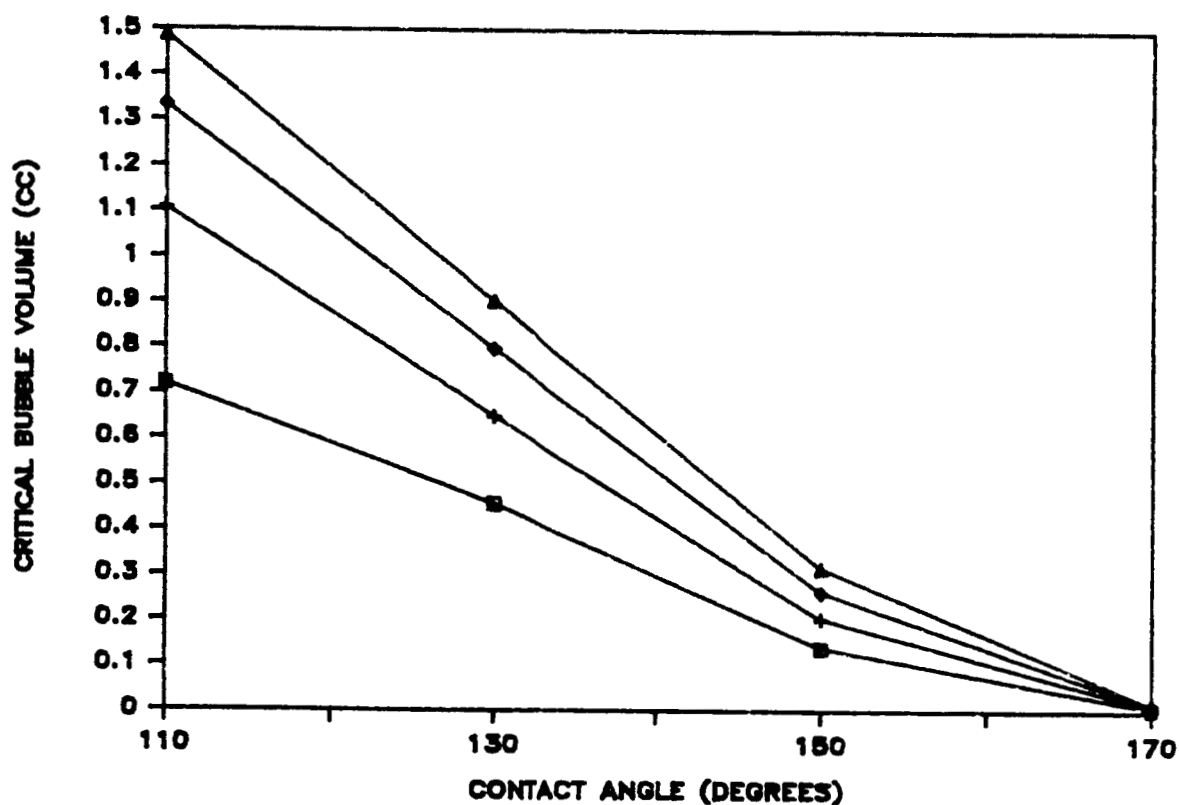


Figure 5. Critical bubble volume versus contact angle θ and liquid/air surface tension for a solid/air surface energy of 78 erg/cm^2 , 20 cm ampoule length and 20 cm^3 of liquid.

Top curve: $\gamma_{la} = 500 \text{ erg/cm}^2$

Second: 400 erg/cm^2

Third: 300 erg/cm^2

Bottom curve: 200 erg/cm^2

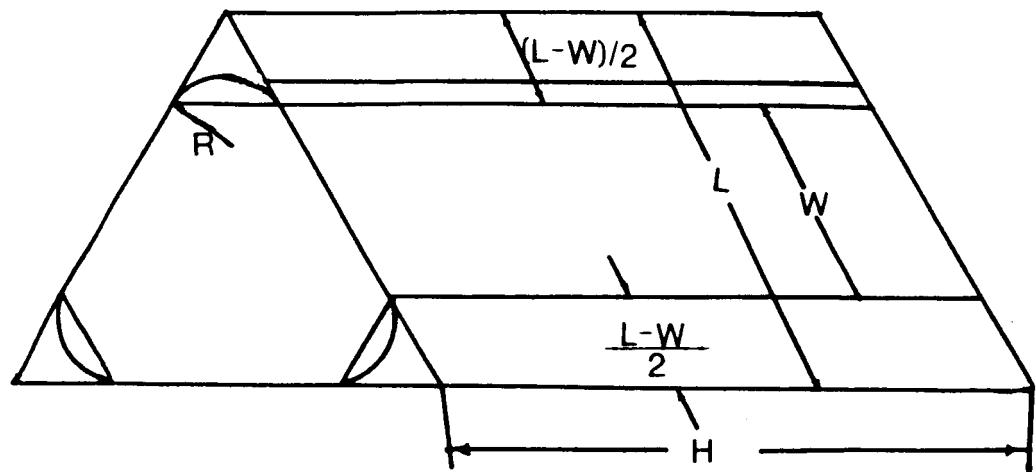


Figure 6. Schematic of the liquid configuration in a triangular ampoule.

End caps not shown.

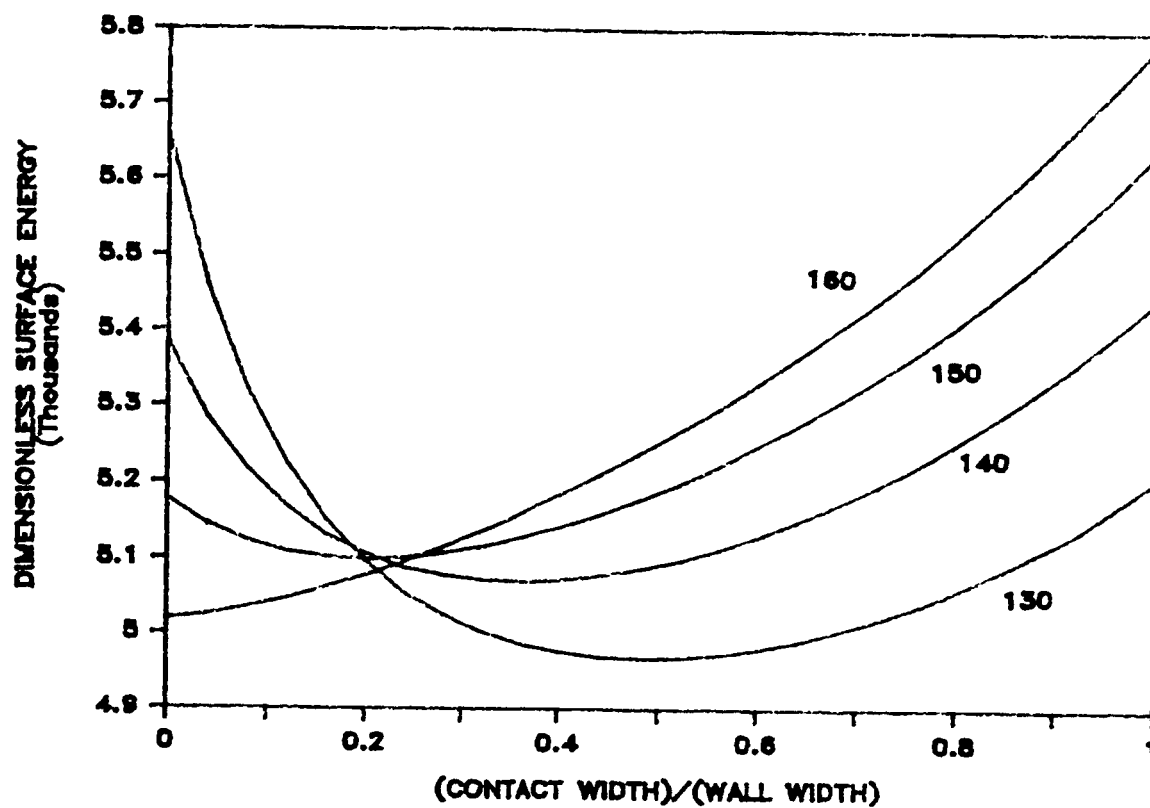


Figure 7. Plot of total dimensionless surface energy F^* versus dimensionless contact width W^* for a liquid/air surface energy of 484 erg/cm^2 , a glass/air surface energy of 78 erg/cm^2 , and four different contact angles (as shown).

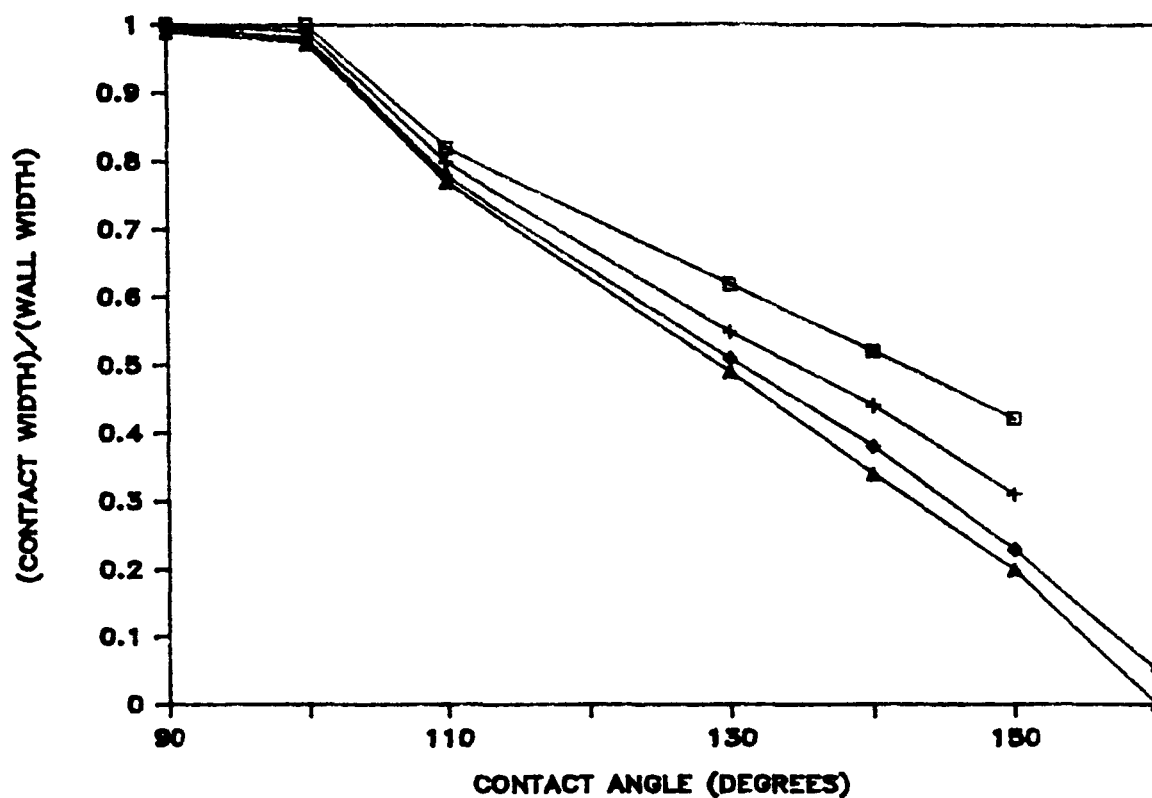


Figure 8. Dimensionless equilibrium contact width versus contact angle θ for a solid/air surface energy of 78 erg/cm^2 and liquid/air surface energies of 484 (bottom), 400, 300 and 200 (top) erg/cm^2 .

APPENDIX G

Journal of Crystal Growth 00 (1986) JCG00790
North-Holland, Amsterdam

TWINNING OF DODECANEDICARBOXYLIC ACID

Radha SEN * and William R. WILCOX

Department of Chemical Engineering, Clarkson University, Potsdam, New York 13676, USA

Received 14 June 1985; manuscript received in final form 9 December 1985

Twinning of 1,10-dodecanedicarboxyl acid (DDA) was observed in 0.1 mm thick films with a polarizing microscope. Twins originated from polycrystalline regions which tended to nucleate on twin faces, and terminated by intersecting one another. Twinning increased dramatically with addition of organic compounds with a similar molecular size and shape. Increasing the freezing rate, increasing the temperature gradient, and addition of silica particles increased twinning. We propose that twins nucleate with polycrystals and sometimes anneal out before they become observable. The impurities may enhance twinning either by lowering the twin energy or by adsorbing on growing faces.

1. Introduction

Mechanical twinning seems to be well understood. On the other hand, formation of twins during crystal growth remains a mystery. The crystallographer explains growth twinning as arising solely from stacking errors or accidents, which are more likely when the energy of the twin is small (e.g., refs. [1,2]). If this viewpoint was accurate, twinning would be a random event increasing with increasing growth rate (e.g., refs. [3-5]). Experimentally, other growth conditions have a large influence. For example, the number of twins formed in directionally-solidified InSb-GaSb alloys was reduced by doing the solidification in space [6,7] and in a magnetic field [8].

Growth twinning has sometimes been attributed to purely mechanical effects (e.g., ref. [9]). Thus, for example, it was speculated that twins in bismuth were caused by small drops of melt trapped during solidification (bismuth expands upon freezing) [10]. Twins in films of silicon held between silica and solidified in the (110) direction were attributed to plastic deformation [11]. Annealing was thought to reduce the number of twins in liquid-encapsulated Czochralski growth of in-

dium phosphide by reducing the differential thermal stress between the InP and the B_2O_3 [12]. On the other hand, straining InSb-GaSb alloys at elevated temperature [13] and CdTe at room temperature [14] had no effect on the number of twins. Twins did form during annealing of fcc metals, but without stress applied [15]. In vacuum evaporation of thin gold films it was suggested that small twins formed by mechanical deformation while large twins formed in growth accidents [16].

Growth twinning has been observed to increase with increased growth rate [14,17] or supercooling [18-20]. On the other hand, diphenyl crystals grown from the vapor twinned less at 4°C undercooling than at 1°C [21]. Twinning is often dependent on the presence of particular impurities, sometimes being increased [19,20,22-27], and sometimes decreased [12,24,28], by the impurity. Addition of silicon to gallium arsenide caused scum to form on the surface of the melt in liquid-encapsulated Czochralski (LEC) growth and subsequent twin formation [29]. Growing with excess arsenic reduced twinning [28]. In LEC of InP, twinning was significantly reduced by maintaining the angle between the surface of the growing crystal and the (111) axis below 19.58° [12]. In hydrothermal growth of epistilbite, twinning decreased sharply with rising temperature [30].

* Current address: University of Minnesota, Minneapolis, Minnesota, USA.

Several investigators have studied twins in solidified aluminum alloys [31–43]. Some claimed the twinned grains originated at a lattice defect [32,40], while others attributed them to growth accidents [36] or to nucleation on the chill face [43]. There are conflicting conclusions on the role of the freezing rate [31–33].

Indium antimonide solidified in $\langle 211 \rangle$ in space had more (111) twins than when grown on earth, with twinning becoming more frequent down the crystal [34]. The lattice constant increased at the same time and a connection with twinning was suggested.

The twin plane observed experimentally does not always correspond to the lowest energy twin plane. Thus, for example, KBr grown from aqueous solutions formed non-coherent (211) twins rather than (111) [24]. Potassium chloride formed twins with a coherent (211) surface while NaCl formed coherent (111) twins [45].

Clear-cut interpretation of prior experimental results was generally not possible because the growth and twinning were not directly observed; only the final twinned solid was studied. We report here on experiments performed on a transparent film with polarized microscopy that permitted twins to be observed as soon as they were formed.

2. Experimental Methods

Details of the experiments are given elsewhere [46]. Cells were prepared by placing a small amount of an organic compound on a glass microscope slide and covering this with a 20×40 mm cover glass. This assembly was placed on a hot plate to melt the organic. The cell was removed from the hot plate and placed on a wooden bench top. A metal spatula was pressed down on the cover glass to force out excess organic and bubbles. When the organic had solidified the excess was scraped from the edges and epoxy cement applied. This procedure produced cells containing a layer of organic about 0.1 mm thick. In one cell, 0.05 mm diameter bare copper and constantan thermocouple wires were run into the organic layer from opposite sides of the 20 mm span of the cover glass. The junction

was located in the center. Directional solidification along the length of a cell was carried out by translating over a 8.3 mm wide heater, which formed a wide molten zone in the organic. In one set of experiments an additional heater was placed at the end of the cell to permit the temperature gradient at the freezing interface to be varied. The temperature profile in the cell was measured by translating the cell containing the thermocouple past the heater at $3.41 \mu\text{m/s}$. The interfacial temperature gradient was obtained by measuring the slope at the DDA melting point and dividing this by the freezing rate.

Twenty seven different organic compounds were tested for their tendency to form twins that are readily observable with a polarizing microscope. Conspicuous twins occurred only with 1,10-dodecanedicarboxylic acid (DDA henceforth). DDA is monoclinic with a melting point of 130°C . The existence of twins was determined by placing a slide under the microscope between crossed polarizers. The slide was rotated so that adjacent twins had the same color and intensity. It was then rotated until a maximum contrast was obtained, and then again for the opposite maximum contrast. The angles between the two positions of maximum contrast and the position of no contrast were equal, about 50° to 60° . During solidification, adjacent twins formed a characteristic re-entrant angle growth interface of about 150° . The twin boundaries were very straight. The number of twin boundaries across the 20 mm width of the cell was counted every 10 to 15 min during a run.

The DDA was purchased from Aldrich Chemical Co. of Milwaukee with a listed purity of 99 to 99.6%. For some experiments this was zone refined with 28 downward passes at 14 mm/h in a 13 mm ID Pyrex tube.

3. Results

Twins originated in the original unmelted starting material, at existing twin boundaries, and polycrystalline regions that formed spontaneously at the growing interface. Fig. 1 shows two sets of twins and the polycrystalline regions from which they grew. The polycrystals nucleated primarily on



Fig. 1. DDA between polarizers adjusted to give the maximum contrast between adjacent twins. The arrows indicate the twin boundaries. The polycrystalline regions are marked with P (80 \times).

growing twin faces, especially when the interface was perturbed by blowing puffs of air on the cell or when the hot stage was moved rapidly. More polycrystals formed at higher cell translation rates.

The initial number of twins propagating from the unmelted solid varied somewhat from cell to cell. To see if rapid cooling during cell preparation influenced this twinning, several cells were prepared by slowly cooling them on the hot plate by turning the power off, while maintaining the spatula pressure. This did not influence the initial number of twins.



Fig. 2. Twin termination by intersection of twin boundaries at A and twin formation at an existing twin boundary at O.

Twins terminated by intersecting one another, as shown in fig. 2. No movement of twin or grain boundaries was observed either during the 1 h heatup prior to initiation of translation or in the solid after solidification. Because of the continued birth and termination of twins, the number of twin boundaries tended to fluctuate down the cell. Occasionally a general downward trend was noted, and less often an upward trend. To provide better statistics, several replicate runs on different cells were performed for a given set of experimental conditions. Using standard Student *t* statistical techniques the 95% confidence limits were calculated for the mean number of twin boundaries for each set of conditions. These are the numbers shown in the tables and represented by the verticle bars in the figures. When least squares lines were calculated, the raw data were used rather than mean values.

3.1 Influence of purity

Table 1 shows that zone refining reduced twinning by over an order of magnitude. Addition of three impurities to zone refined material caused large increases in twinning, three had little effect, and one decreased the number of twin boundaries. It is interesting to note that the three impurities that increased twinning had a molecular structure similar to that of DDA, i.e. aliphatic carboxylic acids. Furthermore, as shown in fig 3, the number of twins increased approximately linearly as the

Table 1
Influence of impurities on number of twin boundaries per 20 mm of interface at a freezing rate of 3.4 $\mu\text{m/s}$

Material	Number of twin boundaries per 20 mm ^{a)}
Original DDA (~ 0.4% impurity)	24.2 to 27.9
Zone refined DDA	1.3 to 2.6
Zone refined plus 7% 1 naphthoic acid	0.0 to 0.8
Zone refined plus ~ 6% maleic anhydride	1.2 to 2.7
Zone refined plus 5% oxalic acid	1.8 to 3.8
Zone refined plus ~ 6% chloroacetic acid	2.2 to 4.2
Zone refined plus ~ 6% succinic acid	10.9 to 14.6
Zone refined plus 5% lauric acid	23.6 to 25.6
Zone refined plus 7% sebacic acid	29.1 to 32.2

^{a)} 95% confidence limits given

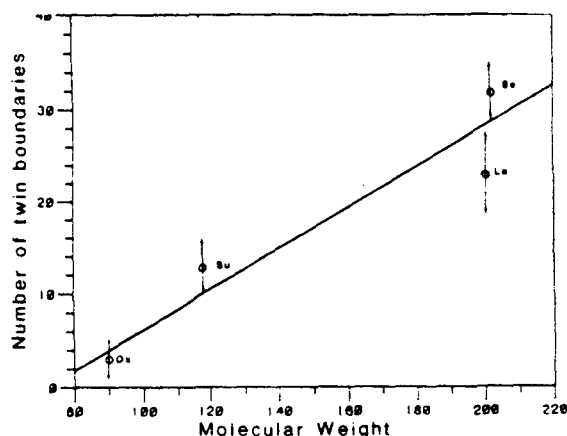


Fig. 3. Twin boundaries per 20 mm of interface versus molecular weight of added impurity. The line is a least-squares fit and the arrows shown 95% confidence limits. Here Ox denotes oxalic acid, Su succinic acid, Se sebacic acid and La lauric acid.

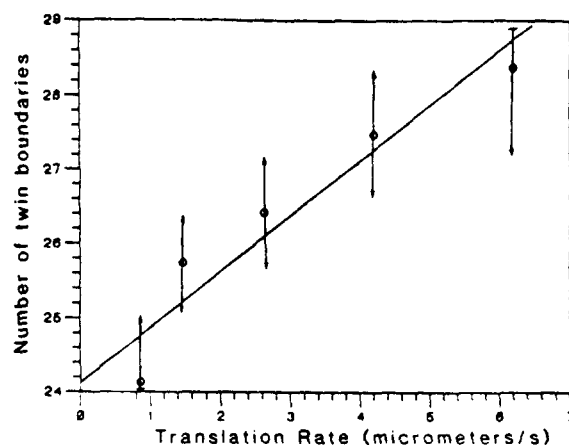


Fig. 4. Influence of freezing rate on twinning of non zone-refined DDA at an interfacial temperature gradient of 1.7 K/cm. The line is given by eq. (1).

molecular weight of these compounds approached that of DDA (230). Note that while sebacic and lauric acids have nearly the same molecular weights, sebacic acid is a decarboxylic acid like DDA while lauric acid is a monocarboxylic acid. More twins were obtained with sebacic acid than with lauric acid.

It is expected that impurity molecules are incorporated more readily in a freezing organic compound when they are near the shape and size of the host molecules. Thus it appears likely that a necessary and sufficient condition for impurities to increase twinning of DDA is for them to be incorporated in the growing crystals, i.e. for the distribution coefficient to be not far from one.

3.2 Influence of freezing rate

Fig 4 shows the influence of cell translation rate on the number of twin boundaries for non-zone refined DDA. The line is a least squares fit to the raw data (not the means at each velocity), and is given by:

$$N = 24 + 0.7V, \quad (1)$$

where N is the number of twin boundaries along the 20 mm interface and V is the translation velocity in $\mu\text{m/s}$. The probability that the slope is

positive is greater than 99.95%. For zone refined DDA the velocity dependence is

$$N = 1.4 + 0.7V, \quad (2)$$

with a 97% probability that the slope is positive. It is interesting to note that the velocity dependence is the same for zone-refined and for non-zone-refined material.

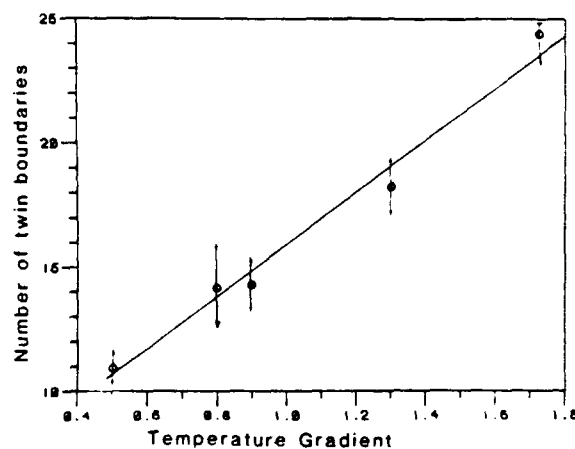


Fig. 5. Influence of interfacial temperature gradient in K/min on twinning of non zone-refined DDA at a freezing rate of 3.41 $\mu\text{m/s}$. The line is given by eq. (2) after conversion to K/min.

3.3 Influence of interfacial temperature gradient

Fig. 5 shows the influence of temperature gradient on twinning, with a least squares fit to the raw data yielding

$$N = 4.9 + 0.23G, \quad (3)$$

where G is in K/cm. The probability that the slope is positive is greater than 99.95%.

All of the other results presented in this paper were obtained in the absence of the auxiliary heater, i.e. for an interfacial temperature gradient of 84 K/cm (1.7 K/min. at 3.41 $\mu\text{m/s}$).

3.4 Influence of foreign particles

Table 2 shows the influence of adding a small amount of insoluble foreign particles to non zone-refined DDA. These are ordered by the mean number of twin boundaries counted. In all cases the particles were immediately engulfed by freezing DDA; no particle movement was observed. In most cases the particles had little influence on twinning. Silicon and SiO_2 caused about a 25%

increase in the number of twin boundaries, with better than 99.95% probability. Since elemental silicon in air is always covered with a layer of SiO_2 , this indicates that surface properties may be important. All of the particles except for Teflon had a coefficient of linear thermal expansion much less than organic compounds, so stress due to differential thermal expansion is unlikely to be responsible for the increased twinning with Si and SiO_2 . It is interesting to note that new twins could not be observed emerging from Si or SiO_2 particles, but came from polycrystals as usual.

Four metals appeared to cause an appreciable decrease in twinning. However these particles tended to produce many polycrystals which could have obscured twins. It was noticed that these particles also tended to cluster together and cause the layer of DDA to be thicker than usual. To investigate the influence of cell thickness several cells were prepared without pressing down on the cover glass. This yielded DDA layers almost twice as thick as normal. These cells, which contained no added particles, produced many polycrystals and no observable twins.

Table 2

Influence of addition of 0.8 to 4.2 wt% of insoluble particles to non-zone-refined DDA, with a translation rate of 3.1 $\mu\text{m/s}$ and an interfacial temperature gradient of 1.7 K/cm; the particles are arranged in order of increasing average number of twin boundaries

Particle	Size (μm)	Twin boundaries	Thermal expansion coefficient (10^{-5} K^{-1})
Cu	8	12.2 to 13.7	1.72
Ni	17	11.7 to 16.3	1.32
Pb	~ 70	13.9 to 17.0	2.92
Al	~ 15	15.1 to 16.8	2.75
FeO	~ 16	17.8 to 21.9	1.20
SiC	50	19.4 to 21.1	0.40
Teflon		18.4 to 22.2	14.70
Ag	~ 6	20.1 to 23.0	1.95
None		21.7 to 22.7	~ 15
LiF	< 1	22.2 to 24.5	3.86
Cr_2O_3	< 1	21.5 to 25.4	0.84
Graphite	~ 3	23.6 to 25.3	0.20
Si	~ 50	26.6 to 27.9	0.20
SiO_2	20 to 25	26.2 to 28.8	1.07

4. Discussion

We have shown that twins emerge from polycrystalline masses, although not all polycrystals give rise to twins and some polycrystals give rise to two twin boundaries. We might expect that nucleation of polycrystals would be enhanced by constitutional supercooling, which in turn is increased by an increased impurity concentration, increased segregation, higher freezing rate, and smaller temperature gradient. While the number of twin boundaries did increase with increased impurity concentration and increased freezing rate, it decreased with increased segregation and smaller temperature gradient. Therefore constitutional supercooling was not responsible for twinning.

DDA solidifies with facets. Thus it probably grows with an appreciable supercooling, increasing with increasing growth rate. The supercooling is probably still more on the twin faces, which were favored sites for polycrystal formation. Furthermore a twin face would be more likely to create its

twin than a randomly oriented grain.

We hypothesize that polycrystals containing twins nucleate preferentially on twin faces due to the supercooling that exists there. A smaller temperature gradient would allow the polycrystal to anneal immediately after its nucleation and sometimes permit twins to anneal out. Impurities incorporated in the solid would be attracted to the twin boundary, to take up some of the mismatch there. This would lower the twin energy and increase its probability of nucleation.

Alternatively, impurities of similar size and shape to DDA might tend to adsorb on the face of a growing twin and enhance the nucleation of other twins. Likewise SiO_2 could nucleate twins due to its surface properties.

Since the "annealing" time after solidification is inversely proportional to the temperature gradient and the freezing rate, it would be interesting to investigate the influence of temperature gradient at a variety of freezing rates. Unfortunately we used a fixed freezing rate.

Acknowledgement

This research was supported by NASA Contract NAS8-34891.

References

- [1] R. Kern, *Bull. Soc. Franç. Minéral. Crist.* 84 (1961) 292.
- [2] G.H. Wolten and A.B. Chase, *J. Chem. Phys.* 41 (1964) 2966.
- [3] T.W. Donnelly, *Am. Mineralogist* 52 (1967) 1.
- [4] M.J. Buerger, *Am. Mineralogist* 30 (1945) 469.
- [5] P. Hartman, *Z. Krist.* 107 (1956) 225.
- [6] J.F. Yee, M.C. Lin, K. Sarma and W.R. Wilcox, *J. Crystal Growth* 30 (1975) 185.
- [7] R.A. Lefever, W.R. Wilcox and K.R. Sarma, *Mater. Res. Bull.* 13 (1978) 1175.
- [8] S. Sen, R.A. Lefever and W.R. Wilcox, *J. Crystal Growth* 43 (1978) 526.
- [9] P.I. Antonov, S.I. Bakhholdin, Yu.G. Nosov and E.S. Kalitina, *Dokl. Akad. Nauk SSSR. Ser. Fiz.* 47 (1983) 2213.
- [10] R.S. Wagner and H. Brown, *Trans. Met. Soc. AIME* 224 (1962) 1185.
- [11] Y. Komen and Z.A. Weinburg, *J. Appl. Phys.* 56 (1984) 2213.
- [12] W.A. Bonner, *J. Crystal Growth* 44 (1981) 1.
- [13] S. Sen, W.R. Wilcox and R.A. Lefever, *Met. Trans.* 9A (1978) 462.
- [14] A.W. Vere, S. Cole and D.J. Williams, *J. Electron. Mater.* 12 (1983) 551.
- [15] H. Glieter, *Acta Met.* 17 (1969) 1421.
- [16] A.H. King, *Phys. Status Solidi* 76(a) (1983) 629.
- [17] A.G. Cullis, N.G. Chew, H.C. Webber and D.J. Smith, *J. Crystal Growth* 68 (1984) 624.
- [18] J.W. Faust and H.F. John, *Trans. Met. Soc. AIME* 233 (1965) 230.
- [19] Y. Aoki and Y. Nakamura, *J. Crystal Growth* 67 (1984) 579.
- [20] G. Mantovani, G. Vaccari, C.A. Accorsi, D. Aquiridano and M. Rubbo, *J. Crystal Growth* 62 (1983) 595.
- [21] A.G. Orlova, O.G. Kozlova and E.D. Dukova, *Vest. Gos. Univ., Geol.* 38 (1983) 37.
- [22] M. Bafleur, A. Munoz-Yague and A. Rocher, *J. Crystal Growth* 59 (1982) 531.
- [23] G.R. Booker and B.A. Joyce, *Phil. Mag.* 14 (1966) 301.
- [24] W.R. Wilcox and A. Leon, *J. Crystal Growth* 8 (1971) 230.
- [25] W.F. Alewijn and P. Honig, in: *Principles of Sugar Technology*, Vol. 1, Ed. P. Honig (Elsevier, Amsterdam, 1959) ch. 9.
- [26] G. Vavrinecz, *Intern. Sugar J.* 41 (1939) 345.
- [27] B.M. Smythe, *Australian J. Chem.* 20 (1967) 1115.
- [28] R.T. Chen and D.E. Holmes, *J. Electrochem. Soc.* 129 (1982) 2382.
- [29] R. Fornari, C. Paonici, L. Zonotti and G. Zucalli, *J. Crystal Growth* 63 (1983) 415.
- [30] H. Ghobarkar, *Crystal Res. Technol.* 19 (1984) 1571.
- [31] S. Miyazawa, U. Honma and S. Oya, *J. Japan Inst. Light Metals* 22 (1972) 143.
- [32] J.A. Eady and L.M. Hogan, *J. Crystal Growth* 23 (1974) 129.
- [33] K. Chattapahyay, S. Lele and P. Ramachandrarao, *J. Crystal Growth* 49 (1980) 322.
- [34] J. Herengual, *J. Metals* 4 (1952) 385.
- [35] K.T. Anst, F.M. Krill and F.R. Morral, *J. Metals* 4 (1952) 865.
- [36] W.D. Walther, C.M. Adams and H.F. Taylor, *Trans. Am. Foundrymen's Soc.* 61 (1953) 664.
- [37] W. Roth and M. Schippers, *Z. Metallk.* 47 (1956) 78.
- [38] L.R. Morris, J.R. Carruthers, A. Plumtree and W.C. Winegard, *Trans. Met. Soc. AIME* 236 (1966) 1286.
- [39] S. Watanabe, U. Honma and S. Oya, *J. Japan Inst. Light Metals* 19 (1969) 279.
- [40] F. Matsiaishi, U. Honma and S. Oya, *J. Japan Inst. Light Metals* 19 (1969) 287.
- [41] H. Fredriksson and Hillert, *J. Mater. Sci.* 6 (1971) 1350.
- [42] L.R. Morris and M. Ryvola, *Microstruct. Sci.* 9 (1981) 241.
- [43] H. Kato and J.R. Cahoon, *Met. Trans.* 16A (1985) 690.
- [44] F.R. Khashimov et al., in: *Proc. 3rd European Symp. on Material Science in Space*, Grenoble, European Space Association SP-142 (1979).
- [45] H. Hattori, *J. Crystal Growth* 66 (1984) 205.
- [46] R. Sen, PhD Thesis, Clarkson University (1985).